Universität Regensburg Juli 2010

Dissertation

Transition Metal Antimony (III) Oxidehalides

Synthesis, Crystal Structure, and Physical Characteristics

Karolina Warzycha

aus Bełchatów, Polen

Zur Erlangung des Doktorgrades der Naturwissenschaften
(Dr. rer. nat.) der Fakultät für Chemie und Pharmazie der
Universität Regensburg

for my family

Acknowledgements

Although every thesis has only one formal author, a great many people contribute directly or indirectly to various stages of its development; from the formulation of the problem, followed by the conception of a possible solution, development of a method to reach the solution, experimental and theoretical verification, and (more often than not) several repetitions of this process. There are many people who deserve my great thanks for their contributions to these cycles.

First must come my thesis advisor Prof. Dr. Arno Pfitzner. He was able to identify a problem, bring together all of the elements necessary to tackle the problem, and then guide the project to a successful completion. I am very grateful to have had the chance to work with him and to learn from his experience.

I would also like to thank Prof. Dr. Werner Massa and Dr. Michael Bräu for their guidelines on crystal structure solutions, insightful analysis of the problems and the time dedicated to constructive discussions. I learnt a great deal working with them, and that knowledge is certainly reflected in this work.

I would especially like to thank Mr. Franz Rau for his great support in the experimental work, for excellent cooperation, and for his friendship.

Special thanks for Marta Walczak, Dr. Irina Anuscă, and Anatoli Esch for their friendship and invaluable assistance in the first weeks of my stay in Germany.

I would like to sincerely thank Dr. Manfred Zabel and Sabine Stempfhuber for the opportunity to perform the single crystal X-ray diffraction measuremants, for their trust, and uncomplicated collaboration.

I am also grateful to Ulrike Schiessl and Manuele Avola for DTA and DSC measurements, Dr. Martina Andratschke for powder X-ray diffraction measurements, Dr. Marc Schlosser and Daniela Garcia for help and valuable instructions concerning Raman spectroscopy, and Bjoern Bartel for EDX measurements.

My gratitude also goes to Dr. Richard Weihrich for his help with electronic band structure calculations.

I would also like to thank Dr. Matthias Sperl for magnetic-moment measurements and Joachim Rewitzer for ICP-OES measurements.

My thanks goes also to Inga Schellenberg from the group of Prof. R. Pöttgen from Westfälische-Wilhelms University in Münster for Mössbauer spectroscopy investigations.

I should also express my thanks to all other members of the research groups of Prof. Dr. Arno Pfitzner and Prof. Dr. Nikolaus Korber for the camaraderie and the good working atmosphere: Sharareh Arab Bagheri, Frederic Bachhuber, Sven Bauernfeind, Dr. Thomas Bernet, Stefan Dankesreiter, Stephan Eckl, Dominik Frank, Wilhelm Haas, Dr. Diana Hoppe, Dr. Inna Ivaschenko, Stefanie Joseph, Katharina Kaschura, Freya von Krziwanek, Dr. Kurt Lange, Alois Lecker, Dr. Michael Leitl, Iris Luber, Patrick Pohla, Thomas Rödl, Nadia Rück, Dr. Stefan Seidlmayer, Florian Truksa.

Most importantly, I would like to thank my family and friends for their unwavering support over the past three years. My family has provided so much support to me, I could never find a place to begin to describe how important they are and how much I appreciate them.

Finally, Wojtek Giziewicz has been a source of so much of my happiness. I am grateful for his support and patience with me and his assistance during the last weeks, days, and minutes of my thesis writing.

Die praktischen Arbeiten wurden von September 2006 bis Dezember 2009 am Institut für Anorganische Chemie der Universität Regensburg am Arbeitskreis Prof. Arno Pfitzner durchgeführt.

Diese Arbeit wurde von Herrn Prof. Dr. Arno Pfitzner angeleitet.
Einreichung des Promotionsgesuchs: Juni 2010
Tag der mündlichen Prüfung: 6. Juli 2010

Prüfungsausschuss:
Vorsitzender: Herr Prof. Dr. F.-M. Matysik
1. Gutachter: Herr Prof. Dr. A. Pfitzner
2. Gutachter: Herr Prof. Dr. N. Korber
Weiterer Prüfer: Herr Prof. Dr. B. Dick

Eidesstattliche Erklärung

Hiermit versichere ich an Eides statt, dass ich die vorliegende Arbeit ohne unzulässige Hilfe Dritter und ohne Benutzung anderer als der angegebenen Hilfsmittel angefertigt habe; die aus anderen Quellen direkt oder indirekt übernommenen Daten und Konzepte sind unter Angabe des Literaturzitats gekennzeichnet. Die Arbeit wurde bisher weder im In- noch im Ausland in gleicher oder ähnlicher Form einer anderen Prüfungsbehörde vorgelegt. Ich versichere an Eides statt, dass ich nach bestem Wissen die reine Wahrheit gesagt und nichts verschwiegen habe.

Regensburg, Juni 2010

Karolina Warzycha

Abstract

The thesis “Transition Metal Antimony (III) Oxidehalides. Synthesis, Crystal structure, and Physical Characteristics” addresses emerging areas in the study of a group of new inorganic compounds, which follow the synthesis concept based on the formation of oxidehalides containing lone-pair cations having an asymmetric coordination due to the presence of stereochemically active lone pairs of electrons and late transition metal cations. The aim of the investigations was to determine the structural parameters and physical properties of the analysed compounds and compare them with one other in order to obtain optimal synthesis strategies. Materials with stereochemically active lone pairs like Te^{4+}, Se^{4+}, Pb^{2+}, Sb^{3+} are of particular interest because of their functional physical properties (for example magnetic, superconducting, or semiconducting properties).

This work also aimed to study the general tendency of bonding preferences in transition metal oxidehalides containing lone pair elements, which is based on the Lewis acidity/alkalinity of lone pair elements prefering to bond with oxygen anions, while transition metals accept both O^{2-} and X^{-} in an oxidehalide environment. In these investigations Sb^{3+} cations were used as the p-element, since the properties of such materials have not yet been described and only a limited number of crystal structures were previously known. Several transition metal cations were used: Co^{2+}, Zn^{2+}, and Cd^{2+}.

The synthesis techniques used were solid state and hydrothermal reactions. All compounds described in this work have been investigated by single crystal and powder X-ray diffraction. The crystal structures were additionally confirmed by spectroscopic methods and material analysis (EDX and other spectroscopic techniques). Diffuse reflectivity measurements were performed to characterise the electronic band gap, followed by successful DFT calculations confirming those results. A magnetic moment measurement was performed for $CoSb_2O_3Cl_2$, resulting in the finding of Co^{2+} with $3d^7$ high-spin configuration.

In all investigated crystal structures lone pairs of electrons, belonging to Sb^{3+} cations and halide anions, both sometimes referred to as “chemical scissors” aggregate to form non-bonded volumes, resulting in low-dimensional materials with a layered or chained character.

Contents

List of Figures

List of Tables

1. Introduction

Various examples of adduct compounds of either neutral or low charged polymers of phosphorus, phosphorus or arsenic chalcogenides, or chalcogen chains have been reported in the past. These electron-rich main group element polymers or cages form adduct compounds on the one hand with electron-rich transition metal ions, for example Cu^{1+} or Hg^{2+} in compounds such as $(CuI)_3P_{12}$ [1,2], $(CuI)_8P_{12}$ [3,2], and $(CuI)_2P_{14}$ [4, 2] consisting of formally neutral phosphorus polymers embedded in a copper iodide matrix. A further example is $HgI_2{\cdot}As_4S_4$ [5], which is built of nearly linear HgI_2 molecules and for the first time preserved As_4S_4 cages in an undistorted manner. On the other hand, adduct compounds are formed with the hard Lewis acidic cations of early transition metals, e.g., Nb^{5+} or Ta^{5+} in compounds such as $(NbCl_5)_2(\beta\text{-}P_4S_4)$ or $(TaCl_5)(\beta\text{-}P_4S_6)$ [6]. In the case of the P_4S_{10} cage, the co-crystal $(Ta_2Cl_{10})(P_4S_{10})_2$ [7] is formed with Ta_2Cl_{10} demonstrating the necessity of dense packing which might even overcome the energy gain due to an adduct formation of the transition metal cation with the cage molecules. Novel allotropes of phosphorus were isolated from the solid materials $(CuI)_8P_{12}$ and $(CuI)_3P_{12}$ by extracting copper with an aqueous solution of KCN, thus demonstrating the strong bonding interactions between Cu^{1+} and neutral strands of elemental phosphorus. On the other hand it becomes obvious from Raman spectroscopic investigations of $HgI_2{\cdot}As_4S_4$ and $(HgBr_2)_3(As_4S_4)_2$ [8] that these adduct compounds are based on very weak bonding interactions between the metal atoms and the ligand cage molecules. This can be regarded as the major reason for the occurrence of uncleaved or even undistorted As_4S_4 cages in these molecular complexes. They are the first examples for complexes with these cages acting as ligands. However, as result of the interdiffusion of solutions of $As_4S_3{\cdot}M(CO)_5$ (M = Cr, W) and $CuCl_n$ (n =1, 2) in CH_2Cl_2 and CH_3CN, respectively, the first examples of solid state phases $As_4S_3(CuCl)_n$ (n = 1, 2) [9] with the novel aspect of only S coordination of the intact As_4S_3 cage were found. Comparison of the Raman frequencies of $As_4S_3(CuCl)$ with freshly prepared As_4S_3 suggested significant interactions between the cage S atoms and the ${}^1_\infty[CuCl]$ chain. A first attempt to describe the nature of these bonding interactions and to quantify them showed the great importance of electron correlation and dispersive forces. Typically the use of state of the art DFT calculations does not provide any insight in this type of extremely weak binding interactions [7]. Presence of the neutral and low-charged structural entities like polymers and cages embedded in a copper halide matrix provides access to the synthesis of compounds based on complex thioanions. Compounds such as $(CuI)_3Cu_2TeS_3$ [10], $CuClCu_2TeS_3$ [11], $CuBrCu_{1.2}TeS_2$ [12] and $(CuI)_2Cu_3SbS_3$ [13] are objects of special interest in terms of ionic conductivity properties. Impedance spectroscopic data allow one to draw the conclusion that the highest conductance was observed in compounds containing a high amount of copper halide, while a low conductivity is associated with a higher chalcogen content.

Regarding this great number of adduct compounds of pure pnicogen, mixed pnicogen chalcogenide, and purely chalcogen atoms containing ligands towards both electron-rich and electron-poor transition metal cations, one might wonder whether oxides of the elements with stereochemically active lone pair of electrons, both pnicogen: Sb^{3+}, Bi^{3+}, As^{3+} and chalcogen Te^{4+}, Se^{4+} are also suitable ligands in similar systems. As reported by Galy *et al.* [14] the effective volume of the lone pair of electrons, named E, is approximately the same as the volume of an O^{2-} ion. The so-called lone pair cation mixed with transition metal cations in the presence of halide ions, can be regarded as "chemical scissors" forcing the transition metals to build chains or layers in the structure. The tendency of segregation of the structure into chalcophile and halophile parts dominates in these compounds. The transition metal cations are typically coordinated to halogen, and the lone pair cations to both oxygen and halogen atoms. This tendency is caused by the chemical nature of so-called lone pair elements, which are rather strong Lewis acids, hence they preferably bond to the strong Lewis base O^{2-}. The non-bonding volume between chalcophilic and halophilic parts is cohabited by the lone pairs of chalcogen atoms and terminal halogens of the halidic substructure. As a result of ongoing investigations of the synthesis concept of using lone pair elements Se(IV) and Te(IV) oxohalogenide containing both Zn(II) and Cu(II) transition metals, the group of isostructural compounds $Zn_2(TeO_3)Cl_2$ [15], β-$Zn_2(SeO_3)Cl_2$ [16], $Zn_2(TeO_3)Br_2$ [17], and $CuZn(TeO_3)Cl_2$ [18] has been reported in recent years. Those compounds typically consist of charge-neutral layers, considered as two-dimensional infinite molecules, connected via weak van der Waals forces. On the other hand, the synthesis strategy of using so-called lone-pair elements, combined with transition metal halides, can be used to design materials with unique magnetic topology [19]. The concept of serching for new transition metal oxides is related to the investigations of low-dimensional superconducting cuprates. As a result of investigations of the system CuO-CuX_2-SeO_2 (X = Cl, Br), a group of interesting compounds with complicated crystal structures was obtained, i.e. $Cu_3(SeO_3)_2X_2$ (X = Cl, Br) [20] and $Cu_9O_2(SeO_3)_4Cl_6$ [21]. A subject to be considered was also the possibility of forming isostructural analogues with Se(IV) and Te(IV) cations. Extensive research in this area resulted in obtaining isostructral crystal structures $Cu_3Bi(TeO_3)_2O_2Cl$ [22] and $Cu_3Bi(SeO_3)_2O_2Cl$ [23]. In contrast to those isostructural analogues, one may cite as a counterexample the structures of $Ni_5(TeO_3)_4Cl_2$ [24] and $Ni_5(SeO_3)_4Cl_2$ [25], which exhibit a similar formula, but a different crystal structure. Both selenium(IV) and tellurium(IV) atoms are asymmetrically three-coordinated by oxygen atoms with trigonal pyramidal or tetragonal geometry, if taking into account the lone pair of electrons. In $Ni_5(SeO_3)_4Cl_2$ the Cl1 and Cl2 anions bridge to two and three nickel(II) ions, respectively, while in $Ni_5(TeO_3)_4Cl_2$ they are not identical and are oriented toward the interlayer space.

Attempts to synthesise low-dimensional quantum phases in the system CuO-CuX_2-TeO_2 resulted in the discovery of two crystal structures $Cu_2Te_2O_5X_2$ (X = Cl, Br) [26, 27]. Both structures may be expected to exhibit very interesting magnetic properties due to the presence of tetrahedral clusters of Cu^{2+} linked by Te-O units in the crystal structure. A measurement of the temperature dependence of the magnetic susceptibility and the calculated susceptibility fit together and permit the assumption that the system consists of independent copper(II) tetrahedra. Several years later the related $CuTe_2O_5$ [28] was investigated. Its crystal structure consists of edge-sharing $[CuO_6]$ octahedra forming Cu^{2+}-Cu^{2+} dimers, connected by Te-O ligands. Analysis of superexchange coupling between the Cu ions within structural dimers resulted in the second strongest coupling, while the strongest coupling was observed between Cu^{2+} linked by Te-O ligands, resulting in a super-superexchange interaction.

Herein, inspired by the large quantity of structurally fascinating compounds exhibiting interesting properties, a new group of compounds containing Sb^{3+} as a lone-pair cation will be presented. To the best of the author's knowledge only a limited number of investigations have been reported in the literature, namely in the systems CuX-Sb_4O_6 (X = Cl, Br, I). Therein, cage molecules Sb_4O_6 are embedded between layers of CuX ($CuSb_2O_3X$, X = Cl, Br) [29] or a complicated, heavily disordered structure is formed ($Cu_{20}Sb_{35}O_{44}Cl_{37}$) [30, 31]. The latter compound does not show a simple adduct character but nevertheless two different regions become obvious in the crystal structure, i.e., an anionic part built by copper(I)-chloride supertetrahedra and a cationic part consisting of cages of Sb, O, and Cl. One may also consider $CuSbTeO_3Cl_2$ [32] along with this group of compounds. Magnetic susceptibility measurements show diamagnetic properties corresponding to the magnetic behaviour of Cu^+, while based on conductivity measurements the compound may be classified as a one-dimensional Cu^+ ion conductor. An additional and final example of adduct compounds with the composition MX_2-Sb_4O_6 (M = transition metal, X = Cl, Br, I) is $CoSb_2O_3Br_2$ [33], comprising structural Co^{2+}-Co^{2+} dimers, with essential inter-dimer coupling within the layers, indicated by observation of long-range antiferromagnetic ordering below $T_N \approx 9$ K. The isostructural compound containing chlorine instead of bromine was found and is described in a subsequent chapter of this thesis.

The investigations presented here followed the "architectural concept" of forming transition metal oxidehalides containing Sb^{3+} cations as the pnicogen atom, resulting in new range of compounds. All compounds presented in this thesis were characterized using the X-ray diffraction method, which is a very important tool in area of materials research, on the borderline between chemistry and physics. The crystallographic characterisation of solid state materials allows for the understanding of the fundamentals of the crystal structure at the atomic level. This knowledge gives the chemist access to a large range of useful information like three dimensional packing of the atoms in solids, stoichiometry, density, symmetry, and finally the precise spatial arrangements of all of the atoms in the crystalline state. The structural chemistry findings open the way for research and understanding on the properties of new materials. One motivation for working with so-called lone-pair elements is to better understand the influence of lone pairs of electrons on structural architecture. Almost all of the compounds described below were grown via solid state reactions, although several were obtained by hydrothermal growth, which is still limited, due to the problems with control of the growth parameters. To more clearly demonstrate the structural informations, the new compounds were additionally characterized by spectroscopic methods.

2. Experiments

2.1. Chemicals and apparatus

2.1.1. List of chemicals

The chemicals listed in Table 2.1 were used in the synthesis of all compounds presented in this work.

Table 2.1.: List of chemicals including purity and manufacturer

Substance	Purity	Producer
α-Sb_2O_3	99%	Merck
$ZnCl_2$	ultra-pure	Ventron
$ZnBr_2$	99%	Acros
ZnI_2	98%	ABCR
ZnO	p.A.	Merck
$CdCl_2$	99.99%	Merck
$CdBr_2$	99.999% (ultra-dry)	Merck
CdI_2	99.999%	Aldrich
CdO	p.A.	Merck
$CoCl_2$	unknown	Synthesised
$CoBr_2$, $CoBr_2\cdot 6H_2O$	99%	Aldrich (dehydrated)
CoI_2	unknown	Synthesised
$SbCl_3$	unknown	Synthesised
$SbBr_3$	unknown	Synthesised
SbI_3	unknown	Synthesised
$Sb_4O_5Cl_2$	unknown	Synthesised
$Sb_4O_5Br_2$	unknown	Synthesised
HCl	p.A.	Merck
HBr	p.A.	Merck

2.1.2. Synthesis of antimony (III) iodide

Antimony (III) iodide was prepared according to Brauer [34]. A solution of iodine in toluene was refluxed with finely pulverized antimony until the characteristic iodine colour disappeared. The resulting yellow-green solution was filtered using an immersion suction filter to separate it from the unconverted Sb and subsequently allowed to crystallise, whereupon SbI_3 precipitates as red leaflets. Toluene was removed from the product in a vacuum desiccator over concentrated H_2SO_4.

$$\mathrm{Sb} + \frac{3}{2}\mathrm{I_2} \rightarrow \mathrm{SbI_3} \tag{2.1}$$

Finally, a recrystallisation with toluene was performed to obtain a pure product.

2.1.3. Synthesis of antimony (III) chloride and antimony (III) bromide

Antimony (III) chloride and antimony (III) bromide were prepared according to Brauer [34] from finely pulverized Sb_2S_3 and hot concentrated HX (X=Cl, Br).

$$\mathrm{Sb_2S_3} + 6\mathrm{HX} \rightarrow 2\mathrm{SbX_3} + 3\mathrm{H_2S} \tag{2.2}$$

Colourless $SbCl_3$ or yellow $SbBr_3$ precipitates were placed in a vacuum desiccator with P_2O_5.

2.1.4. Synthesis of antimony oxychloride and antimony oxybromide

$Sb_4O_5Cl_2$ and $Sb_4O_5Br_2$ were prepared according to Edstrand [35]. In this work solid α-Sb_2O_3 was disolved in HX (X = Cl, Br) and various amounts of water were added. The precipitates were filtered by suction and dried in an desiccator with P_2O_5. The best crystals of $Sb_4O_5Cl_2$ and $Sb_4O_5Br_2$ were obtained by solvothermal reaction of α-Sb_2O_3 and HX in sealed evacuated silica tubes annealed at 180 °C for 8 days.

2.1.5. Synthesis of cobalt (II) chloride

Cobalt (II) chloride was prepared according to the Brauer method [34]. Fine $CoCl_2{\cdot}6H_2O$ powder was placed in a flask with a ground joint and was covered with $SOCl_2$. The solution was refluxed for several hours. The excess $SOCl_2$ was then evaporated in a steam bath. The remaining $SOCl_2$ which clings to the product is removed by repeated evacuation of the flask.

$$\mathrm{CoCl_2} \cdot 6\mathrm{H_2O} + 6\mathrm{SOCl_2} \rightarrow \mathrm{CoCl_2} + 12\mathrm{HCl} + 6\mathrm{SO_2} \tag{2.3}$$

2.1.6. Dehydration of cobalt (II) bromide

Cobalt (II) bromide was prepared by careful heating of $CoBr_2{\cdot}6H_2O$ to 130-150°C under vacuum. [34]

2.1.7. Synthesis of cobalt (II) iodide

Preparation of anhydrous CoI_2 was performed according to Patnaik *et al.* [36] Fine cobalt and iodine powder were annealed in a sealed evacuated quartz ampoule at 400 °C for one week.

The final compositions of all synthesized adducts were confirmed by powder X-ray diffraction, followed by successful stoichiometric synthesis.

2.2. Sample preparation

2.2.1. Synthesis in ampoules

Almost all compounds presented in this work were synthesised by solid-state reactions. Appropriate amounts of precursor materials are weighed using analytical scales (accuracy 0.1 mg) and placed into a glass ampoule. The ampoule is evacuated to a pressure below 0.2×10^{-3} bar and hermetically sealed by melting the open end using a H_2/O_2 burner. The ampoule (length 3-5 cm, diameter 1 cm, wall thickness 1mm) is heated to an appropriate temperature in a furnace (length 0.5 m, diameter 8 cm). Exact reaction conditions will be presented in subsequent chapters. After cooling to room temperature, the ampoule is scored and broken open to remove the reaction product.

2.2.2. Solvothermal synthesis

Solvothermal synthesis is a technique in which the synthesis occurs in a sealed pressure vessel that allows common solvent such as water or alcohols to be heated far above their normal (standard pressure) boiling points. This method is used for liquid-state reactions. Sample preparation is similar to that of synthesis in ampoules, however liquid components are also placed in the ampoule. The contents of the ampoule are then frozen using liquid nitrogen, evacuated, and hermetically sealed. The ampoule is then supplied with water in a hermetically sealed autoclave. The crystal growth is performed under high temperature and pressure conditions. After slow cooling, the solid products of the reaction are removed by filtration and cleaned using appropriate solvents (water, ethanol, or ether).

2.2.3. Chemical transport reaction

A chemical transport reaction is a process for the purification and crystallisation of non-volatile solids. The technique involves the migration of a volatile derivative of the compound of interest through a hermetic reactor (typically an evacuated, hermetically sealed silica ampoule with a length of 15-20 cm) heated in a tube furnace. So-called

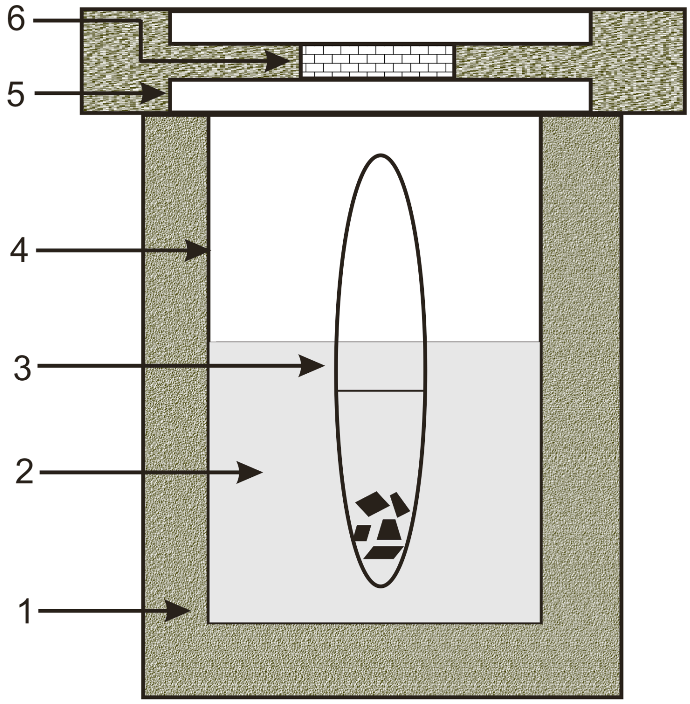

Figure 2.1.: Synthesis apparatus (1) stainless steel autoclave, (2) precursor solution, (3) ampoule, (4) teflon liner, (5) stainless steel lid, (6) spring

two-zone furnaces are employed for this purpose. The two heating zones result in a temperature gradient along the length of the ampoule. At one end of the ampoule, the volatile derivative of the substance of interest is created and migrates to the other end of the ampoule, which is held at a different temperature. At that end, the compound reverts to the desired solid form and the transport agent is liberated.

The general reaction equation can be formulated as shown below.

$$iA_{(s,l)} + kB_{(g)} + \ldots \longrightarrow jC_{(g)} + \ldots \tag{2.4}$$

Chemical transport techniques can be classified according to three basic methods based on gas flow, diffusion, and thermal convection.

In the case of flow transport (as shown in Figure 2.2, the agent B (typically in gas form at room temperature) is passed over a crucible with compound A in pellet or ground form, with temperature maintained at T_2. When C enters a subsequent chamber with different temperature T_1, C breaks down depositing the compound A and releasing the transport agent B. Depending on the transport agent in question, an inert carrier gas may additionally be used to maintain an appropriate equilibrium pressure at T_2. Additionally if B is not gaseous at room temperature a carrier gas and/or an additional chamber at the appropriate temperature may be used to first evaporate the transport agent B.

Diffusion principles are used particularly often, and may even be applied in simple

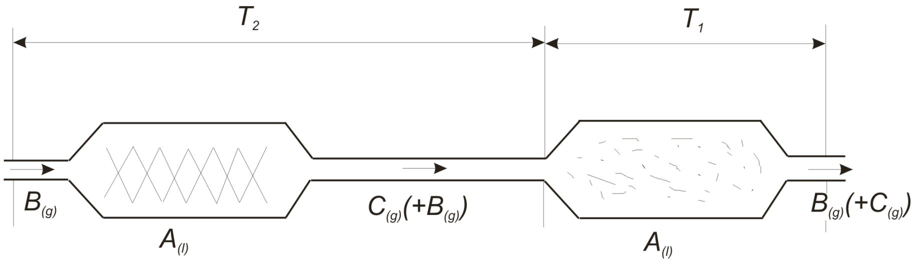

Figure 2.2.: Ideal flow arrangement for sediment transport in the temperature gradient; $iA_{(s,l)} + kB_{(g)} + \ldots \longrightarrow jC_{(g)} + \ldots$ [37]

quartz ampoules. In this case zone 1 is heated and the material travels to zone 2 (held at a lower temperature) due to a diffusion gradient in the gas phase, as shown in Figure 2.3. More complicated schemes can be used to transport material from two connected ampoules, where the "source" ampoule is later sealed off and detached from the "destination" ampoule.

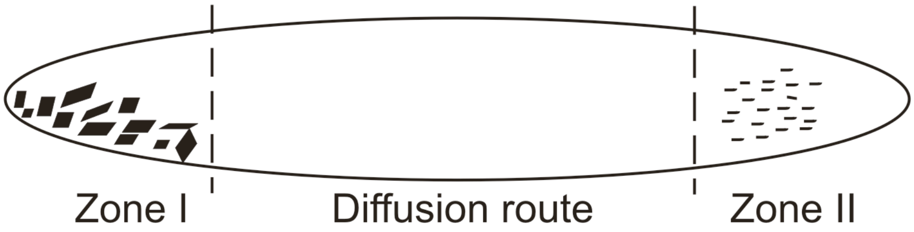

Figure 2.3.: Schematic illustration of chemical transport by diffusion. [37]

If one takes advantage of convection in additional to diffusion, the transport effect can be greatly increased. This is the case, for example, when relatively large diameter tubes or ampoules are held at an angle in a temperature gradient with the hot end pointing downwards and the cold end upwards.

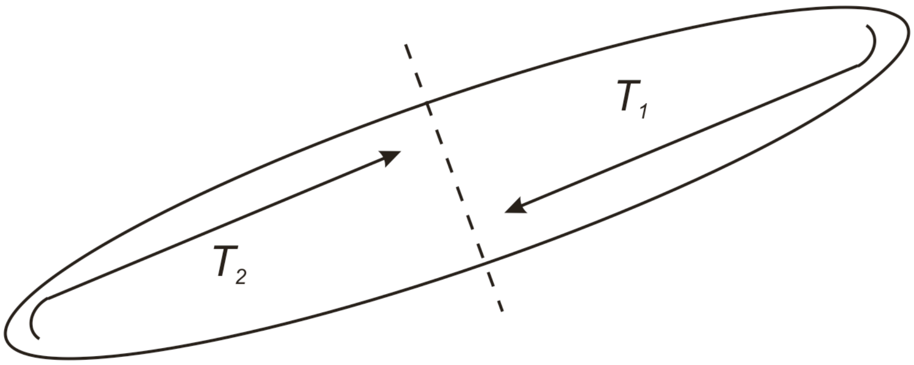

Figure 2.4.: Gas motion through thermal convection. For the temperatures $T_2 > T_1$. [37]

Table 2.2.: Summary of synthesis condition of new compounds (described in detail in subsequent sections)

Compound	Educts	Synthesis conditions
$ZnSb_2O_3Cl_2$	$ZnCl_2$, Sb_4O_6	melted, 400 °C, 14 days
$ZnSb_2O_3Br_2$	$ZnBr_2$, Sb_4O_6	melted, 450 °C, 14 days
$Cd_4Sb_8O_{12.5}Cl_7$	$CdCl_2$, Sb_4O_6	melted, 550 °C, 14 days
$Cd_4Sb_8O_{12.5}Br_7$	$CdBr_2$, Sb_4O_6	melted, 550 °C, 14 days
$ZnSb_2O_3Cl(OH)$	ZnO, $SbCl_3$, Sb_4O_6	hydrothermal, 90 °C, 7 days
	ZnO, $SbCl_3$,	hydrothermal, 90 °C, 7 days
$ZnSb_2O_3Br(OH)$	ZnO, $SbBr_3$, Sb_4O_6	hydrothermal, 90 °C, 7 days
	ZnO, $SbBr_3$,	hydrothermal, 90 °C, 7 days
$ZnSb_2O_3I(OH)$	ZnO, SbI_3, Sb_4O_6	hydrothermal, 90 °C, 7 days
	ZnO, SbI_3	hydrothermal, 90 °C, 7 days
$CdSb_2O_3Cl(OH)$	CdO, $SbCl_3$, Sb_4O_6	hydrothermal, 90 °C, 5 days
	CdO, $SbCl_3$,	hydrothermal, 90 °C, 5 days
$CdSb_2O_3Br(OH)$	CdO, $SbBr_3$, Sb_4O_6	hydrothermal, 90 °C, 5 days
	CdO, $SbBr_3$,	hydrothermal, 90 °C, 5 days
$CdSb_2O_3I(OH)$	CdO, SbI_3, Sb_4O_6	hydrothermal, 90 °C, 5 days
	CdO, SbI_3,	hydrothermal, 90 °C, 5 days
$Cd_2(OH)_3I$	CdO, SbI_3, Sb_4O_6	hydrothermal, 90 °C, 5 days
	$Cd(OH)_2$, I_2	hydrothermal, 90 °C, 4 days
$CdSbO_2Cl$	CdO, $SbCl_3$, Sb_4O_6	hydrothermal, subsequently annealed 600 °C, 7 days
$CdSbO_2Br$	CdO, $SbBr_3$, Sb_4O_6	hydrothermal, subsequently annealed 500 °C, 7 days
$CoSb_2O_3Cl_2$	$CoCl_2$, Sb_4O_6	melted, 450 °C, 10 days
$Sb_4O_5Cl_2$	HCl, Sb_4O_6	hydrothermal, 180 °C, 5 days
SbOCl	HCl, Sb_4O_6	hydrothermal, 90 °C, 5 days
$Sb_8O_{11}I_2$	SbI_3, Sb_4O_6	melted, 500 °C, 5 days

2.3. Characterisation Methods

2.3.1. Energy Dispersive X-ray Analysis (EDX)

Energy dispersive X-ray spectroscopy (EDX) is an analytical tool mostly used for chemical characterization. This method is based on the investigation of a sample through interactions between light and matter, analyzing X-rays in its particular case. The characterization is based in large part on the fundamental principle that each element of the periodic table has a unique electronic structure and a unique response to electromagnetic waves.

The EDX detector measures the intensity of emitted X-rays versus their energy as the material of interest is bombarded by an electron beam. The energy of the X-ray is characteristic of the element from which the X-ray was emitted. A spectrum of energy versus relative counts of the detected X-rays is obtained and evaluated for qualitative and quantitative determinations of the elements present in the sampled volume.

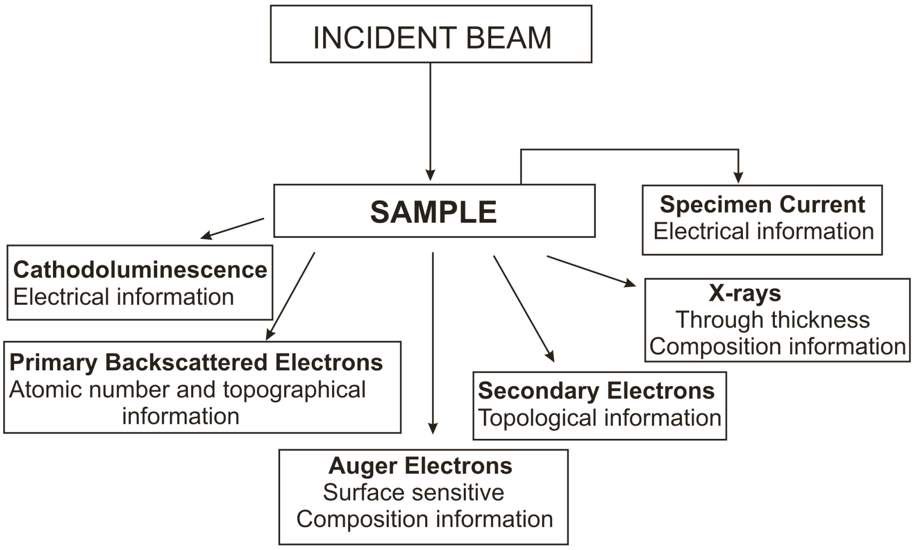

Figure 2.5.: Some of the processes that occur upon the bombardment of samples with electrons. [38]

Typical applications of EDX include:

- Phase identification and distribution
- Small component material analysis
- Coating composition analysis
- Rapid material alloy identification
- Surface contamination analysis
- Corrosion evaluations

Quantitative and qualitative analyses were performed using an FEI Quanta 400 F scanning electron microscope fitted with an EDAX detector. The images were visualised using Genesis [A] software.

2.3.2. Thermal analysis

Thermal analytical methods monitor differences in a particular sample property as temperature increases, or differences in temperature between a sample and a standard as a function of added heat. These methods are usually applied in the characterisation of solid materials.

Commonly thermal analysis techniques are:

- Differential Thermal Analysis (DTA)
- Thermogravimetry (TG)
- Differential Scanning Calorimetry (DSC)

Thermal analysis (DTA, TG and DSC) was performed using a SETARAM TG-DTA 92-16 and a Mettler Toledo DSC 30.

Differential Thermal Analysis (DTA)

Differential thermal analysis (DTA) is a technique that involves heating or cooling a test sample and an inert reference under identical conditions, and recording any temperature difference between the sample and reference. Because an inert reference is not subject to conversions that have signature thermal effects, the measured temperature difference depends on velocity of absorption or generation of heat in the test sample. A DTA diagram shows the differential temperature plotted against time or temperature.

Differential temperatures can also arise between two inert samples, but only when their response to the applied heat-treatment is not identical. In this case, DTA can be used to study thermal properties and phase changes which do not lead to a change in enthalpy. The baseline of the DTA curve should then exhibit discontinuities at the transition temperatures and the slope of the curve at any point will depend on the microstructural constitution at that temperature.

DTA techniques can be used to study substances which are subject to different endothermic or exothermic reactions: chemical reactions (oxidation, decomposition, reduction) and physical conversions (recrystallization, melting). DTA may be used to identify and determine the content of samples based on characteristic heat effects.

In conventional DTA, the basic equipment would be based on something like the system shown schematically in Figure 2.6.

The sample and reference are contained in a small Al_2O_3 crucible which was placed in contact with a thermocouple. The thermocouples should not be placed in direct contact with the sample to avoid contamination and degradation, although sensivity may be compromised. The voltage across the thermocouple is used to control furnace temperature such that the temperature of the sample under test should increase at a constant rate. The DTA signal is the difference between voltages of the sample and reference thermocouples, which is amplified, measured, and plotted as a function of sample temperature. All DTA measurements were performed under flowing argon.

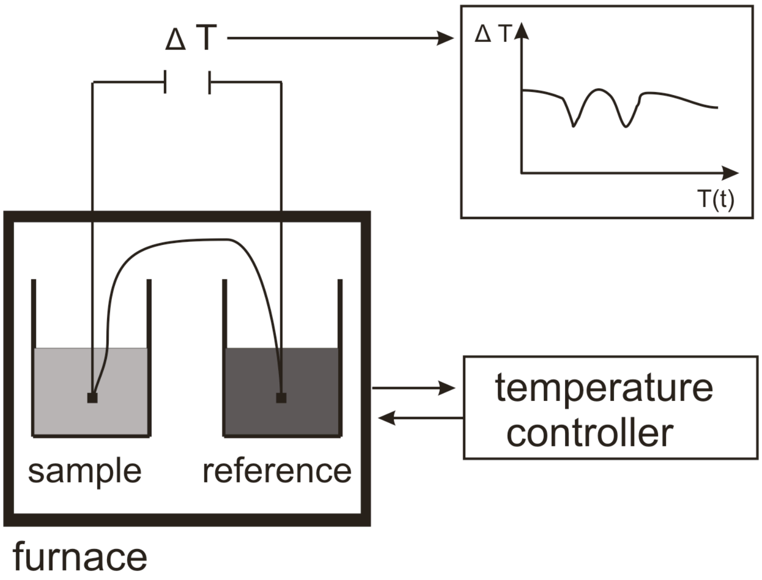

Figure 2.6.: Block schematic diagram of a DTA apparatus [39]

The small amount of sample was heated/cooled in a evacuated ampoules (ca. 3 mm diameter, 1 mm length) or in Al_2O_3 crucibles over the temperature range 25-1200°C.

Thermogravimetry (TG)

Thermogravimetry is an analytical technique that is based on the measurement of the mass of a substance warmed in a controlled atmosphere. Generally, the sample temperature is ramped at a constant rate, or otherwise changed according to a pre-programmed profile. The result of the measurement, called a thermogram, consists of the mass of the substance under test as a function of temperature and/or time. The principle application of TG is the analysis of substances, whose mass changes as temperature rises, either as a result of a chemical reaction (chemical decomposition, oxidation, reduction) or physical conversion (evaporation, sublimation).

The apparatus for TG consists of a precision balance, a furnace with programmable temperature controller, a reaction chamber, and a suitable recording system (Figure 2.7).

TG measurements were performed using a SETARAM TG-DTA 92-16. A small amount of sample material (6-8 mg) was placed into an open Al_2O_3 crucible and held under N_2 atmosphere. The heating rate was 10°C/min. The assembly is capable of continuously registering any weight changes in the test sample while it is being heat-treated.

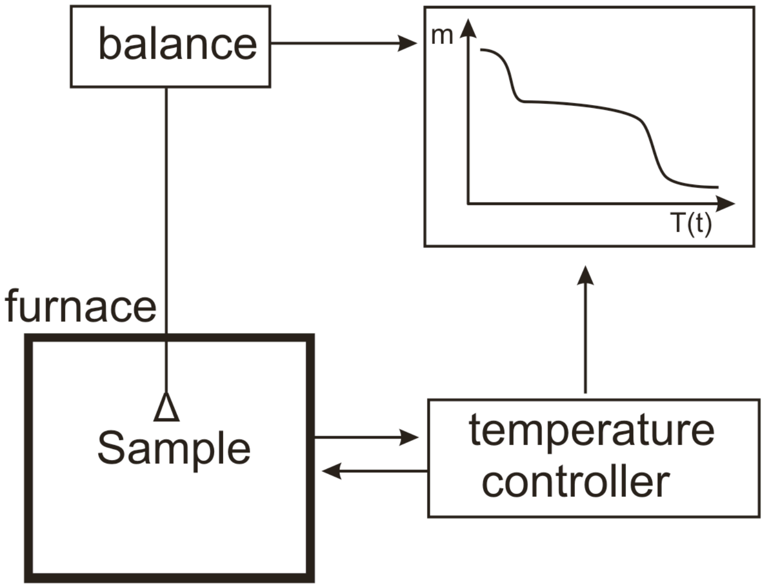

Figure 2.7.: Block schematic diagram of a TG apparatus [39] .

Differential Scanning Calorimetry (DSC)

Differential scanning calorimetry is a thermoanalytical technique in which the difference between the amounts of heat required to increase the temperature of a sample and inert reference material respectively are measured as a function of temperature. Both specimens are subjected to identical temperature regimes in a controlled environment and than heated or cooled at a controlled rate.

There are two types of DSC systems in common use. The first is called heat-flux DSC (Fig. 2.8), in which the sample and reference crucibles are connected by a low-resistance heat-flow path (a metal disc). The assembly is enclosed in a single furnace. Heat capacity or enthalpy changes in the sample result in a difference in its temperature relative to the reference. Calibration experiments are used to record and relate temperature difference to enthalpy change in the sample.

In power-compensation DSC (Figure 2.9), the temperatures of the sample and reference are controlled independently using identical, separate furnaces. The temperatures of the sample and reference are made identical by varying the power input to both furnaces. The power required to satisfy this condition is a measure of enthalpy or heat capacity change in the sample relative to the reference. The applications of the DSC method overlap with those of the DTA method. These include in particular purity determination, measurements of thermodynamic data (mixing, transformations), and analysis of the kinetics and the sequence of reactions. DSC measurements were performed on a Mettler Toledo DSC 30 apparatus.

DSC is widely used in industrial settings as a quality control instrument due to its applicability in evaluating sample purity and for studying polymer curing.

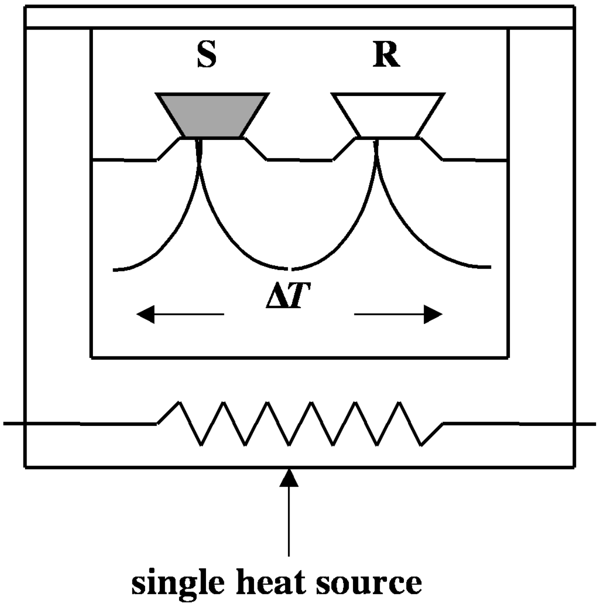

Figure 2.8.: Schematic diagram of a heat flux DSC apparatus. [40]

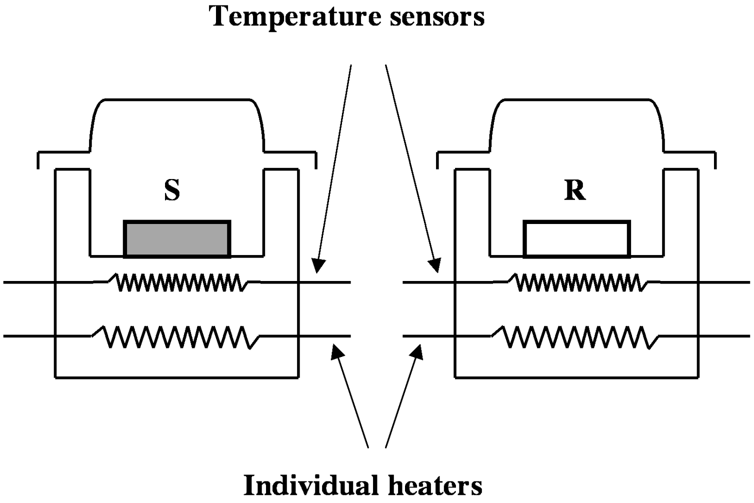

Figure 2.9.: Schematic diagram of a power compensation DSC apparatus. [40]

2.3.3. X-ray diffraction

The diffraction of X-rays by matter results from the combination of two different phenomena: scattering by each individual atom, and interference between the waves scattered by these atoms. This interference occurs because the waves scattered by the individual atoms are coherent with the incident wave, and therefore also with one another.

X-ray diffraction methods for single crystal and polycrystalline materials are widely used to study crystal structure and material properties.

Powder X-ray diffraction

X-ray powder diffraction is a powerful non-destructive testing method for determining a range of physical and chemical characteristics of materials. The applications include phase analysis, i.e. the type and quantities of phases present in the sample, the crystallographic unit cell and crystal structure, crystallographic texture, crystallite size, macro-stress and micro-strain, and also electron radial distribution functions.

In present investigations the X-ray powder diffraction technique was used as standard method of sample characterization. All measurements were carried out with powder samples using a STOE STADI P powder diffractometer (Cu $K_{\alpha 1}$ λ = 1.54051 Å, transmission setup, germanium crystal monochromator, PSD-position sensitive detector, silicon as an external standard). The data from standard measurements were recorded at room temperature from flat samples in a $8^\circ \leqslant 2\theta \leqslant 90^\circ$ range with an exposure time of 160 minutes. For moisture-sensitive substances, X-ray powder diffraction data were collected from measurements of the respective samples in glass capillaries.

The identification and characterisation of X-ray powder diffraction patterns was performed using WinX$^{\mathrm{POW}}$ [B] software. Identification of crystalline phases was performed by comparision of measured X-ray diffraction pattern to the reference pattern from PDF database (Powder Diffraction File), maintained by the ICDD, which contains data either experimentally determined or computed based on crystal structure and Bragg's law patterns. The *Pattern Fitting* routine was used to determine profile parameters and to integrate the intensities of collected powder patterns. Indexing and lattice parameter refinement was performed using the *Index & Refine* module, which comprise three routines: Werner's TREOR [41], Visser's ITO [42], Louër's DICVOL [43]. The software allows for the refinement of the lattice constants for X-ray powder diffraction data from the solution of a single crystal refinement, using the option *Refine*. Additionally, the theoretical pattern was generated by calculation of peak positions and Miller indices from given lattice constants and symmetry information from X-ray single crystal measurement (crystal system, Laue group or space group, atomic coordinates). The theoretical pattern is subsequently compared to the measured X-ray powder diffraction pattern to verify the structural model. If the obtained results are satisfactory, the lattice parameters collected from the X-ray powder pattern are employed in single crystal refinement.

Single crystal X-ray diffraction

X-ray diffraction of a single crystal is one of most precise methods of determining the structures of larger molecules and even biopolymers, proteins, or nucleic acids. Apart from neutron diffraction, there is no other method that provides such an amount of structural information about crystals. X-ray single crystal structure determination consists of several steps, as shown in Figure 2.10.

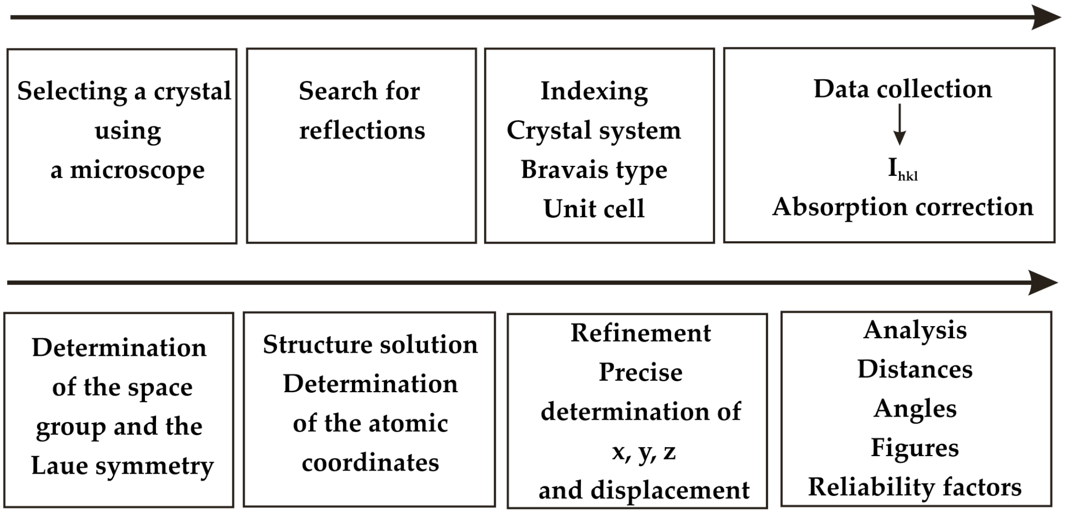

Figure 2.10.: Overview of the steps of a single crystal structure determination [44].

The preciseness of a crystal structure determination depends on many factors. One of the most important factors is the quality of the crystal itself. A very precise measurement strategy and data preparation cannot compensate for mistakes made when choosing the crystal. The first investigation of a crystal takes place under an optical microscope. Crystals that are stable under normal conditions are attached to a glass thread and fixed to the diffractometer goniometer head. In the case of moisture-sensitive crystals or when a temperature-dependent measurement must be carried out, the chosen crystals are mounted in capillaries or are sorted and selected in inert oil under the microscope and directly placed in the nitrogen cooling gas flow. All measurements were performed using a STOE IPDS I (Imaging Plate Diffraction System) diffractometer with CCD camera and FaceitVideo software [C], and an Oxford Cryosystems Cryostream 700 cooler (temperature range: 100K - 450K). For all crystal structures presented in this thesis, single crystal X-ray diffraction data were collected at room temperature. The working principle of IPDS was described by M. Ermrich *et* *al.* [43]. The important components of the STOE Imaging Plate Diffrection System are presented in Table 2.3.

Table 2.3.: Technical specifications of the STOE IPDS I

STOE IPDS I	
Radiation	Mo-K_α (λ = 0.71073 Å)
Monochromator	graphite crystal
Crystal to plate distance	40-200 mm
Collimator	metal tube (9cm length, diameter 0.3-0.8 mm)
Maximum 2θ	66° (at a distance IP-sample of 40 mm)
Maximum d/Å	0.64
Oscillation axis	vertically mounted, variable height
Axis drive	stepping motor, 0.002°/step
Laser excitation beam	15mW He-Ne laser (λ = 632 nm)
Luminescence detector	photomultiplier tube system
Read-out time (incl. erase)	$\approx$ 200 s
Detector	imaging plate (IP), $BaBrF:Eu^{2+}$ grains covered by a layer 10 μm polyethylene
Diameter of IP	180 mm
Thickness of IP including the organic binding agent	150 μm

Data evaluation and integration of reflections was accomplished using STOE X-Area [D] software. The menu of this program block provides procedures for peak searching over a series of images, indexing, cell refinement, and cell transformations. To visualise reciprocal space and give an undistorted view of the peaks which have been found by a peak search routine, the *Recipe* tool is used. Indexing which determines the cell parameters from the peak positions is done using the *Index* procedure, which requires some user interaction. Using the currently selected peaks, all difference vectors between all peak positions are calculated, normalised, and projected onto the horizontal plane of the Ewald sphere. When the crystal is a single crystal and when sufficient peaks have been used, a series of more or less sharp 'lines' can be seen. Each pixel represents a direction in reciprocal space and each 'line' corresponds to a set of parallel, equally spaced layers in reciprocal space. The cell parameters are determined by selection of three lines through densely populated regions. The lines must not all intersect at the same point and they may not be all parallel to each other, otherwise it is not important which lines are selected. A refinement of the cell parameters using the currently selected peaks is performed using option *Refine*. Subsequently a cell refinement using the control reflections from the integration is carried out.

Symmetry analysis and merging of the reflections according to the calculated space group was performed using the program *XPREP* [E].

Solving, refining, and analysing single crystal X-ray diffraction data was performed with the MS-Windows system of programs *WINGX* [F]. In order to solve and search for the best model of the structure, the programs *SIR92* [G], *SHELXS86* [H] or *SHELXS97* [I] were used. Next the structures were refined using the program *SHELXL97* [J].

The program *PLATON* [K] is a useful tool to improve the structure model. First the option *AddSym* may be used to find missing symmetry elements and to established a corrected, more symmetrical space group. Subsequently the *TwinRotMat* option verifies unresolved pseudo merohedral twinning and is particularly useful in identifying the twin law. The next step of crystal structure refinement is absorption correction, which is necessary to obtain meaningful anisotropic displacement parameters, especially when the absorption coefficient is high. Numerical absorption correction using a 3-dimensional integration over all X-ray beam paths in the crystal is perfomered using *X-RED* [L]. The shape and size of the crystal for a numerical absorption correction using symmetry-equivalent reflections or reflections measured more than once was performed using the program *X-SHAPE* [M].

Finally the refined structures were visualized using *Endeavour* [N] or *Diamond* [O].

2.3.4. Crystal twinning

When a crystal structure has been successfully solved and refined by the single crystal X-ray diffraction method, the resulting information generally has a high level of accuracy which can only very exceptionally be obtained by spectroscopic methods. The indirect nature of structure determination can sometimes lead to serious errors. One serious interpretation error which should be avoided is twinning during crystal growth.

The study of twinned crystals can be traced back to early morphological observations by Steno in 1669 [45]. Several definitions of twinning can be found in the literature. Particularly striking is the difference between the "crystallographic-mineralogical" definition, given in terms of lattice, and the "physical" definition, which often is based on phenomenological concepts most typical of transformation twins.

According to the definition of Friedel (1904) [46] twinning is the oriented association of two or more individuals of the same crystalline phase, in which pairs of individuals are related by a geometrical operation termed the twin operation. The twin operation is a symmetry operation for the twinned superstructure but not for the individuals: it relates different individuals in the twin and belongs to a crystallographic point group.

Wider classes like bicrystals, translation domains, growth sectors etc. have been investigated and described by Hahn, Janovec and Klapper, (1999) [47] and Hahn and Klapper (2003) [48]. Twinned crystals can be described and analysed from various points of view. Several criteria are used to classify twins.

Depending on the formation mechanism, twins are classified as: growth twins, transformation twins, and mechanical twins. Morphology divides twins into: contact twins, penetration twins, simple twins, polysynthetic twins, and cyclic twins. According to the twin element, about which the twin operation is performed, twins are classified as: rotation twins, reflection twins, and racemic twins.

Based upon their diffraction patterns, twinned crystals may be grouped into the following general categories:
Twins through merohedry occur when the twin element is an element of the crystal system, but is not a symmetry element of the crystal class. As a consequence, the different orientations of direct and reciprocal lattices coincide exactly with one another.
In the case of twinning without coincidence in the reciprocal lattice, named non-merohedral twinning, the twin element is neither an element of the crystal class nor of the crystal system. The result of non-merohedral twinning is no complete overlapping of the reflections for the two components (which is what is implied by merohedry).
Partial merohedral twinning is observed in the case of coincidence of two components in every second, third or n^{th} layer in the reciprocal lattice.
The common example of pseudomerohedral twinning are structures crystallising in the monoclinic system with $\beta \sim 90°$ or $a \sim c$ with $\beta \sim 120°$. When a model for the structure can be found, it can be refined as a twin, but it is also often possible to arrive at an incorrect solution by assuming a structure with higher symmetry.

The prerequisites for a merohedral or pseudo-merohedral twinned structure refinement are a suitable structure model for the untwinned structure and the knowledge of the twin law. Because of the coincidence of the two reciprocal lattices, the solutions by Patterson and/or direct methods are not easily available. In the case where the contribution of one twin component is small and the twinning is barely observable, the correct space group can be found and the structure solution carried out normally. Due to the fact that there are some irregularities in the structure geometry and in the atomic displacement parameters, and also because the R-factor is higher than expected, it is evident to the experimenter that a twinning refinement is required. The first stage is the determination of the twin law and matrix which will convert the axes of the first component into those of the second. The matrix transforms the indices hkl of the first component into the indices $h'k'l'$ of the second. It also permits one to write the contribution of the second component to the structure factor $\mathrm{F_c}$ or $\mathrm{F_c^2}$ and refine that against the observed $\mathrm{F_o^2}$(twin)-values.

$$F_c^2(hkl)_{twin} = (1-x)F_c^2(hkl) + xF_c^2(h'k'l') \tag{2.5}$$

The software used for twin structure refinement is *SHELXL* [J] using F_o^2 data, and *JANA* [R] using either F_o^2 or F_o data.

Partial-merohedral and non-merohedral twin structures can be solved and refined using the *HKLF5* command of *SHELXL* [J]. For that purpose, each reflection in the data set should be marked with the number 1 or 2, to point out to which of two domains it belongs. Overlapping reflections are entered twice, with the appropriate indices for each domain, but the total intensity for both. For partially overlapping reflections the integration area on the detector system should be large enough to contain both components. If this requirement cannot be met, the data are best omitted. A detailed description on this issue is contained in the book W. Massa [49].

The following are characteristic warnings that can indicate the presence of a twinning problem:

- Metric symmetry higher than Laue symmetry
- The mean value for $|E^2 - 1|$ is much lower than the 0.736 expected for a noncentrosymmetric crystal
- The data exhibit implausible or unusual systematic absences (a possible partial-merohedral twin)
- The space group appears to be either tetragonal or trigonal
- For the most poorly fit data, the F_o^2 values are consistently larger than the F_c^2 values
- The R_{int} for a higher symmetry Laue group is slightly higher that the R_{int} for a lower symmetry Laue group
- The structure model is in a centrosymmetric space group and is disordered
- The data exhibit no systematic absences for glide planes or screw axes, and the structure is difficult to solve or not solvable
- The cell has one or more unusually long axes and many of the data are weak or absent
- The cell is indexed and refined with great difficulty
- The collected data are sharp and some appear to be split

2.3.5. Spectroscopy

Spectroscopy is a branch of physics that deals with the interaction between radiation and matter. The tremendous development of new experimental techniques, as well as the sophistication of those that already exist, gives rise to the regular development of new spectroscopic techniques. The different spectroscopies are rooted in a basic phenomenon: the absorption, reflection, emission, or scattering of radiation by matter in a selective range of frequencies and under certain conditions. Figure 2.11 shows the electromagnetic spectrum with different microscopic excitation sources and the spectroscopic techniques relevant to the different spectral regions.

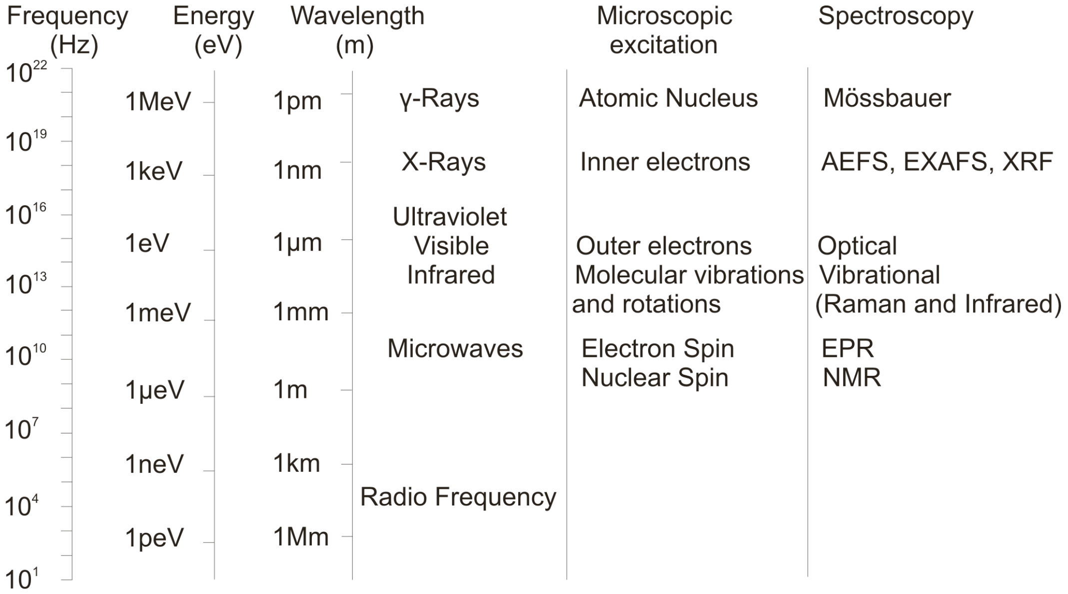

Figure 2.11.: The electromagnetic spectrum, showing the different microscopic excitation sources and the spectroscopies related to the different spectral regions. (XRF - X-Ray Fluorescence; AEFS - Absorption Edge Fine Structure; EXAFS - Extended X-ray Absorption Fine Structure; NMR - Nuclear Magnetic Resonance; EPR - Electron Paramagnetic Resonance). [50]

Ultraviolet - Visible spectroscopy

Optical spectroscopy can be attributed to any kind of optical photon interactions with matter. The two most general classes of such interactions are absorption and emission. UV-Vis reflectance spectroscopy is ideal for characterizing optical and electronic properties of many different materials. Our research is primarily interested in characterizing and determining the electronic band gap of semiconductor materials. The absorption coefficient of a clear substance can be determined by application of the well-known Bouguer-Lambert absorption law. It is applied to measurements of the radiation transmitted by a layer of a substance of known thickness. This direct transmission spectrophotometric approach is clearly not applicable in the case of powdered materials, because the complicated problem of multiple scattering event of light within the powder is not accounted for.

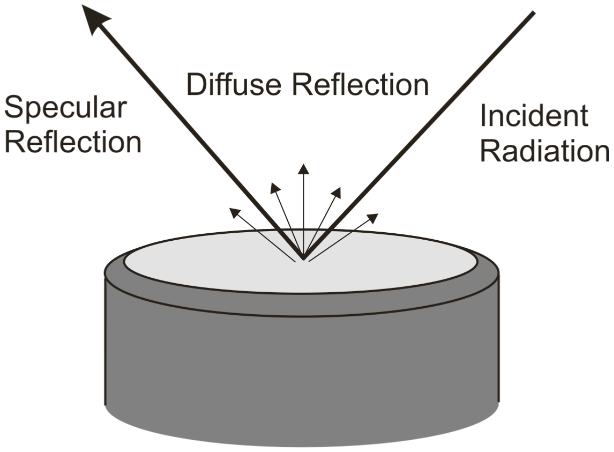

Figure 2.12.: Schematic representation of diffuse reflectance.

One may consider a layer of powdered material which is illuminated from one side by a beam of monochromatic light. It is possible to measure the fraction of the light that is scattered back away from the incident surface (diffuse reflection) and the fraction that passes throught the sample and is scattered in the forward direction (diffuse transmission). The law of conservation of energy defines the fraction of incident energy that is absorbed by the sample. It is not trivial to relate this measurement of absorbed energy to the fundamental optical properties of the individual particles of which the sample is composed. To account for scattering within the sample, a far more complex theoretical model is required. The widely applied theory for such a case was developed by Kubelka and Munk [51], and later improved by Kubelka [52]. The Kubelka-Munk theory treats the diffusing layer as a continuous medium, thus the absorption coefficient is an average for a volume of the sample including voids between the particles of powder. This conception does not require knowledge of particle size nor of real refractive index, so it provides a reasonable means of relating the average absorption coefficient of a bulk powder sample to the measurable optical properties such as diffuse reflection and diffuse transmission.

One of the most important results of Kubelka-Munk theory is the following expression:

$$F(R) = \frac{k}{s} = \frac{(1-R_\infty)^2}{2R_\infty} \tag{2.6}$$

which relates k, the bulk absorption coefficient per unit pathlength, and s, the scattering coefficient per unit pathlength, to R_∞, the diffuse reflectance of a layer of powder that is infinitely thick. In the case of a sample whose thickness d is not sufficient to prevent some light from passing through the layer, the two quantities can be measured: diffuse reflectance R_0 (when the layer is no longer infinitely thick) and the diffuse transmitance T. It is expressed as follows:

$$\begin{aligned} \alpha &= \frac{1 + R_0^2 - T^2}{2R_0} && (2.7) \\ b &= \sqrt{(\alpha^2 - 1)} && (2.8) \\ s &= \frac{1}{2bd} tanh^{-1}(\frac{bR_0}{1 - \alpha R_0}) && (2.9) \\ k &= (\alpha - 1)s && (2.10) \end{aligned}$$

The quantities α and b are dimensionless intermediate parameters introduced to simplify the explicit form of equation 2.9.

While the absorption edge is indicative of the location of the band gap, accurate estimation of the band gap requires the construction of the Tauc plot [53]. The electronic bandgap is the intercept of the straight line obtained by plotting $(F(R) \cdot h\nu)^n$ versus $h\nu$.

For direct band gap semiconductors and photon energies close to the band gap:

$$k(h\nu) \propto F(R) \propto \frac{\sqrt{h\nu - E_{gap}}}{h\nu} \tag{2.11}$$

For indirect band gap semiconductors:

$$k(h\nu) \propto F(R) \propto \frac{(h\nu - E_{gap})^2}{h\nu} \tag{2.12}$$

where k is the absorption coefficient, $h\nu$ is the energy of incident photons and $F(R)$ is the Kubelka-Munk function. These expressions also assume that the scattering coefficient is constant with photon energy.

The value of the optical band gap is obtained by extrapolating the linear region of the plots to the photon energy ($h\nu$) axis.

UV-Vis spectra presented in this thesis were recorded on an OMEGA 20 two-wave photometer from Bruins Instruments, in the range 190-2800 nm, using a diffuse reflectance measurement. Ground polycrystalline samples were applied to the surface of a $BaSO_4$ sample holder. Subsequently the absorption data (k/s) were calculated from the recorded reflectance data using the Kubelka-Munk function [51,52,166]. All data were calculated using OMEGA software [S]. The energy gaps were determined from Tauc plots [53].

Origin of Infrared and Raman spectra

Vibrational transitions can be observed in Raman or IR absorption spectra. However the physical origins of these two spectra are considerably different. Infrared spec-

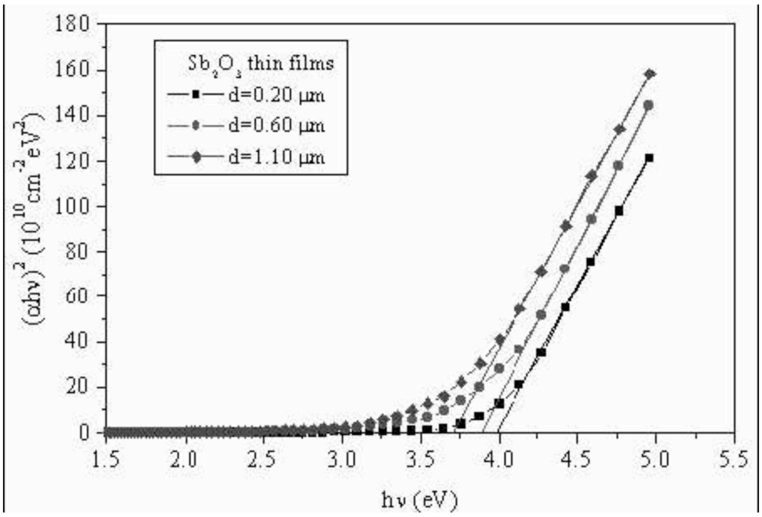

Figure 2.13.: Plots $(F(R) \cdot h\nu)^2$ vs. $h\nu$ for Sb_2O_3 thin films with different thickness [55]. In this work, the authors found that the band gap of the thin-film material varied with film thickness.

tra are based on absorption of photons in the infrared region (10^2-10^4 cm^{-1}). Photons are absorbed by transitions between two vibrational levels of the molecule in the electronic ground state. On the other hand, Raman spectra have their origin in the electronic polarization caused by ultraviolet, visible, and near-IR light. Figure 2.14 illustrates the difference between IR and Raman techniques.

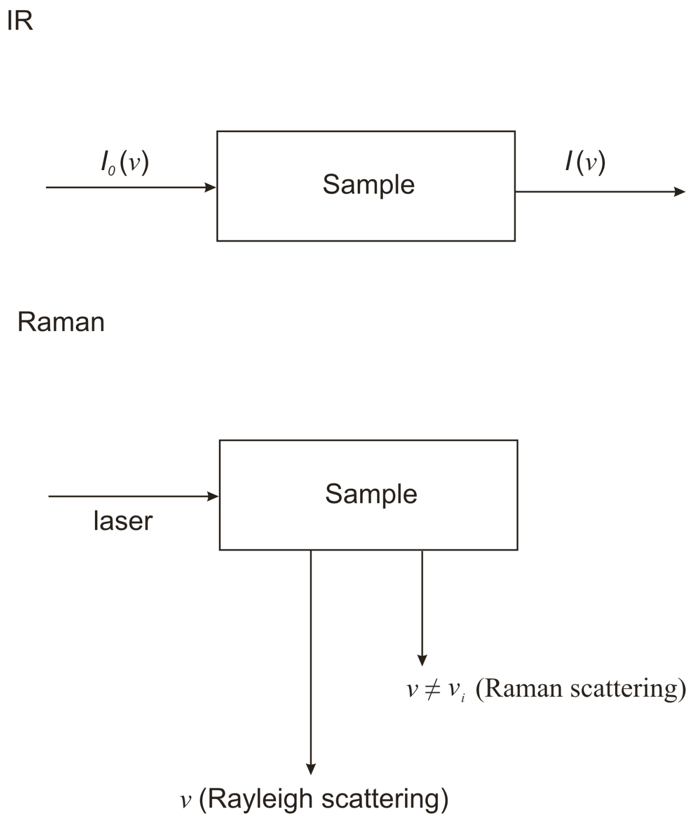

Figure 2.14.: Schematic representation of infrared absorption and Raman scattering measurement mechanisms. [56]

Raman spectroscopy

Raman spectroscopy is a powerful technique based on light scattering, used to investigate the microscopic structure of molecules and crystals. Vibrational techniques are also very useful in identifying vibrating complexes in different materials and in characterizing structural changes in solids. In a light scattering experiment, light of a known wavelength and polarization is scattered from a sample. The scattered light is then analyzed for polarization and wavelength. Raman scattered light is frequency-shifted with respect to the excitation wavelength, but the magnitude of the shift is independent of the excitation wavelength.

The interaction between matter and light can be interpreted as a collision between an incident photon and a vibrating molecule or lattice, and three different results are possible, as presented schematically in Figure 2.15.

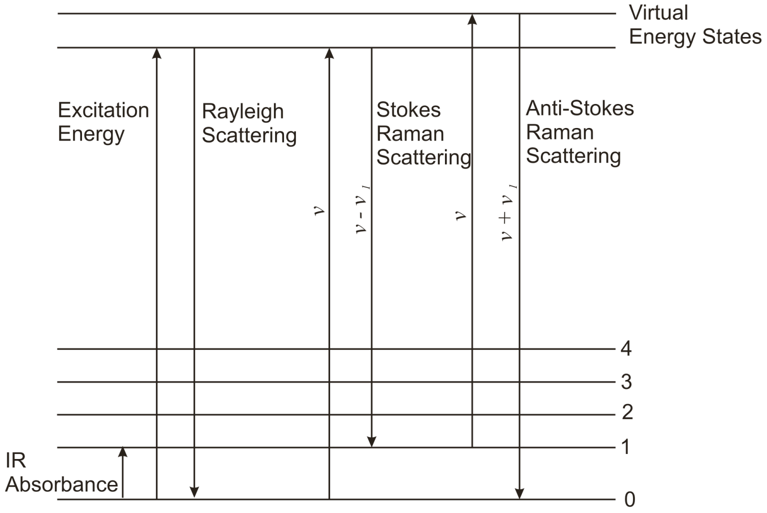

Figure 2.15.: Energy level diagram showing the states involved in a Raman signal [56].

If the collision is elastic, the energy of the photon as well as the energy of the molecule do not change after the collision. The elastic scattering of the photon is called Rayleigh scattering.

The inelastic collision between a photon and a molecule is known as the Raman effect. The energy difference between the inelastic scattered photons and the incident photons is exactly the difference between two energy levels of a molecular vibration. In the case when the vibrational energy of the molecule is increased after the collision, the energy of the scattered photons is decreased by the same amount and, therefore, can be detected at longer wavelengths. The respective spectral lines are said to be Stokes-shifted. If the vibrational energy of the molecule is decreased after the collision, the energy of the scattered photons is increased for the same amount and can be detected at shorter wavelengths. The respective spectral lines are said to be anti-Stokes-shifted. This is only possible if the molecule is in an excited vibrational state before the collision.

To determine how many bands are expected for each type of molecule in the vibrating unit and also to ascertaine differences in spectra of polymorphous materials, factor group theory [56, 57, 58, 59] is a useful tool. It is possible using easily applicable procedures to calculate the vibrational behavior for crystals from their symmetry properties (e.g. the number of possible interactions, whether they are visible in the Raman and/or IR absorption spectra). The method requires knowledge of the space group, population of the equipoints, and selection rules of vibrational modes of crystals.

The Raman effect can be masked by simultaneously stimulated fluorescence. These effects exhibit large differences in their intensities by several orders of magnitude. In this case it is almost impossible to collect a Raman spectrum. One may avoid stimulating fluorescence by choosing an excitation wavelength far away from any electronic transitions. For example, if the Raman effect is stimulated in the near infrared (NIR) region at a wavelength of 1064 nm, many materials no longer exhibit fluorescence. However, since the intensity of Raman scattering is dependent on the fourth power of the excitation wavelength this results in a strong decrease of the measurable signal due to the Raman effect. Figure 2.16 presents the situation described above.

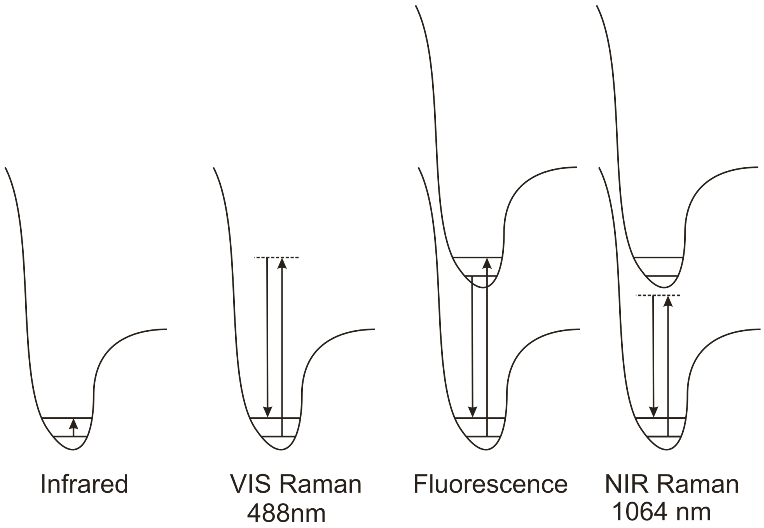

Figure 2.16.: Mechanisms of electronic transitions.

Raman spectroscopy in contrast to the IR technique does not require sample preparation procedures, and samples can be analyzed inside glass containers. FT-Raman (Fourier Transformation Raman) spectra in this work were collected on a Varian FT-Raman module with near infrared Nd:YAG (Neodymium-doped Yttrium Aluminium Garnet, Nd:$Y_3Al_2(AlO_4)_3$) laser operating at 1064 nm. The powders were analyzed in thin-walled glass capillaries (80 × 1.5 mm). A liquid nitrogen-cooled germanium detector was used. The laser was focused on the sample with an approximately 1mm diameter spot with a variable power. The spectra were recorded in the wavenumber range 4000-130 cm^{-1} at a resolution of 2 cm^{-1}. The spectra were analyzed using Resolution Pro [T] software from Varian Inc.

Infrared spectroscopy

Infrared spectroscopy is a reliable technique, which can be used to characterize, identify, and also quantify many substances. One of the strengths of IR spectroscopy is its ability as an analitycal technique to obtain spectra from a very wide range of solids, liquids, and gases. However, for traditional IR measurements based on transmission of infrared radiation directly through the sample, some form of sample preperation is required in order to obtain a good quality spectrum. There are two most common forms of sample preparation for solids. Both involve grinding the material to a fine powder and dispersing it in a matrix. The ground material can be dispersed in a mineral oil (nujol), creating a paste which is than spread between two infrared transparent windows made from NaCl, KBr, CaF_2, or CsI. The material most widely used as a matrix is potassium bromide. About 1-3 mg of sample is mixed accurately with about 350 mg of ground KBr. The mixture is then placed in a suitable press and compressed at about 12000 psi for 1-3 minutes. During the pressing, the sample can optionally be evacuated. The result of recrystallization of KBr is a transparent glassy disk about 1 mm thick, which is then ready to be analyzed. Sample preparation is sometimes problematic and is always time consuming. The materials involved are fragile and hygroscopic and the quality of measurements can be adversely affected if the materials are handled or stored incorrectly. A measurement method that is currently widely used and does not require special sample preparation is ATR (Attenuated Total Reflectance).

ATR-IR measurement

Attenuated total reflectance is based on measurement of the changes that occur in a totally internally reflected infrared beam, when the beam comes into contact with the sample as shown in Figure 2.17.

An infrared beam is coupled into an optically dense crystal with a high refractive index at a certain angle. The total internal reflection of the beam in the crystal creates an evanescent wave that extends beyond the surface of the crystal into the sample held in contact with the crystal. The evanescent wave protrudes only a few microns (0.5 μm-5 μm) and as a consequence of this, there must be a good contact between sample and the crystal surface. In the region of the infrared spectrum where the sample absorbs energy, the evanescent field interacts with the sample and the light guided in the crystal is thereby attenuated, and this attenuation is measured by the detector.

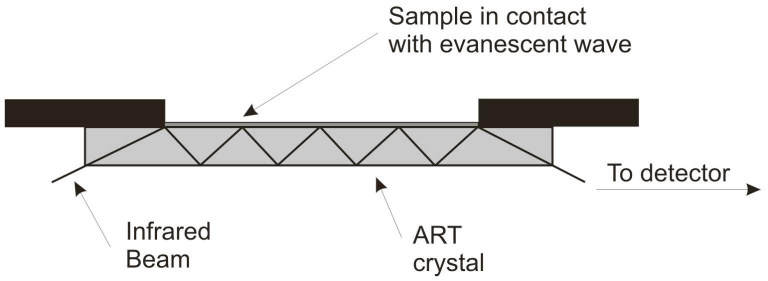

Figure 2.17.: Schematic diagram of multiple reflection ATR system. [60]

For the analysis of solids, diamond is the preferred choice for most applications because of its robustness and durability. The solid sample material is placed on a clean background area and subsequently some pressure is applied to the sample, pushing it onto the diamond surface.

The crystal used in an ATR cell should have a high refractive index and penetration depth, which is a function of the wavelength, the refractive index of the crystal being used, and the angle of incidence of the beam. Table 2.4 presents physical properties of commonly used ATR crystals.

Table 2.4.: Physical properties of commonly used ATR crystals [61].

Material	Spectral Range (cm^{-1})	Refractive Index	Penetration Depth (μm)
Diamond	45000 - 2500 1667-33	2.4	1.66
Ge	5500	4	0.65
KRS-5	20000 - 400	2.37	1.73
Si	8300 - 1500 360-70	2.37	1.73
ZnSe	20000 - 650	2.4	1.66

ATR spectra are similar to transmission spectra. However, subtle differences exist for the same general physical phenomenon. One of them is the penetration depth d_p which is defined as:

$$d_p = \lambda/2\pi\sqrt{n_1^2 \sin^2\theta_1 - n_2^2} \tag{2.13}$$

where λ is the wavelength of light, θ is the angle of incidence of the IR beam (between the incident ray and the normal of the surface of the crystal), n_1 and n_2 are refractive indices of the crystal and the sample, respectively. This results in more interaction and therefore higher IR absorption bands at long wavelengths than at shorter wavelengths. This is shown in Figure 2.18.

In the case where a transmission spectrum representation is desired from the recorded ATR spectrum, a correction for the relative band intensity must be carried out. The

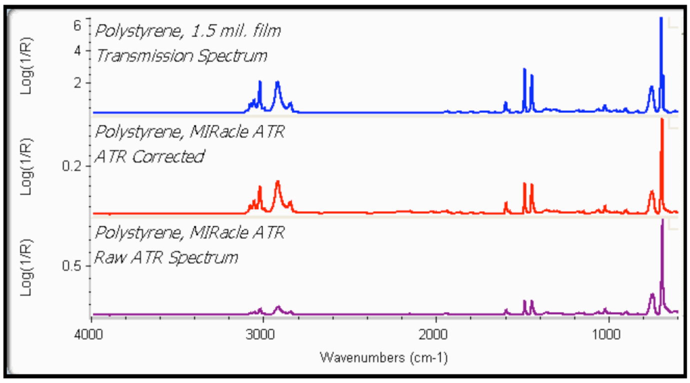

Figure 2.18.: FTIR spectra collected for polystyrene by transmission (upper spectrum), after ATR correction (middle spectrum), and by ATR (lower spectrum) [62].

resulting spectrum with ATR correction is presented in the middle spectrum of Figure 2.18.

All IR absorption spectra presented in this thesis were recorded on a Varian 670-IR FT-IR spectrometer. Samples were measured using ATR technique, on Gladi ATR Base Optic Assembly with a 2.2 mm × 3.0 mm ATR diamond crystal sampling area, located in the center of the plate. The samples were compressed by application of pressure in order to make intimate contact for good quality ATR spectral data. Analysis of FTIR spectra were performed using Resolution Pro [T] software.

To more clearly demonstrate the complementary nature of the spectral information, a comparision between the fundamental vibrational techniques, Raman and IR, is often applied. Both techniques provide a spectral response for the same vibrational mode, which is governed by the selection rules for each technique. The Raman and IR spectra are rich with spectral information, while Raman spectra typically appear less congested with narrower peaks. Infrared spectroscopy is more sensitive to hydrogen bonding effects that result in wider absorption peak widths, leading to the appearance of a congested spectrum.

Mössbauer spectroscopy

Mössbauer spectroscopy is based on the fact that the excitation energy of a nucleus due to the absorption of gamma rays is influenced by the chemical environment. In a resonance absorption experiment, the energy of incident radiation should exactly match the energy separation between the two levels of the absorption system. The Mössbauer effect is observed when a nucleus with Z protons and N neutrons in an excited state of energy E_e undergoes transition to the ground state of energy E_g by emitting a gamma quantum of energy $E_e - E_g$. Subsequently the gamma quantum may be absorbed by a nucleus of the same kind (same Z and N) in its ground state, whereby transition to the excited state of energy E_e takes place (resonant absorption). The subsequent transition to the ground state emits a conversion electron e- or a γ-quantum (resonant fluorescence). This is shown schematically in the Figure 2.19.

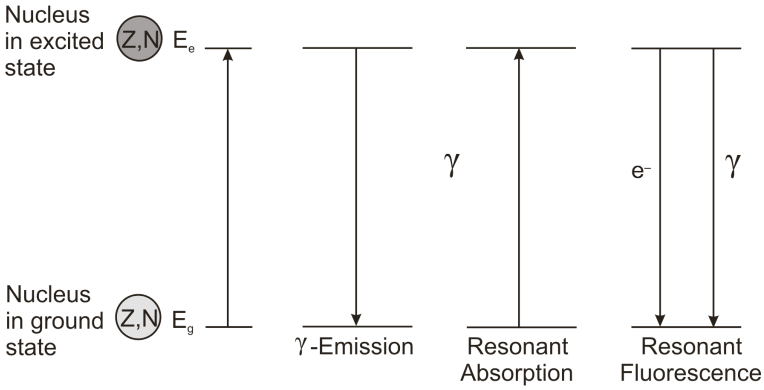

Figure 2.19.: Recoilless nuclear resonance absorption and fluorescence of γ-radiation.

The Mössbauer effect has been observed in more than 40 elements. The most prominent element studied using this technique is ^{57}Fe. Also frequently studied are ^{129}I, ^{119}Sn, and ^{121}Sb. There are three parameters: isomer shift, quadrupole splitting, and hyperfine splitting by which a particular compound can be identified. The isomer shift is related to the electron density at the nucleus and is observed in the spectra as a shift of all peaks corresponding to a particular atomic environment. Quadrupole splitting reflects the interaction between the nuclear quadrupole and the surrounding electric field gradient, and is observed in the spectrum as splitting or degeneration of nuclear transitions from a single peak into two peaks. The third interaction is hyperfine splitting and results as a consequence of the interaction between the nucleus and any surrounding magnetic field.

Mössbauer spectroscopy is widely used in investigations of the local electronic environment in solid state materials. The results obtained from these measurements can be summarized in terms of two parameters. First is a Mössbauer isomer shift δ linearly correlated to the electron density of the nucleus $\rho(0)$:

$$\delta = \alpha(\rho_{\mathrm{a}}(0) - \rho_{\mathrm{s}}(0)) \tag{2.14}$$

The subscripts a and s denote the absorber and source materials, respectively, and α is a nuclear calibration constant. The second parameter is the quadrupolar interaction Δ, which is an indicator of the asymmetry of the electron distribution around the investigated atom:

$$\Delta = eQV_{\mathrm{ZZ}}\left(1 + \frac{\eta^2}{3}\right)^{1/2} \tag{2.15}$$

where eQ is the quadrupolar moment of the nucleus, V_{ZZ} is the principal component of the electric field gradient tensor, and η is the asymmetry parameter [63,64].

The Mössbauer parameters δ and Δ for several compounds containing antimony as a lone pair element have been presented by Lippens [63] and Olivier-Fourcade *et al.* [64]. On the basis of a wide range of compounds it can be concluded that the values in the range $\delta > 0$ or $\delta < 0$ characterize the tendencies for Sb to be in its V or III oxidation state, respectively. This correlation is been shown in Figure 2.20.

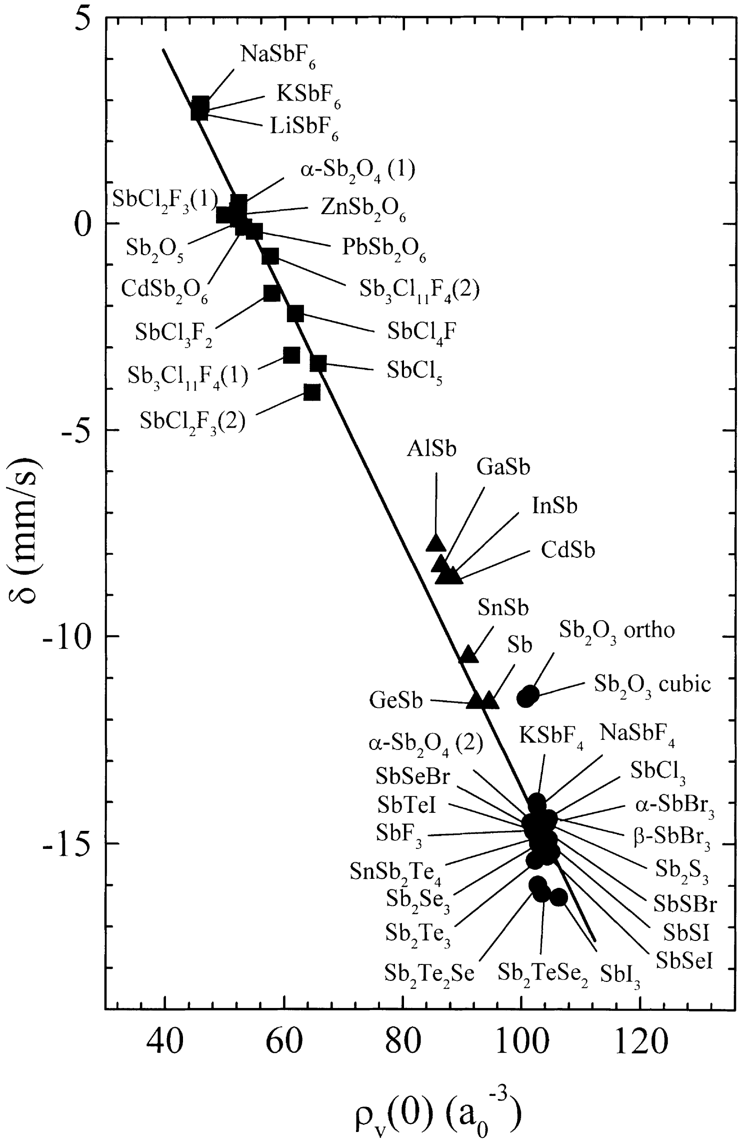

Figure 2.20.: Linear correlation between the experimental values of the ^{121}Sb Mössbauer isomer shift δ (relative to $BaSnO_3$) and the calculated values of the electron density at the nucleus $\rho(0)$ for a series of Sb(V) (squares), Sb(0) (triangles) and Sb(III) (dots) compounds. [63]

All possible environments of Sb can be described on the basis of an octahedron, as shown in Figure 2.21. When the one of the coordinating atoms is missing, the stereochemical activity of the lone pairs increases. The pairs are considered to be very active in the case of small coordination polyhedra and strongly covalent bonds.

Mössbauer spectroscopy also provides opportunities to characterise the activity of the lone pair of electrons. The pair is considered to be inactive and spherically symmetric around Sb when δ is mininal and $\Delta = 0$. In this case the "s" electron density at the Sb nucleus is maximal and the bonds have an ionic character. The coordination polyhedron is a weakly distorted octahedron. In the case of intermediate δ and $\Delta < 0$ the lone pairs remains inactive, but "s" electron density decreases. This results in a partial delocalization of lone pairs and bonds that are predominantly metallic. Maximum δ and $\Delta > 0$ correspond to an active lone pair of electrons. The "s" electron density at the Sb nucleus decreases and the bonds have a distinctly covalent character.

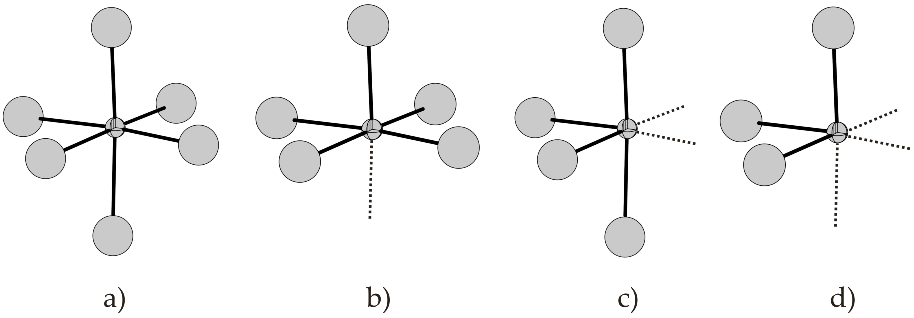

Figure 2.21.: Idealized Sb environment based on a perfect octahedron with n missing atoms.(a) n=0, (b) n=1, (c) n=2, (d) n=3. [64]

Mössbauer spectroscopic experiments were performed using a Ba^{121m}SnO$_3$ source, carried out in the usual transmission geometry. The measurements were performed with a commercial helium-bath cryostat. The temperature of the absorber was varied between 4.2 K and room temperature, while the source was kept at room temperature. The temperature was controlled by a resistance thermometer (±0.5 K accuracy). The samples were enclosed in small PVC containers at a thickness corresponding to about 10 mg Mössbauer active element/cm^2. Mössbauer measurements were carried out through cooperation with Prof. R. Pöttgen from Westfälische-Wilhelms University in Münster.

2.3.6. Theoretical calculations

Certain material characterisation results in this work were confirmed by theoretical calculations based on the derived crystal structure. These calculations were performed by collaborators and are not a central element of this work, nonetheless it is informative to briefly introduce the methods used. The goal of any numerical method is to solve the Schrödinger equation for the ground state energy of the system, following which various other parameters of interest may be derived and/or calculated. There are however various methods to arrive at this goal of an appropriate description of electronic motion as kinetic, Coulomb, exchange, and correlation energy terms (and wavefunction).

Traditional methods of quantum chemistry are formulated in terms of the many-electron wave function $\Psi(r_1, r_2, ...)$. An *ansatz* for the wavefunction is assumed and the wavefunction is refined by iteration. The Hartree-Fock (HF) method for example defines an appropriate initial guess of the wavefunction and an iteration procedure. HF describes kinetic, Coulomb, and exchange terms of the wave function exactly, but does not describe correlation. Correlation is considered by so-called post-HF methods, like Moller-Plesset perturbation theory (MP2). These theories are intrinsically approximate, but the wavefunction may be solved to any arbitrary accuracy given sufficient computing time. They are generally most suitable in few-atom system ($\leq 5-10$) and when high accuracy is required.

In recent years density functional theory (DFT) has become very popular with theoretical chemists, particularly in work with many-atom systems. This method was used to verify experimental results in this work. This method is based on the electron distribution $n(r)$ instead of the many-electron wavefunction. It relies on two important points from the Hohenberg-Kohn theorem

- For interacting electrons, $E[n]$ is only a functional of the electron density.
- The ground state energy is the energy of the system with the ground state electron density, i.e. $E_{GS} = E[n_{GS}]$

DFT provides a solution for the ground state electron density, which therefore leads directly to the ground state wavefunction. This is then conceptually similar to the Hartee-Fock method. One may write the Hamiltonian as $H = T+U+V$, where V is the external potential (e.g. due to atom nuclei or external field), T is the electron kinetic energy, and U is the electron-electron interaction energy. The starting point of DFT is the lemma of Hohenberg and Kohn: the specification of the ground state density $n(r)$ determines the external potential $v(r)$ uniquely. For a given $v(r)$, one defines the energy functional of $n(r)$ where the T and U contributions are separated into three terms: the kinetic energy of a non-interacting system, the classical expression for the electron-electron interaction energy, and the so-called exchange correlation energy. In the DFT method, one must at the outset come up with a suitable approximation for the exchange correlation energy E_{xc}, and the accuracy of this approximation determines the accuracy of the entire calculation. It is in this sense that DFT is intrinsically exact, provided that an exact expression for E_{xc} could be found.

The simplest approximation for E_{xc} is the local density approximation (LDA), derived from the exchange-correlation energy per particle of a uniform interacting electron gas, which is known to a high accuracy. The LDA approaches an exact expression when the length scale over which nr varies is large compared to the mean particle spacing and to the hydrogen radius. However, it also gives useful results for most applications where this condition is *not* met. LDA may be generalised to include electron spin (called local spin-density approximation, LSDA). The next "level" of approximations include for example generalised gradient approximations (GGA) that take into account the local electron density and also the gradient of the density. Still more exact approximations are the topic of active research in the quantum chemistry field. However DFT can not be optimised systematically like HF. The success of DFT is due to the fact that computational costs are reduced by orders of magnitude compared to HF. Results are surprisingly good keeping in mind that the exact functional for exchange and correlation is not known. Applying LDA (local density approximation), GGA (generalized gradient approximation) of hybrid (B3LYP) functionals a certain modulation is possible with respect to metal, covalent or ionic bonding, dense or less dense chemical compounds.

A more complete introduction to DFT and various exchange-correlation energy approximations may be found in [65, 66]. For this work, calculations were performed primarily using LDA.

3. Educts

3.1. $ZnSb_2O_3X_2$ (X = Cl, Br, I)

3.1.1. Synthesis

New quaternary compounds $ZnSb_2O_3Cl_2$ and $ZnSb_2O_3Br_2$ were obtained by solid state reaction of ZnX_2 (X = Cl, Br, I) and Sb_4O_6 in a 2:1 molar ratio. The reactants were mixed in an agate mortar and placed in sealed evacuated silica tubes. All preparatory work was carried out in a glovebox. Subsequently the reactants were melted and annealed at 400°C and 450°C respectively for 14 days. In both cases, the products were colourless polycrystalline samples containing numerous single crystals. The analogous iodine phase was not obtained as single crystals. Multiphase powder indicated the presence of ZnI_2, Sb_4O_6 and $ZnSb_2O_4$ (Appendix, Figure B.5).

3.1.2. Single crystal and powder X-ray diffraction analysis

The crystal structures were determined from colourless needle-shaped crystals by single crystal X-ray diffraction at room temperature. The structural solution was performed by direct methods using the program *SHELXS-97* [I]. Refinement of the model structure was done using the least squares method using the program *SHELXL-97* [J]. The compounds crystallize in the orthorhombic system, space group *Pnma* (No. 62) with $Z = 4$, $a =$ 17.1160(6) Å, $b = 5.556(1)$ Å, and $c = 6.480(1)$ Å for $ZnSb_2O_3Cl_2$ and $Z = 4$, $a = 17.5970(4)$ Å, $b = 5.5832(9)$ Å, and $c = 6.691(1)$ Å for $ZnSb_2O_3Br_2$. The refinement converged at R_1, $wR_2[I > 3\sigma(I)] = 0.0233, 0.0584$ and $R_1, wR_2[\text{all data}] = 0.0260, 0.0594$ for $ZnSb_2O_3Cl_2$ and at $R_1, wR_2[I > 3\sigma(I)] = 0.0260, 0.0594$ and $R_1, wR_2[\text{all data}] = 0.0275, 0.0700$ for $ZnSb_2O_3Br_2$. Further details concerning the crystal structure solution and refinement data are presented in Table 3.1.

Final atomic coordinates and equivalent isotropic displacement parameters for $ZnSb_2O_3Cl_2$ and $ZnSb_2O_3Br_2$ are listed in the appendix in Tables B.1 and B.2, while Tables B.3 and B.4 include anisotropic displacement parameters.

The crystal structures of $ZnSb_2O_3Cl_2$ and $ZnSb_2O_3Br_2$ are isostructural. The structures consist of puckered layers of condensed SbO_3^{3-} units which are terminated by $[ZnO_2Cl_2]$ or $[ZnO_2Br_2]$ tetrahedra, as shown in Figure 3.1. Trigonal pyramids SbO_3 constitute *Sechserrings* (Figure 3.2), which form corrugated $[SbO_3^{3-}]$ layers perpendic-

Table 3.1.: Details of the data collection and results of the structure refinement for $ZnSb_2O_3Cl_2$ and $ZnSb_2O_3Br_2$.

Crystal data		
Chemical formula	$ZnSb_2O_3Cl_2$	$ZnSb_2O_3Br_2$
Crystal colour/habit	colourless/needle	colourless/needle
Crystal size	$0.3 \times 0.1 \times 0.1$ mm	$0.24 \times 0.15 \times 0.1$ mm
Molecular weight	427.77 g mol^{-1}	516.69 g mol^{-1}
Calculated density	4.611 g cm^{-3}	5.211 g cm^{-3}
Space group	$Pnma$ (No. 62)	$Pnma$ (No. 62)
Lattice parameters	$a = 17.1160(6)$ Å	$a = 17.5970(4)$ Å
	$b = 5.556(1)$ Å	$b = 5.5832(9)$ Å
	$c = 6.480(1)$ Å	$c = 6.691(1)$ Å
Cell volume, Z	616.2(2) Å^3, 4	657.4(2) Å^3, 4
Data collection		
Device	STOE IPDS I	
Radiation	Mo-Kα, 0.71073 Å	
	graphite monochromator	
Temperature	293K	
Scan range	$2.38° \leqslant 2\theta \leqslant 26.55°$	$2.31° \leqslant 2\theta \leqslant 26.60°$
hkl range	$-21 \leqslant h \leqslant 21$	$-21 \leqslant h \leqslant 21$
	$-6 \leqslant k \leqslant 6$	$-6 \leqslant k \leqslant 6$
	$-8 \leqslant l \leqslant 8$	$-8 \leqslant l \leqslant 8$
Structure solution and refinement	$ZnSb_2O_3Cl_2$	$ZnSb_2O_3Br_2$
Measured reflections	5442	8371
Independent reflections	708	680
Independent reflections with $F_O > 4\sigma(F_O)$	655	653
R_{int}	0.0404	0.0650
R_σ	0.0177	0.0257
Structure solution	SHELXS97 [I]	
Structure refinement	SHELXL97 [J]	
Number of parameters	46	47
Absorption correction	numerical: X-RED [L], X-SHAPE [M]	
Absorption coefficient (Mo-Kα)	13.342 mm^{-1}	23.850 mm^{-1}
$R_1, wR_2[I > 3\sigma(I)]$	0.0233, 0.0584	0.0262, 0.0694
R_1, wR_2[all reflections]	0.0260, 0.0594	0.0275, 0.0700
GooF	1.177	1.237
F(000)	760	904
Residual electron density	1.091, -0.783 e Å^{-3}	1.149, -1.151 e Å^{-3}

ular to the a axis, as seen in Figure 3.3. To the best of the author's knowledge these are the first structures where antimony (III) oxide occurs in this form. Analogous *Sechserrings* were discovered by Alonso in 1998 [67] for $SbTeO_3Cl$. That structure consists of *Sechserrings* built up by trigonal pyramids [SbO_3] and [TeO_3], where antimony and tellurium are asymmertically coordinated by three oxygen atoms due to the presence of stereochemically active lone pairs.

On the other hand, as a result of ongoing investigations of the structural chemistry of lone pair elements Se(IV) and Te(IV) oxohalogenide containing Zn(II) or Cu(II), the isostructural compounds $Zn_2(TeO_3)Cl_2$ [15], $Zn_2(TeO_3)Br_2$ [17], $Zn_2(SeO_3)Cl_2$ [16], $CuZn(TeO_3)_2$ [18] have been reported in recent years. In these compounds, the hard Lewis acids Se(IV) and Te(IV) tend to bond to the hard Lewis base O^{2-}, which results in one-sided threefold coordination due to the presence of lone pair $4s^2$ and $5s^2$, respectively. The softer Lewis acids Zn(II) or Cu(II) accept both O^{2-} and X^- (X = Cl, Br) creating an oxohalide environment.

This chapter reports on the first investigations of using Sb_4O_6 as a ligand in adduct compounds with zinc chloride and zinc bromide. Analoguous to the crystal structures discussed above [15,17,16,18], these structures consist of charge-neutral infinite layers, connected by van der Waals interactions. In contrast to structures containing Se(IV) and Te(IV), coordinated by oxygens and forming negatively-charged structural entities, this work presents the first structures where Sb(III) coordinated only by oxygen build a new charge-neutral pattern, so-called *Sechserrings*.

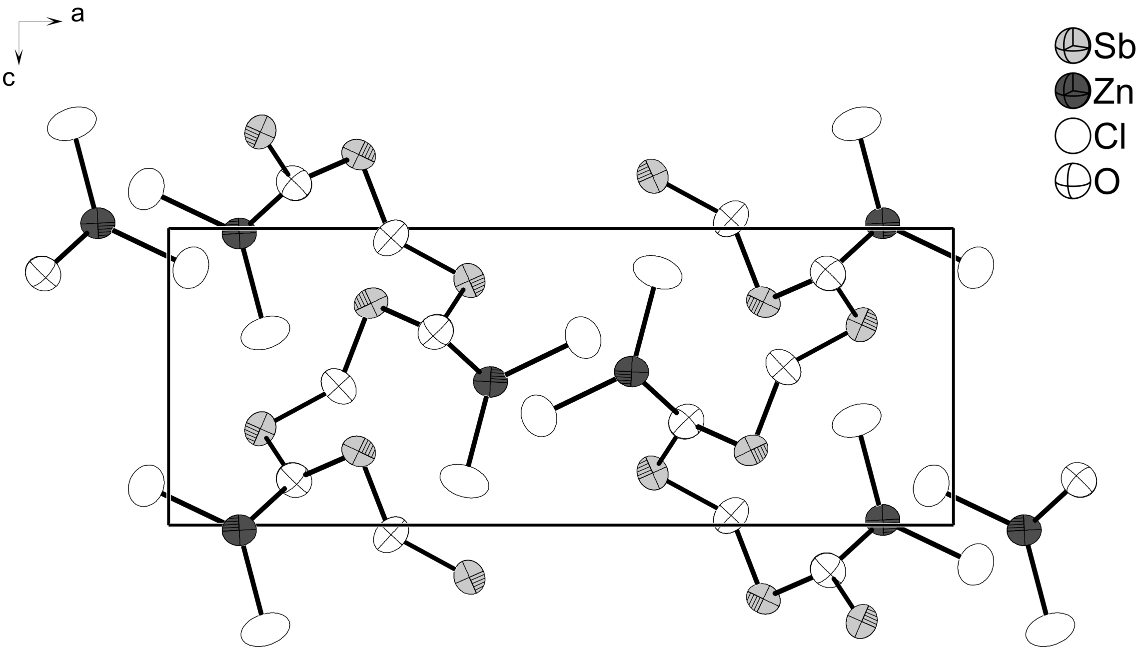

Figure 3.1.: Projection of the crystal structure of $ZnSb_2O_3Cl_2$ along [010] emphasizing the puckered layers of Sb_2O_3. $ZnCl_2$ moieties are attached to these layers. (90% probabillity level).

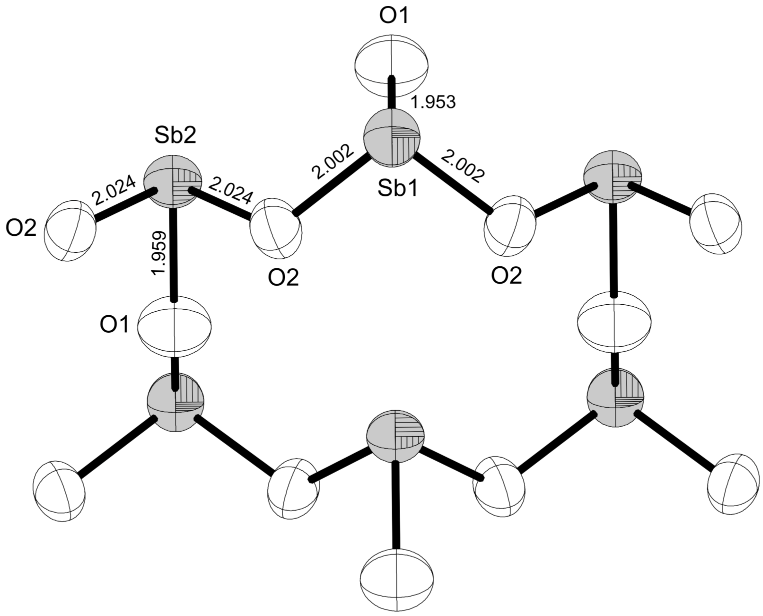

Figure 3.2.: Sechser ring formed by six [SbO_3^{3-}] units for $ZnSb_2O_3Cl_2$. All distances are given in Å.

In the ${}^{2}_{\infty}$[$ZnSb_2O_3X_2$] layers Cl^-/Br^- anions from [ZnO_2Cl_2]/[ZnO_2Br_2] tetrahedra are at relatively long distances from antimony atoms: 3.325 Å for d(Sb-Cl) in $ZnSb_2O_3Cl_2$ and 3.473 Å for d(Sb-Br) in $ZnSb_2O_3Br_2$, which suggest that only weak van der Waals forces connect the layers. Bonding distances d(Sb-O) are in the range 1.943-2.015 Å for $ZnSb_2O_3Cl_2$ and 1.943-2.019 Å for $ZnSb_2O_3Br_2$. The average d(Sb-O) distance 1.976 Å for $ZnSb_2O_3Cl_2$ and 1.978 Å for $ZnSb_2O_3Br_2$ are in the typical range for Sb(III)-O bonds, compared to the value 1.977 Å for senarmontite [104, 68] and shorter than average bond length 2.006 Å for valentinite [68, 69], two modifications of antimony (III) oxide. α-Sb_2O_3 (senarmontite) is the most stable phase below 570 °C. This cubic modification of antimony (III) oxide is composed of spherical isolated Sb_4O_6 cages, which form an adamantanoid cage. Senarmontite is isostructural with As_4O_6 [70] and P_4O_6 [71]. From 570°C to the melting point at 656°C, the thermodynamically stable form is the orthorhombic modification β-Sb_2O_3 (valentinite). It is a polymeric compound, which consists of so-called *Viererrings*, built of trigonal pyramids [SbO_3]. Figures 3.4 and 3.5 present the modifications of antimony (III) oxide.

J. A. Alonso [67] and J. Galy *et al.* [14] considered the stereochemistry of Ge (II), As (III), Se (IV), Br (V), Sn (II), Sb (III), Te (IV), I (V), Xe (VI), Tl (I), Pb (II), and Bi (III) (oxides, fluorides, and oxifluorides) containing a lone electron pair, which is thought physically to occupy a volume similar to that of an oxygen anion. With reference to these studies, the author of this work reached the conclusion that corrugation of layers formed by [SbO_3] pyramids is a consequence of the electrostatic repulsion of the $5s^2$ lone pairs of Sb (III).

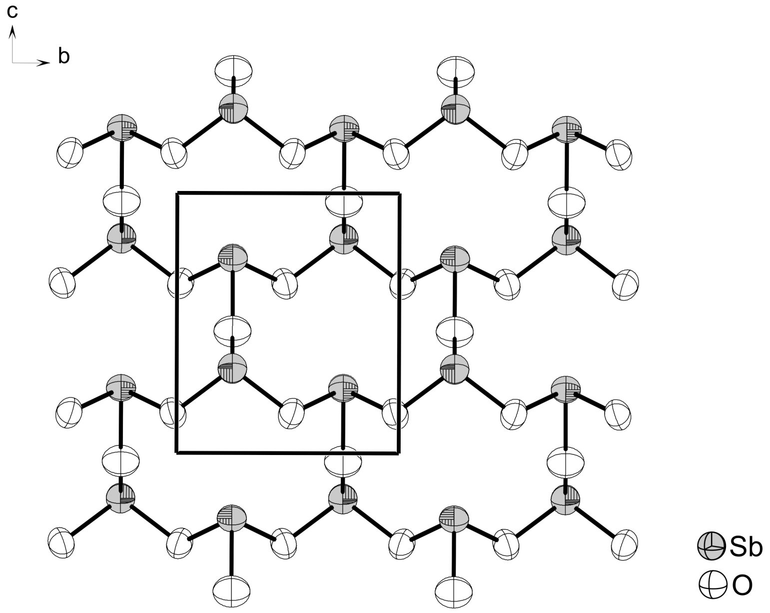

Figure 3.3.: Section of the crystal structure of $ZnSb_2O_3Cl_2$ showing one puckered layer of condensed $[SbO_3]$ units. Ellipsoids represent a probability of 90%.

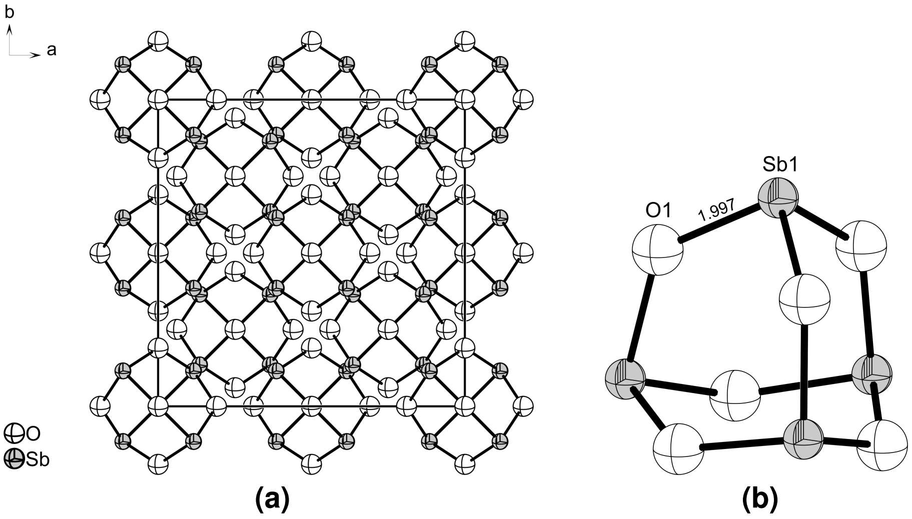

(a) **(b)**

Figure 3.4.: Projection of the crystal structure of α-Sb_2O_3 (a), Sb_4O_6 cage in cubic Sb_2O_3 (b). All distances are given in Å.

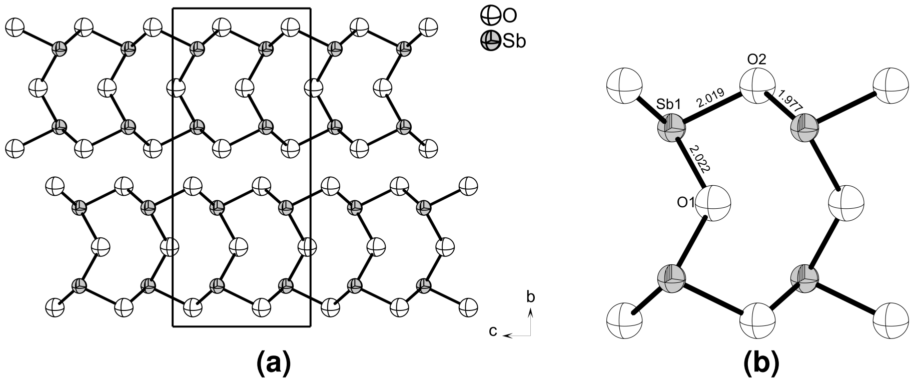

Figure 3.5.: Projection of the crystal structure of β-Sb_2O_3 (a), *Viererring* in orthorhombic Sb_2O_3 (b). All distances are given in Å.

Coordination of zinc by two chlorine/bromine and two oxygen atoms results in a strongly distorted tetrahedral environment, as seen in Figure 3.6. It must be pointed out that the average distances d(Zn-Cl) = 2.245 Å and d(Zn-Br) = 2.391 Å are slightly shorter than in pure $ZnCl_2$ [72] and $ZnBr_2$ [73], whereas d(Zn-O) = 2.076 Å in $ZnSb_2O_3Cl_2$ and d(Zn-O) = 2.068 Å in $ZnSb_2O_3Br_2$ are about 0.1 Å longer than in pure ZnO [74]. Compounds with an analogous distorted tetrahedral environment of zinc were reported by Johnsson *et al.* [15,17,16,18]. They consist of trigonal pyramids $[SeO_3]$ or $[TeO_3]$ and distorted tetrahedra $[ZnO_2Cl_2]$ or $[ZnO_2Br_2]$.

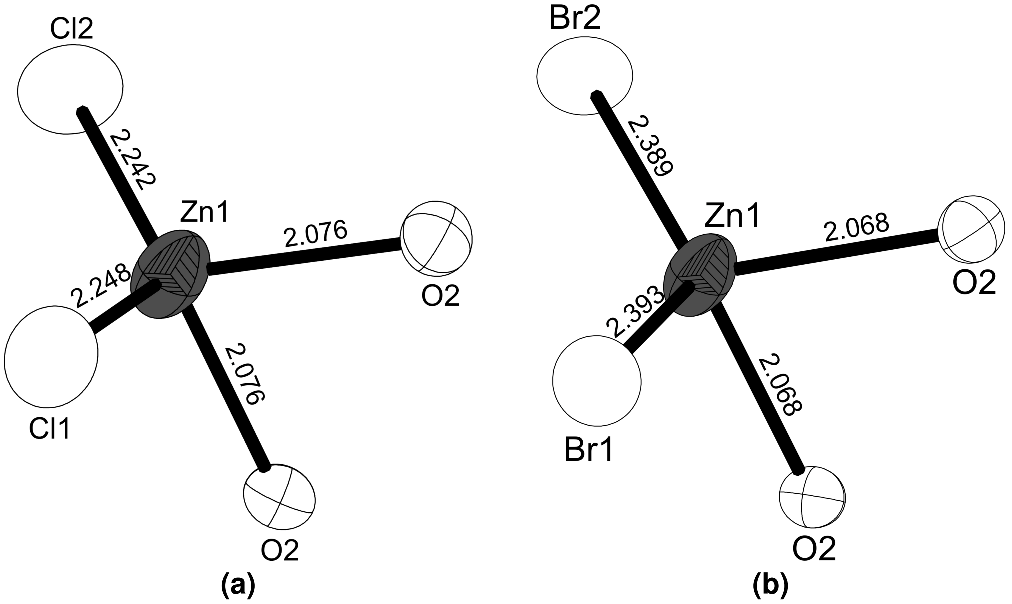

Figure 3.6.: Coordination of zinc by two chloride (a) / bromide (b) and two oxygen atoms resulting in a strongly disorted tetrahedral environment. Ellipsoids represent a probability of 90%. All distances are given in Å.

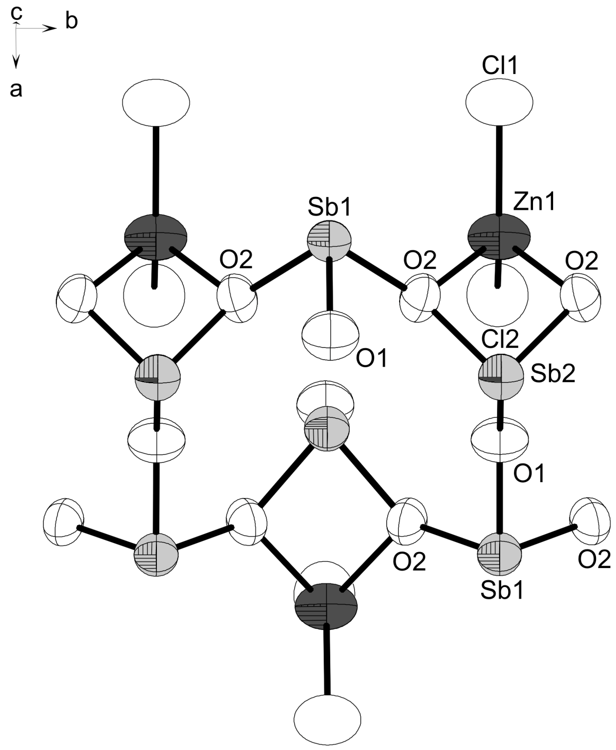

Figure 3.7.: Fragment of *Sechserring* with $[ZnO_2Cl_2]$ tetrahedra. (90% probability level).

The final composition of $ZnSb_2O_3Cl_2$ and $ZnSb_2O_3Br_2$ was additionally confirmed by EDX analysis and powder X-ray diffraction, followed by successful stoichiometric synthesis. All peaks of the X-ray powder diffraction diagrams of both compounds were unequivocally indexed in an orthorhombic unit cell. On the basis of 41 reflections, of which 33 were single and 0 were unindexed lines, for $ZnSb_2O_3Cl_2$ the unit cell (*Pnma*, $a = 17.116(6)$ Å, $b = 5.5563(1)$ Å, $c = 6.4796(1)$ Å) was determined. The unit cell of $ZnSb_2O_3Br_2$ was calculated on the basis of 45 reflections, of which 37 were single and 0 were unindexed lines (*Pnma*, $a = 17.597(4)$ Å, $b = 5.5832(9)$ Å, $c = 6.6912(1)$ Å). Since the lattice parameters from powder X-ray diffraction measurements are much more reproducible and accurate than those obtained from single crystal data, cell parameters collected from powder XRD pattern were employed in single crystal refinement. Subsequently to verify the structural models for $ZnSb_2O_3Cl_2$ and $ZnSb_2O_3Br_2$, calculated patterns were compared with X-ray powder diffraction patterns. All figures are presented in the appendix (Figures B.1-B.4).

3.1.3. Thermal analysis of $ZnSb_2O_3Cl_2$ and $ZnSb_2O_3Br_2$

Antimony (III) oxide exists as two crystalline polymorphs: the low-temperature cubic form consisting of Sb_4O_6 molecules termed as senarmontite, and valentinite, an orthorhombic structure of bands of $[SbO_3]$ trigonal pyramids. In the process of heating, senarmontite undergoes a solid-solid phase transition to the high-temperature stable valentinite. Several researchers reported polymerisation temperature values in the range 556-655°C. According to R. G. Orman *et al.* [75] the summary flow diagram of thermal events in α-Sb_2O_3 and β-Sb_2O_3 is presented in Figure 3.8.

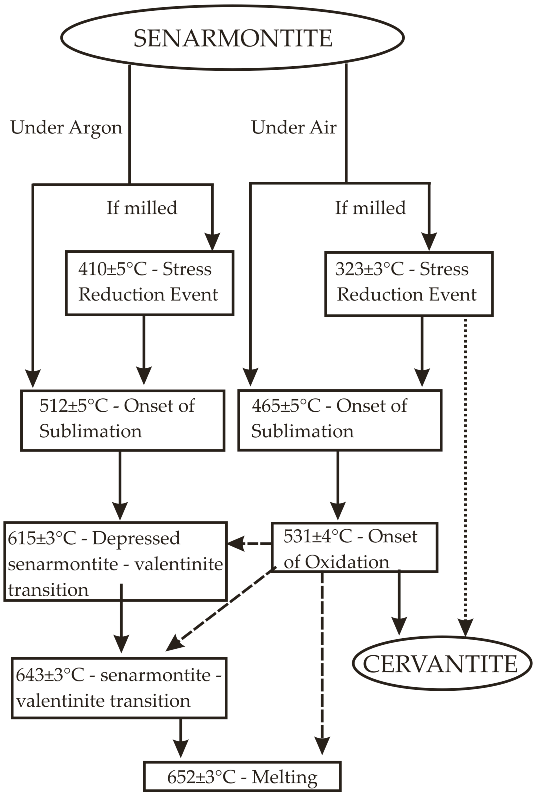

Figure 3.8.: Flow diagram summarising the thermal events occuring in Sb_2O_3. [75]

Thermal data for commercial senarmontite [Sb_4O_6] (99%, Merck) used as a substrate for all syntheses presented in this work is shown in Figure 3.9. Combined DTA and TG data for senarmontite [Sb_4O_6] were collected at a heating rate 10°C/min under flowing argon. The sample was heated/cooled in an Al_2O_3 crucible over the temperature range 100 - 700°C. TG results are drawn with a dotted line. The peak marked with the letter A indicates the senarmontite-valentinite transition, which occurs at 649°C. The melting peak occurs at 650°C and is labelled with letter B.

Thermal analysis for $ZnSb_2O_3Cl_2$ and $ZnSb_2O_3Br_2$ was performed using DTA/TG equipment providing temperature control for a small quantity of sample material. The $ZnSb_2O_3Cl_2$ sample was heated in an open Al_2O_3 crucible, while $ZnSb_2O_3Br_2$ was heated in an evacuated ampoule under flowing argon, followed by cooling to determine reversibility. The melting point was found to be 512°C for $ZnSb_2O_3Cl_2$ (Figure 3.10) and 463°C for $ZnSb_2O_3Br_2$ (Figure 3.11). There was no exothermic effect on the cooling curve, which suggests the formation of an amorphous phase [76].

Subsequently substances were removed from the crucible or ampoule respectively

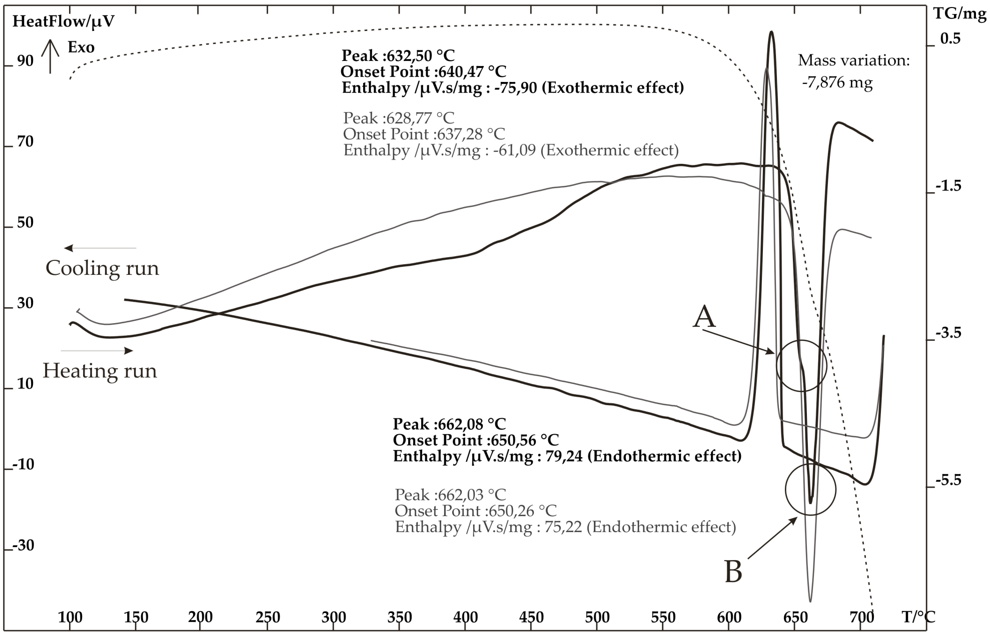

Figure 3.9.: Thermal data for senarmontite [Sb_4O_6]. The direction of the heating and cooling run is indicated by the corresponding arrow.

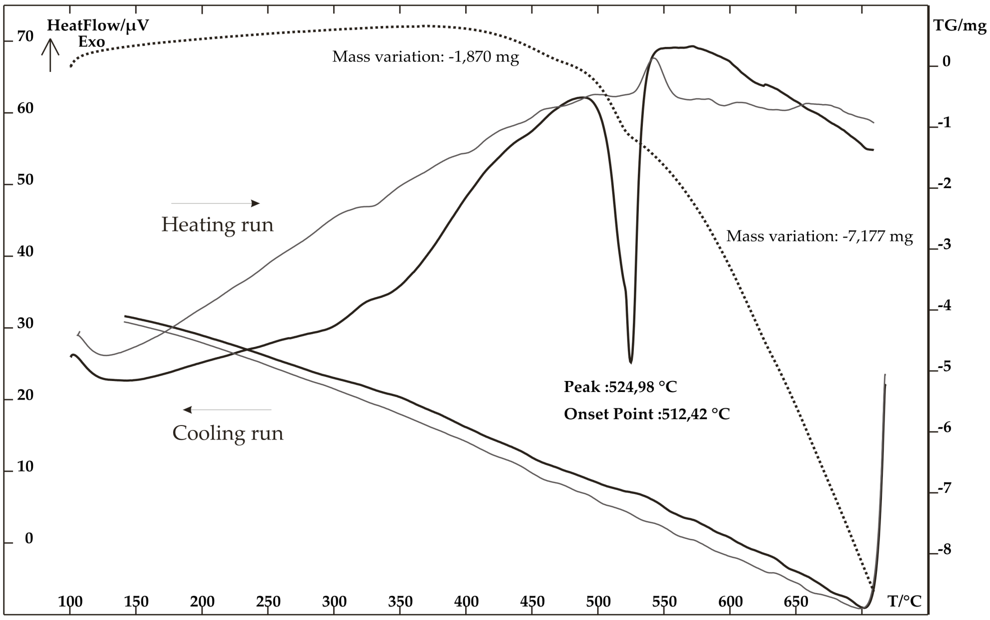

Figure 3.10.: DTA and TG measurement of $ZnSb_2O_3Cl_2$. The measurement was performed in temperature range 25-700°C with heating rate 10°C/min. Two heating and cooling cycles are shown. The direction of the heating and cooling run is indicated by the corresponding arrow.

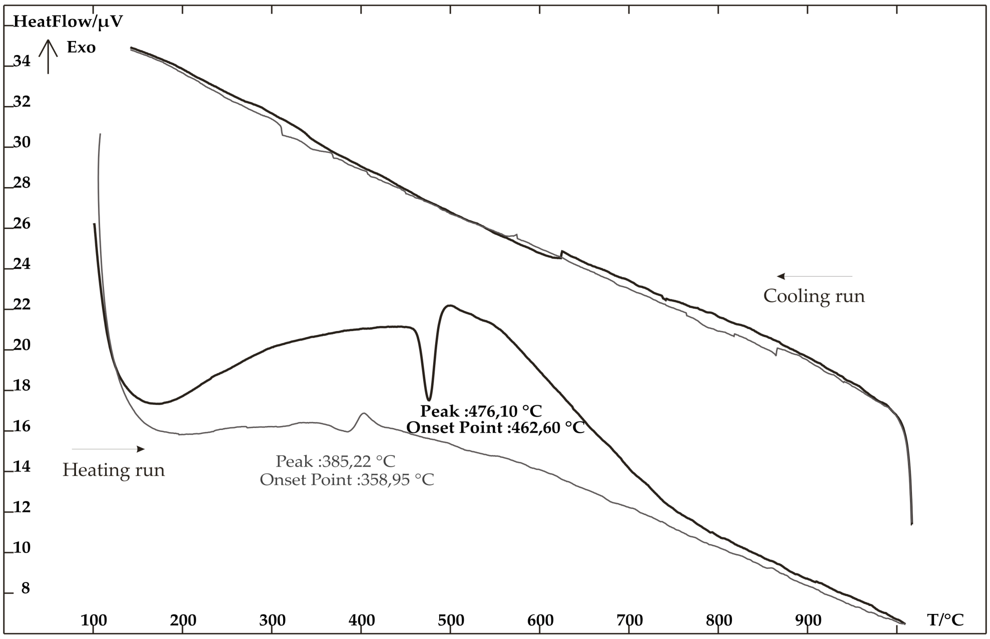

Figure 3.11.: DTA measurement of $ZnSb_2O_3Br_2$. The measurement was performed in temperature range 25-1000°C with heating rate 10°C/min. Two heating and cooling cycles are shown. The direction of the heating and cooling run is indicated by the corresponding arrow.

and analysed by powder X-ray diffraction in order to confirm DTA results, specifically the hypothesis about the possibility of the formation of amorphous structures. Figures 3.12 and 3.13 show the diffraction patterns for $ZnSb_2O_3Cl_2$, and Figures 3.14 and 3.15 show the diffraction patterns for $ZnSb_2O_3Br_2$, in both pairs of figures before and after DTA measurement respectively.

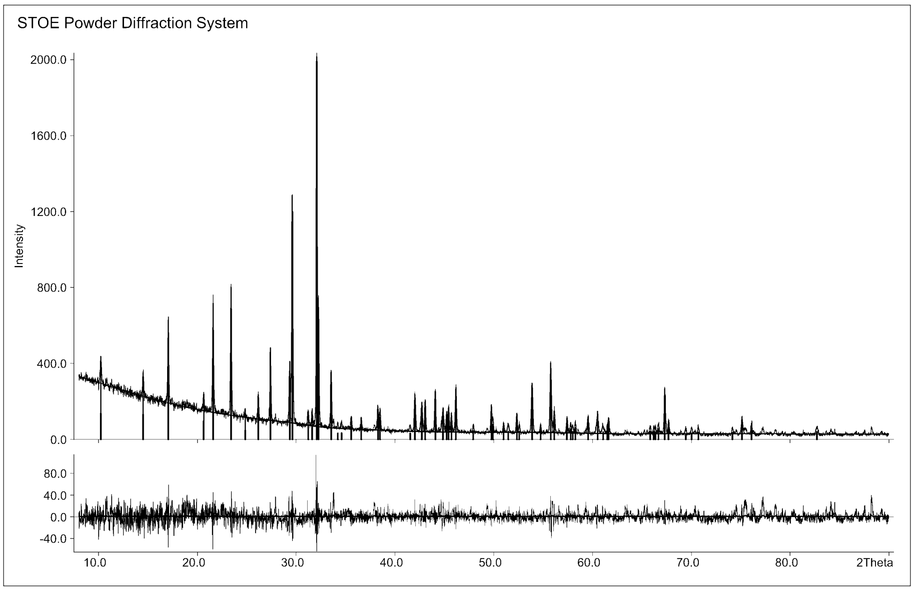

Figure 3.12.: X-ray powder diffraction pattern of crystalline $ZnSb_2O_3Cl_2$.

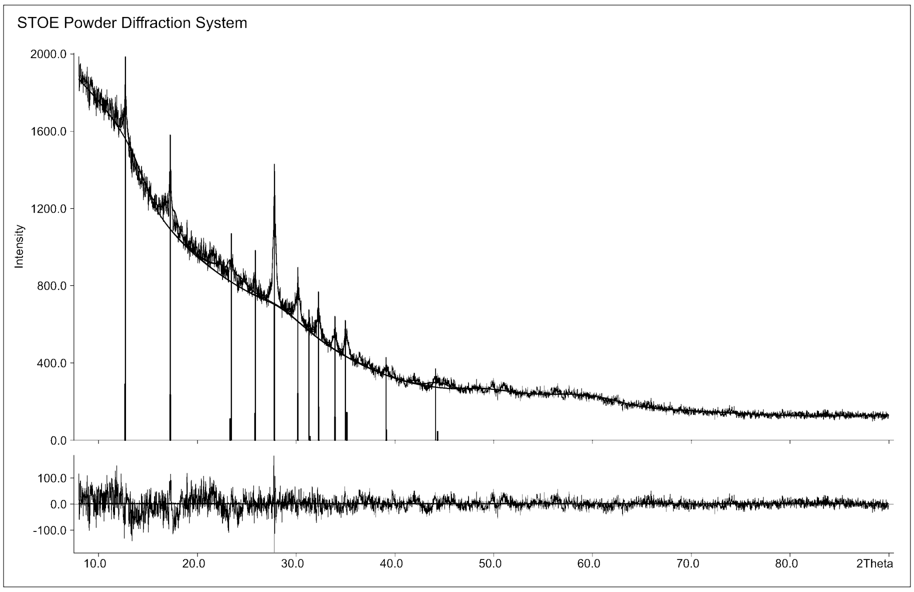

Figure 3.13.: X-ray powder pattern of $ZnSb_2O_3Cl_2$ after DTA measurement.

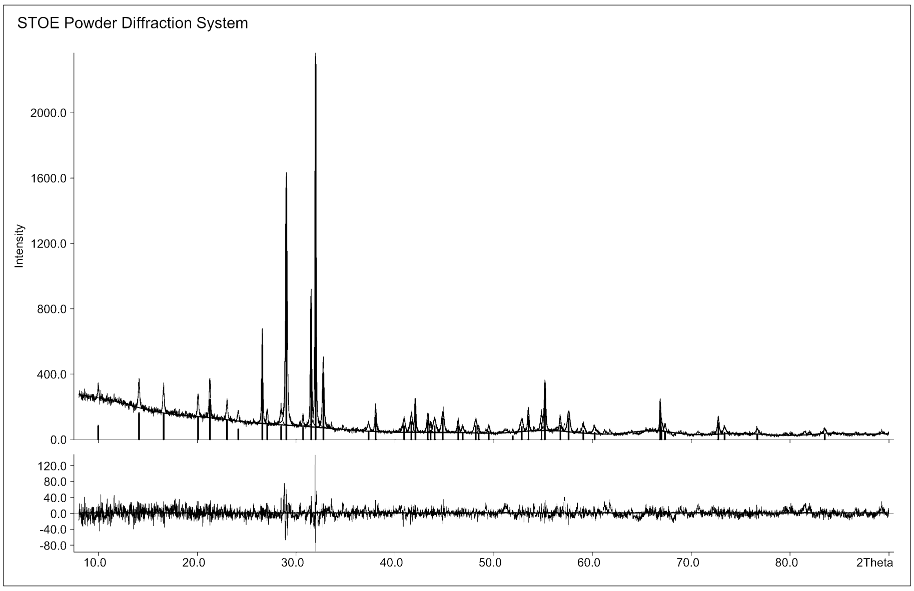

Figure 3.14.: X-ray powder diffraction pattern of crystalline $ZnSb_2O_3Br_2$.

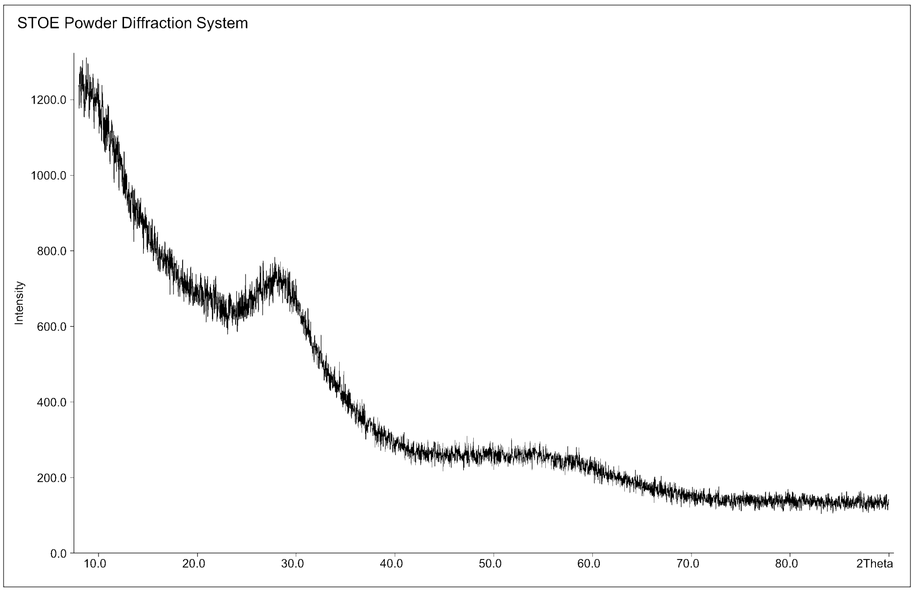

Figure 3.15.: X-ray powder pattern of $ZnSb_2O_3Br_2$ after DTA measurement.

3.1.4. Raman spectroscopy

Raman spectroscopic investigations of the compounds show vibrations which can be attributed to the starting materials ZnX_2 and Sb_4O_6 (Figure 3.16) with strong bands at 200, 264, 394, 445, 517, 627, 678 cm^{-1} for $ZnSb_2O_3Cl_2$ and at 149, 208, 273, 395, 506, 619 cm^{-1} for $ZnSb_2O_3Br_2$ corresponding to Sb-O vibrations [77, 78], and at 157, 231, 319 cm^{-1} for $ZnSb_2O_3Cl_2$ and at 149, 160, 226 cm^{-1} $ZnSb_2O_3Br_2$ corresponding to the respective Zn-X vibrations [80]. Bands indicating Zn-O stretch occur at 798 and 788 cm^{-1}. Vibrational spectra were recorded on a Varian FT-Raman module with dielectric YAG rejection filters, with 1 cm^{-1} resolution.

An exact correlation of the Raman modes with the peaks in the Raman spectra can only be carried out by way of a theoretical calculation of the Raman spectra based on the extracted crystal structures. These calculations will be one of the goals of future work in this area.

3.1.5. ATR-IR

ATR spectra of $ZnSb_2O_3X_2$ (X = Cl, Br) were recorded on a Varian 670-IR FT-IR spectrometer. Samples were measured using the ATR technique, on a Gladi ATR Base Optic Assembly with a 2.2 mm $\times$ 3.0 mm ATR diamond crystal sampling area. To clearly demonstrate the complementary nature of the spectral information, a comparison of Raman and IR absorption modes is shown in Table 3.2. The corresponding IR spectra are presented in the appendix (Figure B.6 and B.7).

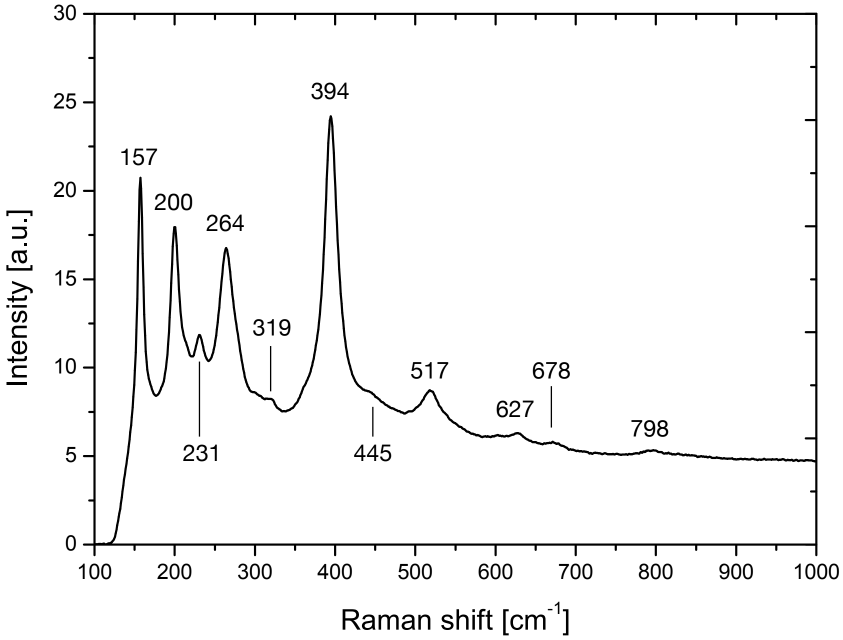

(a) $ZnSb_2O_3Cl_2$

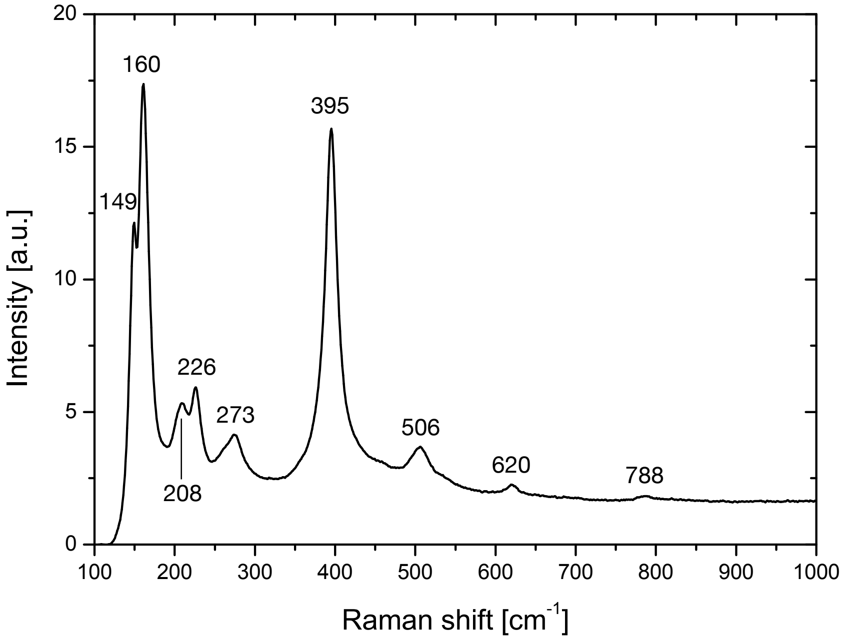

(b) $ZnSb_2O_3Br_2$

Figure 3.16.: Raman spectrum of $ZnSb_2O_3Cl_2$ and $ZnSb_2O_3Br_2$ showing significant vibrations only for ν_{Sb-O} and ν_{Zn-Cl} (a) and ν_{Sb-O} and ν_{Zn-Br} (b)

Table 3.2.: Summary of modes occurring in Raman and IR spectra of compounds representing the system $ZnSb_2O_3X_2$ (X = Cl, Br).

Raman		IR		Comments
$ZnSb_2O_3Cl_2$	$ZnSb_2O_3Br_2$	$ZnSb_2O_3Cl_2$	$ZnSb_2O_3Br_2$	
	149		148	ν(Zn-Br) or (Sb-O) lattice vibrations
157		156		ν(Zn-Cl)
	160	168	161	ν(Zn-X)
		185	187	δ(Sb-O) twisting
200	208	199	198	δ(Sb-O) wagging
231	226	223	223	ν(Zn-X)
		254	242	
264	273		260	δ(Sb-O) scissoring
319			319	ν(Zn-Cl)
		358	347	ν_{sym}(Sb-O)
		379	377	ν_{sym}(Sb-O)
394	395	395	393	ν_{sym}(Sb-O)
		431	435	ν_{sym}(Sb-O)
445		443	443	ν_{sym}(Sb-O)
517	506	498	488	ν_{sym}(Sb-O)
627	619	628	621	ν_{asym}(Sb-O)
678		702	691	ν_{asym}(Sb-O)
798	788	785	777	ν(Zn-O)
		1176	1171	
		1617	1602	

3.1.6. UV-Vis spectroscopy and electronic band gap calculations

Diffuse reflectivity measurements were used to investigate the optical properties of $ZnSb_2O_3X_2$ (X = Cl, Br). Absorption data were calculated from the measured values using the Kubelka-Munk function [51, 52], see Figure 3.17. The energy gaps were determined from Tauc plots [53]. The analysis suggests a direct band gap around 3.88 eV for $ZnSb_2O_3Cl_2$, as shown in Figure 3.18. Several attempts were made to gather data for $ZnSb_2O_3Br_2$ without success.

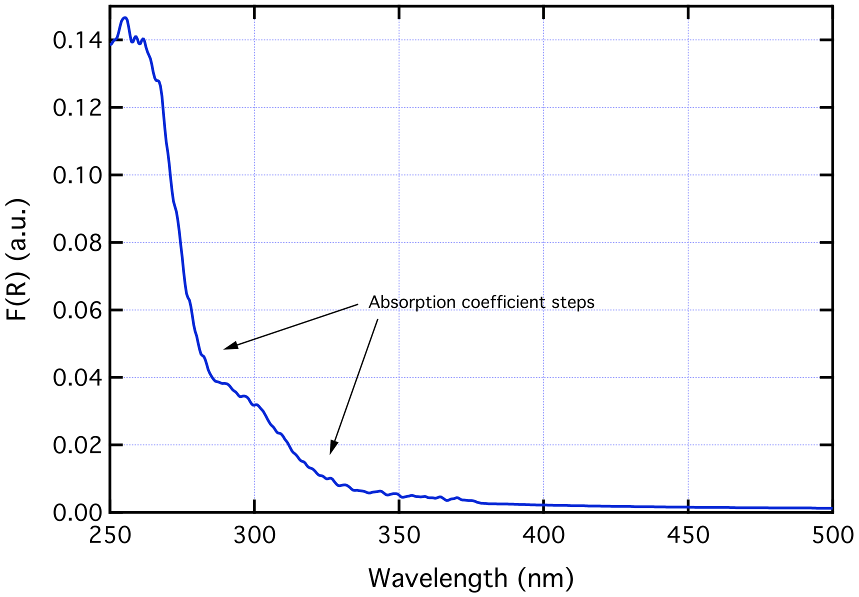

Figure 3.17.: Kubelka-Munk coefficient (proportional to absorption coefficient) for $ZnSb_2O_3Cl_2$ derived from UV-Vis spectroscopy. Two abrupt changes in the absorption coefficient are apparent.

Electronic band structure calculations were performed using LDA with the Perdew-Wang parametrization [54]. The full potential local orbital method in the scalar relativistic version which is implemented in the FPLO code (version 9.00-34) was used [81]. A k-mesh of $12 \times 12 \times 12$ points in the irreducible part of the Brillouin zone was employed to provide convergence in density and accurate results, especially for states close to the Fermi level. Experimental lattice parameters were applied for both calculating band structures and density of states (DOS).

The insulating state of $ZnSb_2O_3Cl_2$ is represented by an indirect band gap of 3.6 eV. The valence band maximum is at the Γ-point of the Brillouin zone, whereas the conduction band minimum is between Γ and Z. Furthermore, a direct band gap of 3.8 eV at the Γ-point is observed, as shown in Figure 3.20. This is in good agreement with the measured UV-Vis spectra. The contribution of Sb 5s orbitals to the valence band structure is highlighted by the thick lines in the figure.

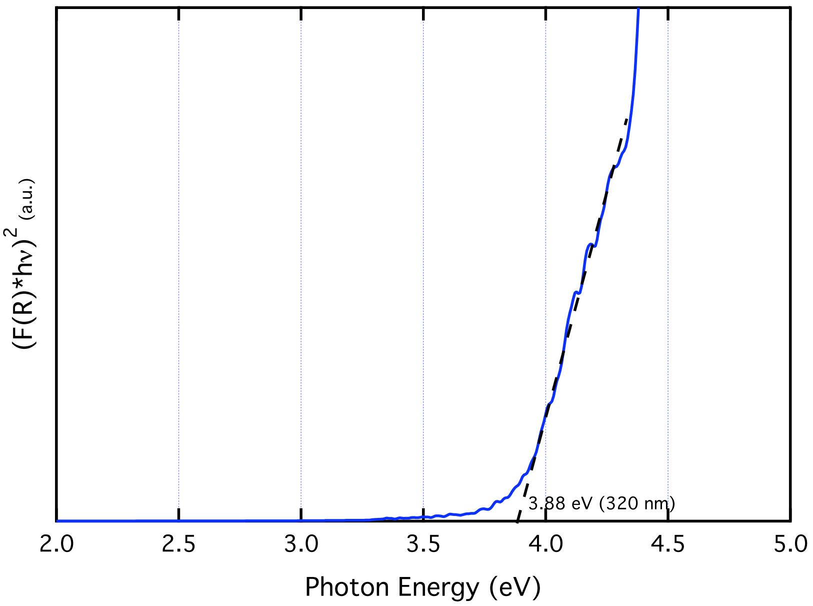

Figure 3.18.: Tauc plot for $ZnSb_2O_3Cl_2$ with exponent 2 for a semiconductor with direct electronic band gap.

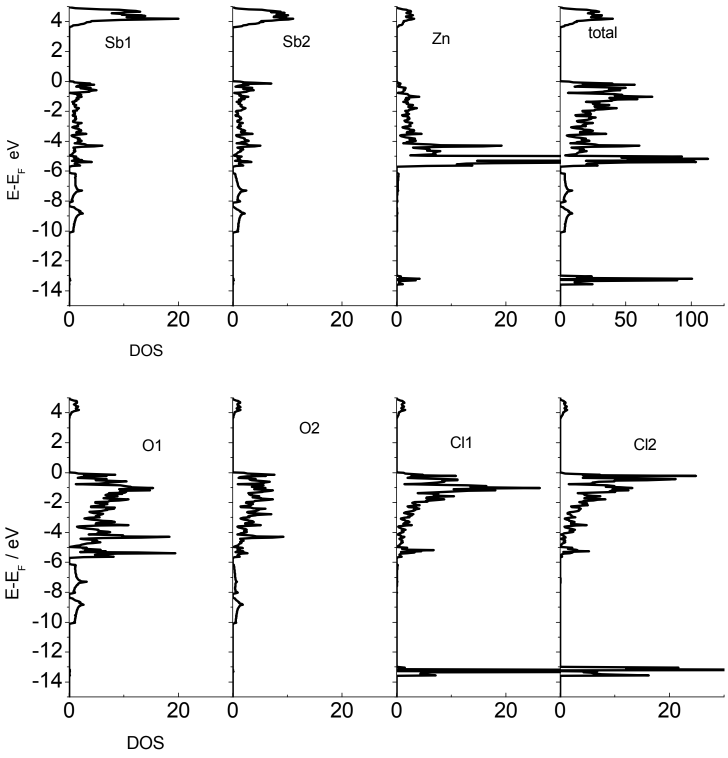

Figure 3.19.: Density of states for $ZnSb_2O_3Cl_2$.

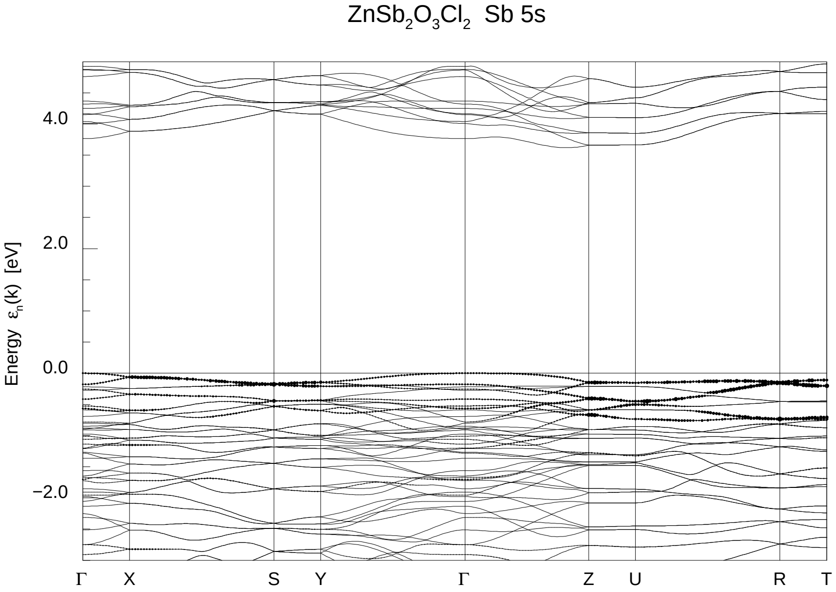

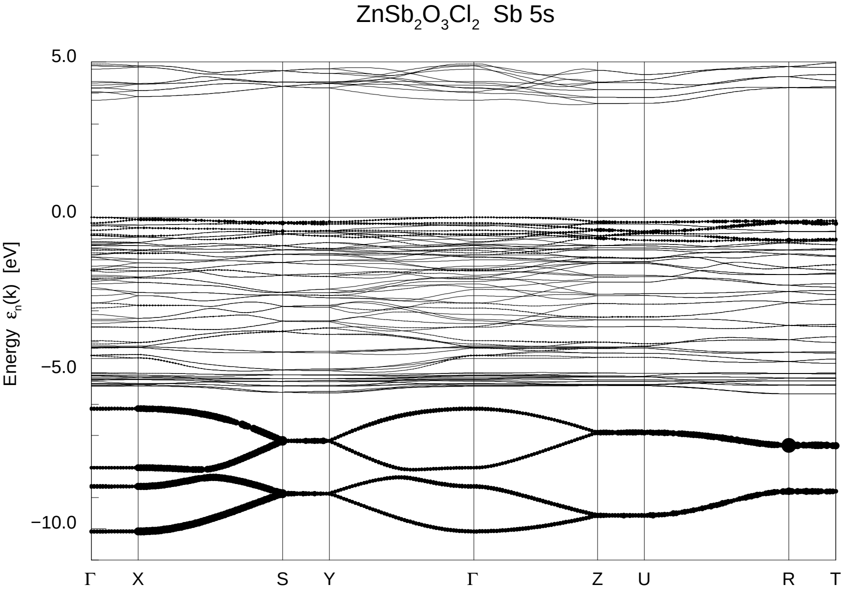

Figure 3.20.: Electronic band structure of $ZnSb_2O_3Cl_2$. The lower figure highlights the participation of Sb 5s orbitals deep in the valence band.

3.2. $Cd_4Sb_8O_{12.5}X_7$ (X = Cl, Br)

3.2.1. Synthesis

New quaternary compounds representing the system $Cd_4Sb_8O_{12.5}X_7$ (X = Cl, Br) were synthesised from ultra dry CdX_2 (X = Cl, Br) and Sb_4O_6 mixed in a 2:1 molar ratio. All the reactants were loaded in an argon-filled drybox, homogenized by grinding, placed into a sealed evacuated quartz tube, and heated at 600°C for 14 days. In both cases, the products were colourless polycrystalline samples containing numerous single crystals.

3.2.2. Single crystal and powder X-ray diffraction analysis

Single crystal X-ray diffraction data of $Cd_4Sb_8O_{12.5}X_7$ (X = Cl, Br) were collected on an STOE IPDS I, equipped with a Mo-Kα source. The diffraction patterns could be indexed in the Laue class $2/m$, with a C-centered monoclinic cell. The value of the $|E^2 - 1|$ criterion was 1.005, indicating a centrosymmetric space group as more likely. The extinction conditions indicated the space groups $C2/m$, $C2$, and Cm. Because of the $|E^2 - 1|$ criterion the structure was therefore solved in $C2/m$. Integration of the reflection intensities and absorption correction were performed using *X-Area* [D]. All structures were solved by direct methods using *SIR92* [G], and refined by full matrix least-squares fitting on F^2 using *SHELXL-97* [J]. Crystallographic data and structural refinements for both compounds are summarized in Table 3.3.

The preliminary crystal structure refinement resulted in $[Cd_2Sb_8O_{14}][Cd_2X_6]X$ (X = Cl, Br), exhibiting the problem of charge imbalance. Partial oxidation of Sb(III) to Sb(V) was suspected, but was however excluded by Mössbauer spectroscopy analysis of the samples, the results of which are presented in Section 3.2.4. The suspected possibility of the presence of a hydroxy group was excluded by infrared absorption spectroscopy measurements described later in this chapter. The possibility of a superstructure was also excluded by performing measurements with a very long radiation time. Herein, $[Cd_2Sb_8O_{12.5}][Cd_2X_6]X$ (X = Cl, Br) is presented as the proposed structure model, where oxygen atom positions O3 and O4 are occupied to 63.0%. The fractional occupancy was suggested by findings of higher displacement parameters in $Cd_4Sb_8O_{12.5}Cl_7$, amounting to 0.107(7) and 0.101(7), respectively. In $Cd_4Sb_8O_{12.5}Br_7$ the displacement parameters were 0.114(9), 0.101 for O3 and O4, respectively. Final atomic coordinates and equivalent isotropic displacement parameters for these structures are listed in the appendix in Table B.5 and B.6, while Table B.7 and Table B.8 include anisotropic displacement parameters. Anisotropic displacement parameters were used for all atoms. An extinction parameter was included in the last refinement cycles. All atoms were set on their standard positions using the *Structur Tidy* routine in *PLATON* [K].

The final composition of $Cd_4Sb_8O_{12.5}X_7$ (X = Cl, Br) was additionally confirmed by powder X-ray diffraction and EDX analysis followed by successful stoichiometric synthesis. All data concerning phase analysis are presented in the appendix (Figures B.8-B.11). The EDX analyses based on 5 different crystals confirmed the stoichiometry and presence of heavy atoms in the ratio 11.69% Cd, 23.75% Sb, 21.61% Cl for $Cd_4Sb_8O_{12.5}Cl_7$ and 11.93% Cd, 24.12% Sb, 21.77% Br for $Cd_4Sb_8O_{12.5}Br_7$. The values derived from EDX analysis are in reasonable agreement with the structural solution.

In order to determine the presence of cadmium and antimony in the investigated materials, and also for quantitative analysis, ICP-OES (Inductively Coupled Plasma Optical Emission Spectroscopy) measurements were performed using a Spectro ICP-OES Spectroflame modula EOP spectrometer. ICP-OES analysis was carried out after the solid was dissolved in hydrochloric acid (1 mol/l, Merck p.a.). The calibration was performed with the series of standard solutions prepared from Sb_2O_3 (Merck, 99%) and CdO (Merck, p.a.) dissolved in HCl (1 mol/l, Merck p.a.) and diluted in water. Two series of ICP-OES measurements resulted in the confirmation of stoichiometry and presence of metal atoms in the ratio: $5.82 \pm 0.07\%$ ($5.79 \pm 0.07\%$) Cd, $12.01 \pm 0.2\%$ ($11.97 \pm 0.3\%$) Sb in $Cd_4Sb_8O_{12.5}Cl_7$, and $3.69 \pm 0.08\%$ ($3.66 \pm 0.08\%$) Cd, $7.51 \pm 0.7\%$ ($7.49 \pm 0.3\%$) Sb in $Cd_4Sb_8O_{12.5}Br_7$. The values in parentheses are from the second series of measurements.

New quaternary compounds $Cd_4Sb_8O_{12.5}X_7$ (X = Cl, Br) have been found to be isostructural. The crystal structure consists of two isolated building blocks: negatively charged 1D double chains $[Cd_2X_6]^{2-}$ (X =Cl, Br) and positively charged $[Cd_2Sb_8O_{12.5}]^{3+}$ layers, propagating along the [010] direction. The empty space between adjacent cadmium(II) antimony(III) halide layers is occupied by halide anions $[Cl^-$ / $Br^-]$ as shown in Figure 3.21. Both quaternary $Cd_4Sb_8O_{12.5}X_7$ (X = Cl, Br) structures feature rather unusual substructures. The structure shows a significant similarity to previously reported $[Cd_2(Te_6O_{13})][Cd_2Cl_6]$ [82], which consists of novel polymeric tellurium(IV) oxide anions and cadmium chloride units. Such isolated double chains $[Cd_2Cl_6]^{2-}$ have been also reported in the organic compound $[C_3H_7N_2S][CdCl_3]$ [83].

One-dimensional double chains form Cd^{2+}-centered $[Cd(2)X_6]$ (X = Cl, Br) octahedra, sharing common equatorial edges. Bond distances d(Cd-X) within the octahedra fall in the range 2.499(4)-2.732(2) Å for $Cd_4Sb_8O_{12.5}Cl_7$ and 2.624(2)-2.842(2) Å for $Cd_4Sb_8O_{12.5}Br_7$, and are comparable to those reported for pure $CdCl_2$ [84] and $CdBr_2$ [85,86]. The projection of the $[Cd_2Cl_6]^{2-}$ polymer is presented in Figure 3.22.

$[Cd(1)_2Sb_8O_{12.5}]^{3+}$ layers are built with $Cd(1)^{2+}$ seven-coordinated by oxygen atoms forming 1D double chains along [010], as seen in Figure 3.23. The values for effective coordination numbers for Cd1 amounts to ECoN($Cd(1)^{2+}/O^{2-}$)=6.7 in $Cd_4Sb_8O_{12.5}Cl_7$ and ECoN($Cd(1)^{2+}/O^{2-}$)=6.8 in $Cd_4Sb_8O_{12.5}Br_7$. The calculations were performed us-

Table 3.3.: Details of the data collection and results of the structure refinement for $Cd_4Sb_8O_{12.5}X_7$ (X = Cl, Br)

Crystal data		
Chemical formula	$Cd_4Sb_8O_{12.5}Cl_7$	$Cd_4Sb_8O_{12.5}Br_7$
Crystal colour/habit	colourless/needle	colourless/needle
Crystal size	0.1 × 0.05× 0.03 mm	0.3 × 0.2 × 0.1 mm
Molecular weight	1895.75 g mol^{-1}	2206.97 g mol^{-1}
Calculated density	5.273 g cm^{-3}	5.743 g cm^{-3}
Space group	$C2/m$ (No. 12)	$C2/m$ (No. 12)
Lattice parameters	$a = 23.923(5)$ Å	$a = 24.465(5)$ Å
	$b = 3.9927(7)$ Å $\beta = 118.811(1)°$	$b = 4.0569(7)$ Å $\beta = 119.348(1)°$
	$c = 14.2520(4)$ Å	$c = 14.751(3)$ Å
Cell volume, Z	1192.8(3) Å^3, 2	1276.2(4) Å^3, 2
Data collection		
Device, Radiation, Temperature	STOE IPDS I, Mo-Kα, 0.71073 Å	
	graphite monochromator, 293 (2)K	
Scan range	$1.94° \leqslant 2\theta \leqslant 25.50°$	$1.91° \leqslant 2\theta \leqslant 25.10°$
hkl range	$-28 \leqslant h \leqslant 28$	$-28 \leqslant h \leqslant 28$
	$-4 \leqslant k \leqslant 4$	$-4 \leqslant k \leqslant 4$
	$-17 \leqslant l \leqslant 17$	$-17 \leqslant l \leqslant 17$
Structure solution and refinement	$Cd_4Sb_8O_{12.5}Cl_7$	$Cd_4Sb_8O_{12.5}Br_7$
Measured reflections	8201	8471
Independent reflections	1282	1310
Independent reflections with $F_O > 4\sigma(F_O)$	1186	1250
R_{int}	0.0296	0.0837
R_σ	0.0152	0.0340
Structure solution, refinement	SIR92[G], SHELXL97 [J]	
Number of parameters	102	102
Absorption correction	numerical: X-RED [L], X-SHAPE [M]	
Absorption coefficient	13.226 mm^{-1}	22.589 mm^{-1}
$R_1, wR_2[I > 3\sigma(I)]$	0.0423, 0.1115	0.0612, 0.1590
R_1, wR_2[all reflections]	0.0449, 0.1133	0.0629, 0.1614
GooF	1.099	1.081
F(000)	1662	1914
Residual electron density	1.966, -2.834 e Å^{-3}	4.566, -3.687 e Å^{-3}

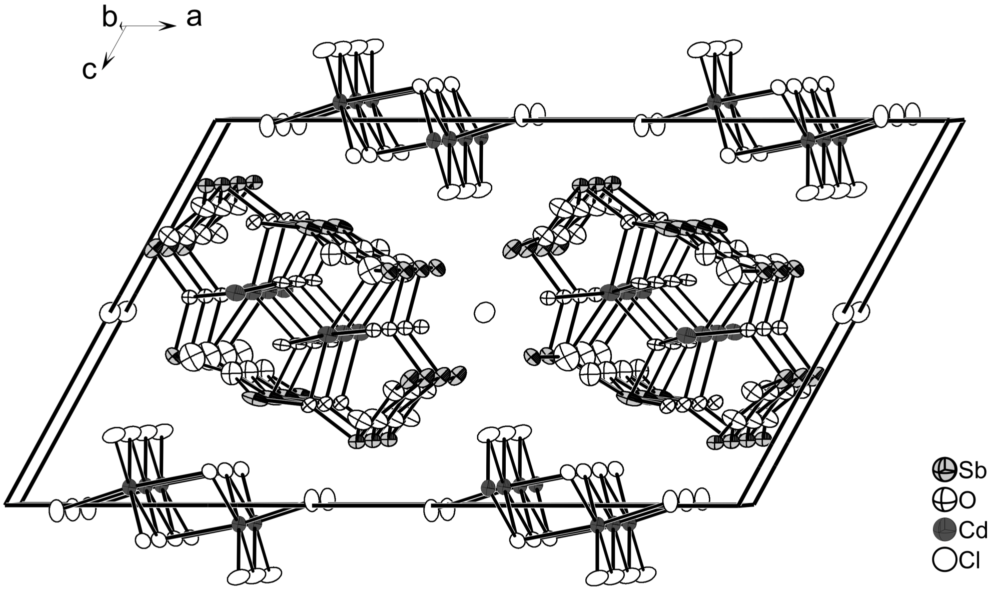

Figure 3.21.: Crystal structure section of $Cd_4Sb_8O_{12.5}Cl_7$ along [010], 50% probability level.

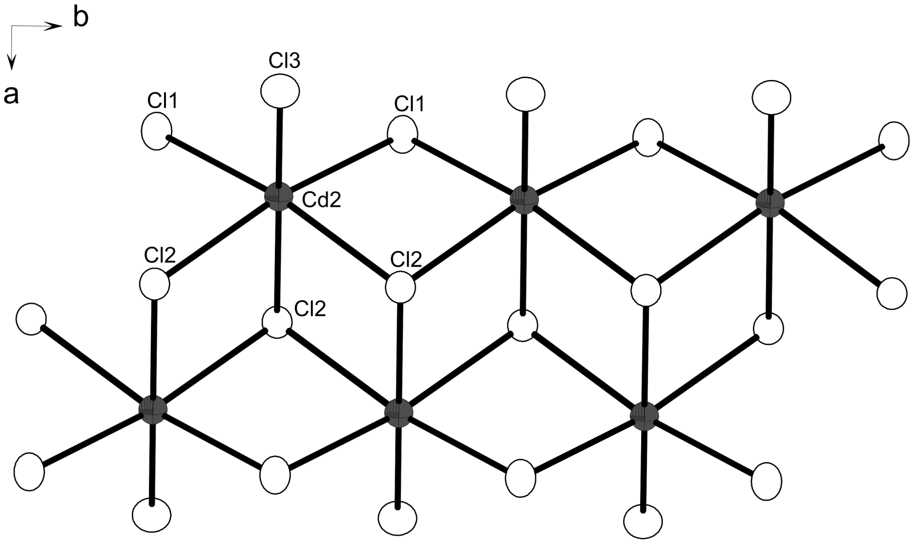

Figure 3.22.: Projection of the 1D double chain $[Cd(2)_2Cl_6]^{2-}$ built by edge-sharing $[Cd(2)X_6]$ octahedra. (50% probabillity level). All distances are given in Å.

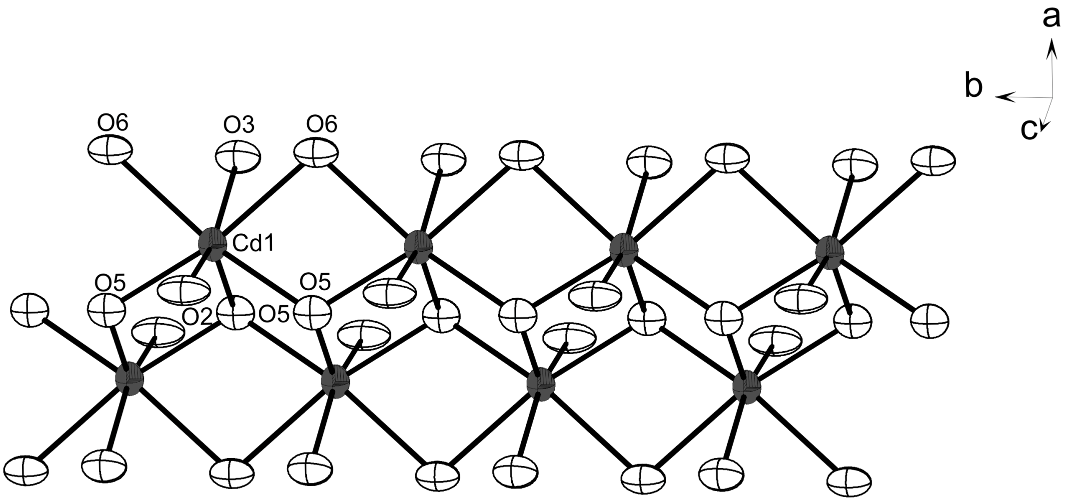

Figure 3.23.: Projection of edge-sharing $[Cd(1)O_7]$ units forming a 1D double chain along [010]. (50% probability level).

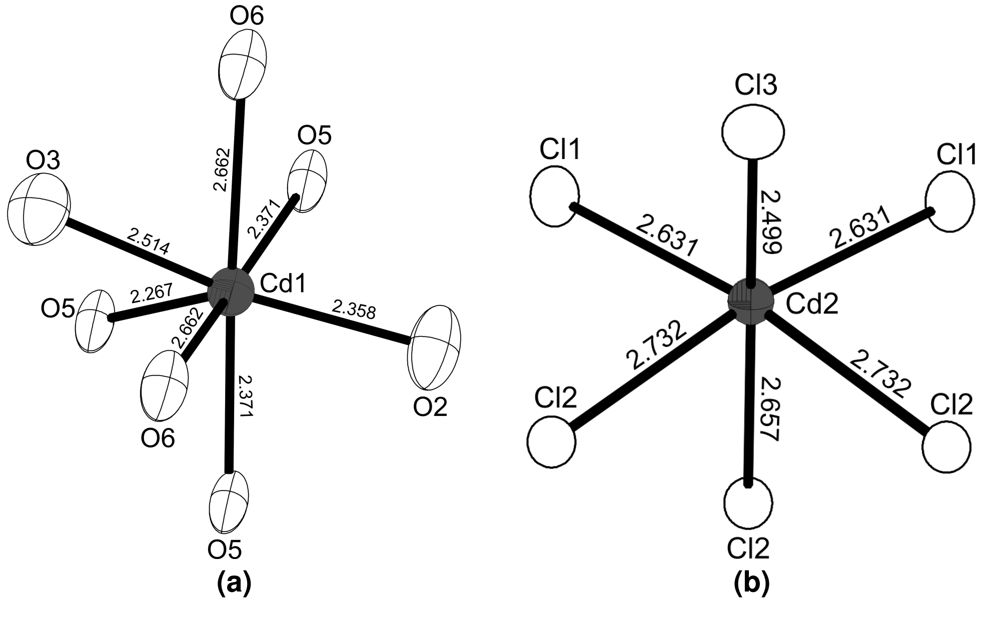

Figure 3.24.: Coordination geometry about the Cd1 and Cd2 atoms. Cd-O and Cd-Cl distances are shown in units of Å. (50% probability level).

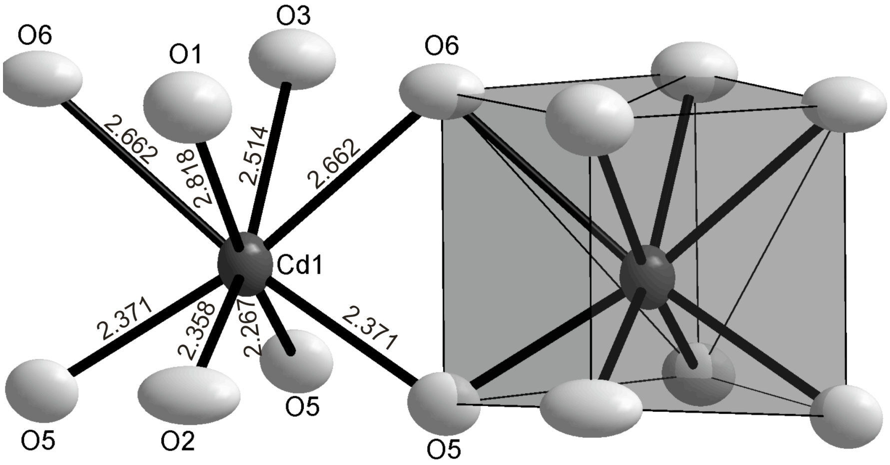

Figure 3.25.: Coordination geometry about Cd1 resulting in cubic environment. Cd-O distances are shown in units of Å. (50% probability level).

ing MAPLE [87, 88, 89]. The CN values obtained for Cd1 demonstrate that in both compounds the $Cd(1)^{2+}$ build $[Cd(1)O_7]$ units. The coordination sphere of $Cd(1)^{2+}$ ions of eight was also considered, forming cubes as coordination polyhedra, as shown in Figure 3.25. This is a rather unexpected finding of coordination polyhedra for Cd^{2+}. It was also examined whether the Cd1 atom was not in fact an antimony atom, since it is difficult to distinguish those two elements based on single crystal X-ray diffraction measurement. This possibility was excluded by bond valence sum (BVS) calculations. The bond length d(Cd1-O1)= 2.818(1) Å is about 0.6 Å longer than the average d(Cd-O)=2.2906 Å in pure CdO [90], and can be considered as non-bonded. The bond lengths d(Cd(1)-O) in the range 2.272(2)-2.662(1) Å in $Cd_4Sb_8O_{12.5}Cl_7$ and 2.256(2)-2.688(1) Å in $Cd_4Sb_8O_{12.5}Br_7$ are comparable to the values in the range 2.307(8)-2.550(8) Å in $[Cd_2(Te_6O_{13})][Cd_2Cl_6]$ [82].

The cationic cadmium(II) antimony(III) oxide constitutes infinite tubes propagating along the b axis. The $[Cd(1)O_7]$ units are connected by common edges and corners with $[Sb_8O_{12.5}]^-$ slabs built by SbO_4 and SbO_6 polyhedra, as seen in Figure 3.26. All antimony atoms, except Sb4, have tetragonal pyramidal coordination, or trigonal bipyramidal if taking lone pairs of electrons into account. Antimony cations have an asymmetric coordination environment due to the presence of stereochemically active lone pairs of electrons. The Sb-O distances fall in the range 1.959(1)-2.178(5) Å in $Cd_4Sb_8O_{12.5}Cl_7$ and 1.97(2)-2.204(7) Å in $Cd_4Sb_8O_{12.5}Br_7$. Those values are in reasonable agreement with d(Sb-O) bonds found in onoratoite [91], where antimony atoms also form SbO_4 groups. On the other hand, $Sb(4)^{3+}$ is six-coordinated by oxygens, what is a rather unusual finding. On account of the refinement of oxygen atoms O3 and O4 with partial occupation amounting to 63.0%, the $Sb(4)^{3+}$ cations should be considered as four-coordinated by oxygens. The bond distances falling in the range 1.957(1)-2.46(2) Å in $Cd_4Sb_8O_{12.5}Cl_7$ and 1.937(2)-2.44(3) Å in $Cd_4Sb_8O_{12.5}Br_7$ are in reasonable agreement with onoratoite [91], where the Sb-O distances in [SbO_4E] are in the range 1.96(2)-2.59(2) Å. The details of bonding and bond valences in $Cd_4Sb_8O_{12.5}X_7$ (X = Cl, Br) are presented in Table 3.4.

Bond valence calculations give values which are close to the expected valences for most ions, as shown in Table 3.5 and Table 3.6. Halogen atoms are the exception to this rule. Chlorine has a values in the range 0.46-0.80 vu, and bromine in the range 0.49-0.83 vu. This suggests that halogen atoms are fully integrated in the covalent/ionic network. Taking into account the interlayer distances Sb...X (X = Cl, Br) below 4 Å, the BVS values oscillate between 0.59 and 0.85 for chlorine atoms and between 0.63 to 0.90 for bromine. However these values are still far from the expected value of 1. The case of underbonding halides is rather common in oxidehalides and has been previously reported in $CoSbO_2Br_2$ [33], $FeTe_2O_5X$ (X = Cl, Br) [92], $Fe_3Te_3O_{10}Cl$ [93], $Fe_5Te_6O_{18}Cl_2$ and $Fe_8Te_{12}O_{32}Cl_3Br_3$ [94]. Bond valence sum calculations were performed according to Brown [95] using BVS calculator [W]. The bond valences were determined using emphirical parameters: $b = 0.37$ Å, r_0(Sb^{3+}-O) = 1.973 Å, r_0(Cd^{2+}-Cl) = 2.212 Å, r_0(Cd^{2+}-Br) = 2.362 Å, r_0(Cd^{2+}-O) = 1.904 Å.

The shortest cation-anion distances between the adjacent building blocks varies in the range 3.276(2)-3.912(4) Å for $Cd_4Sb_8O_{12.5}Cl_7$ and 3.377(3)-3.860(4) Å for $Cd_4Sb_8O_{12.5}Br_7$. The closest cation-cation separations within a layer are in the range 3.664(2)-3.993(1) Å for $Cd_4Sb_8O_{12.5}Cl_7$ and 3.478(5)-4.057(1) Å for $Cd_4Sb_8O_{12.5}Br_7$. The cation-anion separation between building blocks are quite similar to the cation-cation distances within the layers, suggesting an absence of bonding contact between the adjacent building blocks, and it can thus be concluded that only weak van der Waals forces connect the layers to one another.

The division in the structure of cationic and anionic substructures can be explained by the strong influence of Lewis acidity/alkalinity in the bonding preferences. The antimony cation Sb^{3+} as a rather strong Lewis acid prefer to form a bond with strong Lewis base O^{2-}. On the other hand, the halogen anion as a softer Lewis base tends to bond with the transition metal cation, a soft Lewis acid.

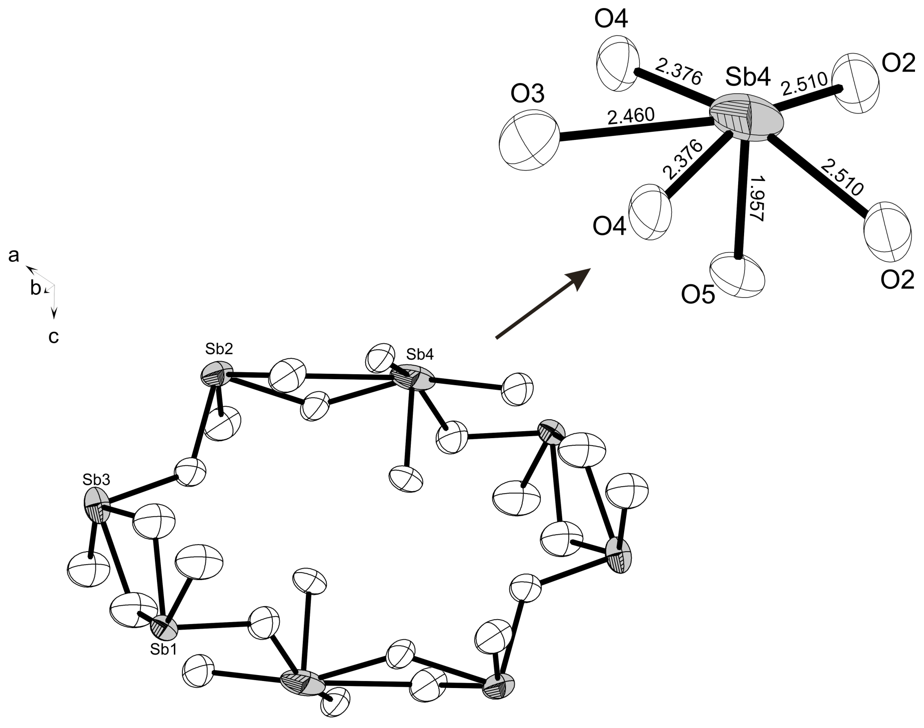

Figure 3.26.: One dimensional slab $[Sb_8O_{12.5}]^-$ in $Cd_4Sb_8O_{12.5}Cl_7$. (50% probability level).

Table 3.4.: Geometric parameters and bond valence for $Cd_4Sb_8O_{12.5}X_7$ (X = Cl, Br). Symmetry codes: (i) 0.5-x, 0.5-y, 1-z; (ii) 0.5-x, 0.5+y, 1-z; (iii) 0.5-x, 0.5+y, -z.

$Cd_4Sb_8O_{12.5}Cl_7$	Bond distance (Å)	Bond valence
Cd(1)-O(2)	2.364(2)	0.29
Cd(1)-O(3)	2.524(3)	0.19
Cd(1)-O(5)	2.272(2)	0.37
Cd(1)-O(5)^{i}	2.369(6)	0.29
Cd(1)-O(5)^{ii}	2.369(6)	0.29
Cd(1)-O(6)	2×2.662(1)	2×0.13
Cd(2)-Cl(1)	2×2.631(2)	2×0.32
Cd(2)-Cl(2)	2.657(3)	0.30
Cd(2)-Cl(2)^{iii}	2×2.732(2)	2×0.25
Cd(2)-Cl(3)	2.499(4)	0.46
Sb(1)-O(1)	2.039(1)	0.84
Sb(1)-O(2)	1.959(1)	1.04
Sb(1)-O(7)	2×2.153(5)	2×0.62
Sb(2)-O(3)	2×2.173(8)	2×0.58
Sb(2)-O(4)	1.976(2)	0.99
Sb(2)-O(6)	1.989(1)	0.96
Sb(3)-O(1)	2×2.178(5)	2×0.58
Sb(3)-O(6)	1.973(1)	1.00
Sb(3)-O(7)	2.085(1)	0.74
Sb(4)-O(2)	2×2.511(7)	2×0.23
Sb(4)-O(3)	2.46(2)	0.27
Sb(4)-O(4)	2×2.375(9)	2×0.34
Sb(4)-O(5)	1.957(1)	1.04
$Cd_4Sb_8O_{12.5}Br_7$	Bond distance [Å]	Bond valence
Cd(1)-O(2)	2.365(2)	0.29
Cd(1)-O(3)	2.521(3)	0.19
Cd(1)-O(5)	2.256(2)	0.39
Cd(1)-O(5)^{i}	2.417(8)	0.25
Cd(1)-O(5)^{ii}	2.417(8)	0.25
Cd(1)-O(6)	2×2.688(1)	2×0.12
Cd(2)-Br(1)	2×2.752(2)	2×0.35
Cd(2)-Br(2)	2.826(2)	0.29
Cd(2)-Br(2)^{iii}	2×2.842(2)	2×0.27
Cd(2)-Br(3)	2.624(2)	0.49
Sb(1)-O(1)	2.058(2)	0.80
Sb(1)-O(2)	1.982(1)	0.98
Sb(1)-O(7)	2×2.180(7)	2×0.57
Sb(2)-O(3)	2×2.198(1)	2×0.54
Sb(2)-O(4)	1.97(2)	1.01
Sb(2)-O(6)	1.998(1)	0.94
Sb(3)-O(1)	2×2.204(7)	2×0.54
Sb(3)-O(6)	1.972(1)	1.00
Sb(3)-O(7)	2.06(2)	0.79
Sb(4)-O(2)	2×2.510(9)	2×0.23
Sb(4)-O(3)	2.44(3)	0.28
Sb(4)-O(4)	2×2.396(1)	2×0.32
Sb(4)-O(5)	1.937(2)	1.10

Table 3.5.: Atomic coordinate equivalent isotropic displacement parameter [Å^2] and bond valence sum for $Cd_4Sb_8O_{12.5}Cl_7$.

Atom	x	y	z	U_{eq}	BVS
Sb(1)	0.05724(4)	0	0.16707(7)	0.0245(3)	3.12
Sb(2)	0.37018(5)	0	0.38843(8)	0.0397(4)	3.11
Sb(3)	0.52167(4)	0	0.33082(8)	0.0330(3)	2.89
Sb(4)	0.71755(7)	0	0.27925(9)	0.0603(4)	2.44
O(1)	0.0450(7)	0	0.2991(1)	0.063(3)	2.00
O(2)	0.1497(5)	0	0.2624(9)	0.058(4)	1.79
O(3)	0.1655(1)	0	0.6114(2)	0.056(7)	1.62
O(4)	0.2781(8)	0	0.3434(1)	0.052(7)	1.67
O(5)	0.2787(5)	0	0.5805(8)	0.039(2)	1.99
O(6)	0.3928(5)	0	0.5422(8)	0.046(3)	2.22
O(7)	0.5583(7)	0	0.2245(1)	0.068(4)	1.98
Cd(1)	0.17676(5)	0	0.44488(8)	0.0351(3)	1.56
Cd(2)	0.33326(4)	0	0.04905(7)	0.0251(3)	1.90
Cl(1)	0.11740(2)	0	0.8151(3)	0.0358(8)	0.64
Cl(2)	0.23575(1)	0	0.0893(2)	0.0252(7)	0.80
Cl(3)	0.58521(2)	0	0.0129(3)	0.0399(9)	0.46

Table 3.6.: Atomic coordinate equivalent isotropic displacement parameter [Å^2] and bond valence sum for $Cd_4Sb_8O_{12.5}Br_7$.

Atom	x	y	z	U_{eq}	BVS
Sb(1)	0.05927(6)	0	0.18097(9)	0.0287(4)	2.92
Sb(2)	0.36442(7)	0	0.38686(1)	0.0415(5)	3.03
Sb(3)	0.52695(6)	0	0.34044(1)	0.0312(4)	2.87
Sb(4)	0.71584(1)	0	0.28544(1)	0.0838(9)	2.48
O(1)	0.0512(9)	0	0.3134(1)	0.060(4)	1.88
O(2)	0.1516(7)	0	0.2711(1)	0.050(4)	1.73
O(3)	0.1699(1)	0	0.612(2)	0.055(9)	1.83
O(4)	0.2750(9)	0	0.3468(2)	0.048(8)	1.65
O(5)	0.2778(7)	0	0.5784(1)	0.050(4)	1.99
O(6)	0.3888(7)	0	0.5360(1)	0.047(4)	2.18
O(7)	0.5590(1)	0	0.2349(1)	0.078(6)	1.93
Cd(1)	0.17797(8)	0	0.44769(1)	0.0443(5)	1.61
Cd(2)	0.33531(6)	0	0.04531(1)	0.0265(5)	2.02
Br(1)	0.11017(9)	0	0.81203(1)	0.0324(5)	0.70
Br(2)	0.23843(8)	0	0.09727(1)	0.0254(5)	0.83
Br(3)	0.58220(9)	0	0.01960(2)	0.0337(5)	0.49

3.2.3. Thermal analysis of $Cd_4Sb_8O_{12.5}X_7$ (X = Cl, Br)

DTA measurements were carried out in evacuated ampoules with a diameter of 2 mm and a length of approximately 10 mm under flowing argon. Precise measurement conditions for individual compounds are described below the DTA diagrams. Heating and cooling thermograms for compounds representing the system $Cd_4Sb_8O_{12.5}X_7$ (X = Cl, Br, I) are shown, respectively, in Figure 3.27 and Figure 3.28. It is seen from the figures, that one transition occurs in the heating DTA curve (melting point) at 608 (608)°C for $Cd_4Sb_8O_{12.5}Cl_7$, and one at 590 (587)°C for $Cd_4Sb_8O_{12.5}Br_7$. The exothermic effects on the cooling DTA curves occur at 502 (495)°C for $Cd_4Sb_8O_{12.5}Cl_7$ and at 494 (482)°C for $Cd_4Sb_8O_{12.5}Br_7$. The values in parentheses comes from a second series of sample heating/cooling. Thermal analysis additionally confirmed that synthesis by using CdX_2 and Sb_4O_6 in a 2:1 ratio tends to result in single phase samples.

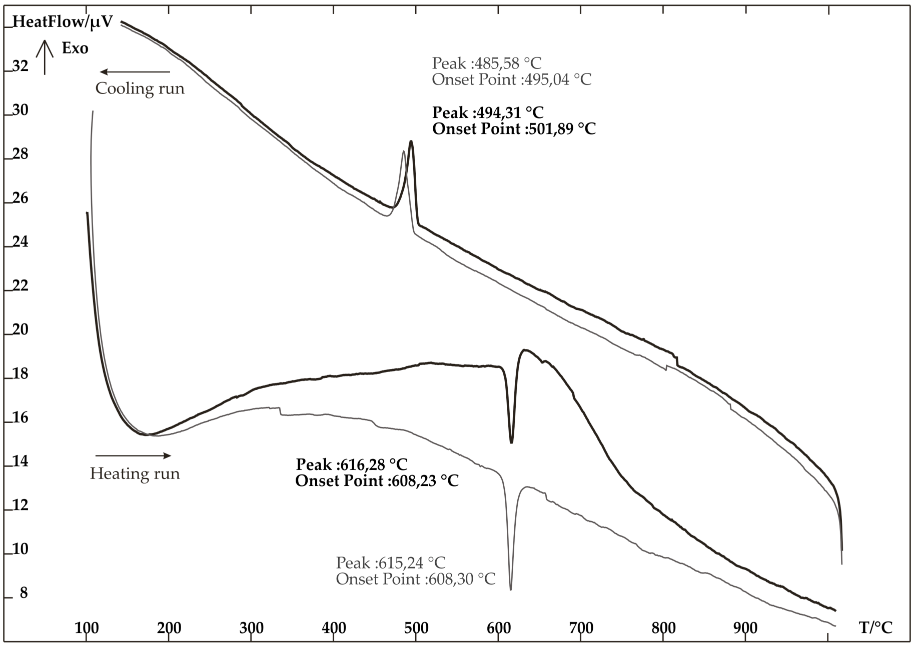

Figure 3.27.: DTA measurement of $Cd_4Sb_8O_{12.5}Cl_7$. The measurement was performed in the temperature range 100-1000°C with heating speed 10°C/min. The figure presents two series of sample heating/cooling. Heating and cooling is indicated by the corresponding arrow.

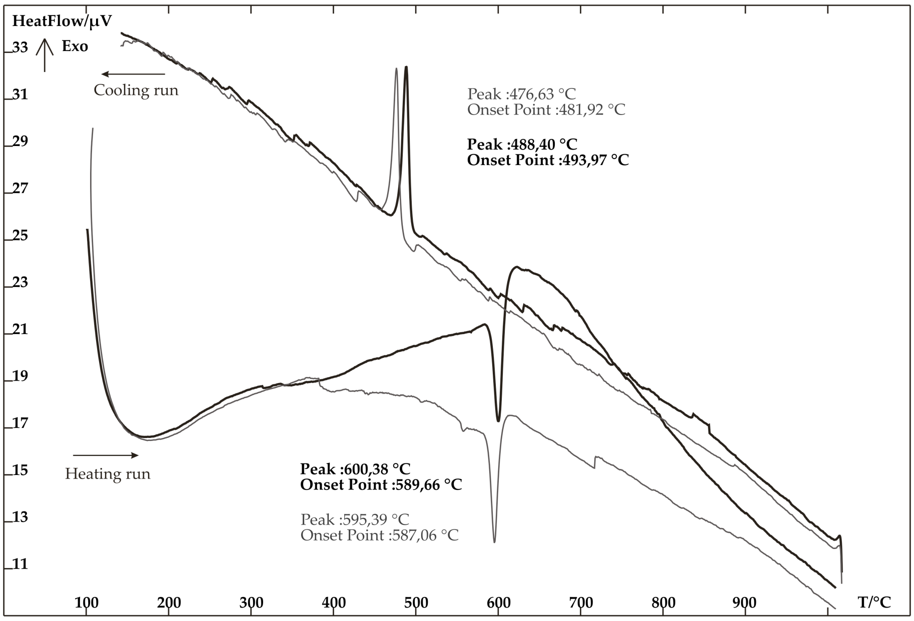

Figure 3.28.: DTA measurement of $Cd_4Sb_8O_{12.5}Br_7$. The measurement was performed in the temperature range 100-1000°C with heating speed 10°C/min. The figure presents two series of sample heating/cooling. Heating and cooling is indicated by the corresponding arrow.

3.2.4. Mössbauer spectroscopy

In order to determine the oxidation state and the antimony distribution over the four cation positions ^{121}Sb-Mössbauer spectra of new compounds $Cd_4Sb_8O_{12.5}X_7$ (X = Cl, Br) were recorded. A $Ba^{121}mSnO_3$ source was used for the Mössbauer spectroscopic experiments, which were conducted in the usual transmission geometry. The measurements were performed with a commercial helium-bath cryostat. The temperature of the absorber was varied between 4.2 K and room temperature, while the source was kept at room temperature. The temperature was controlled by a resistance thermometer (±0.5 K accuracy). The samples were enclosed in small PVC containers at a thickness corresponding to about 10 mg Mössbauer active element/cm^2.

Table 3.7.: Fitting parameters of ^{121}Sb Mössbauer spectroscopic measurements of different compounds. Numbers in parentheses represent the statistical errors in the last digit. (δ), isomer shift; (Γ), experimental line width.

Compound	T (K)	δ (mm·s^{-1})	Γ (mm·s^{-1})	ΔE_Q (mm·s^{-1})
$Cd_4Sb_8O_{12.5}Cl_7$	77	-13.10(2)	3.63(7)	-0.44(1)
$Cd_4Sb_8O_{12.5}Br_7$	77	-13.11(3)	3.87(9)	-0.42(1)

The ^{121}Sb spectra of $Cd_4Sb_8O_{12.5}Cl_7$ and $Cd_4Sb_8O_{12.5}Br_7$ at 77 K are presented in Figure 3.29. The spectra were well reproduced by a single signal at an isomer shift of around -13.10 mm/s, subjected to weak quadrupole splitting of -0.43 mm/s. Although the $Cd_4Sb_8O_{12.5}X_7$ (X = Cl, Br) structures contain more than one crystallographically independent antimony site, we observe a superposition of the almost identical single signals. The experimental line width is close to the observed value in compound $AgSbP_{14}$ with covalently bonded Sb(III) [96]. The various ^{121}Sb shifts with respect to a $Ba^{121m}SnO_3$ source were systemized by Lippens [63]. $Cd_4Sb_8O_{12.5}Cl_7$ and $Cd_4Sb_8O_{12.5}Br_7$ fall into the range for Sb(III) compounds.

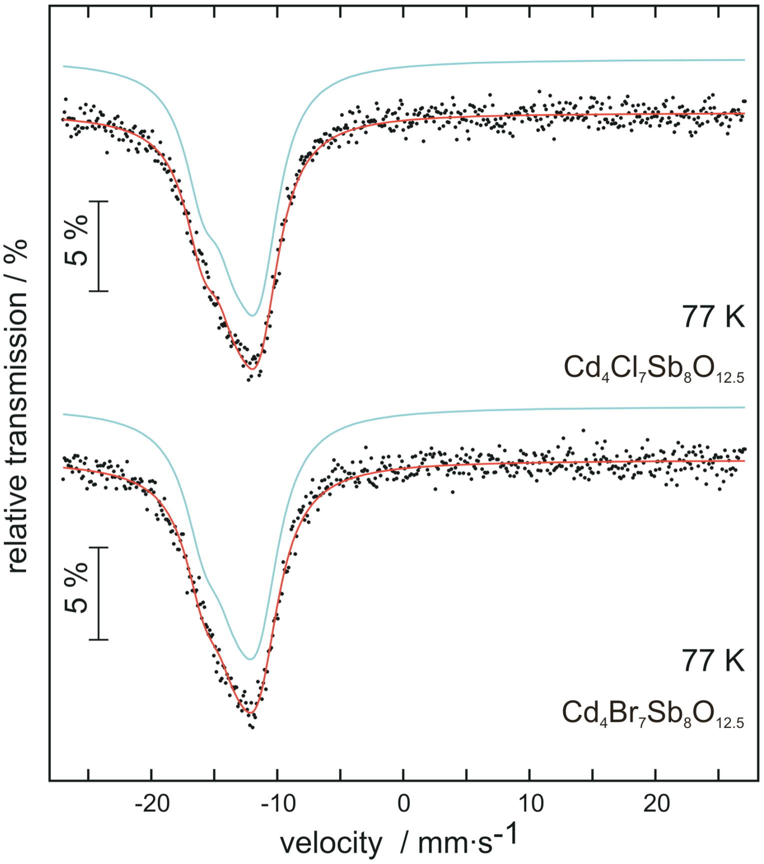

Figure 3.29.: Experimental and simulated ^{121}Sb Mössbauer spectra of $Cd_4Sb_8O_{12.5}X_7$ (X = Cl, Br) at 77 K.

3.2.5. Raman spectroscopy

Raman spectra of $Cd_4Sb_8O_{12.5}X_7$ (X = Cl, Br) were recorded on a Varian FT-Raman module with near infrared Nd:YAG laser operating at 1064 nm. The powders were analyzed in thin-walled glass capillaries. A liquid nitrogen-cooled germanium detector was used. The laser was focused on the sample with an approximately 1 mm diameter spot with a variable power. The spectra were recorded in the wavenumber range 4000-130 cm^{-1} at a resolution of 2 cm^{-1}. The spectra were analyzed using Resolution Pro [T] software from Varian Inc.

Raman lines in the recorded spectra were observed in the frequency range from 130-800 cm^{-1}, as seen in Figure 3.30 and Figure 3.31. The vibrational modes can be attributed to CdO, CdX_2 and Sb_2O_3. Bands at 362 (370), 471(465) cm^{-1} appear to be as a result of Cd-O vibrations [97]. Bands at 155 (155) cm^{-1} are thought to result from Cd-X vibrations [98,99,100,101]. Modes attributable to Sb-O vibrations [77,78,102,103] occur at 217, 256 (266), 362 (370), 471 (465), 553 (547), 653 (652) cm^{-1}. Values in parenthesis in the above description refer to wavenumbers appear in the Raman spectra for sample of $Cd_4Sb_8O_{12.5}Br_7$. The data of Raman and IR results are summarised in Table 3.8.

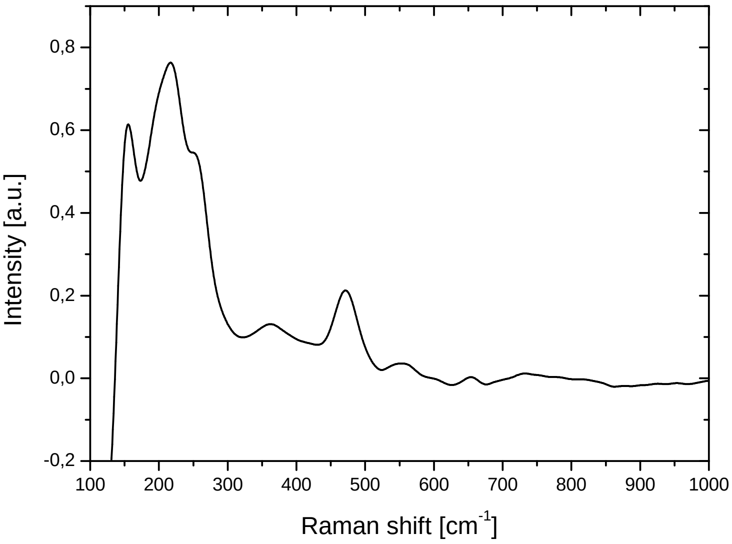

Figure 3.30.: Raman spectrum of $Cd_4Sb_8O_{12.5}Cl_7$ showing significant vibrations for only $\nu_{\mathrm{Cd-O}}$, $\nu_{\mathrm{Sb-O}}$, and $\nu_{\mathrm{Cd-Cl}}$.

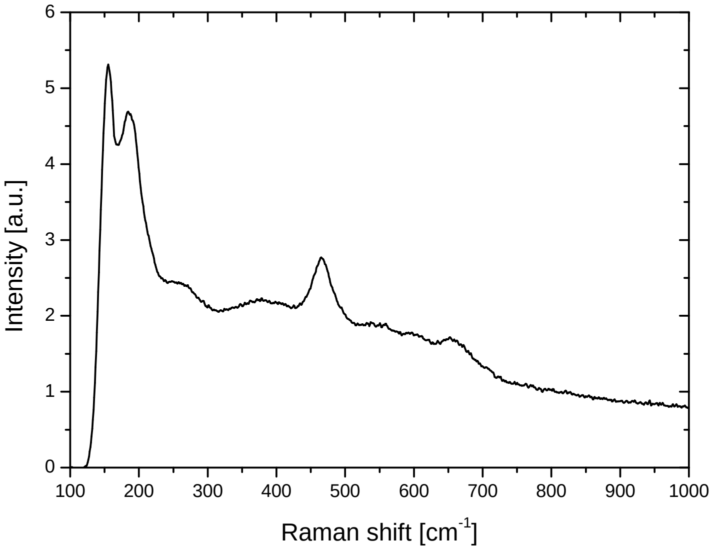

Figure 3.31.: Raman spectrum of $Cd_4Sb_8O_{12.5}Br_7$ showing significant vibrations for only $\nu_{\mathrm{Cd-O}}$, $\nu_{\mathrm{Sb-O}}$, and $\nu_{\mathrm{Cd-Br}}$.

3.2.6. ATR-IR

In order to complete the spectroscopic information for $Cd_4Sb_8O_{12.5}X_7$ (X = Cl, Br) infrared absorption spectra were recorded. ATR-IR measurements were performed in range 150-400 cm^{-1} (F-IR) and 400-4000 cm^{-1} (M-IR). The list of modes occuring in Raman and IR spectra is presented in Table 3.8.

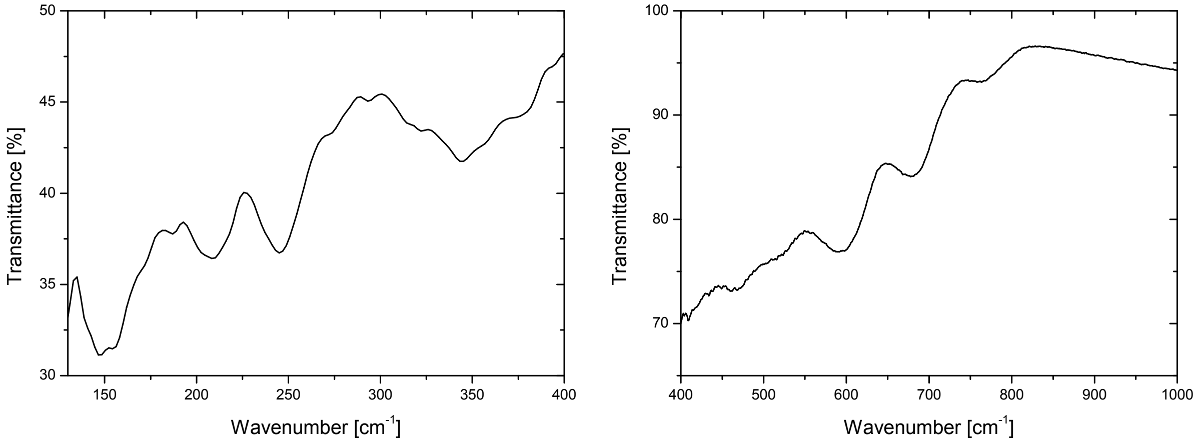

(a) **(b)**

Figure 3.32.: Infrared spectrum of $Cd_4Sb_8O_{12.5}Cl_7$ showing significant vibrations only for ν_{Cd-O}, ν_{Sb-O}, and ν_{Cd-Cl}. There were no bands in the range 1000-4000 cm^{-1}.

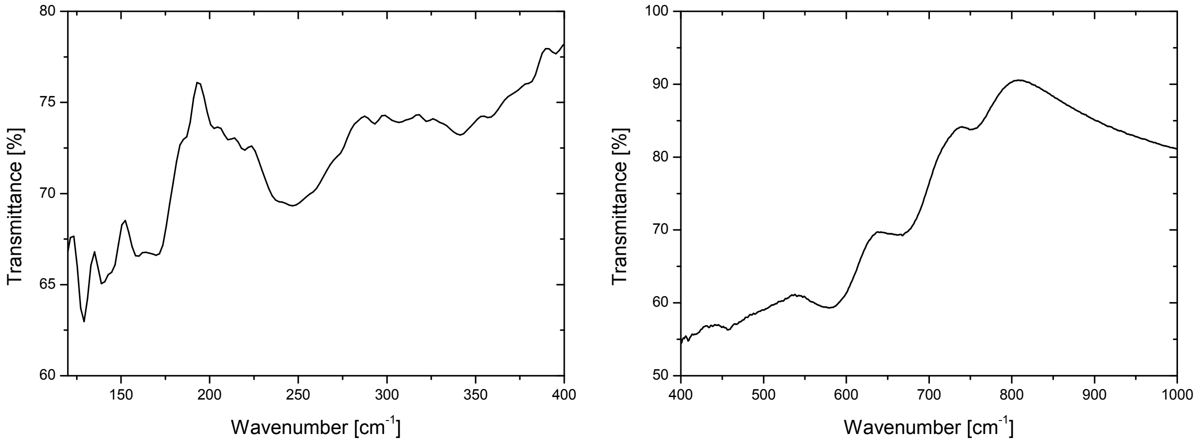

(a) **(b)**

Figure 3.33.: Infrared spectrum of $Cd_4Sb_8O_{12.5}Br_7$ showing significant vibrations only for ν_{Cd-O}, ν_{Sb-O}, and ν_{Cd-Br}. There were no bands in the range 1000-4000 cm^{-1}.

Table 3.8.: Summary of modes occuring in Raman and IR spectra of structures representing the system $Cd_4Sb_8O_{12.5}X_7$ (X = Cl, Br).

Raman (cm^{-1})		IR (cm^{-1})		Comments
$Cd_4Sb_8O_{12.5}Cl_7$	$Cd_4Sb_8O_{12.5}Br_7$	$Cd_4Sb_8O_{12.5}Cl_7$	$Cd_4Sb_8O_{12.5}Br_7$	
		149	145	ν(Cd-X) / (Sb-O) lattice vibrations
155	155		158	ν(Cd-X) / (Sb-O) lattice vibrations
			166	ν(Cd-X) / (Sb-O) lattice vibrations
	184	185		δ(Sb-O) twisting
		208	207	δ(Sb-O) twisting
217				δ(Sb-O) wagging
256	266	245	250	δ(Sb-O) scissoring
		345	342	ν(Cd-O) / ν_{sym}(Sb-O)
362	370			ν(Cd-O) / ν_{sym}(Sb-O)
471	465	466	467	ν(Cd-O) / ν_{sym}(Sb-O)
553	547			ν_{asym}(Sb-O)
		591	579	ν_{asym}(Sb-O)
653	652			ν_{asym}(Sb-O)
		678	672	ν_{asym}(Sb-O)
		758	749	ν(Cd-X)

3.3. $ZnSb_2O_3X(OH)$ (X = Cl, Br, I)

3.3.1. Synthesis

Single crystals of new compounds with the composition $ZnSb_2O_3X(OH)$ (X = Cl, Br, I) were grown *via* two different hydrothermal reaction methods: ZnO, SbX_3 (X = Cl, Br, I) called *synthesis 1* from here onwards, and ZnO, SbX_3 (X = Cl, Br, I) and Sb_4O_6 called *synthesis 2* from here onwards. The starting materials for synthesis 1 were mixed in the stoichiometric molar ratio 2:1 and for synthesis 2 in a 6:2:1 ratio. Reactants and water were placed into silica tubes, then all were frozen by using liquid nitrogen, evacuated, and sealed. Next the ampoules were placed into a teflon tub with water and heated at 90 °C for 5 days. After slow cooling, the solid products were removed by filtration and cleaned with water and ethanol. In both cases, the products consisted of colourless crystals of $ZnSb_2O_3X(OH)$ (X = Cl, Br, I) and white powder, which was identified by powder X-ray diffraction. Detailed information concerning phase analysis is presented in the following subsection.

3.3.2. Single crystal and powder X-ray diffraction analysis

Single crystal X-ray diffraction data were collected on a STOE IPDS I, mounted with a Mo-Kα source. Integration of the reflection intensities and absorption correction were performed using *X-Area* [D]. All structures were solved by direct methods using *SIR92* [G], and refined by full-matrix least-squares fitting on F^2 using *SHELXL-97* [J]. Crystallographic data and structural refinements for the three compounds are summarized in Table 3.9. Final atomic coordinates and equivalent isotropic displacement parameters for structures from the system $ZnSb_2O_3X(OH)$ (X = Cl, Br, I) are listed in the appendix (Table B.9, B.10, B.11), while Table B.12, Table B.13 and Table B.14 include anisotropic displacement parameters. Anisotropic displacement parameters were used for all atoms except hydrogen atoms. An extinction parameter was included in the last refinement cycles.

The structures consist of corrugated puckered layers of distorted $[ZnO_3X]$ (X = Cl, Br, I) tetrahedra and one-dimensional polymers built of Sb^{3+} cations asymmetrically four-coordinated by three oxygen atoms and by one hydroxy group, as seen in Figure 3.34. The possibility of intermolecular hydrogen bonds O-H...X (X = Cl, Br, I) has been found in the investigated crystal structures. Therein, OH is the proton donor and the halide atoms are proton acceptors.

Antimony cations are four-coordinated by three oxygen atoms and one hydroxy group, forming one-dimensional polymers (Figure 3.35). The average d(Sb-O) distances 2.0858 Å in $ZnSb_2O_3Cl(OH)$, 2.0918 Å in $ZnSb_2O_3Br(OH)$ and 2.096 Å in $ZnSb_2O_3I(OH)$ are about 0.1 Å longer than the bond length d(Sb-O) = 1.9779 Å in

Table 3.9.: Details of the data collection and results of the structure refinement for $ZnSb_2O_3Cl(OH)$, $ZnSb_2O_3Br(OH)$, and $ZnSb_2O_3I(OH)$.

Crystal data			
Chemical formula	$ZnSb_2O_3Cl(OH)$	$ZnSb_2O_3Br(OH)$	$ZnSb_2O_3I(OH)$
Crystal colour/habit	colourless/needle	colourless/plate	colourless/needle
Crystal size	0.09 × 0.06× 0.05 mm	0.06 × 0.02 × 0.01 mm	0.17 × 0.04 × 0.02 mm
Molecular weight	409.33 g mol^{-1}	453.79 g mol^{-1}	500.78 g mol^{-1}
Calculated density	4.635 g cm^{-3}	4.927 g cm^{-3}	5.134 g cm^{-3}
Space group	$P2_1/m$ (No. 11)	$P2_1/m$ (No. 11)	$P2_1/m$ (No. 11)
Lattice parameters	$a = 5.149(1)$ Å	$a = 5.202(1)$ Å	$a = 5.211(1)$ Å
	$b = 8.240(2)$ Å	$b = 8.319(2)$ Å	$b = 8.416(2)$ Å
	$c = 6.929(1)$ Å	$c = 7.088(1)$ Å	$c = 7.409(2)$ Å
	$\beta = 93.92(3)°$	$\beta = 94.25(3)°$	$\beta = 94.41(3)°$
Cell volume, Z	293.3(1) Å^3, 2	305.9(1) Å^3, 2	324.0(1) Å^3, 2
Data collection			
Device, Radiation, Temperature	STOE IPDS I, Mo-Kα, 0.71073 Å, graphite monochromator, 293K		
Scan range	$2.95° \leqslant 2\theta \leqslant 27.54°$	$2.88° \leqslant 2\theta \leqslant 26.49°$	$2.76° \leqslant 2\theta \leqslant 26.52°$
hkl range	$-6 \leqslant h \leqslant 6$	$-6 \leqslant h \leqslant 6$	$-6 \leqslant h \leqslant 6$
	$-10 \leqslant k \leqslant 10$	$-9 \leqslant k \leqslant 9$	$-10 \leqslant k \leqslant 10$
	$-8 \leqslant l \leqslant 8$	$-8 \leqslant l \leqslant 8$	$-9 \leqslant k \leqslant 9$
Structure solution and refinement	$ZnSb_2O_3Cl(OH)$	$ZnSb_2O_3Br(OH)$	$ZnSb_2O_3I(OH)$
Measured reflections	4946	3648	4944
Independent reflections	716	668	718
Independent reflections with $F_O > 4\sigma(F_O)$	679	606	672
R_{int}	0.0736	0.0535	0.0506
R_σ	0.0343	0.0309	0.0235
Structure solution, refinement	SHELXS97 [I], SHELXL97 [J]		
Number of parameters	46	46	46
Absorption correction (Mo-Kα)	numerical: X-RED [L], X-SHAPE [M]		
Absorption coefficient	13.576 mm^{-1}	19.111 mm^{-1}	16.644 mm^{-1}
$R_1, wR_2[I > 3\sigma(I)]$	0.0246, 0.0578	0.0220, 0.0512	0.0199, 0.0472
R_1, wR_2[all reflections]	0.0263, 0.0585	0.0252, 0.0522	0.0222, 0.0480
GooF	1.098	1.035	1.088
F(000)	364	400	436
Residual electron density	1.42, -0.724 e Å^{-3}	1.175, -0.641 e Å^{-3}	1.109, -0.726 e Å^{-3}

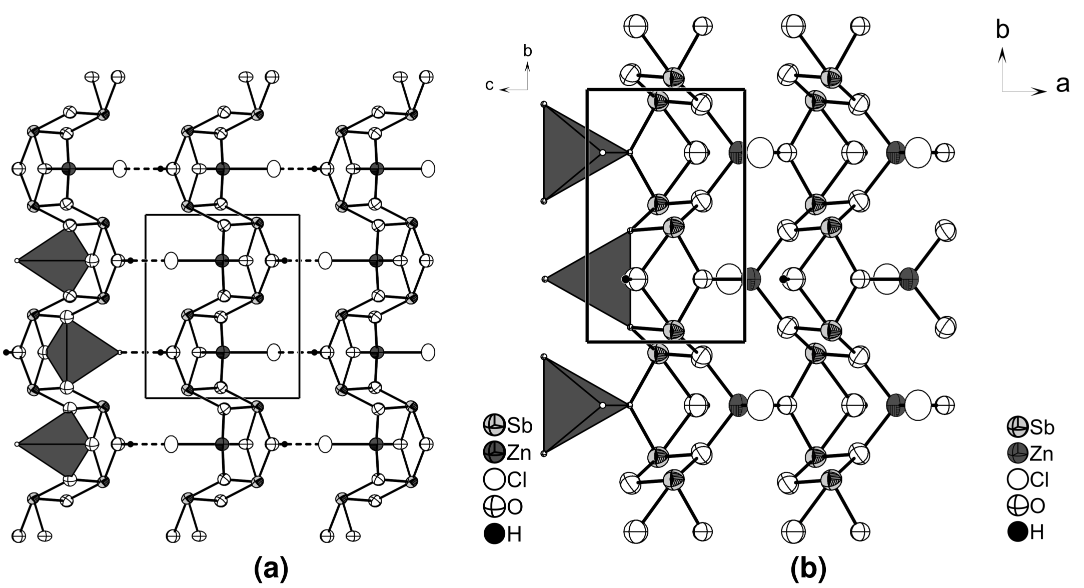

Figure 3.34.: Projection of the crystal structure (a) of $ZnSb_2O_3Cl(OH)$ emphasizing the corrugated puckered layers of $[ZnO_3Cl]$ tetrahedra and Sb^{3+} cations four-coordinate by three oxygens and one hydroxy group, forming one-dimensional polymers, viewed along [100] and (b) a layer propagating in the ab plane, viewed along [001]. (90% probability level).

senarmontite [104, 68] and than the average bond length d(Sb-O) = 2.0059 Å in valentinite [69, 70], what is expected since the antimony in α- and β-Sb_2O_3 is only three-coordinate by oxygen atoms. In general, as postulated by Shannon [105] on the basis of experimental data concerning groups of halides and chalcogenides, the radius of an ion increases as the coordination number increases. The explanation for this tendency is that increasing the number of ions around a central atom increases the repulsion between ligands, which should lead to an increase in the central atom-ligand internuclear distance. An increase in the CN of an ion causes the valence electrons to be distributed among more bonds. This results in a reduction of covalent character of the bonds and an increase of the ionic radius [106]. However the bond lengths in $ZnSb_2O_3X(OH)$ (X=Cl, Br, I) are in reasonable agreement with average $d(Sb^{3+}\text{-}O) \approx 2.1$ Å in $SbTaO_4$ [107, 108], $SbNbO_4$ [108, 123, 124], and $Sb_{1.92}V_{0.08}O_{3.67}$ [109], where antimony(III) is four-coordinated by oxygens and builds similar structural entities as in $ZnSb_2O_3X(OH)$ (X=Cl, Br, I). Positions of hydrogen atoms were found in the electron density map. The single crystal X-ray diffraction data were confirmed by the calculations of Madelung Part of Lattice Energy (MAPLE) [87, 88, 89]. The calculations confirmed that the oxygen atom O3 takes part in the formation of a hydroxy group.

Coordination of zinc by one chlorine/bromine/iodine atom, and three oxygen atoms results in a distorted tetrahedral environment, as shown Figure 3.36 and Figure 3.37.

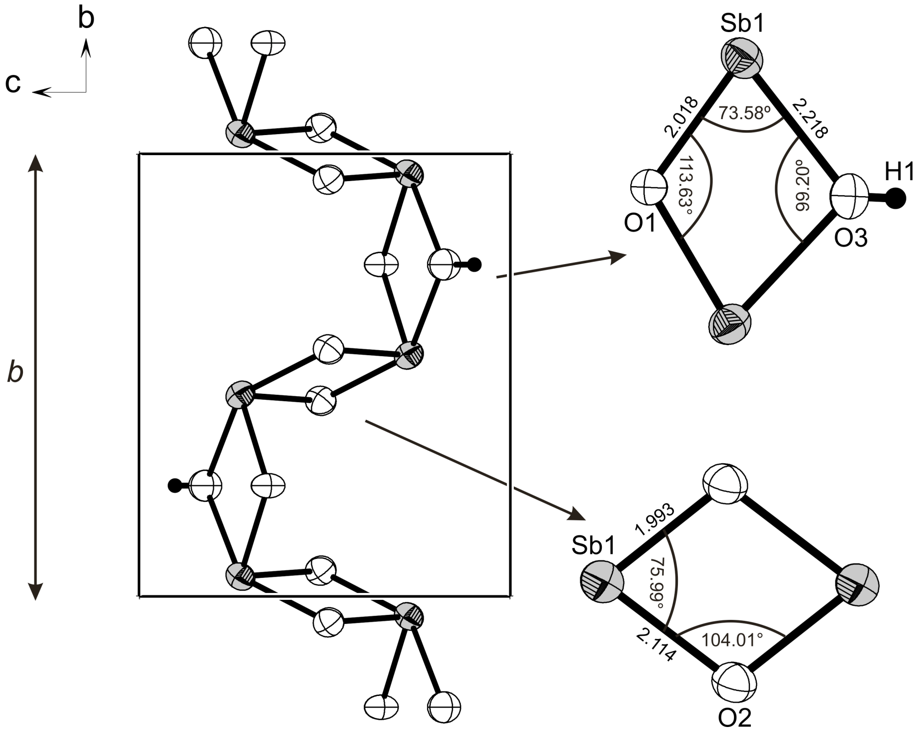

Figure 3.35.: Projection of the one-dimensional polymer formed by Sb^{3+} cations four-coordinated by three oxygens and one hydroxy group. (90% probability level).

It is important to underscore the fact that the distances d(Zn-Cl) = 2.356 Å, d(Zn-Br) = 2.523 Å, and d(Zn-I) = 2.753 Å are longer than the average bond length 2.3031 Å in pure $ZnCl_2$ [72], 2.4186 Å in pure $ZnBr_2$ [73], and 2.6275 Å in pure ZnI_2 [110], whereas the average values of three short axial bonds: d(Zn-O) = 1.9795 Å in $ZnSb_2O_3Cl(OH)$, d(Zn-O) = 1.982 Å in $ZnSb_2O_3Br(OH)$ and d(Zn-O) = 1.9755 Å in $ZnSb_2O_3I(OH)$ are markedly similar to the average bond length d(Zn-O) = 1.9783 Å in pure ZnO [74]. By contrast, the oxygen atoms that are involved in the creation of the hydroxy group are located at long distances, d(Zn-OH): 2.555 Å, 2.476 Å, and 2.387 Å respectively. These distances are significantly larger than d(Zn-OH)=1.965(2) Å found in ϵ-$Zn(OH)_2$ [111] and the average d(Zn-OH)=1.96(2) Å in γ-$Zn(OH)_2$ [112], therefore a hydroxy group was not taken into account when considering primary coordination sphere of zinc. Selected bond distances and angles for compounds representing the composition $ZnSb_2O_3X(OH)$ (X= Cl, Br, I) are presented in the Table 3.10.

In the investigated structures $ZnSb_2O_3X(OH)$ (X=Cl, Br, I), there is the possibility of hydrogen bonding of the type O-H...X (X = Cl, Br, I). According to Lutz *et al.* [113, 114, 115] it would be expected that the strongest hydrogen bond occurs in the structure where a chlorine atom acts as a proton acceptor. Table 3.12 shows the geometry of the hydrogen bonds. In Raman spectroscopy one would expect that the peak corresponding to the O-H stretch in structures with chlorine should appear at lower values of Raman shift, because of the strongest hydrogen bond in this struc-

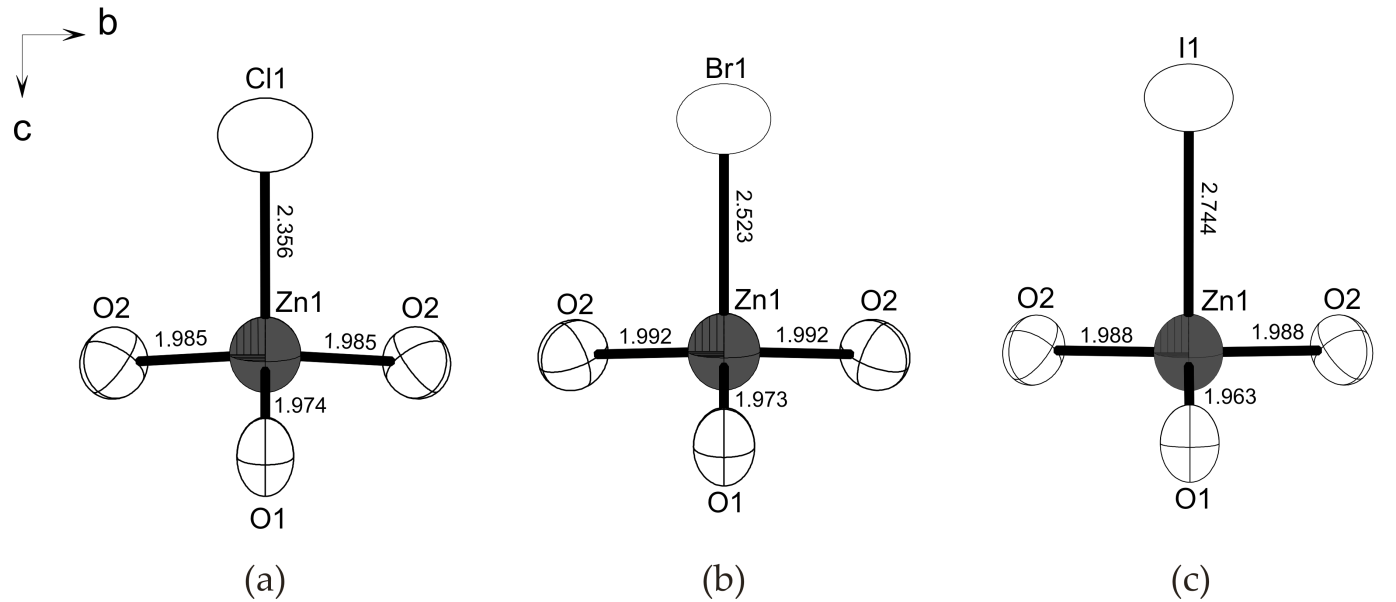

Figure 3.36.: Coordination of zinc by three oxygens, one chlorine (a), bromine (b) and iodine (c) atoms resulting in [ZnO_3X] tetrahedra. (90% probability level). All distances are given in Å.

Table 3.10.: Selected interatomic distances (in Å) and angles (in degrees) for $ZnSb_2O_3X(OH)$ (X=Cl, Br, I) at room temperature. Symmetry codes: $i = x, 0.5-y, z$.

$ZnSb_2O_3Cl(OH)$				
Sb(1)-O(1)	2.018(2)	O(2)-Sb(1)-O(1)		94.7(1)
Sb(1)-O(2)	1.993(3)	O(2)-Sb(1)-O(2)		76.0(1)
Sb(1)-O(2)	$2.114(3)^i$	O(1)-Sb(1)-O(2)		84.5(1)
Sb(1)-O(3)	2.218(3)	O(2)-Sb(1)-O(3)		78.4(1)
		O(1)-Sb(1)-O(3)		73.6(1)
		O(2)-Sb(1)-O(3)		144.6(1)
		Sb(1)-O(1)-Sb(1)		113.6(2)
		Sb(1)-O(2)-Sb(1)		104.0(1
		Sb(1)-O(3)-Sb(1)		99.2(2)
Zn(1)-O(1)	1.974(4)	O(1)-Zn(1)-O(2)	2x	118.9(1)
Zn(1)-O(2)	1.985(3)	O(2)-Zn(1)-O(2)		105.4(2)
Zn(1)-O(2)	$1.985(3)^i$	O(1)-Zn(1)-O(3)		86.0(2)
Zn(1)-Cl(1)	2.356(2)	O(2)-Zn(1)-O(3)	2x	70.7(1)
		O(1)-Zn(1)-Cl(1)		109.2(1)
		O(2)-Zn(1)-Cl(1)	2x	100.8(9)
		O(3)-Zn(1)-Cl(1)		164.8(1)
$ZnSb_2O_3Br(OH)$				
Sb(1)-O(1)	2.028(2)	O(2)-Sb(1)-O(1)		94.8(2)
Sb(1)-O(2)	1.998(3)	O(2)-Sb(1)-O(2)		75.8(1)
Sb(1)-O(2)	$2.114(3)^i$	O(1)-Sb(1)-O(2)		85.2(1)
Sb(1)-O(3)	2.227(3)	O(2)-Sb(1)-O(3)		77.4(2)
		O(1)-Sb(1)-O(3)		73.7(2)
		O(2)-Sb(1)-O(3)		144.1(2)
		Sb(1)-O(1)-Sb(1)		113.5(2)
		Sb(1)-O(2)-Sb(1)		104.2(1)
		Sb(1)-O(3)-Sb(1)		99.2(2)
Zn(1)-O(1)	1.973(4)	O(1)-Zn(1)-O(2)	2x	120.6(1)
Zn(1)-O(2)	1.992(3)	O(2)-Zn(1)-O(2)		106.0(2)
Zn(1)-O(2)	$1.992(3)^i$	O(1)-Zn(1)-O(3)		88.9(2)
Zn(1)-Cl(1)	2.523(1)	O(2)-Zn(1)-O(3)	2x	71.8(1)
		O(1)-Zn(1)-Cl(1)		107.0(1)
		O(2)-Zn(1)-Cl(1)	2x	99.2(1)
		O(3)-Zn(1)-Cl(1)		164.1(1)
$ZnSb_2O_3I(OH)$				
Sb(1)-O(1)	2.029(2)	O(2)-Sb(1)-O(1)		94.5(2)
Sb(1)-O(2)	1.991(3)	O(2)-Sb(1)-O(2)		75.6(1)
Sb(1)-O(2)	$2.098(3)^i$	O(1)-Sb(1)-O(2)		86.0(1)
Sb(1)-O(3)	2.235(3)	O(2)-Sb(1)-O(3)		76.6(2)
		O(1)-Sb(1)-O(3)		74.0(1)
		O(2)-Sb(1)-O(3)		144.1(2)
		Sb(1)-O(1)-Sb(1)		113.3(2)
		Sb(1)-O(2)-Sb(1)		104.4(1)
		Sb(1)-O(3)-Sb(1)		98.6(2)
Zn(1)-O(1)	1.963(4)	O(1)-Zn(1)-O(2)	2x	121.5(1)
Zn(1)-O(2)	1.988(3)	O(2)-Zn(1)-O(2)		107.7(2)
Zn(1)-O(2)	$1.988(3)^i$	O(1)-Zn(1)-O(3)		91.8(2)
Zn(1)-Cl(1)	2.744(1)	O(2)-Zn(1)-O(3)	2x	73.1(1)
		O(1)-Zn(1)-Cl(1)		104.4(1)
		O(2)-Zn(1)-Cl(1)	2x	97.8(1)
		O(3)-Zn(1)-Cl(1)		163.7(1)

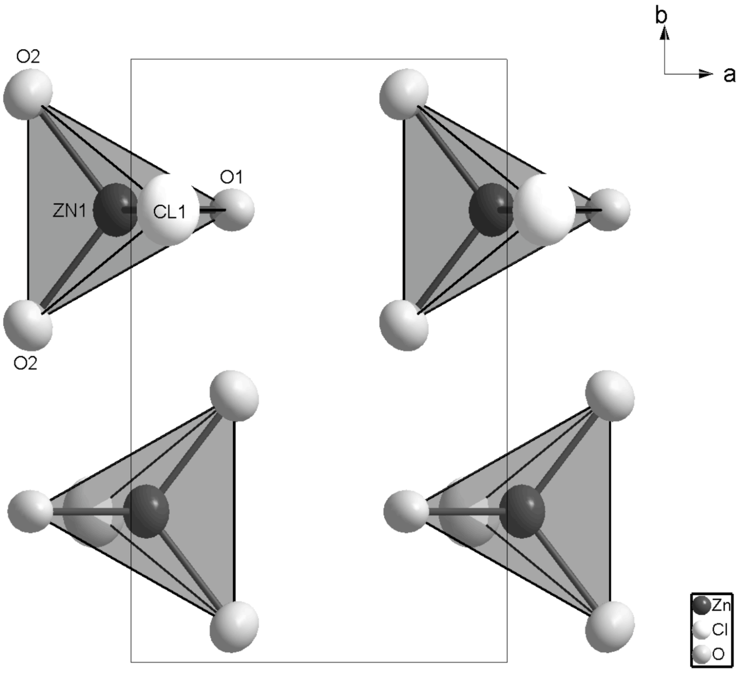

Figure 3.37.: Projection of the [ZnO_3Cl] tetrahedra in $ZnSb_2O_3Cl(OH)$.

ture. As can be seen in Table 3.11 the results obtained from Raman spectroscopy and X-ray diffraction do not correlate with one another. One possible reason for the inconsistency of these data is the observation that positions of hydrogen atoms using X-ray structural analysis is not precise because of low electron density. Positions of hydrogen atoms determined using X-ray diffraction do not coincide with real nuclei positions, because the electron density is significantly shifted in the direction of the atom which forms a covalent bond with the hydrogen atom. In order to find accurate location of hydrogen atoms, the application of neutron diffraction measurement is required.

Table 3.11.: Summary of O-H stretching modes occuring in Raman spectra of structures represented by the composition $ZnSb_2O_3X(OH)$ (X = Cl, Br, I).

Compound	O-H stretch (cm^{-1})	
	Synthesis 1	Synthesis 2
$ZnSb_2O_3Cl(OH)$	3425	3426
$ZnSb_2O_3Br(OH)$	3421	3422
$ZnSb_2O_3I(OH)$	3425	3423

The comparision of O-H stretching modes occurring in $ZnSb_2O_3X(OH)$ (X= Cl, Br, I) with fundamental O-H vibrational frequency of free (i.e. gaseous) hydroxide ions serves as proof for the existences of hydrogen bonding in these structures. Previously both experimental and theoretical investigations tended to assume the vibrational energy of free OH^- to be near 3700 cm^{-1} [116]. Further progress in research on non-H-bonded OH^- ions in alkaline and alkaline earth hydroxides resulted in values of about 3570 cm^{-1} [116], while experiments on the basis of vibration-rotation spectra of gaseous OH^- ions [117, 118] yielded values of 3555.59 and 3547 cm^{-1}. The O-H...X interactions were presented by Maltese *et al.* and later by Lutz *et al.* [119, 120]. The stretching vibrations of non-hydrogen-bonded hydroxide ions have been found to vary from 3690 to 3500 cm^{-1}. These results allow us to classify OH^- ions in $ZnSb_2O_3X(OH)$ (X= Cl, Br, I) as weakly bonded. However the presence or absence of hydrogen bonding of type O-H...X (X= F, Cl, Br, I) can be examined in terms of the temperature dependence of the O-H or O-D stretching modes [116, 120]. A small negative temperature shift refutes the presence of hydrogen bridges, while a positive temperature shift of the streching frequency is considered as proof that hydrogen bonds are present.

Table 3.12.: Geometrical parameters of the hydrogen bond O-H...X (X = Cl, Br, I) for $ZnSb_2O_3X(OH)$ (X = Cl, Br, I) from X-ray diffraction experiments.

Compound	D-H (Å)	H...A (Å)	D...A (Å)	< D-H...A (°)
$ZnSb_2O_3Cl(OH)$	0.660(1)	2.647(2)	3.288(5)	164.83(2)
$ZnSb_2O_3Br(OH)$	0.562(1)	2.864(2)	3.399(5)	160.37(2)
$ZnSb_2O_3I(OH)$	0.603(9)	3.017(1)	3.559(5)	151.64(1)

For a deeper knowledge of the nature of hydrogen bonding, it is possible to carry out *ab initio* calculations for model systems. The analysis of all parameters describing hydrogen bonds will ask for the energy of these interactions and the relationship between the geometric and energy parameters in more complex structures of crystals. In order to compare the geometry of hydrogen bonds observed in the structures of crystals with the geometry of model systems, a normalization of the hydrogen bond is routinely performed (see Table 3.13). It involves extension of the bond length donor-proton to the average length of D-H designated from neutron diffraction measurement. Standard lengths of D-H bonds: C-H = 1.083 Å, N-H = 1.009 Å, O-H = 0.983 Å [121]. The normalization of hydrogen bonds was performed using functions *Norm H-bond / Calc H-bond* in *PLATON* [K].

3.3.3. Raman Spectroscopy

The samples were studied by Raman spectroscopy. In the Raman spectra of $ZnSb_2O_3X(OH)$ (X = Cl, Br, I), 12-14 modes in the frequency regime in 130-4000 cm^{-1} were identified as presented in Figures 3.38, 3.39, and 3.40 for synthesis 1, and Figures 3.41, 3.42, and 3.43 for synthesis 2. All modes occurring in Raman spectra for the studied structures are shown in Table 3.14.

Table 3.13.: Geometrical parameters of the hydrogen bond O-H...X (X = Cl, Br, I) for $ZnSb_2O_3X(OH)$ (X = Cl, Br, I) from X-ray diffraction experiment after normalisation of the O-H bond length to a distance of 0.98 Å.

Compound	D-H (Å)	H...A (Å)	D...A (Å)	< D-H...A (°)
$ZnSb_2O_3Cl(OH)$	0.98	2.34	3.289(5)	163
$ZnSb_2O_3Br(OH)$	0.98	2.47	3.399(5)	157
$ZnSb_2O_3I(OH)$	0.98	2.69	3.559(5)	148

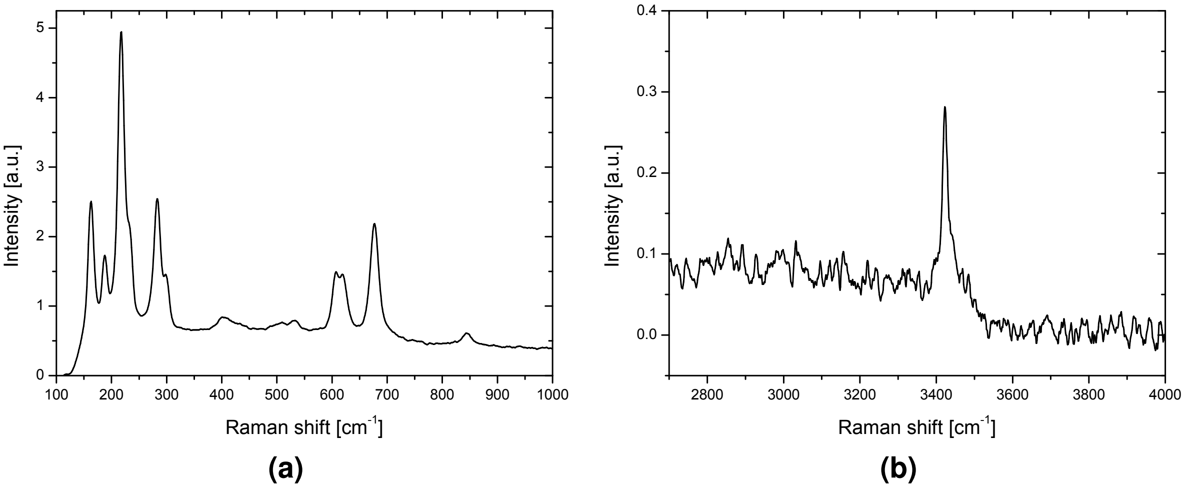

(a) (b)

Figure 3.38.: Raman spectrum of $ZnSb_2O_3Cl(OH)$ obtained using the first synthesis method. Plot a) shows a detailed view of the 100-1000 cm^{-1} frequency range, while plot b) shows the OH response. There were no vibrational modes in range 1000-2700 cm^{-1}.

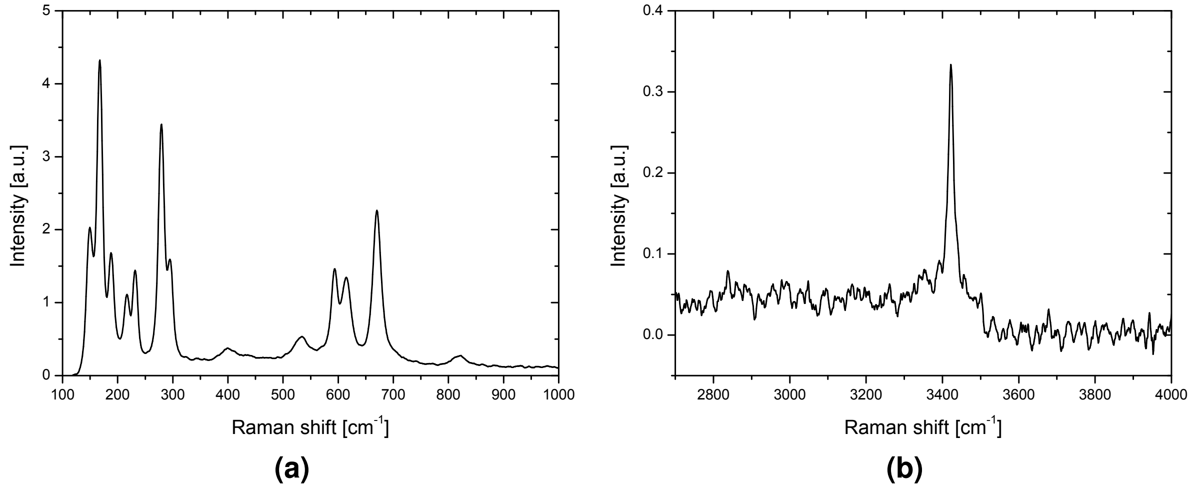

Figure 3.39.: Raman spectrum of $ZnSb_2O_3Br(OH)$ obtained using the first synthesis method. Plot a) shows a detailed view of the 100-1000 cm^{-1} frequency range, while plot b) shows the OH response. There were no vibrational modes in range 1000-2700 cm^{-1}.

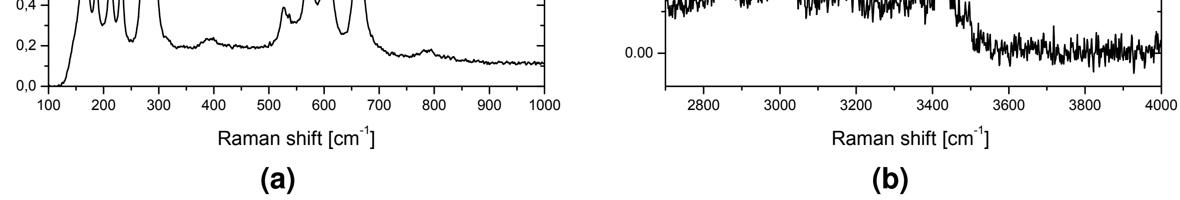

Figure 3.40.: Raman spectrum of $ZnSb_2O_3I(OH)$ obtained using the first synthesis method. Plot a) shows a detailed view of the 100-1000 cm^{-1} frequency range, while plot b) shows the OH response. There were no vibrational modes in range 1000-2700 cm^{-1}.

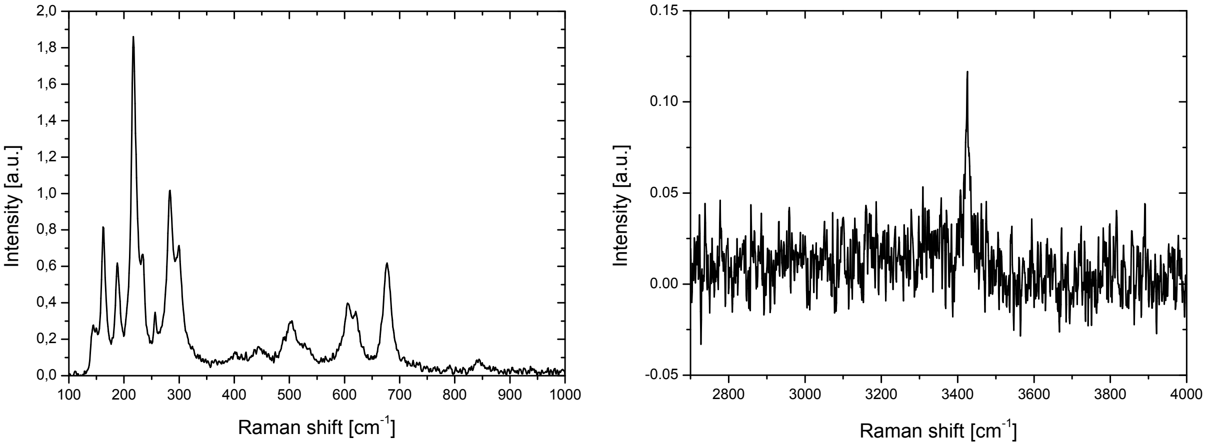

(a) (b)

Figure 3.41.: Raman spectrum of $ZnSb_2O_3Cl(OH)$ obtained using the second synthesis method. Plot a) shows a detailed view of the 100-1000 cm^{-1} frequency range, while plot b) shows the OH response. There were no vibrational modes in range 1000-2700 cm^{-1}.

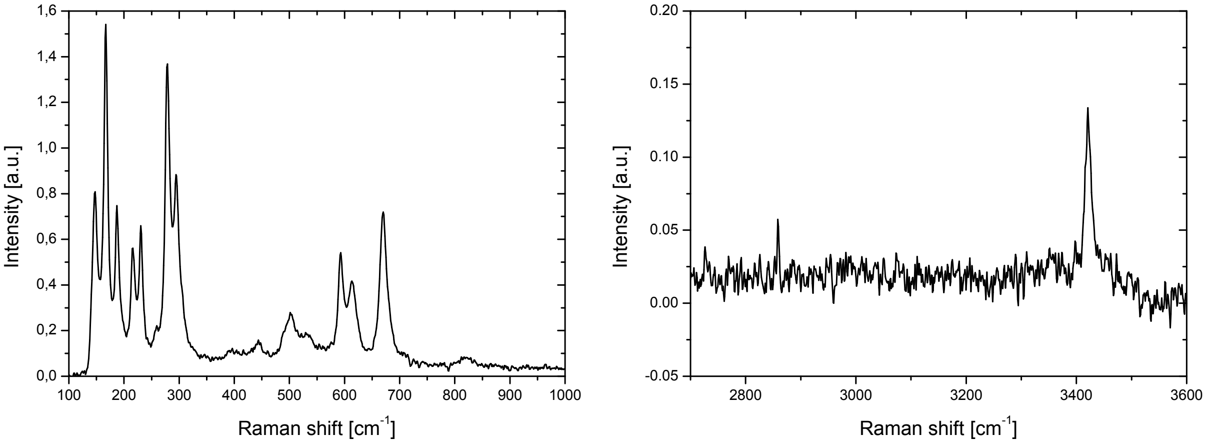

(a) (b)

Figure 3.42.: Raman spectrum of $ZnSb_2O_3Br(OH)$ obtained using the second synthesis method. Plot a) shows a detailed view of the 100-1000 cm^{-1} frequency range, while plot b) shows the OH response. There were no vibrational modes in range 1000-2700 cm^{-1}.

Table 3.14.: Summary of modes occurring in Raman spectra of structures representing the system $ZnSb_2O_3X(OH)$ (X = Cl, Br, I).

$ZnSb_2O_3Cl(OH)$		$ZnSb_2O_3Br(OH)$		$ZnSb_2O_3I(OH)$		Comments
Synthesis 1 (cm^{-1})	Synthesis 2 (cm^{-1})	Synthesis 1 (cm^{-1})	Synthesis 2 (cm^{-1})	Synthesis1 (cm^{-1})	Synthesis 2 (cm^{-1})	
144		147	150			ν(Zn-X)/ (Sb-O) lattice vibrations
162	163	166	168	165	166	ν(Zn-X)
187	188	187	188	186	186	δ(Sb-O) twisting
216	218	215	217	212	212	δ(Sb-O) wagging
233	232	230	232	232	232	ν(Zn-X)
256		259				δ(Sb-O) scissoring
283	283	278	279	275	275	δ(Sb-O) scissoring
299	298	294	295	290	290	δ(Sb-O) scissoring
504	509	501				ν_{sym}(Sb-O)
			534	526	530	ν_{sym}(Sb-O)
605	607	593	594	573	573	ν_{asym}(Sb-O)
				606	606	ν_{asym}(Sb-O)
620	619	613	615			ν_{asym}(Sb-O)
677	677	670	670	662	662	ν_{asym}(Sb-O)
				776	785	ν(Zn-O)
		820	822			ν(Zn-O)
844	843					ν(Zn-O)

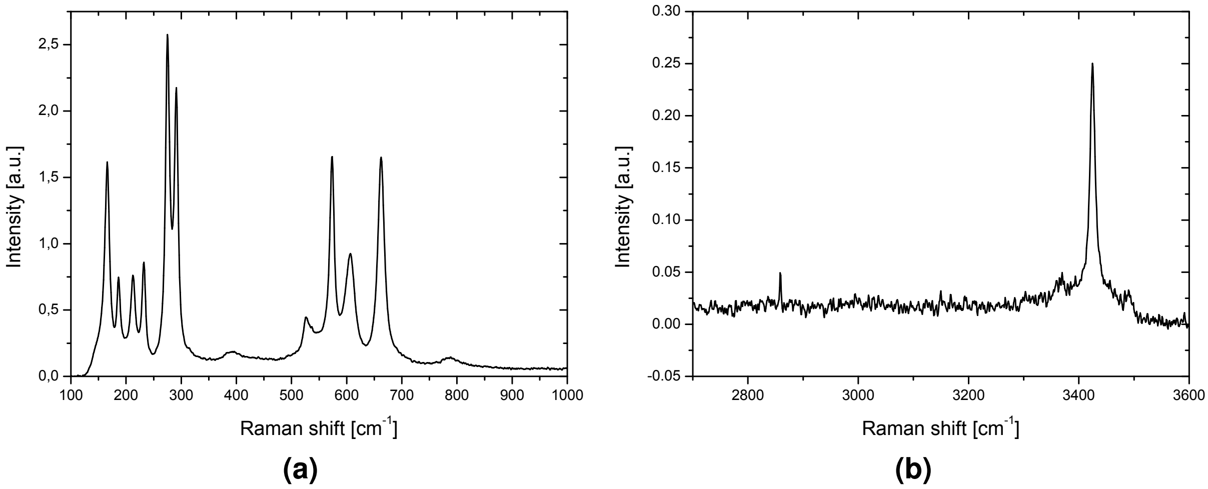

Figure 3.43.: Raman spectrum of $ZnSb_2O_3I(OH)$ obtained using the second synthesis method. Plot a) shows a detailed view of the 100-1000 cm^{-1} frequency range, while plot b) shows the OH response. There were no vibrational modes in range 1000-2700 cm^{-1}.

Vibrational spectra were recorded on a Varian FT-Raman module with dielectric YAG rejection filters, with 2 cm^{-1} resolution. In the following summary, values in parentheses represent wavenumbers appearing in the Raman spectra for crystals obtained by the second synthesis method and values without parentheses represent wavenumbers appearing in the Raman spectra for crystals obtained by the first synthesis method. Raman spectroscopic investigations of these samples show only vibrations which can be attributed to the Zn-O, Zn-X, Sb-O and O-H with bands at 844 (843) cm^{-1} for $ZnSb_2O_3Cl(OH)$, 820 (822) cm^{-1} for $ZnSb_2O_3Br(OH)$ and 776 (785) cm^{-1} for $ZnSb_2O_3I(OH)$ attributable to Zn-O vibrations [122]; at 144, 162 (163), 233 (232) cm^{-1} for $ZnSb_2O_3Cl(OH)$, 147 (150), 166 (168), 230 (232) cm^{-1} for $ZnSb_2O_3Br(OH)$ and at 165 (166), 232 (232) cm^{-1} for $ZnSb_2O_3I(OH)$ resulting from Zn-X vibrations [79,80]. Modes attributable to Sb-O vibrations [77,78,102,103] occur at 144, 187 (188), 216 (218), 283 (283), 299 (298), 504 (509), 605 (607), 620 (619), and 677 (677) cm^{-1} for $ZnSb_2O_3Cl(OH)$, at 147 (150), 187 (188), 215 (217), 259, 278 (279), 294 (295), 501 (534), 593 (594), 613 (615), and 670 (670) cm^{-1} for $ZnSb_2O_3Br(OH)$, and at 186 (186), 212 (212), 275 (275), 290 (290), 526 (530), 573 (573), 606 (606), and 662 (662) cm^{-1} for $ZnSb_2O_3I(OH)$. The bands observed at 3425 (3426) cm^{-1} for $ZnSb_2O_3Cl(OH)$, 3421 (3422) cm^{-1} for $ZnSb_2O_3Br(OH)$, and 3425 (3423)cm^{-1} for $ZnSb_2O_3I(OH)$ (see Table 3.11) must be assigned to the O-H stretching modes. However, infrared spectroscopy is a more appropriate technique for determining O-H modes, because of the weak polarizability and large dipole moment of the hydroxy group.

An exact identification of the peaks in the Raman spectra can only be carried out by way of a theoretical calculation of the Raman spectra based on the extracted crystal structures. These calculations will be one of the goals of future work in this area.

3.3.4. ATR-IR

IR measurements were performed in range 120-400 cm^{-1} (F-IR) and 400-4000 cm^{-1} (M-IR). IR absorption modes are presented in Table 3.15. As shown in the table, wide bands corresponding to the ν(O-H) streching modes were observed above 3420 cm^{-1}, and above 1500 cm^{-1} for δ(O-H) bending modes, which additionally confirmed the occurrence of a hydroxy group in $ZnSb_2O_3X(OH)$ (X = Cl, Br, I).

All measurements were carried out in the manner described in Section 2.3.5.

Table 3.15.: Summary of modes occurring in IR spectra of structures representing the system $ZnSb_2O_3X(OH)$ (X = Cl, Br, I).

$ZnSb_2O_3Cl(OH)$		$ZnSb_2O_3Br(OH)$		$ZnSb_2O_3I(OH)$		Comments
Synthesis 1 (cm^{-1})	Synthesis 2 (cm^{-1})	Synthesis 1 (cm^{-1})	Synthesis 2 (cm^{-1})	Synthesis1 (cm^{-1})	Synthesis 2 (cm^{-1})	
133	135	132	134	131	129	ν(Zn-X) / (Sb-O) lattice vibrations
145	146		143			ν(Zn-X) / (Sb-O) lattice vibrations
	153		152			ν(Zn-X)
164	160	160		167	166	ν(Zn-X)
186	190	187	184	185	183	δ(Sb-O) twisting
			203	205	204	δ(Sb-O) wagging
232	229	234		233	227	ν(Zn-X)
296	293	294	289	289	288	δ(Sb-O) scissoring
		339	339	340	340	ν_{sym}(Sb-O)
			391		390	ν_{sym}(Sb-O)
399	398		397	397	395	ν_{sym}(Sb-O)
407		406				ν_{sym}(Sb-O)
434	434	435	436	435	435	ν_{sym}(Sb-O)
441		441		442	441	ν_{sym}(Sb-O) / ν(Zn-O)
480	480	481	480	480	483	ν_{sym}(Sb-O)
546	545	535	535			ν_{asym}(Sb-O)
565	565	565	561	558	561	ν_{asym}(Sb-O)
629	630	622	618	610	612	ν_{asym}(Sb-O)
	719		689	649	650	ν_{asym}(Sb-O)
				781	783	ν(Zn-O)
835	836	812	810	830	830	ν_{asym}(Sb-O)
926	903		870			ν_{asym}(Sb-O)
1043	1043	1046	983			
1394		1381				
1506	1617	1504	1606	1506	1509	δ(O-H)bending
3422	3425	3422	3422	3425	3427	ν(O-H)streching

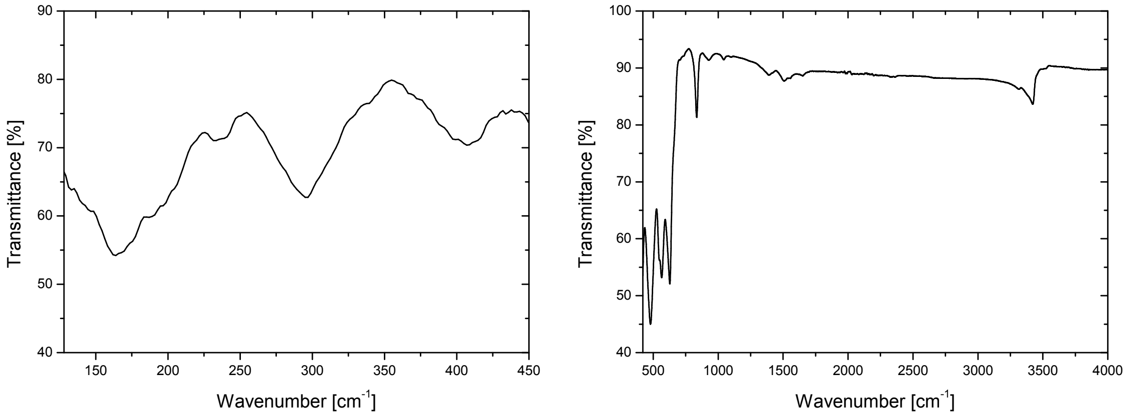

(a) $ZnSb_2O_3Cl(OH)$, F-IR **(b)** $ZnSb_2O_3Cl(OH)$, M-IR

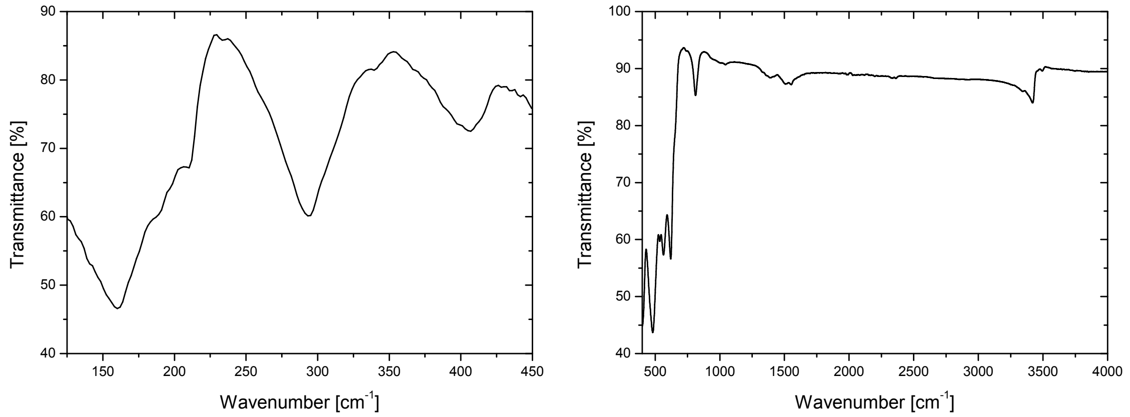

(c) $ZnSb_2O_3Br(OH)$, F-IR **(d)** $ZnSb_2O_3Br(OH)$, M-IR

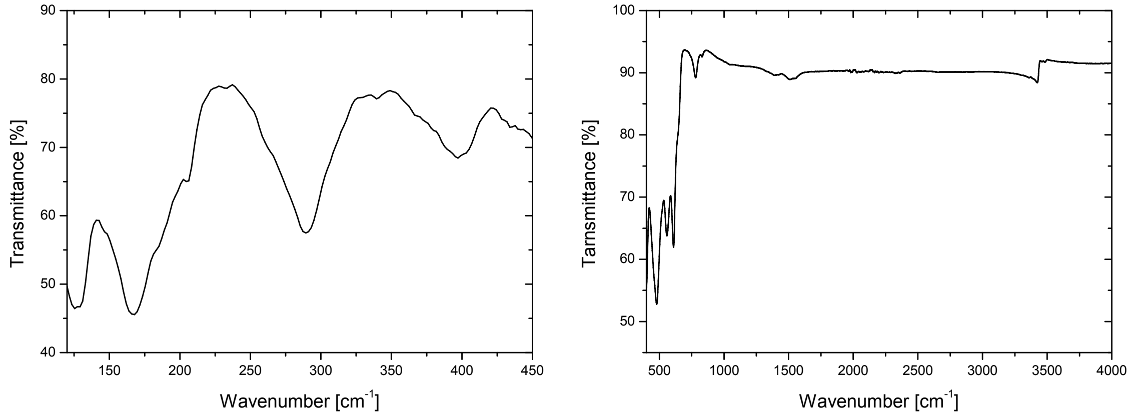

(e) $ZnSb_2O_3I(OH)$, F-IR **(f)** $ZnSb_2O_3I(OH)$, M-IR

Figure 3.44.: Infrared spectrum of $ZnSb_2O_3X(OH)$ according to synthesis method 1, showing significant vibrations only for ν_{Zn-O}, ν_{Sb-O}, ν_{Zn-Cl}, and ν_{O-H}.

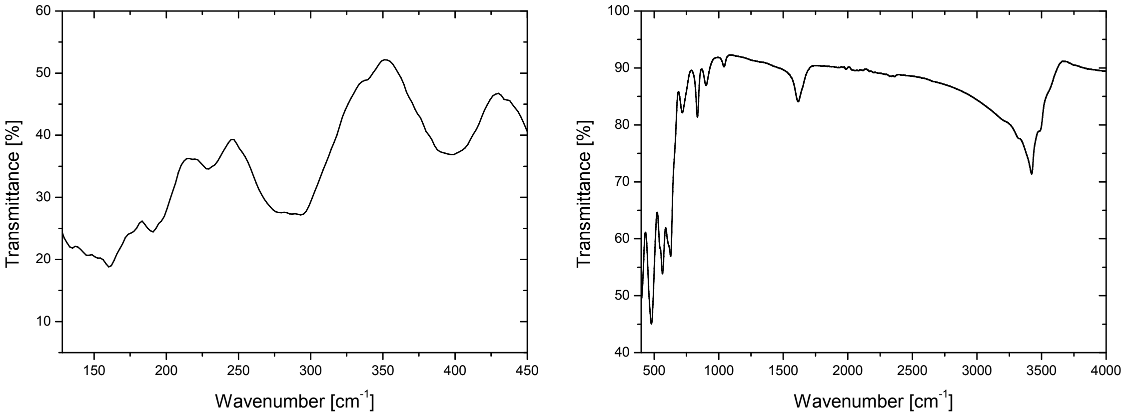

(a) $ZnSb_2O_3Cl(OH)$, F-IR **(b)** $ZnSb_2O_3Cl(OH)$, M-IR

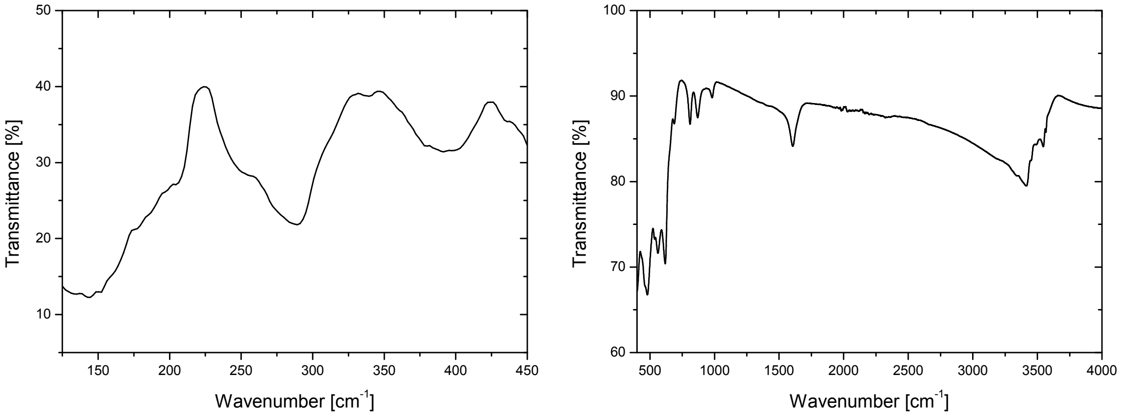

(c) $ZnSb_2O_3Br(OH)$, F-IR **(d)** $ZnSb_2O_3Br(OH)$, M-IR

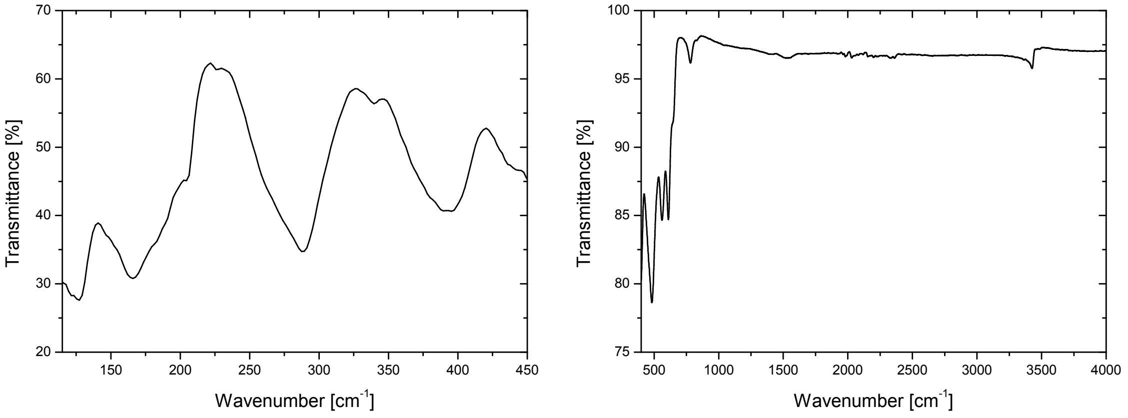

(e) $ZnSb_2O_3I(OH)$, F-IR **(f)** $ZnSb_2O_3I(OH)$, M-IR

Figure 3.45.: Infrared spectrum of $ZnSb_2O_3X(OH)(X=Cl, Br, I)$ according to synthesis method 2, showing significant vibrations only for $\nu_{\mathrm{Zn-O}}$, $\nu_{\mathrm{Sb-O}}$, $\nu_{\mathrm{Zn-X}}$, and $\nu_{\mathrm{O-H}}$.

3.4. $CdSb_2O_3X(OH)$ (X = Cl, Br, I)

3.4.1. Synthesis

Single crystals of new compounds represented by the composition $CdSb_2O_3X(OH)$ (X = Cl, Br, I) were grown via hydrothermal reaction of CdO, SbX_3 (X = Cl, Br, I) and CdO, SbX_3 (X = Cl, Br, I) and Sb_4O_6, hereafter referred to as synthesis methods 1 and 2, respectively. The chemicals for synthesis 1 were mixed in the stoichiometric molar ratio 2:1 and for synthesis 2 in a 6:2:1 ratio. Reactants were placed into silica tubes, then 3 ml water were added and the mixture was frozen using liquid nitrogen, evacuated, and tightly closed by melting the quartz using an H_2/O_2-burner. The reactions were carried out in a 40 ml Teflon-lined stainless steel autoclave at 90°C for 5 days. After slow cooling, solid products were removed by filtration and cleaned with the aid of water or ethanol. In both cases, the synthesis product consisted of colourless crystals of $CdSb_2O_3X(OH)$ (X = Cl, Br, I) and white powder, which was identified by powder X-ray diffraction. Detailed information concerning phase analysis is presented in the following chapter.

3.4.2. Single crystal analysis and powder X-ray diffraction

To carry out single crystal X-ray diffraction measurement at room temperature, a single crystal was glued on a glass capillary and mounted on an IPDS (STOE) single crystal diffractometer providing monochromatic Mo-Kα radiation (λ = 0.71073 Å). For compounds containing chlorine and bromine atoms, the diffraction pattern shows a monoclinic unit cell $P2_1/c$ (No.14) with the parameters $a = 7.018(1)$ Å, $b = 8.300(2)$ Å, $c = 10.903(2)$ Å, $\beta = 96.03(3)^\circ$ for $CdSb_2O_3Cl(OH)$ and $a = 7.232(1)$ Å, $b = 8.320(2)$ Å, $c = 11.008(2)$ Å, $\beta = 96.38(3)^\circ$ for $CdSb_2O_3Br(OH)$. The space groups were derived from systematic extinction and were confirmed by the subsequent refinement. $CdSb_2O_3I(OH)$ however crystallized in space group $P2_1/m$ with lattice constants $a = 7.570(2)$ Å, $b = 8.335(2)$ Å, $c = 5.496(1)$ Å, $\beta = 96.53(3)^\circ$. Several specimens were examined for quality, demonstrating systematic overgrowth, before a needle-shaped crystal was chosen for single crystal diffraction measurement. The diffraction pattern could be indexed in the Laue class $2/m$, with primitive P monoclinic lattice. The value of the $|E^2\text{-}1|$ criterion was 1.000, corresponding to a centrosymmetric space group. The extinction conditions indicated the space groups $P2_1$ and $P2_1/m$. Because of the $|E^2\text{-}1|$ criterion the structure was therefore solved in $P2_1/m$. Within the crystal structures represented by the composition $CdSb_2O_3X(OH)$ (X= Cl, Br, I), a *klassengleiche* group-subgroup relation occurs. The symmetry reduction takes place by the loss of translation symmetry. Figure 3.46 presents the Bärnighausen tree. The intensities of the reflections were integrated using the STOE *X-Area* [D] software. All intensity data were corrected for Lorentz and polarization effects. Absorption correction was carried out numerically, after crystal shape optimisation, using *X-SHAPE* [M]. Direct methods were applied to solve the structure and provide the positions of three metal atoms, one Cl/Br, and four O atoms for $CdSb_2O_3X(OH)$ (X = Cl, Br), and of three heavy atoms and three O atoms for $CdSb_2O_3I(OH)$. The most important measurement and refinement data are summarized in Table 3.16.

Final atomic coordinates and equivalent isotropic displacement parameters for structures from the system $CdSb_2O_3X(OH)$ (X = Cl, Br, I) are listed in the appendix (Table B.15, B.17, and B.19). Table B.16, B.18, and B.20 include anisotropic displacement parameters. Anisotropic displacement parameters were used for all atoms except hydrogen. An extinction parameter was included in the last refinement cycles.

The final composition of compounds $CdSb_2O_3X(OH)$ (X = Cl, Br, I) was additionally confirmed by powder X-ray diffraction. All data and detailed analysis is present in the appendix (Figures B.24-B.35).

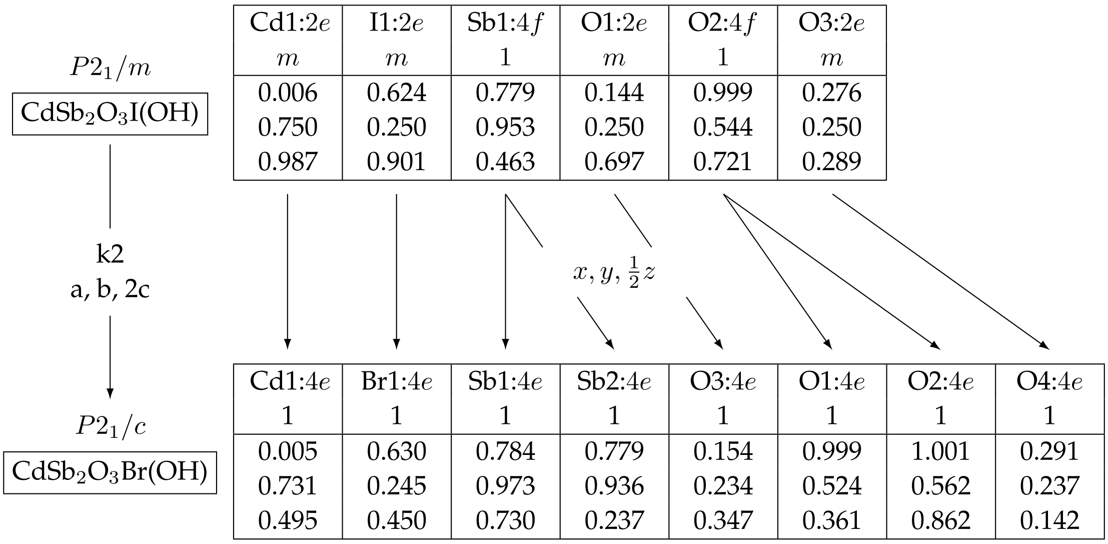

Cd1:$2e$	I1:$2e$	Sb1:$4f$	O1:$2e$	O2:$4f$	O3:$2e$
m	m	1	m	1	m
0.006	0.624	0.779	0.144	0.999	0.276
0.750	0.250	0.953	0.250	0.544	0.250
0.987	0.901	0.463	0.697	0.721	0.289

Cd1:$4e$	Br1:$4e$	Sb1:$4e$	Sb2:$4e$	O3:$4e$	O1:$4e$	O2:$4e$	O4:$4e$
1	1	1	1	1	1	1	1
0.005	0.630	0.784	0.779	0.154	0.999	1.001	0.291
0.731	0.245	0.973	0.936	0.234	0.524	0.562	0.237
0.495	0.450	0.730	0.237	0.347	0.361	0.862	0.142

Figure 3.46.: Bärnighausen tree presenting the group-subgroup relation in $CdSb_2O_3X(OH)$ (X= Cl, Br, I).

$CdSb_2O_3X(OH)$ (X = Cl, Br) are isostructural. They consist of puckered layers of distorted $[CdO_3X]$ (X = Cl, Br) tetrahedra and Sb^{3+} cations asymmetrically four-coordinated by oxygen, forming one-dimensional polymers (see Figure 3.47). In the crystal structures $CdSb_2O_3X(OH)$ (X = Cl, Br, I), there is the possibility of intermolecular hydrogen bonds O-H...X (X = Cl, Br, I), where OH is a proton donor and halide atoms act as proton acceptors. Positions of hydrogen atoms were found in the electron density map. The single crystal X-ray diffraction data were confirmed by the calculations of Madelung Part of Lattice Energy (MAPLE) [87,88,89]. The calculations confirmed the oxygen atom O4 as underbinding and taking part in forming a hydroxy group.

Table 3.16.: Details of the data collection and results of the structure refinement for $CdSb_2O_3Cl(OH)$, $CdSb_2O_3Br(OH)$, and $CdSb_2O_3I(OH)$.

Crystal data			
Chemical formula	$CdSb_2O_3Cl(OH)$	$CdSb_2O_3Br(OH)$	$CdSb_2O_3I(OH)$
Crystal colour/habit	colourless/needle	colourless/needle	colourless/needle
Crystal size	0.2 × 0.07× 0.05 mm	0.12 × 0.03 × 0.02 mm	0.08 × 0.04 × 0.03 mm
Molecular weight	912.72 g mol^{-1}	1001.64 g mol^{-1}	547.81 g mol^{-1}
Calculated density	4.800 g cm^{-3}	5.053 g cm^{-3}	5.281 g cm^{-3}
Space group	$P2_1/c$ (No. 14)	$P2_1/c$ (No. 14)	$P2_1/m$ (No. 11)
Lattice parameters	$a = 7.018(1)$ Å	$a = 7.232(1)$ Å	$a = 7.570(2)$ Å
	$b = 8.300(2)$ Å	$b = 8.320(2)$ Å	$b = 8.335(2)$ Å
	$c = 10.903(2)$ Å	$c = 11.008(2)$ Å	$c = 5.496(1)$ Å
	$\beta = 96.03(3)°$	$\beta = 96.38(3)°$	$\beta = 96.53(3)°$
Cell volume, Z	631.5(2) Å^3, 2	658.3(2) Å^3, 2	344.51(1) Å^3, 2
Data collection			
Device, Radiation, Temperature	STOE IPDS I, Mo-Kα, 0.71073 Å, graphite monochromator, 293K		
Scan range	$2.92° \leqslant 2\theta \leqslant 26.51°$	$2.83° \leqslant 2\theta \leqslant 26.49°$	$2.71° \leqslant 2\theta \leqslant 26.54°$
hkl range	$-8 \leqslant h \leqslant 8$	$-9 \leqslant h \leqslant 9$	$-9 \leqslant h \leqslant 9$
	$-10 \leqslant k \leqslant 10$	$-10 \leqslant k \leqslant 10$	$-10 \leqslant k \leqslant 10$
	$-13 \leqslant l \leqslant 13$	$-13 \leqslant l \leqslant 13$	$-6 \leqslant k \leqslant 6$
Structure solution and refinement	$CdSb_2O_3Cl(OH)$	$CdSb_2O_3Br(OH)$	$CdSb_2O_3I(OH)$
Measured reflections	9219	9494	4218
Independent reflections	1308	1335	764
Independent reflections with $F_O > 4\sigma(F_O)$	1159	1073	603
R_{int}	0.0394	0.0321	0.0793
R_σ	0.0186	0.0195	0.0466
Structure solution, refinement	SHELXS97 [I], SHELXL97 [J]		
Number of parameters	77	77	46
Absorption correction	numerical: X-RED [L], X-SHAPE [M]		
Absorption coefficient	12.179 mm^{-1}	17.347 mm^{-1}	15.257 mm^{-1}
$R_1, wR_2[I > 3\sigma(I)]$	0.0206, 0.0477	0.0211, 0.0484	0.0381, 0.0866
R_1, wR_2[all reflections]	0.0256, 0.0489	0.0314, 0.0509	0.0513, 0.0903
GooF	1.064	0.940	0.994
F(000)	800	872	472
Residual electron density	0.778, -0.733 e Å^{-3}	1.167, -1.018 e Å^{-3}	2.087, -0.975 e Å^{-3}

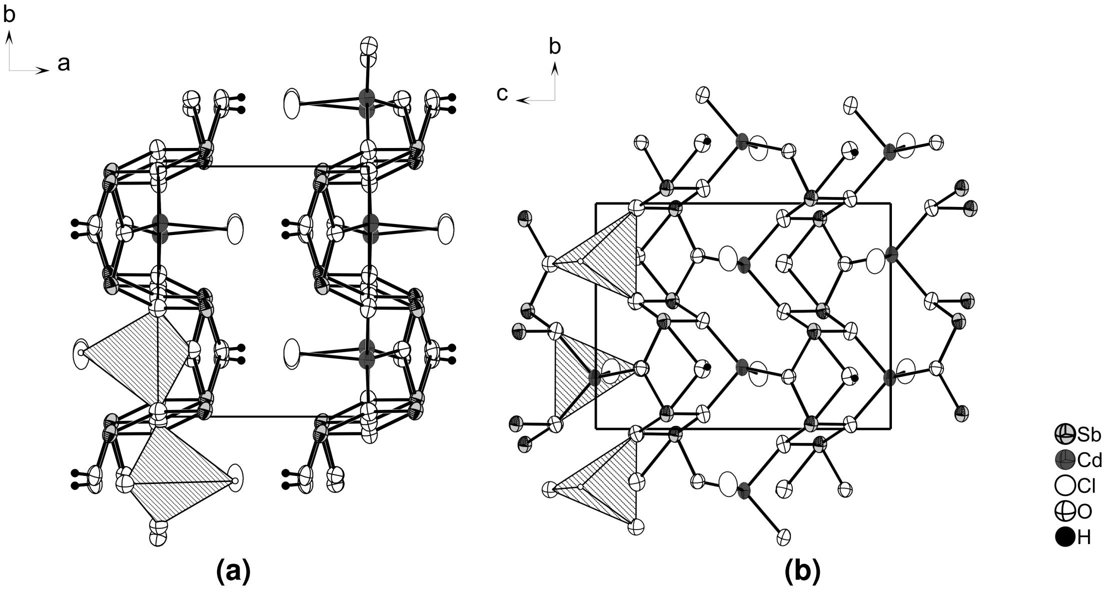

Figure 3.47.: Projection of the crystal structure of $CdSb_2O_3Cl(OH)$ emphasizing the corrugated puckered layers ((a) view along *c* axis) of $[CdO_3Cl]$ tetrahedra, and Sb^{3+} cations three-coordinate by oxygen and one-coordinate by hydroxy group, forming one-dimensional polymers.((b) view along *a* axis). (90% probability level).

All of the polyhedra occuring in the crystal structures represented by the composition $CdSb_2O_3X(OH)$ (X = Cl, Br) are substantially distorted. Coordination of cadmium by one chlorine/bromine atom and three oxygen atoms results in a distorted tetrahedral environment (first coordination sphere), as shown Figure 3.48. Three shorter bonds can be distinguished with d(Cd-O) falling in the range 2.211(3)-2.251(3) Å in $CdSb_2O_3Cl(OH)$, and 2.210(3)-2.261(4) Å in $CdSb_2O_3Br(OH)$, corresponding to the average bond length d(Cd-O) = 2.348 Å in pure CdO [90]. However two d(Cd-O) bonds occurring in the structure with length 2.569(3) Å in $CdSb_2O_3Cl(OH)$, and 2.650(2) Å in $CdSb_2O_3Br(OH)$ are about 0.3 Å longer than those reported for cadmium oxide. The oxygen atoms in axial positions that are involved in the creation of O-H...X (X = Cl, Br) hydrogen bonds have distances d(Cd-O) = 2.501(4) Å and 2.482(4) Å, which are also longer than those found in CdO. Halide atoms also take axial positions. The bond lengths d(Cd-Cl) = 2.518(1) Å and d(Cd-Br) = 2.649(9) Å are slightly shorter than 2.637 Å and 2.785 Å reported in pure $CdCl_2$ [84] and $CdBr_2$ [85, 86], respectively. Analysis of bond lengths in structures with the composition $CdSb_2O_3X(OH)$ (X= Cl, Br) shows that it is possible to describe the environment around the cadmium atom as 4+2 coordination. The selected bond lengths and angles are listed in Table 3.17.

Antimony cations are four-coordinated by oxygen atoms and form one-dimensional polymers along [010] (Figure 3.50), similarly as in compounds with composition $ZnSb_2O_3X$ (X= Cl, Br, I) and $CdSbO_2Br$. The average d(Sb-O) distances of 2.0976 Å in $CdSb_2O_3Cl(OH)$ and 2.1014 Å in $CdSb_2O_3Br(OH)$ are about 0.1 Å longer than the bond

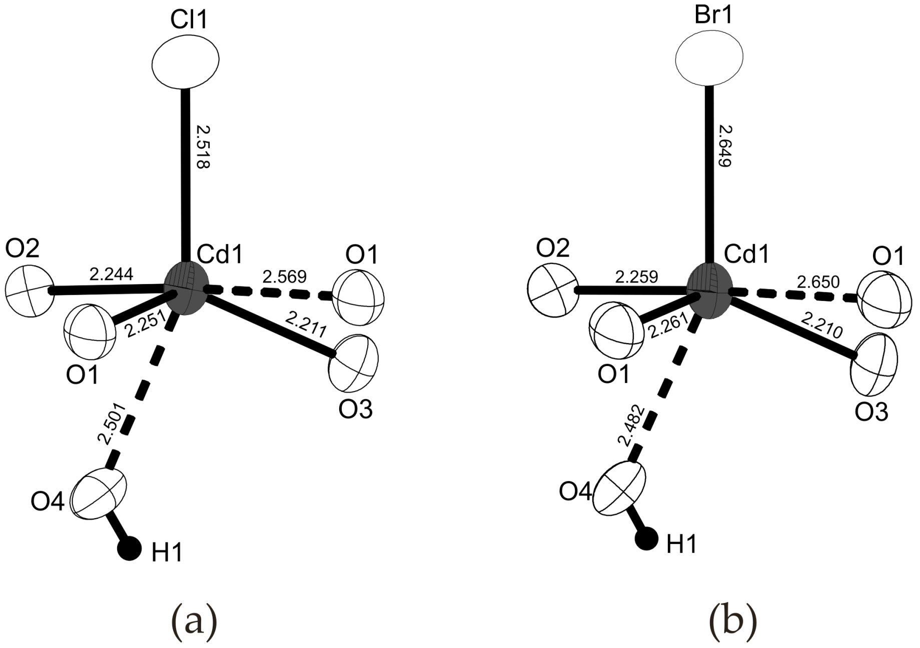

Figure 3.48.: Coordination of cadmium by three oxygens, one chlorine (a), bromine (b) atoms resulting in [CdO$_3$X] tetrahedra. (90% probability level). All distances are given in Å.

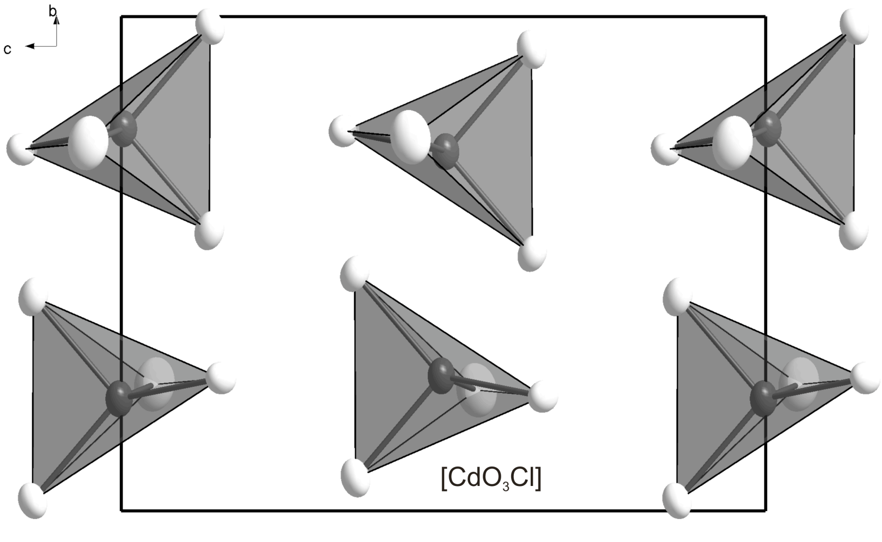

Figure 3.49.: Projection of the [CdO$_3$Cl] tetrahedra in CdSb$_2$O$_3$Cl(OH) (90% probability level).

length d(Sb-O) = 1.9779 Å in senarmontite [104, 68] and than the average bond length d(Sb-O) = 2.0059 Å in valentinite [69, 70], as expected taking the coordination number into account [105, 106]. The bond lengths in $CdSb_2O_3X(OH)$ (X=Cl, Br, I) are in resonable agreement with average $d(Sb^{3+}\text{-}O) \approx 2.1$ Å in $SbTaO_4$ [107, 108], $SbNbO_4$ [108, 123, 124], and $Sb_{1.92}V_{0.08}O_{3.67}$ [109], where antimony(III) is four-coordinated by oxygens and builds similar structural entities as in $CdSb_2O_3X(OH)$ (X=Cl, Br, I). The distances d(Sb-OH) between antimony and oxygen atoms that are involved in the creation of a hydrogen bond amounts to 2.200(9), 2.359(1) Å in $CdSb_2O_3Cl(OH)$ and 2.221(9), 2.345(1) Å in $CdSb_2O_3Br(OH)$. This is much longer than $d(Sb\text{-}O) \approx 2.00$ Å in Sb_2O_3 [104, 68, 69, 70]. Selected bond lengths and angles are presented in Table 3.17.

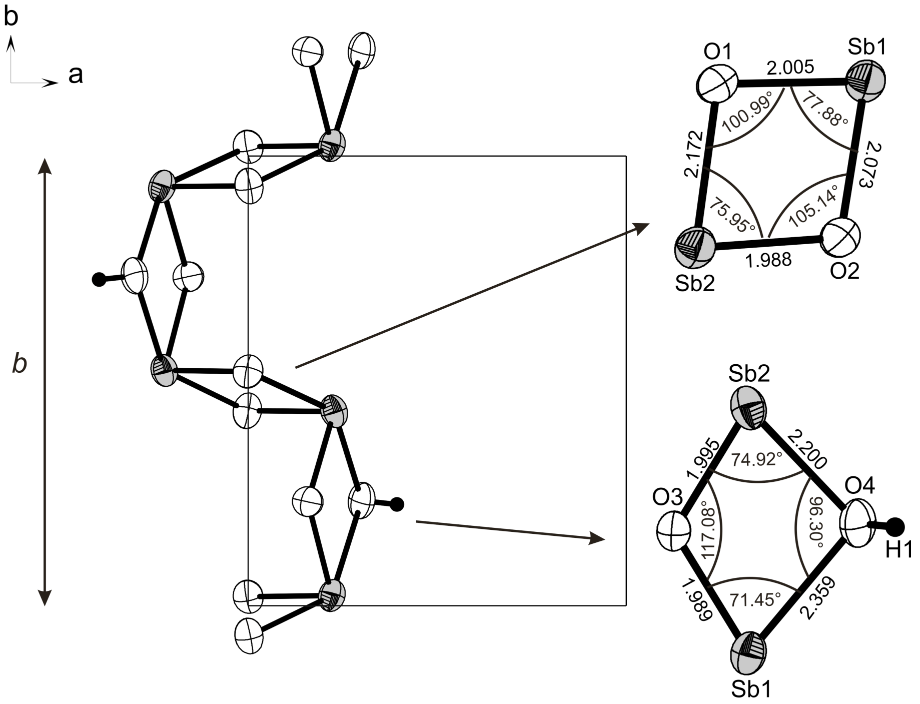

Figure 3.50.: Projection of the one-dimensional polymer formed by Sb^{3+} cations four-coordinate by oxygen atoms. (90% probability level).

$CdSb_2O_3I(OH)$

The new layered compound $CdSb_2O_3I(OH)$ crystallizes in the centrosymmetric space group $P2_1/m$ (No. 11), rather than the expected $P2_1/c$ (No. 14) as in the compounds containing chlorine and bromine atoms described earlier. Isostructurality was found to the compounds with the composition $ZnSb_2O_3X(OH)$ (X=Cl, Br, I). In order to perform a comparative analysis of $CdSb_2O_3I(OH)$ and $ZnSb_2O_3X(OH)$ (X=Cl, Br, I), it is necessary to exchange the a and c lattice parameters. Exchange of cell parameters a and c force the representation of $CdSb_2O_3X(OH)$ (X=Cl,Br) in $P2_1/a$, because of the group-subgroup relationship in this system. It is however preferred to present the

Table 3.17.: Selected interatomic distances (in Å) and angles (in degrees) for $CdSb_2O_3X(OH)$ (X=Cl, Br) at room temperature.

$CdSb_2O_3Cl(OH)$			
Sb(1)-O(1)	2.005(3)	O(3)-Sb(1)-O(1)	96.7(1)
Sb(1)-O(2)	2.073(3)	O(3)-Sb(1)-O(2)	84.1(1)
Sb(1)-O(3)	1.989(3)	O(1)-Sb(1)-O(2)	77.9(1)
Sb(1)-O(4)	2.359(4)	O(3)-Sb(1)-O(4)	71.5(1)
Sb(2)-O(1)	2.172(3)	O(1)-Sb(1)-O(4)	77.7(1)
Sb(2)-O(2)	1.988(3)	O(2)-Sb(1)-O(4)	142.9(1)
Sb(2)-O(3)	1.995(3)	O(2)-Sb(2)-O(3)	95.7(1)
Sb(2)-O(4)	2.200(4)	O(2)-Sb(1)-O(1)	76.0(1)
		O(3)-Sb(2)-O(1)	79.1(1)
		O(2)-Sb(2)-O(4)	79.8(1)
		O(3)-Sb(2)-O(4)	74.9(1)
		O(1)-Sb(2)-O(4)	142.2(1)
Cd(1)-O(1)	2.251(3)	O(3)-Cd(1)-O(2)	114.0(1)
Cd(1)-O(2)	2.243(3)	O(3)-Cd(1)-O(1)	130.1(1)
Cd(1)-O(3)	2.211(3)	O(2)-Cd(1)-O(1)	99.3(1)
Cd(1)-Cl(1)	2.518(1)	O(3)-Cd(1)-Cl(1)	113.4(9)
		O(2)-Cd(1)-Cl(1)	92.0(9)
		O(1)-Cd(1)-Cl(1)	100.9(9)
$CdSb_2O_3Br(OH)$			
Sb(1)-O(1)	2.007(4)	O(3)-Sb(1)-O(1)	96.9(2)
Sb(1)-O(2)	2.083(4)	O(3)-Sb(1)-O(2)	83.6(2)
Sb(1)-O(3)	1.996(4)	O(1)-Sb(1)-O(2)	77.5(2)
Sb(1)-O(4)	2.345(5)	O(3)-Sb(1)-O(4)	71.7(1)
Sb(2)-O(1)	2.162(4)	O(1)-Sb(1)-O(4)	77.6(2)
Sb(2)-O(2)	1.994(4)	O(2)-Sb(1)-O(4)	142.3(2)
Sb(2)-O(3)	2.003(4)	O(2)-Sb(2)-O(3)	96.0(2)
Sb(2)-O(4)	2.221(5)	O(2)-Sb(1)-O(1)	76.0(2)
		O(3)-Sb(2)-O(1)	79.8(2)
		O(2)-Sb(2)-O(4)	79.1(2)
		O(3)-Sb(2)-O(4)	74.4(2)
		O(1)-Sb(2)-O(4)	141.8(2)
Cd(1)-O(1)	2.261(4)	O(3)-Cd(1)-O(2)	116.2(1)
Cd(1)-O(2)	2.259(4)	O(3)-Cd(1)-O(1)	129.6(2)
Cd(1)-O(3)	2.210(3)	O(2)-Cd(1)-O(1)	99.0(2)
Cd(1)-Cl(1)	2.6489(9)	O(3)-Cd(1)-Cl(1)	113.8(1)
		O(2)-Cd(1)-Cl(1)	92.7(1)
		O(1)-Cd(1)-Cl(1)	99.0(1)

crystal structure data as described earlier, since in the monoclinic system, the favoured space group is $P2_1/c$. The crystal structure of $CdSb_2O_3I(OH)$ consists of corrugated layers perpendicular to the [001] direction, as shown in Figure 3.51a. Each layer is built by cadmium-centred tetrahedra $[CdO_3I]$ (Figures 3.51b and 3.52) and Sb^{3+} cations asymmetrically four-coordinated by oxygen atoms forming one-dimensional polymers, as shown in Figure 3.50. It is particularly notable that the b lattice parameter in all three structures remains constant.

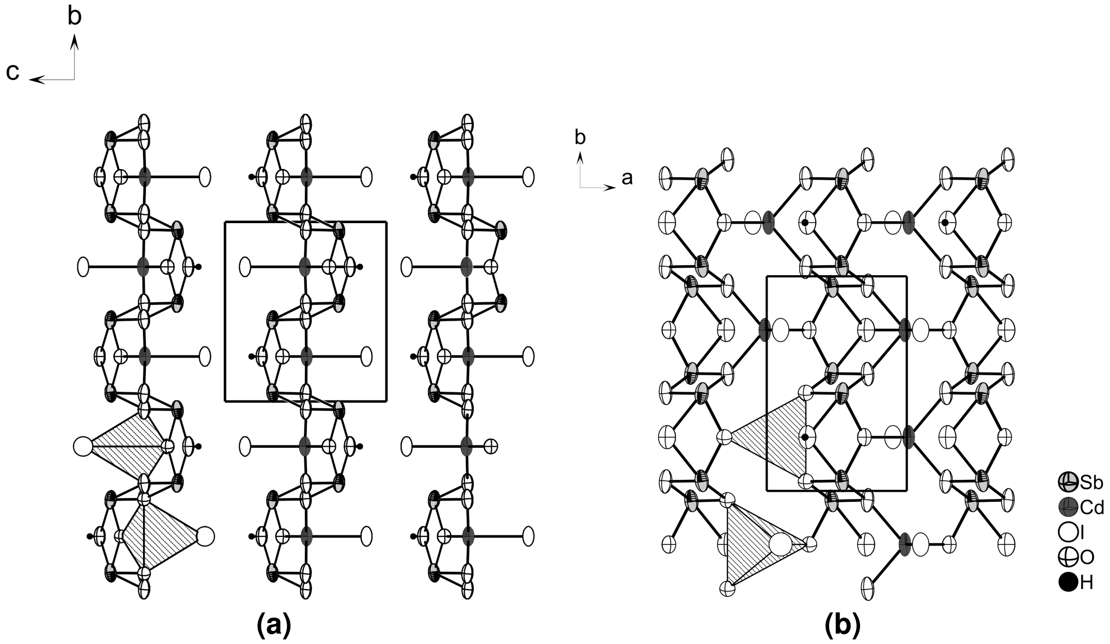

Figure 3.51.: Projection of the crystal structure of $CdSb_2O_3I(OH)$ emphasizing the corrugated puckered layers ((a) view along a axis) of $[CdO_3I]$ tetrahedra, and Sb^{3+} cations four-coordinated by oxygen, forming one-dimensional polymers. ((b) view along c axis). (90% probability level).

The three shorter d(Cd-O) distances fall in the range 2.179(9)-2.253(8) Å, slightly shorter than the average bond length d(Cd-O) = 2.348 Å in pure CdO [90]. On the other hand, the longer bonds d(Cd-O) amount to 2.457(4) and 2.930(1) Å , which are significantly longer than in cadmium oxide. As shown by the distances and angles the coordination of Cd with regards to O and I can be regarded as 4+2. The average d(Sb-O) distance 2.085 Å in $CdSb_2O_3I(OH)$ is about 0.1 Å longer than the bond length d(Sb-O) = 1.9779 Å in senarmontite [104,68] and than the average bond length d(Sb-O) = 2.0059 Å in valentinite [69,70], which is rather expected because of a greater number of ligands than in Sb_2O_3.

The crystal structures representing the systems $MXSb_2O_3(OH)$ (M = Zn, Cd; X = Cl, Br, I) all exhibit a similar tendency of forming building blocks. This suggests that the Lewis acidity and the softness of the metal cations thus have significant influence on the resulting crystal structure because of their bonding preference. The hard Lewis

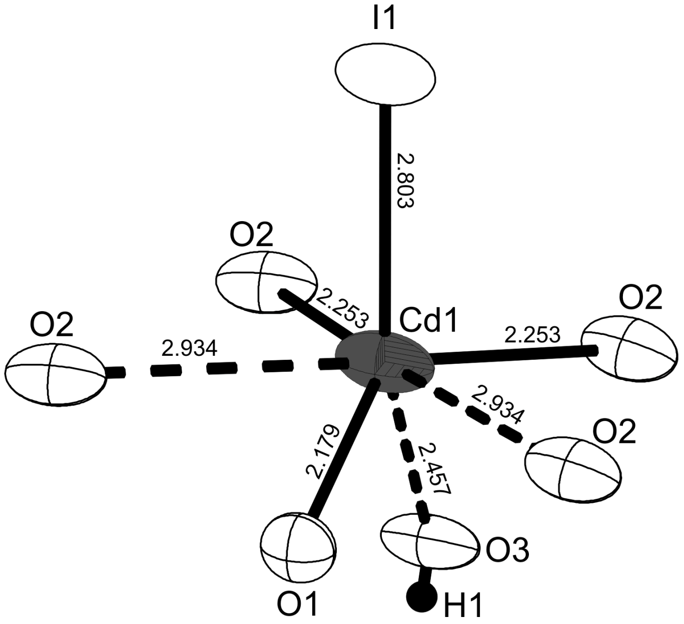

Figure 3.52.: Coordination sphere of the cadmium ion in $CdSb_2O_3I(OH)$ resulting in $[CdO_3I]$ tetrahedra. All distances are shown in Å. (90% probability level).

Table 3.18.: Selected interatomic distances (in Å) and angles (in degrees) for $CdSb_2O_3I(OH)$ at room temperature. Symmetry codes: $i = x, 0.5 - y, z$.

$CdSb_2O_3I(OH)$					
Sb(1)-O(1)		1.992(5)	O(2)-Sb(1)-O(1)		96.8(4)
Sb(1)-O(2)		1.983(7)	O(2)-Sb(1)-O(2)		76.7(3)
Sb(1)-O(2)		2.100(6)	O(1)-Sb(1)-O(2)		82.2(3)
Sb(1)-O(3)		2.265(8)^i	O(2)-Sb(1)-O(3)		78.0(4)
			O(1)-Sb(1)-O(3)		73.1(3)
			O(2)-Sb(2)-O(3)		141.9(3)
			Sb(1)-O(1)-Sb(1)		116.6(4)
			Sb(1)-O(2)-Sb(1)		103.3(3)
			Sb(1)-O(3)-Sb(1)		96.9(4)
Cd(1)-O(1)		2.179(9)	O(1)-Cd(1)-O(2)	2×	122.9(2)
Cd(1)-O(2)	2×	2.253(8)	O(2)-Cd(1)-O(2)		99.4(4)
Cd(1)-O(3)		2.46(1)	O(1)-Cd(1)-I(1)		115.0(3)
Cd(1)-I(1)		2.803(1)	O(2)-Cd(1)-I(1)	2×	95.15(2)

acid Sb^{3+} prefers the hard Lewis base O^{2-}, while the softer Lewis acids Zn^{2+} and Cd^{2+} accept both O^{2-} and X^{-} in an oxyhalide environment.

The possibility of hydrogen bonding exists in the investigated compounds $CdSb_2O_3X(OH)$ (X = Cl, Br, I). The halide atoms from neighbouring molecules participate in O-H...X (X = Cl, Br, I) hydrogen bonds. As expected, the strongest hydrogen bond occurs in the structure in which a chlorine atom acts as a proton acceptor, which has the highest electronegativity among the three investigated halides. Table 3.19 shows the geometry of the hydrogen bonds. In order to better understand the nature of hydrogen bonding, it is possible to carry out *ab initio* calculations for model systems. Applying the Bader theory "atoms in molecules" [125] enables a topological analysis for model systems. Geometrical and topological parameters of hydrogen bonds correlate with each other. The distance O...H correlates not only with the electron density at a bond critical point, but also with the Laplace operator of the density. The smaller the proton-acceptor distance, the greater the value of electron density and of the Laplace operator at the critical point of the hydrogen bond, and hence the greater the value of the bond energy. In order to compare the geometry of hydrogen bonds observed in the crystal structures with the geometry of model systems, the hydrogen bond is routinely normalized (Table 3.20). This involves extension of the donor-proton bond length to the average length of D-H designated from neutron diffraction measurement. Standard lengths of D-H bonds are: C-H = 1.083 Å, N-H = 1.009 Å, O-H = 0.983 Å [121]. The normalization of hydrogen bonds was performed using the functions *Norm H-bond/Calc H-bond* in *PLATON* [K].

The application of neutron scattering measurements would be required to find accurate locations of hydrogen atoms. Useful experimental techniques for studying the presence, nature, and energy (strength) of hydrogen bonds in inorganic solids include Raman and infrared spectroscopy, nuclear magnetic and nuclear quadrupole resonance measurements (NMR, NQR).

In Raman spectroscopy one would expect that the peak corresponding to the O-H stretch for structures with chlorine should appear at lower values of Raman shift, because of the strongest hydrogen bond in this structure [113, 114, 115]. As can be seen the results obtained from Raman spectroscopy (Table 3.21) and X-ray diffraction correlate with one another. However, no band for O-H stretch was observed in the Raman spectrum for $CdSb_2O_3Cl(OH)$ obtained using synthesis method 2 , although it was observed in the IR spectrum. This is believed to be a measurement artefact due to insufficient signal to noise ratio.

Based on a comparison of O-H stretching modes that occur in $CdSb_2O_3X(OH)$ (X= Cl, Br, I), and with fundamental O-H vibrational frequency of free (i.e., gaseous) hydroxide ions, it is reasonable to classify OH^{-} ions in $CdSb_2O_3X(OH)$ (X= Cl, Br, I) as weak bonded, similar to the case of $ZnSb_2O_3X(OH)$ (X= Cl, Br, I). Experimental and theoretical investigations tend to assume the vibrational energy of free OH^- to be near 3700 cm^{-1} [116]. Further study on non-H-bonded OH^- ions in alkaline and alkaline earth hydroxides resulted in values of about 3570 cm^{-1} [120], while experiments on the basis of vibration-rotation spectra of gaseous OH^- ions [117,118] yielded values of 3555.59 and 3547 cm^{-1}. The stretching vibrations of non-hydrogen-bonded hydroxide ions in O-H...X interactions have been found to vary from 3690 to 3500 cm^{-1} [119,120].

Table 3.19.: Geometrical parameters of the hydrogen bond O-H...X (X = Cl, Br, I) for $CdSb_2O_3X(OH)$ (X = Cl, Br, I) from X-ray diffraction experiment.

Compound	D-H (Å)	H...A (Å)	D...A (Å)	< D-H...A (°)
$CdSb_2O_3Cl(OH)$	0.708(7)	2.667(8)	3.295(4)	149.26(7)
$CdSb_2O_3Br(OH)$	0.670(7)	2.807(8)	3.417(5)	152.96(7)
$CdSb_2O_3I(OH)$	0.673(1)	2.998(2)	3.582(5)	147.11(2)

Table 3.20.: Geometrical parameters of the hydrogen bond O-H...X (X = Cl, Br, I) for $CdSb_2O_3X(OH)$ (X = Cl, Br, I) from X-ray diffraction experiment after normalisation of the O-H bond length to a distance of 0.98 Å.

Compound	D-H (Å)	H...A (Å)	D...A (Å)	< D-H...A (°)
$CdSb_2O_3Cl(OH)$	0.98	2.43	3.296(4)	146
$CdSb_2O_3Br(OH)$	0.98	2.53	3.417(4)	150
$CdSb_2O_3I(OH)$	0.98	2.74	3.582(1)	144

3.4.3. Raman spectroscopy

Vibrational spectra were recorded on a Varian FT-Raman module with dielectric YAG rejection filters, with 2 cm^{-1} resolution. The samples were studied by Raman spectroscopy. In the Raman spectra of $CdSb_2O_3X(OH)$ (X = Cl, Br, I), 10-12 modes were identified in the frequency range 130-4000 cm^{-1} as presented in Figures 3.53, 3.54, and 3.55 for synthesis 1, and Figures 3.56, 3.57, and 3.58 for synthesis 2. All modes occuring in the Raman spectra for $CdSb_2O_3X(OH)$ (X = Cl, Br, I) are shown in Table 3.22.

Table 3.21.: Summary of O-H stretching modes occuring in Raman spectra of compounds $CdSb_2O_3X(OH)$ (X = Cl, Br, I).

Compound	O-H stretch (cm^{-1})	
	Synthesis 1	Synthesis 2
$CdSb_2O_3Cl(OH)$	3397	
$CdSb_2O_3Br(OH)$	3417	3417
$CdSb_2O_3I(OH)$	3437	3437

In the following summary, values in parentheses represent wavenumbers appearing in the Raman spectra for crystals obtained by the second synthesis method and values without parentheses represent wavenumbers appearing in the Raman spectra for crystals obtained by the first synthesis method. Raman spectroscopic investigations of these samples show only modes which can be attributed to Cd-O, Cd-X and Sb-O. Bands at (444), (501), 543 cm^{-1} for $CdSb_2O_3Cl(OH)$, 453 (444) cm^{-1} for $CdSb_2O_3Br(OH)$ and at 500 (502), 536 (539) cm^{-1} for $CdSb_2O_3I(OH)$ appear to be the result of Cd-O vibrations [97]. Bands at 158 (143), 227, 289 (293), (681) cm^{-1} for $CdSb_2O_3Cl(OH)$, 159 (159), 286 (286), 396, 672 (680) cm^{-1} for $CdSb_2O_3Br(OH)$ and at 151 (149), 281 (281) cm^{-1} for $CdSb_2O_3I(OH)$ are thought to result from Cd-X vibrations [98,99,100,126,101]. Modes attributable to Sb-O vibrations [77,78,102,103] occur at 179 (188), 213(215), 259(254), (444), (501), 543, 592(595), 637(636) cm^{-1} for $CdSb_2O_3Cl(OH)$, at 180(180), 201(201), 219 (219), 257 (256), 453 (444), 593 (594), 634 (634) cm^{-1} for $CdSb_2O_3Br(OH)$, and at 177 (177), 199, 215 (212), 254 (254), 500 (502), 536 (539), 600 (602), 628 (628) cm^{-1} for $CdSb_2O_3I(OH)$. The bands observed at 3397 cm^{-1} for $CdSb_2O_3Cl(OH)$, 3417 (3417) cm^{-1} for $CdSb_2O_3Br(OH)$, and 3437 (3437) cm^{-1} for $CdSb_2O_3I(OH)$ (see Table 3.21) must be assigned to the O-H stretching modes. The weak bands at 577(577)cm^{-1} for $CdSb_2O_3I(OH)$ could not be identified.

An exact identification of the peaks in the Raman spectra can only be carried out by way of a theoretical calculation of the Raman spectra based on the extracted crystal structures. These calculations will be one of the goals of future work in this area.

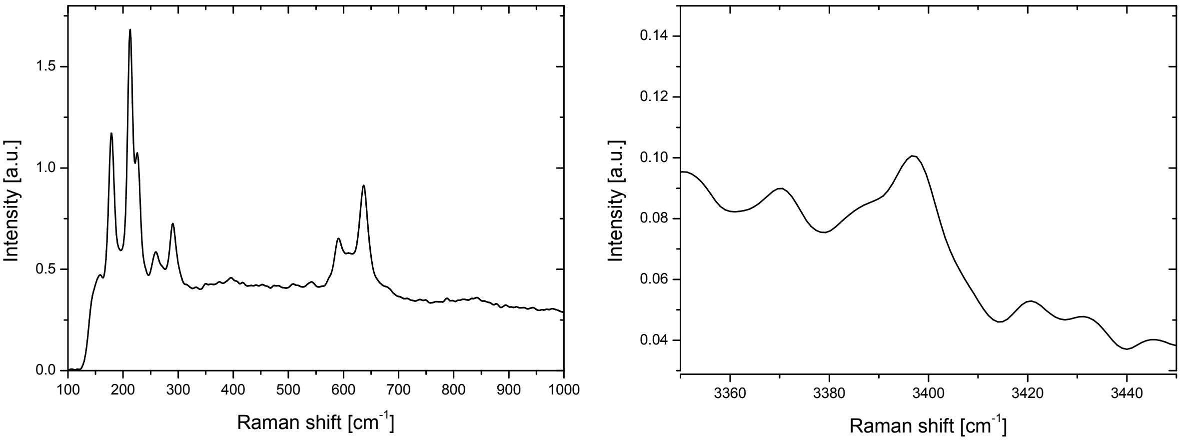

(a) **(b)**

Figure 3.53.: Raman spectrum of $CdSb_2O_3Cl(OH)$ obtained using the first synthesis method. Plot a) shows a detailed view of the 100-1000 cm^{-1} frequency range, while plot b) shows the OH response. There were no vibrational modes in range 1000-3350 cm^{-1}.

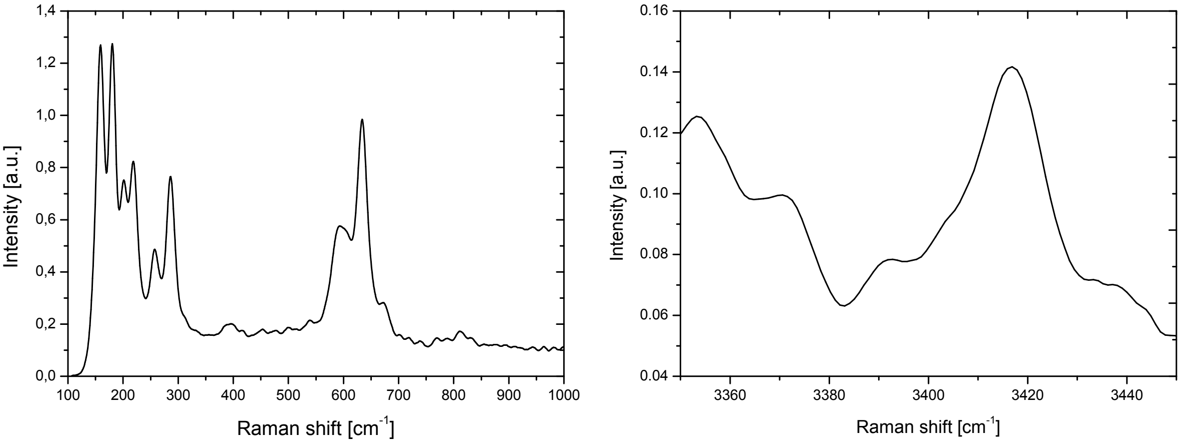

(a) **(b)**

Figure 3.54.: Raman spectrum of $CdSb_2O_3Br(OH)$ obtained using the first synthesis method. Plot a) shows a detailed view of the 100-1000 cm^{-1} frequency range, while plot b) shows the OH response. There were no vibrational modes in range 1000-3350 cm^{-1}.

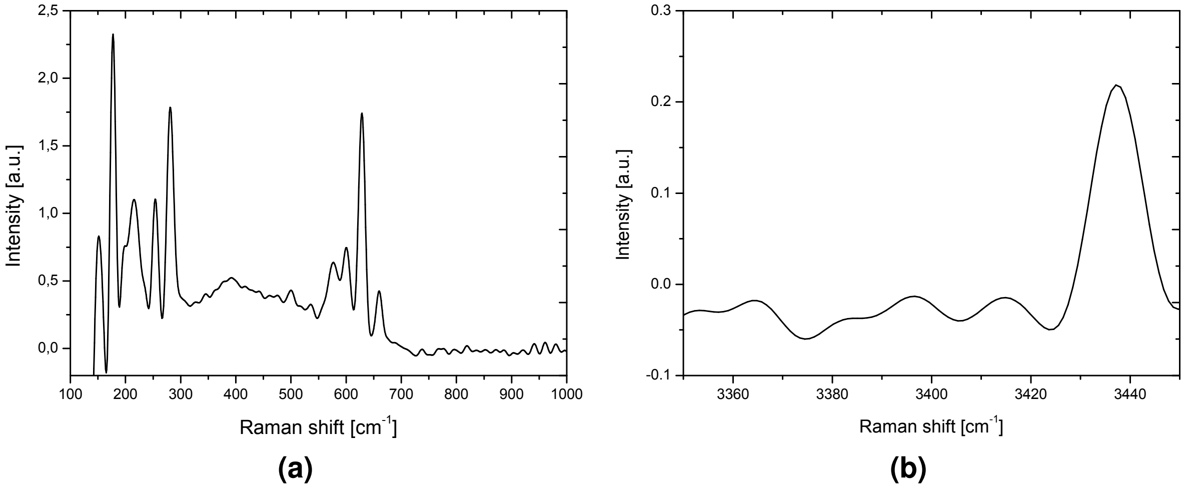

Figure 3.55.: Raman spectrum of $CdSb_2O_3I(OH)$ obtained using the first synthesis method. Plot a) shows a detailed view of the 100-1000 cm^{-1} frequency range, while plot b) shows the OH response. There were no vibrational modes in range 1000-3350 cm^{-1}.

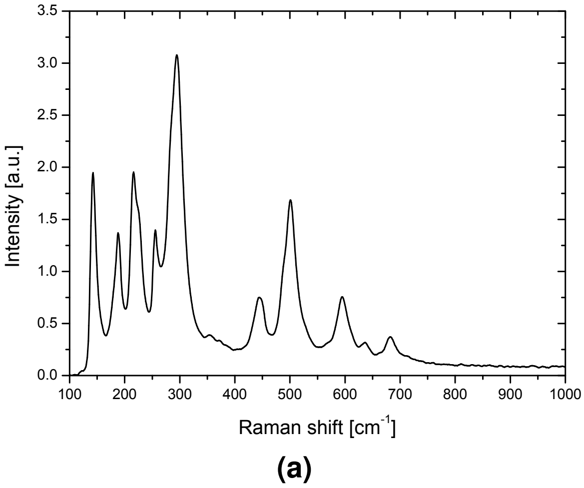

Figure 3.56.: Raman spectrum of $CdSb_2O_3Cl(OH)$ obtained using the second synthesis method. No OH peak was observed for this compound. There were no vibrational modes in range 1000-4000 cm^{-1}.

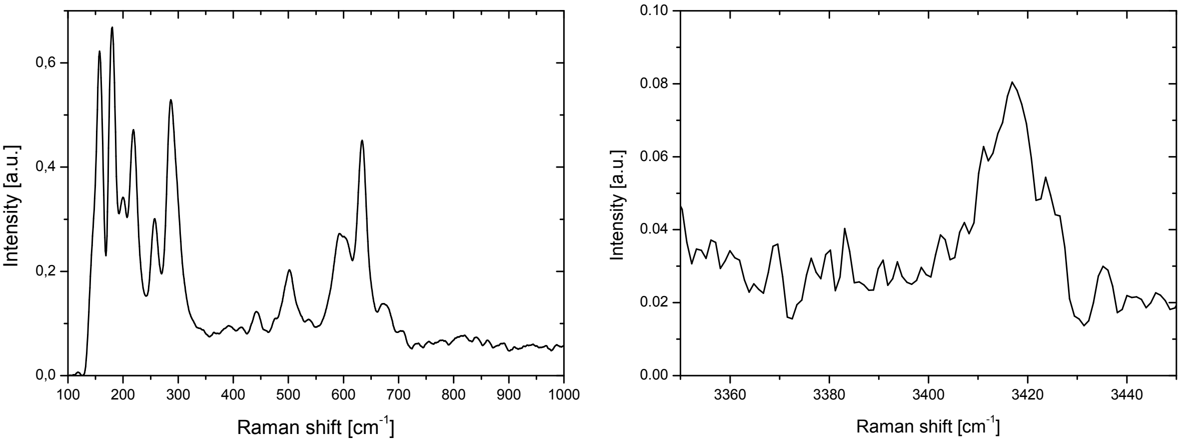

(a) **(b)**

Figure 3.57.: Raman spectrum of $CdSb_2O_3Br(OH)$ obtained using the second synthesis method. Plot a) shows a detailed view of the 100-1000 cm^{-1} frequency range, while plot b) shows the OH response. There were no vibrational modes in range 1000-3350 cm^{-1}.

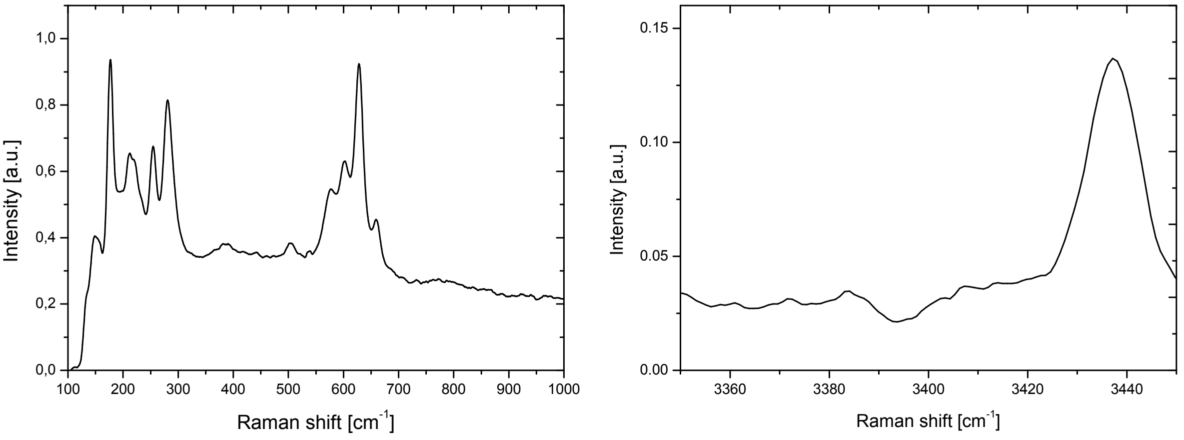

(a) **(b)**

Figure 3.58.: Raman spectrum of $CdSb_2O_3I(OH)$ obtained using the second synthesis method. Plot a) shows a detailed view of the 100-1000 cm^{-1} frequency range, while plot b) shows the OH response. There were no vibrational modes in range 1000-3350 cm^{-1}.

Table 3.22.: Summary of modes occurring in the Raman spectra of $CdSb_2O_3X(OH)$ (X = Cl, Br, I).

$CdSb_2O_3Cl(OH)$		$CdSb_2O_3Br(OH)$		$CdSb_2O_3I(OH)$		Comments
Synthesis 1 (cm^{-1})	Synthesis 2 (cm^{-1})	Synthesis 1 (cm^{-1})	Synthesis 2 (cm^{-1})	Synthesis1 (cm^{-1})	Synthesis 2 (cm^{-1})	
158	143	159	159	151	149	ν(Cd-X)/(Sb-O) lattice vibrations
179	188	180	180	177	177	δ(Sb-O) twisting
		201	201	199		δ(Sb-O) wagging
213	215	219	219	215	212	δ(Sb-O) wagging
227						ν(Cd-Cl)
259	254	257	256	254	254	δ(Sb-O) scissoring
289	293	286	286	281	281	ν(Cd-X)
		396				ν(Cd-X)
	444	453	444			ν_{sym}(Sb-O)/ν(Cd-O)
	501			500	502	ν_{sym}(Sb-O)/ν(Cd-O)
543				536	539	ν_{sym}(Sb-O)/ν(Cd-O)
				577	577	
592	595	593	594	600	602	ν_{asym}(Sb-O)/ν(Cd-O)
637	636	634	634	628	628	ν_{asym}(Sb-O)/ν(Cd-O)
	681	672	680	660	659	ν(Cd-X)

3.4.4. ATR-IR

IR measurements were performed in range 120-400 cm^{-1} (F-IR) and 400-4000 cm^{-1} (M-IR). This method is a better tool than Raman spectroscopy in the investigations of solid hydrates and hydroxides, due to the low polarizability and large dipole moment of O-H group. As shown in Table 3.23, wide bands corresponding to the O-H bond were observed above 3410 cm^{-1}, and δ(O-H) bending above 1390 cm^{-1} which additionally confirmed the occurrence of a hydroxy group in $CdSb_2O_3X(OH)$ (X = Br, I). All measurements were carried out in the manner described in Chapter 2.3.5.

Table 3.23.: Summary of modes occurring in IR spectra of structures representing the system $CdSb_2O_3X(OH)$ (X = Cl, Br, I).

$CdSb_2O_3Cl(OH)$		$CdSb_2O_3Br(OH)$		$CdSb_2O_3I(OH)$		Comments
Synthesis 1 (cm^{-1})	Synthesis 2 (cm^{-1})	Synthesis 1 (cm^{-1})	Synthesis 2 (cm^{-1})	Synthesis1 (cm^{-1})	Synthesis 2 (cm^{-1})	
130	129	130	129	126	128	ν(Cd-X)/(Sb-O) lattice vibrations
139	137	138	139	138	138	ν(Cd-X)/(Sb-O) lattice vibrations
146	146	146	155	147	150	ν(Cd-X)/(Sb-O) lattice vibrations
			173		171	δ(Sb-O) twisting
187	187	188	186	187	187	δ(Sb-O) twisting
208	200	200	207	206	206	δ(Sb-O) twisting
247		251	246	246	247	δ(Sb-O) scissoring
		295	291	291	291	ν(Cd-X)
				322	321	ν_{sym}(Sb-O)
				382	382	ν_{sym}(Sb-O)
394	395	395	394	393		ν(Cd-X)
447	442	449	446	449	449	ν_{sym}(Sb-O)/ν(Cd-O)
536	538	530	520	519	515	ν_{asym}(Sb-O)
624	587	618	608	603	600	ν_{asym}(Sb-O)
		665	640	651	654	ν_{asym}(Sb-O)
671	678					ν(Cd-Cl)
723	723	723	722	722	723	ν(Cd-X)
		810	807			ν(Sb-O)
834						ν(Sb-O)
860	859	860	859	861	859	ν(Cd-O)
1426	1419	1436	1411	1419	1399	δ(O-H) bending
3396		3417	3415	3436	3432	ν(O-H) streching
3522			3503		3559	ν(Cd-X)

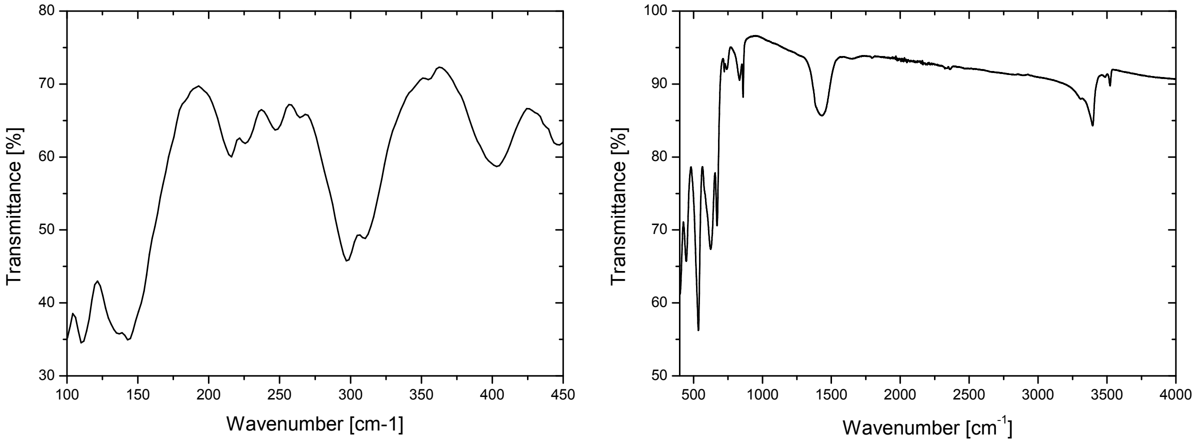

(a) CdSb$_2$O$_3$Cl(OH), F-IR **(b)** CdSb$_2$O$_3$Cl(OH), M-IR

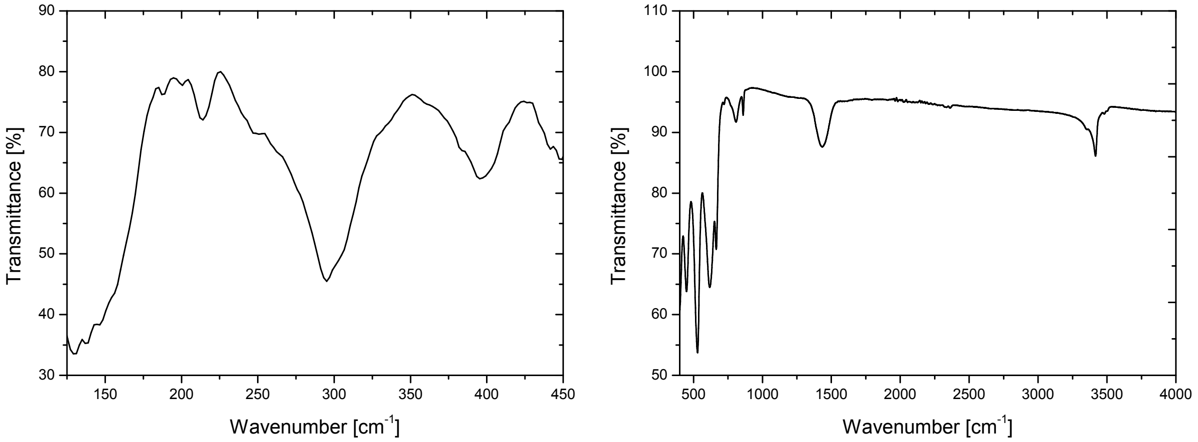

(c) CdSb$_2$O$_3$Br(OH), F-IR **(d)** CdSb$_2$O$_3$Br(OH), M-IR

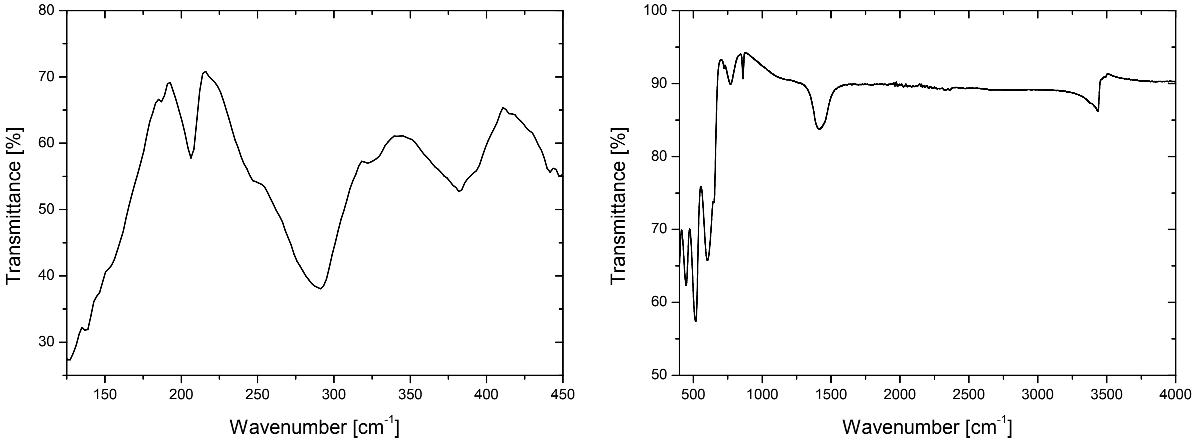

(e) CdSb$_2$O$_3$I(OH), F-IR **(f)** CdSb$_2$O$_3$I(OH), M-IR

Figure 3.59.: Infrared spectrum of CdSb$_2$O$_3$X(OH) according to synthesis method 1, showing significant vibrations only for $\nu_{\mathrm{Cd-O}}$, $\nu_{\mathrm{Sb-O}}$, $\nu_{\mathrm{Cd-X}}$, and $\nu_{\mathrm{O-H}}$.

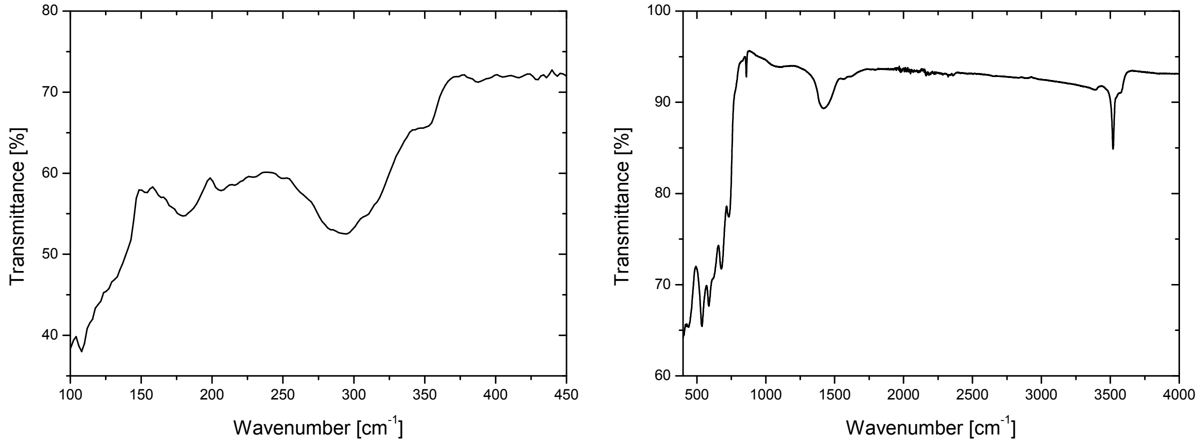

(a) $CdSb_2O_3Cl(OH)$, F-IR **(b)** $CdSb_2O_3Cl(OH)$, M-IR

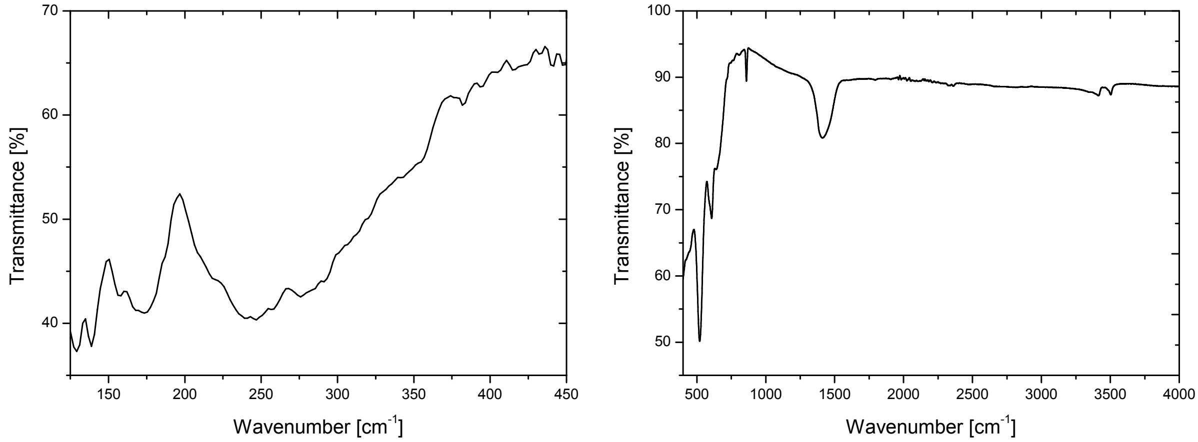

(c) $CdSb_2O_3Br(OH)$, F-IR **(d)** $CdSb_2O_3Br(OH)$, M-IR

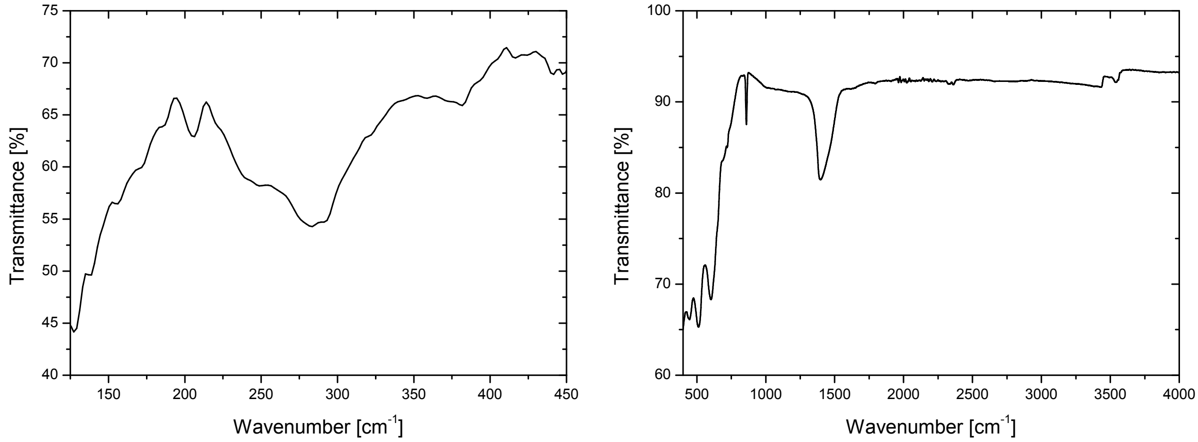

(e) $CdSb_2O_3I(OH)$, F-IR **(f)** $CdSb_2O_3I(OH)$, M-IR

Figure 3.60.: Infrared spectrum of $CdSb_2O_3X(OH)$ according to synthesis method 2, showing significant vibrations only for ν_{Cd-O}, ν_{Sb-O}, ν_{Cd-X}, and ν_{O-H}.

3.5. $Cd_2(OH)_3I$

3.5.1. Synthesis

Single crystals of new quaternary compound $Cd_2(OH)_3I$ were grown via hydrothermal reaction of CdO, SbI_3 and Sb_4O_6, mixed in the stoichiometric molar ratio 6:2:1. Reactants were placed into silica tubes with 3 ml of water. The mixture was subsequently frozen by using liquid nitrogen, evacuated, and hermetically closed. Reaction was carried out in a 40 ml Teflon-lined stainless steel autoclave at 90 °C for 5 days. After slow cooling, solid products were removed by filtration and cleaned with the aid of solvents such as water and ethanol. The synthesis products contained colourless crystals of $CdSb_2O_3I(OH)$, and $Cd_2(OH)_3I$, and a white powder which was identified by powder X-ray diffraction. According to structural data which resulted in obtaining $Cd_2(OH)_3I$, an attempt was made to synthesise this compound via hydrothermal reaction using $Cd(OH)_2$ and I_2 in a 4:1 molar ratio. Synthesis products contained numerous single crystals of the expected $Cd_2(OH)_3I$. Detailed information concerning phase analysis is presented in this chapter.

3.5.2. Single crystal and powder X-ray diffraction analysis

A single colourless, chunk-shaped crystal was fixed on top of a glass capillary and mounted on a STOE IPDS single ϕ-axis diffractometer using Mo-Kα radiation (λ = 0.71073 Å). The intensities of the reflections were integrated with the software *X-Area* [D]. Absorption correction were carried out numerically after crystal shape optimization using *X-RED* [L] and *X-SHAPE* [M]. Direct methods were applied to solve the structural model. Structure solution was performed using *SIR-92* [G]. It provided the positions of the two metal atoms, one I, and two O atoms. The positions of two hydrogen atoms were found in the electron density map. The refinement was performed by full matrix least squares on F^2 using *SHELXL-97* [J]. All atoms except hydrogens were refined with anisotropic displacement parameters. $Cd_2(OH)_3I$ crystallize orthorombically in the $Cu_2(OH)_3Cl$ structure type [127, 128, 129]. The compound is isotypic to previously reported $Cd_2(OH)_3Cl$ [130, 131]. Further information concerning the crystal structure solution and refinement data are presented in Table 3.24.

The structure of new $Cd_2(OH)_3I$ is a 3D network built by edge-sharing [Cd(1)O_5I] and [Cd(2)O_4I_2] octahedra, as shown in Figure 3.61. The [Cd(1)O_5I] octahedra, connected by common edges, build one-dimensional chains along [100] (Figure 3.62a). The edge-sharing [Cd(2)O_4I_2] units form chains extending in the [010] direction (Figure 3.62b). Those chains intertwine with each other perpendiculary and build puckered layers of octahedra with channels along [100] (Figure 3.63a) and [010] (Figure 3.63b).

Table 3.24.: Details of the data collection and results of the structure refinement for $Cd_2(OH)_3I$.

Crystal data	
Chemical formula	$Cd_2(OH)_3I$
Crystal colour/habit	colourless/chunk
Crystal size	$0.12 \times 0.15 \times 0.21$ mm
Molecular weight	288.31 g mol^{-1}
Calculated density	3.482 g cm^{-3}
Space group	$Pnma$ (No. 62)
Lattice parameters	$a = 6.9820(7)$ Å $b = 7.706(6)$ Å $c = 10.221(8)$ Å
Cell volume, Z	549.9(6) $Å^3$, 4
Data collection	
Device	STOE IPDS I
Radiation	Mo-Kα, 0.71073 Å graphite monochromator
Temperature	293(2)K
Scan range	$3.31° \leqslant 2\theta \leqslant 26.57°$
hkl range	$-8 \leqslant h \leqslant 8$ $-9 \leqslant k \leqslant 9$ $-12 \leqslant l \leqslant 12$
Structure solution and refinement	$Cd_2(OH)_3I$
Measured reflections	6776
Independent reflections	569
Independent reflections with $F_O > 4\sigma(F_O)$	540
R_{int}	0.0276
R_σ	0.0107
Structure solution	SIR-92[G]
Structure refinement	SHELXL97 [J]
Number of parameters	42
Absorption correction	numerical: X-RED [L], X-SHAPE [M]
Absorption coefficient	9.462 mm^{-1}
$R_1, wR_2[I > 3\sigma(I)]$	0.0162, 0.0346
R_1, wR_2[all reflections]	0.0179, 0.0350
GooF	1.191
F(000)	504
Residual electron density	0.646, -0.787 e $Å^{-3}$

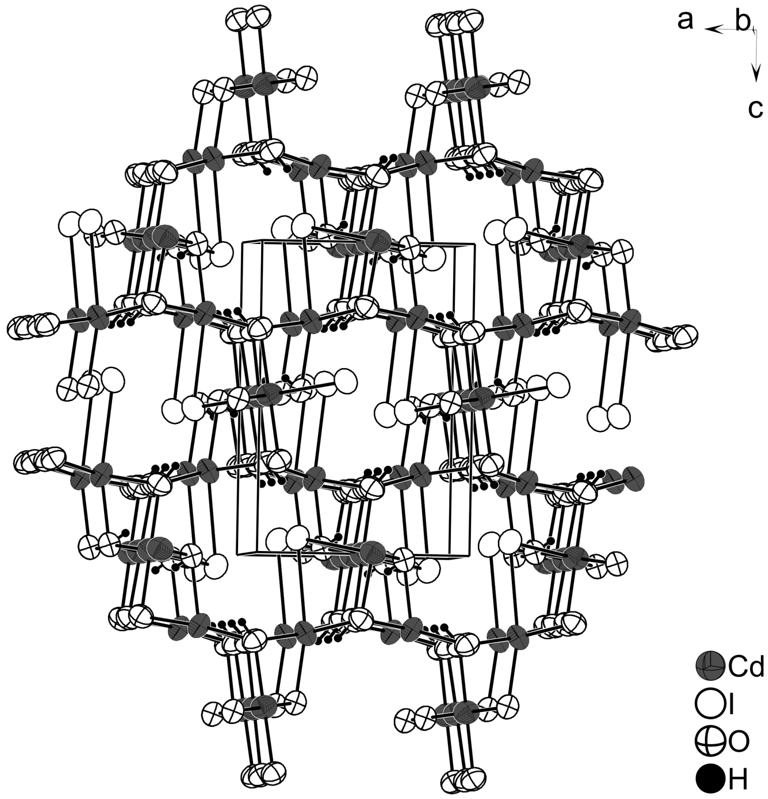

Figure 3.61.: Projection of the crystal structure of $Cd_2(OH)_3I$ emphasizing a 3D network with channels along [010]. (90% probability level).

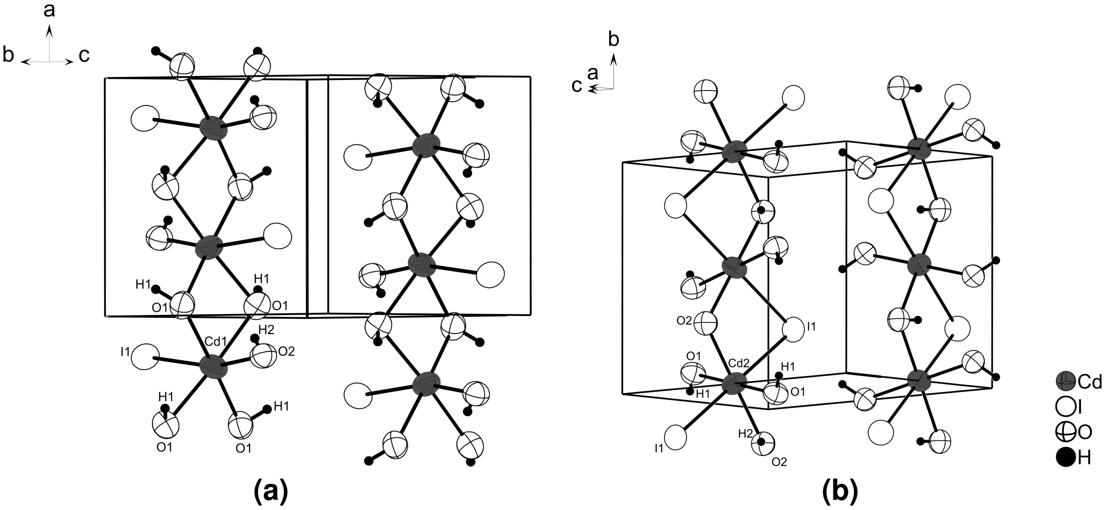

(a) (b)

Figure 3.62.: Projection of the edge-sharing $[Cd(1)O_5I]$ (a) and $[Cd(2)O_4I_2]$ (b) octahedra in $Cd_2(OH)_3I$ forming one-dimensional chains. (90% probability level).

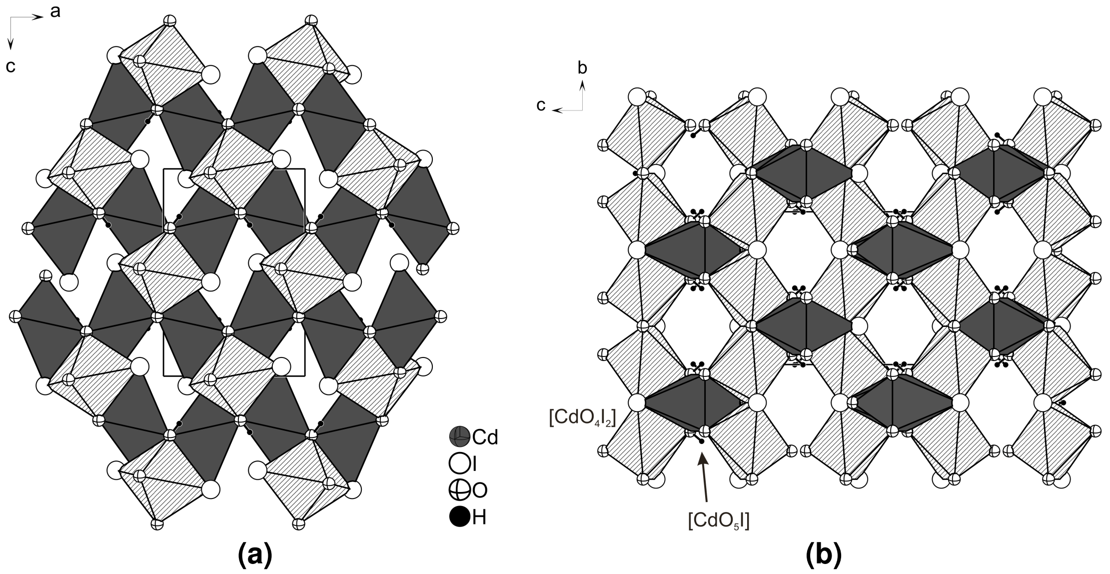

(a) (b)

Figure 3.63.: Projection of the edge-sharing [Cd(1)O_5I] and [Cd(2)O_4I_2] octahedra in $Cd_2(OH)_3I$ emphasizing chains of connected (a) [Cd(1)O_5I] and (b) [Cd(2)O_4I_2] octahedra. (90% probability level).

The average value of distances d(Cd-O) = 2.277 Å is in reasonable agreement with d(Cd-O) = 2.258 Å in $Cd_2(OH)_3Cl$ [130, 131]. All the Cd-O distances in $Cd_2(OH)_3I$ are in almost the same range as for previously reported compounds: d(Cd-O) = 2.185(8) Å ($CdSb_2O_6$ [132]), d(Cd-O) = 2.326 Å ($Cd_2O_7Sb_2$ [133]), and the average d(Cd-O) = 2.3065 Å ($Cd(IO_3)_2$ [134]). On the other hand, the average bond length d(Cd-I) = 3.084 Å is about 0.1-0.2 Å longer than the average d(Cd-I) = 2.985 Å in pure CdI_2 [135] and d(Cd-I) = 2.803 Å in $CdSb_2O_3I(OH)$, reported first in this thesis. The shortest cation-cation separation intra-layer are Cd1...Cd1 = 3.496(0) Å and Cd2...Cd2 = 3.853(3) Å. The coordination polyhedra for cadmium cations are presented in Figure 3.64. The calculations of effective coordination number performed using MAPLE [87, 88, 89] give the values ECoN (Cd1) = 5.9873 and ECoN (Cd2) = 5.9943, which additionaly confirmed the octahedral environment around the cadmium cations. The octahedral coordination with O and halide is common for Cd^{2+} [136,82,137,138]. Selected bond distances and angles are listed in Table 3.25. Two residual peaks at x=0.11095, y=0.49817, z=0.22947, and x=0.09557, y=0.25, z=0.55628 in the F_0-F_c map were attributed to the H1 and H2 atom positions, respectively. Positions of hydrogen atoms determined using X-ray diffraction do not coincide with real nuclei positions, because the electron density is significantly shifted in the direction of the atom which forms a covalent bond with the hydrogen atom. In order to find accurate location of hydrogen atoms, the application of the neutron diffraction measurement is required. The suspicion of O-H...I hydrogen bonds was excluded by attempting a bond length normalisation, involving extension of the bond length donor-proton to the average length of D-H designated from neutron diffraction measurement (O-H = 0.983 Å [121]). The use of standard procedures in *PLATON* [K] resulted in no discovery of classical hydrogen bonds. This result was additionaly confirmed by spectroscopic data for $Cd_2(OH)_3I$, where the O-H stretching mode occurs above 3500 cm^{-1}. According to Maltese *et al.* and Lutz *et al.* [119,120] the stretching vibrations of non-hydrogen-bonded hydroxide ions in O-H...X interactions have been found to vary from 3690 to 3500 cm^{-1}.

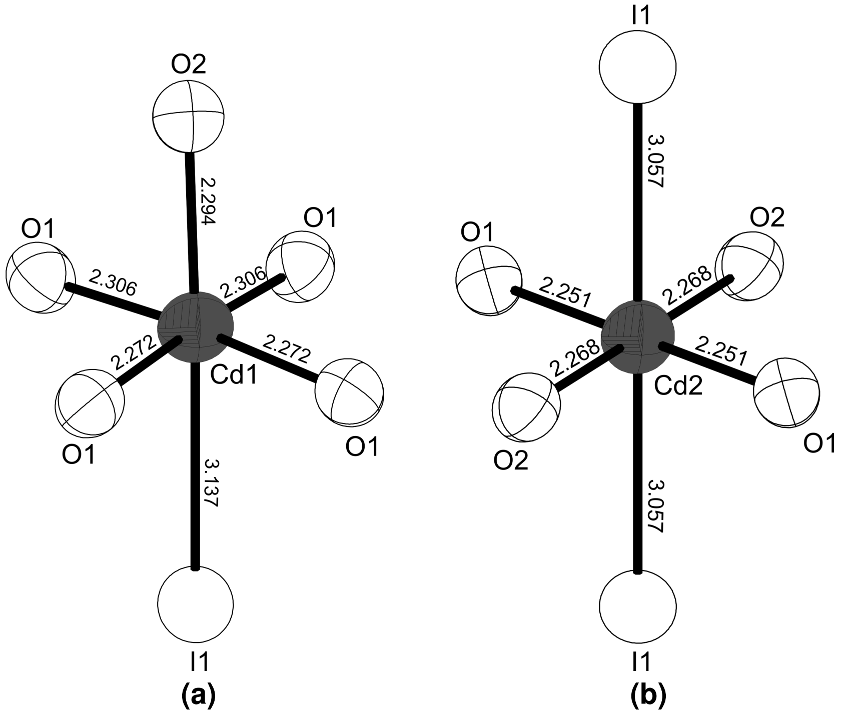

Figure 3.64.: Coordination of cadmium by five oxygens and one iodine atom resulting in $[Cd(1)O_5I]$ octahedra (a) and by four oxygens and two iodine atoms resulting in $[Cd(2)O_4I_2]$ octahedra (b). (90% probability level). All distances are given in Å .

The final composition of $Cd_2(OH)_3I$ was additionally confirmed by powder X-ray diffraction measurement. For samples resulting from hydrothermal synthesis of CdO, SbI_3 and Sb_4O_6, mixed in the stoichiometric molar ratio 6:2:1, the cell ($Pnma$, a = 6.982(7) Å, b = 7.706(6) Å, c = 10.221(8) Å) was determined on the basis of 76 reflections. Powder X-ray diffraction analysis of samples resulting from an attempt to synthesise $Cd_2(OH)_3I$ as a single phase, by hydrothermal reaction of $Cd(OH)_2$ and I_2 in a 4:1 molar ratio, reveal the presence of the additional crystalline product $Cd_7(OH)_{10}I_4$. On the basis of 61 reflections the cell ($Pnma$, $a = 6.982(1)$ Å, $b = 7.699(1)$ Å, $c = 10.228(2)$ Å) was determined. All data concerning powder X-ray diffraction analysis of $Cd_2(OH)_3I$ are presented in the appendix in Figures B.36-B.39.

Table 3.25.: Selected interatomic distances (in Å) and angles (in degrees) for $Cd_2(OH)_3I$ at room temperature, symmetry codes: (i) -x, y-0.5, -z+1;

Cd(1)-O(1)	2x	2.271(2)	O(1)-Cd(1)-O(1)		77.90(1)
Cd(1)-O(2)		2.293(4)	O(1)-Cd(1)-O(2)	2x	107.80(9)
Cd(1)-O(1)^{i}	2x	2.308(2)	O(1)-Cd(1)-O(1)	2x	174.74(4)
Cd(1)-I(1)		3.138(2)	O(1)-Cd(1)-O(1)	2x	102.58(1)
			O(2)-Cd(1)-O(1)	2x	77.12(9)
			O(1)-Cd(1)-O(1)		76.46(1)
			O(1)-Cd(1)-I(1)	2x	82.31(6)
			O(1)-Cd(1)-I(1)	2x	92.54(6)
			O(2)-Cd(1)-I(1)		166.75(9)
Cd(2)-O(1)	2x	2.252(3)	O(1)-Cd(2)-O(1)	2x	180.00(1)
Cd(2)-O(2)	2x	2.269(2)	O(1)-Cd(2)-O(2)	2x	78.76(1)
Cd(2)-I(1)	2x	3.057(1)	O(1)-Cd(2)-O(2)		101.24(1)
			O(1)-Cd(2)-I(1)	2x	95.949(6)
			O(1)-Cd(2)-I(1)	2x	84.51(6)
			O(2)-Cd(2)-I(1)	2x	97.22(8)
			O(2)-Cd(2)-I(1)	2x	82.78(8)
			I(1)-Cd(2)-I(1)		180.000(7)

3.5.3. Raman and infrared spectroscopy

The Raman spectrum of $Cd_2(OH)_3I$ was recorded in the 130-4000 cm^{-1} wavenumber range at a resolution of 2 cm^{-1}. The Raman spectrum of $Cd_2(OH)_3I$ exhibits vibrations at 235, 730 cm^{-1}, which can be attributed to $\nu_{\mathrm{Cd-I}}$ [98, 99, 126] and at 314, 341, 382, 398, 683, 764 cm^{-1} for $\nu_{\mathrm{Cd-O}}$ [97]. The frequencies which can be attributed to O-H stretching vibrations occur at 3540 and 3548 cm^{-1}.

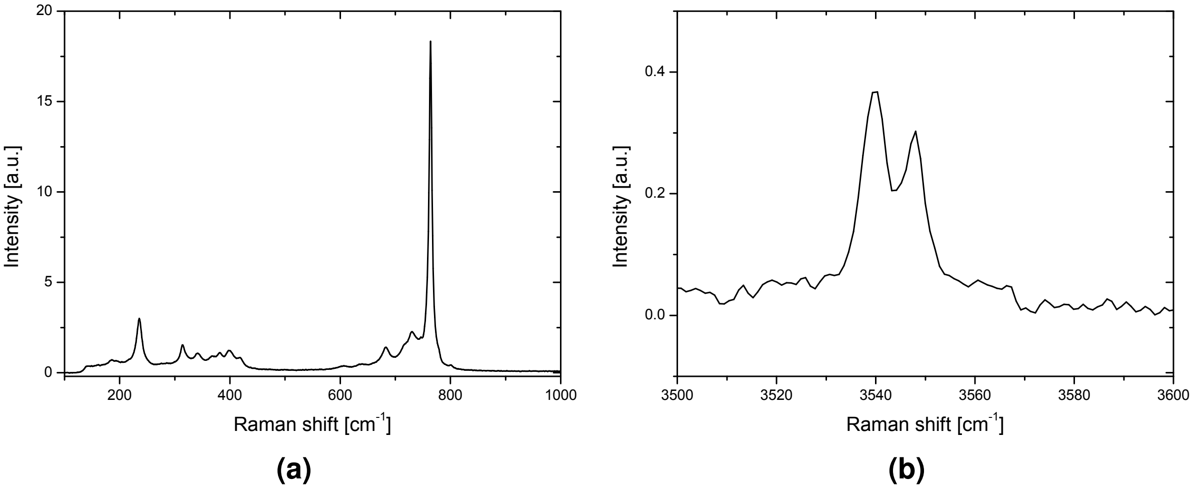

Figure 3.65.: Raman spectrum of $Cd_2(OH)_3I$ showing significant vibrations only for $\nu_{\mathrm{Cd-O}}$, $\nu_{\mathrm{Cd-I}}$ and $\nu_{\mathrm{O-H}}$

In order to confirm the presence of hydroxy group the infrared spectrum of $Cd_2(OH)_3I$ was recorded, using the ATR technique. Analysis of FTIR spectra was performed using *Resolution Pro* [T]. IR measurement was performed in the ranges 120-400 cm^{-1} (F-IR) and 400-4000 cm^{-1} (M-IR). Table 3.26 presents a comparison of Raman and IR spectral data for $Cd_2(OH)_3I$.

An exact identification of the modes in the Raman and IR spectra can only be carried out by way of a theoretical calculation of the Raman spectra based on the extracted crystal structures. These calculations will be one of the goals of future work in this area.

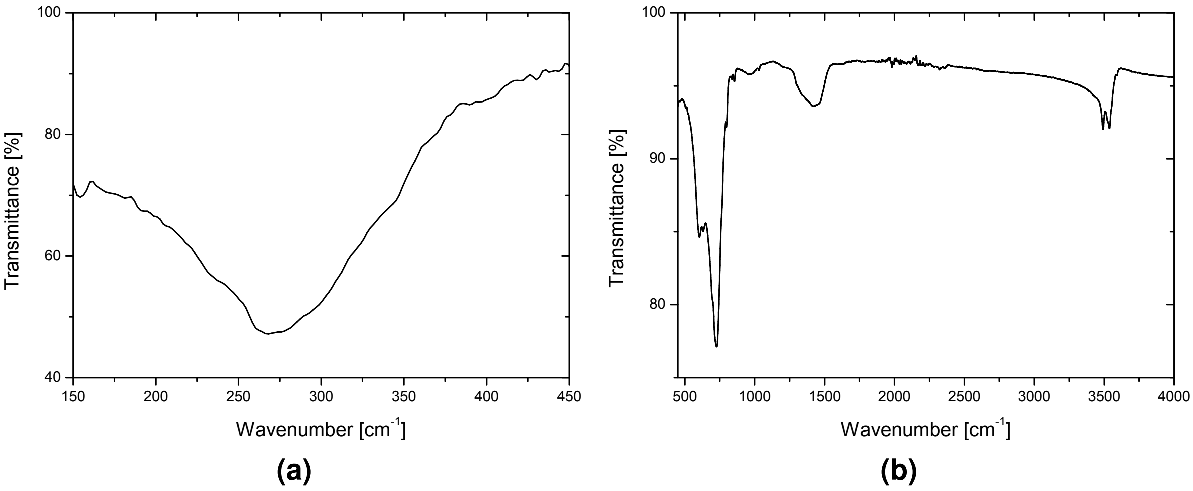

Figure 3.66.: F-IR and M-IR spectra of $Cd_2(OH)_3I$ showing significant vibrations only for ν_{Cd-O}, ν_{Cd-I} and ν_{O-H}.

Table 3.26.: Summary of modes occurring in Raman and IR spectra of $Cd_2(OH)_3I$.

Raman (cm^{-1})	IR (cm^{-1})	Comments
	154	ν(Cd-I)
235		ν(Cd-I)
	268	
314		ν(Cd-O)
341		ν(Cd-O)
382		ν(Cd-O)
398		ν(Cd-O)
	603	ν(Cd-O)
	630	
683		ν(Cd-O)
730	743	ν(Cd-I)
764		ν(Cd-O)
	799	
	838	ν(Cd-O)
	855	ν(Cd-O)
	1422	δ(O-H)bending
3540	3492	ν(O-H) stretching
3548	3538	ν(O-H) stretching

3.6. $CdSbO_2X$ (X = Cl, Br)

Compounds with the composition $MPnQ_2X$ (M = transition metal or alkaline-earth metal, Pn = Sb or Bi; Q = O, S, Se; X = Cl, Br, or I) have been investigated in recent years. The most prevalent examples of layered materials are compounds contain manganese and iron for the sake of interesting magnetic properties. Those compounds can be divided into two groups. The first group consists of isotypic compounds $MnSbSe_2I$ [139, 140], which are a distorted variant of the orthorhombic $UFeS_3$ [141] structure type, $MnBiSe_2I$ [142], $MnBiS_2Br$ [143], and $MnSbS_2Br$ [140] crystallize in the monoclinic system. In this crystal structure type, manganese adopts two types of octahedral environments $[MnQ_2X_4]$ and $[MnQ_6]$, whereas Bi and Sb atoms are located within a distorted bi-capped trigonal prism (5Q + 3X), where a pnicogen atom is exclusively coordinated to a chalcogen atom in its first coordination sphere. The second group of isotypic compounds containing managanese and crystallizing in orthorhombic symmetry are: $MnSbS_2Cl$ [144], $MnBiS_2Cl$ [145], $MnSbSe_2Br$ and $MnBiSe_2Br$ [140]. They consists of edge-sharing metal-centred octahedra $[MnQ_4X_2]$, and of Bi or Sb atoms presenting a (5Q + 3X) coordination. A mineral-related group of compounds containing iron is berthierite $FeSb_2S_4$ [146]. The next group of layered materials are mixed-framework chalcohalide semiconductors, containing cadmium [147]. These include the compounds represented by the systems: $CdSbS_2X$ (X = Cl, Br), $CdBiS_2X$ (X = Cl, Br), and $CdBiSe_2X$ (X = Br, I), which crystallize in an orhthorombic or monoclinic crystallographic system depending upon the combination of chalcohalide anions. The orthorhombic structure adopted by sulfochlorides and selenobromides contains $[CdQ_4X_2]$ octahedra, while sulfobromides and selenoiodides crystallized in the monoclinic system consist of both $[CdQ_6]$ and $[CdQ_2X_4]$ octahedra.

A variety of complete ordering of the M^{2+} and Pn^{3+} cations contributing to the fluorite layers is demonstrated by the family of oxyhalides with divalent elements $M^{II}PnO_2X$ (M^{II} = Ca, Sr, Ba, Cd; Pn = Sb, Bi). The first members of those compounds is the Sillén series of layered bismuth-based oxyhalides. Their crystal structures can be regarded as $[M_2O_2]^+$ slices and single $[X]^-$, double $[X_2]^-$, or triple $[M'_xX_3]^-$ halide layers, which occur in such compounds that crystallise in a tetragonal crystallographic system: $CaBiO_2Br$ [148], $CaBiO_2I$ [149], $BaBiO_2Cl$ [149, 150, 151], $BaBiO_2Br$ [149, 150], $CdBiO_2Br$ [152], $CdBiO_2I$ [153]. Several years later bismuth oxychloride and oxybromide containing a Ba^{2+} cation were found to be orthorhombic [149, 154], not tetragonal as reported orginally by Sillén in 1941. Inclination to deviations from an idealized tetragonal structure arise from cation-side ordering and size. The larger Sr^{2+} and Ba^{2+} result in the orthorhombic superstructure found for $SrBiO_2X$ (X = Cl, Br, I) [155] and $BaBiO_2I$ [149], while the smaller Ca^{2+} and Cd^{2+} yield a monoclinic structure for compounds $CaBiO_2Cl$ [155] and $CdBiO_2Cl$ [156]. The next group of compounds investigated since 1941 are minerals and synthetic materials containing lead. The natural mineral perite $PbBiO_2Cl$ [157] crystallises in the orthorhombic structure, coresponding to isotypic mineral nadorite $PbSbO_2Cl$ [158]. However, all synthetic homologues of perite and nadorite are always tetragonal, as discussed in [159, 160]. They typically crystallise in the anti-$ThCr_2Si_2$ structure with lead and pnicogen atoms statistically disordered on one common position. The result of ongoing investigations in this area is a new group of synthetic compounds containing As, Sb, or Bi as the pnicogen atom [161]. Their crystal structures typically consist of metal oxide substructures with halide ions between them. Those compounds are attractive in advanced materials research due to their semiconducting properties [160, 161].

Following the family of numerous compounds with composition $MPnQ_2X$ (M = transition metal or alkaline-earth metal, Pn = Sb or Bi; Q = O, S, or Se; X = Cl, Br, or I) this chapter reports on the synthesis, single crystal X-ray analysis, and optical band gap determination of new cadmium antimony-based oxyhalides.

Table 3.27.: Overview of compounds representing the system $MPnQ_2X$ (M = transition metal or alkaline-earth metals, Pn = Sb or Bi; Q = O, S, or Se; X = Cl, Br, or I). Compounds marked with * are new compounds synthesised and investigated in this work.

Compound	Space group	a	b	c	β
$PbSbO_2Br$ [160]	$I4/mmm$	3.9463(3)	3.9463(3)	12.8487(12)	
$PbSbO_2I$ [160]	$I4/mmm$	4.0073(3)	4.0074(3)	13.6269(15)	
$PbBiO_2Cl$ [157]	$Bmmb$	5.627(50)	5.575(20)	12.425(90)	
$PbBiO_2Br$ [160]	$I4/mmm$	3.9818(4)	3.9818(4)	12.7655(16)	
$CaBiO_2I$ [149]	$I4/mmm$	4.01943(4)	4.01943(4)	13.2144(1)	
$BaBiO_2Cl$ [149, 150, 151]	$I4/mmm$	4.019	4.019	12.98	
$BaBiO_2Br$ [149, 150]	$I4/mmm$	4.068	4.068	13.20	
$CdBiO_2Br$ [152]	$I4/mmm$	3.943	3.943	12.62	
$CdBiO_2I$ [153]	$I4/mmm$	3.97	3.97	13.24	
$FeSbS_2Cl$ [162]	$Cmcm$	3.731(8)	12.371(2)	9.459(2)	
$FeSbSe_2Br$ [162]	$Cmcm$	3.903(7)	12.960(2)	9.897(2)	
$PbSbO_2Cl$ [158]	$Cmcm$	5.603(5)	12.245(8)	5.448(7)	
$BaSbO_2Cl$ [163]	$Cmcm$	5.849(3)	12.793(6)	5.514(2)	
$BaBiO_2Cl$ [151]	$Cmcm$	5.880(4)	12.945(18)	5.677(3)	
$BaBiO_2I$ [149]	$Cmcm$	6.0492(1)	14.0224(2)	5.8212(1)	
$SrBiO_2Cl$ [155]	$Cmcm$	5.7109(2)	12.4081(5)	5.5888(2)	
$SrBiO_2Br$ [155]	$Cmcm$	5.7676(1)	12.8246(4)	5.6460(1)	
$SrBiO_2I$ [155]	$Cmcm$	5.8723(1)	13.5344(2)	5.7363(1)	
$FeSbS_2Br$ [162]	$C2/m$	12.560(2)	3.809(5)	9.497(19)	91.52(2)
$MnSbS_2Br$ [140]	$C2/m$	12.669(3)	3.851(8)	9.585(2)	91.00(3)
$MnBiS_2Br$ [143]	$C2/m$	12.767(2)	3.947(4)	9.574(1)	90.87(2)
$MnSbSe_2I$ [139, 140]	$C2/m$	13.319(3)	4.036(8)	10.105(2)	91.27(3)
$MnBiSe_2I$ [142]	$C2/m$	13.428(2)	4.112(1)	10.130(2)	90.97(2)
$CdSbS_2Br$ [147]	$C2/m$	12.938(3)	3.931(8)	9.661(19)	91.11(3)
$CdBiS_2Br$ [147]	$C2/m$	12.977(3)	4.0120(8)	9.584(2)	91.07(3)
$CdBiSe_2I$ [147]	$C2/m$	13.659(3)	4.192(8)	10.193(2)	90.88(3)
$MnBiS_2Cl$ [145]	$Pnma$	9.502(2)	3.8802(8)	12.305(3)	
$MnSbS_2Cl$ [144]	$Pnma$	9.535(2)	3.816(8)	12.245(2)	
$MnBiSe_2Br$ [140]	$Pnma$	9.995(2)	4.028(8)	12.928(3)	
$MnSbSe_2Br$ [140]	$Pnma$	10.005(2)	3.972(8)	12.871(3)	
$CdBiS_2Cl$ [147]	$Pnma$	9.541(2)	3.970(8)	12.545(3)	
$CdSbS_2Cl$ [147]	$Pnma$	9.585(2)	3.991(8)	12.443(3)	
$CdBiSe_2Br$ [147]	$Pnma$	10.025(2)	4.119(8)	13.143(3)	
$CdSbO_2Br$ *	$Pnma$	15.8770 (1)	4.0850 (3)	12.2340 (1)	
$CaBiO_2Cl$ [157]	$P2_1/m$	7.7311(1)	4.1234(1)	6.3979(2)	105.215
$CdBiO_2Cl$ [156]	$P2_1/m$	7.5878(7)	4.1397(4)	6.0594(6)	101.529(11)
$CdSbO_2Cl$*	$P2_1/m$	7.5668(1)	3.9846(7)	6.0869(1)	103.617(1)

$CdSbO_2Cl$

3.6.1. Synthesis

Colourless single crystals of new quaternary compound $CdSbO_2Cl$ were obtained in a similar way as in the case of $CdSbO_2Br$, by prereacting a mixture of CdO, $SbCl_3$ and Sb_4O_6 in a 6:2:1 molar ratio in water for one week at 90 °C. After hydrothermal reaction the precipitate was filtrated, dried, and annealed in an Al_2O_3 crucible at 600°C for 14 days.

3.6.2. Single crystal analysis and powder X-ray diffraction

The crystal structure was determined from a colourless needle-shaped crystal using single crystal X-ray diffraction measurement at room temperature. Solution of the structural model was performed using the program *SIR-92* [G] and refined using *SHELXL-97* [J]. The compound crystallizes in the monoclinic system, space group $P2_1/m$ (No. 11) with Z = 2, $a = 7.5662(2)$ Å, $b = 3.9838(1)$ Å, $c = 6.0864(2)$ Å, and $\beta = 103.604(2)°$. The refinement converged at $R_1, wR_2[I > 3\sigma(I)] = 0.0180, 0.0451$ and $R_1, wR_2[alldata] = 0.0203, 0.0458$. Further information concerning the crystal structure solution and refinement data is presented in Table 3.28. Final atomic coordinates and equivalent isotropic displacement parameters for $CdSbO_2Cl$ are listed in the appendix in Table B.23, while Table B.24 includes anisotropic displacement parameters.

The final composition of $CdSbO_2Cl$ was additionally analized by X-ray powder diffraction. On the basis of 97 reflections the cell ($P2_1/m$, $a = 7.5662(2)$ Å, $b = 3.9838(1)$ Å, $c = 6.0864(2)$ Å, $\beta = 103.604(2)°$) was determined. Comparison of the 28 unindexed lines to reference patterns from the PDF database resulted in the identification of the additional crystalline products $Sb_8O_{11}Cl_2$, CdO and $Sb_4O_5Cl_2$. Details concerning powder X-ray analysis of $CdSbO_2Cl$ sample are presented in the appendix (Figure B.40, B.41).

The crystal structure of new quaternary compound $CdSbO_2Cl$ consists of puckered layers of edge-sharing [CdO_3Cl_3] octahedra, perpendicular to the [100] direction. The layers are connected to one another by one-dimensional polymers built by edge-sharing [SbO_4] square pyramids. The crystal structure is a 3D network with channels along the b axis. The general network is shown in Figure 3.67 by the projection onto the [010] plane. The $5s^2$ lone pairs of the Sb^{3+} cations are directed to the interior of channels.

The Cd^{2+}, three-coordinated by oxygens and three-coordinated by chlorine atoms (as seen in Figure 3.68), are connected by sharing common equatorial edges and forming compact layers extending in the bc plane, as seen in Figure 3.69 and Figure 3.70. The average distances d(Cd-O) = 2.2906 Å and are in reasonable agreement with

Table 3.28.: Details of the data collection and results of the structure refinement for $CdSbO_2Cl$.

Crystal data		
Chemical formula	$CdSbO_2Cl$	
Crystal colour/habit	colourless/needle	
Crystal size	0.18 × 0.08× 0.03 mm	
Molecular weight	301.60 g mol^{-1}	
Calculated density	5.617 g cm^{-3}	
Space group	$P2_1/m$ (No. 11)	
Lattice parameters	$a = 7.5662(2)$ Å	
	$b = 3.9838(1)$ Å	$\beta = 103.604(2)°$
	$c = 6.0864(1)$ Å	
Cell volume, Z	178.31(5) $Å^3$, 2	
Data collection		
Device	STOE IPDS I	
Radiation	Mo-Kα, 0.71073 Å	
	graphite monochromator	
Temperature	293(2)K	
Scan range	$2.77° \leqslant 2\theta \leqslant 26.67°$	
hkl range	$-9 \leqslant h \leqslant 9$	
	$-4 \leqslant k \leqslant 4$	
	$-7 \leqslant l \leqslant 7$	
Structure solution and refinement	$CdSbO_2Cl$	
Measured reflections	2713	
Independent reflections	425	
Independent reflections with $F_O > 4\sigma(F_O)$	393	
R_{int}	0.0231	
R_σ	0.0120	
Structure solution	SIR-92 [G]	
Structure refinement	SHELXL97 [J]	
Number of parameters	32	
Absorption correction	numerical: X-RED [L], X-SHAPE [M]	
Absorption coefficient	14.064 mm^{-1}	
$R_1, wR_2[I > 3\sigma(I)]$	0.0180, 0.0451	
R_1, wR_2[all reflections]	0.0203, 0.0458	
GooF	1.228	
Residual electron density	0.753, -1.137 e $Å^{-3}$	

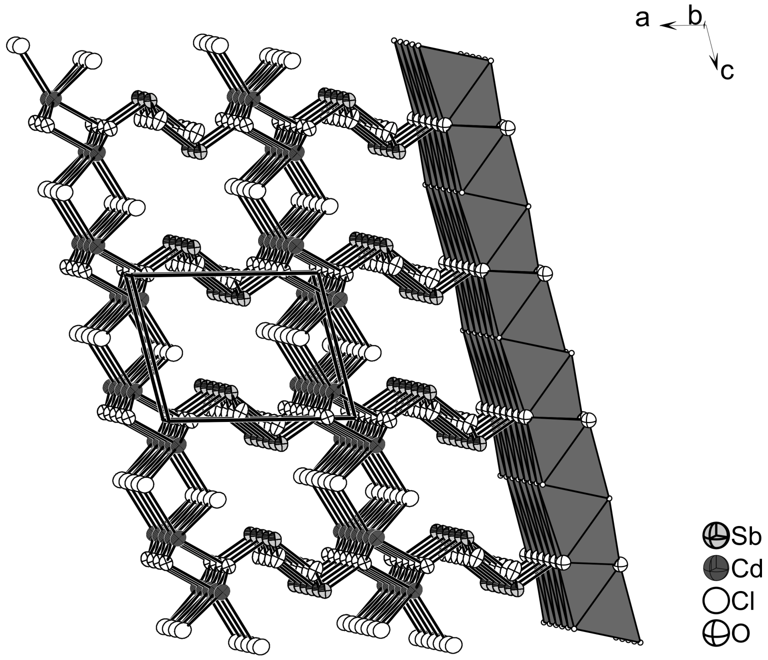

Figure 3.67.: Projection of of the crystal structure of $CdSbO_2Cl$ emphasizing the puckered layers of edge-sharing octahedra $[CdO_3Cl_3]$ connected by one-dimensional polymers $^{1}_{\infty}[SbO_2^-]$ forming channels along [010]. (90% probability level).

2.348 Å in pure CdO [90]. On the other hand, the average *d*(Cd-Cl) distance equaling 2.8054 Å are about 0.2 Å longer than 2.637 Å in pure $CdCl_2$ [84]. More details concerning bond distances and angles within the octahedra $[CdO_3Cl_3]$ are presented in Table 3.29. The octahedral coordination of cadmium was additionally confirmed by calculations of effective coordination number using MAPLE [87, 88]. The $ECoN(Cd^{2+}/O^{2-}/Cl^-) = 5.9$, indicating that the cadmium atom is six-coordinated. The shortest cation-cation distances within the layer amounts to 3.367(1) Å.

Table 3.29.: Selected interatomic distances (in Å) and angles (in degrees) for $CdSbO_2Cl$ at room temperature.

Cd(1)-O(1)	2x	2.2715(2)	O(1)-Cd(1)-O(1)	2x	85.89(9)
Cd(1)-O(1)		2.329(2)	O(1)-Cd(1)-Cl(1)	2x	74.41(8)
Cd(1)-Cl(1)	2x	2.9369(1)	O(1)-Cd(1)-Cl(1)	2x	79.74(7)
Cd(1)-Cl(1)		2.5423(2)	Cl(1)-Cd(1)-Cl(1)	2x	78.78(4)
			Cl(1)-Cd(1)-Cl(1)		85.41(4)
			O(1)-Cd(1)-Cl(1)	2x	107.20(8)
			O(1)-Cd(1)-Cl(1)		150.61(9)
			O(1)-Cd(1)-Cl(1)	2x	157.05(8)
			O(1)-Cd(1)-Cl(1)		122.55(2)

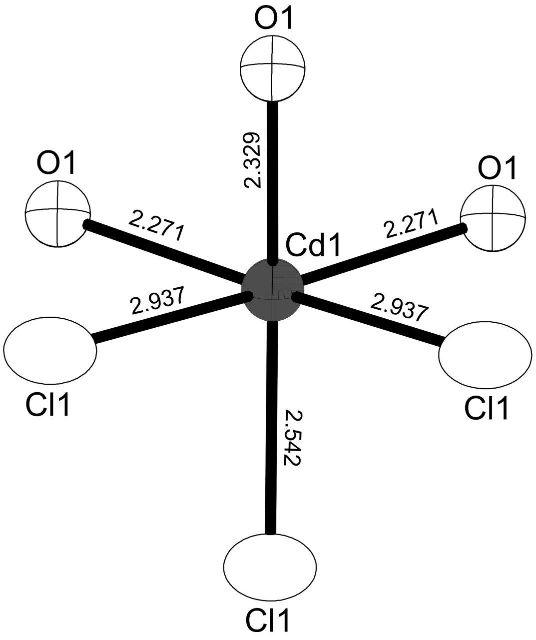

Figure 3.68.: Coordination geometry about Cd1 atom resulting in $[CdO_3Cl_3]$ octahedra. All bond distances are given in Å. (90% probability level)

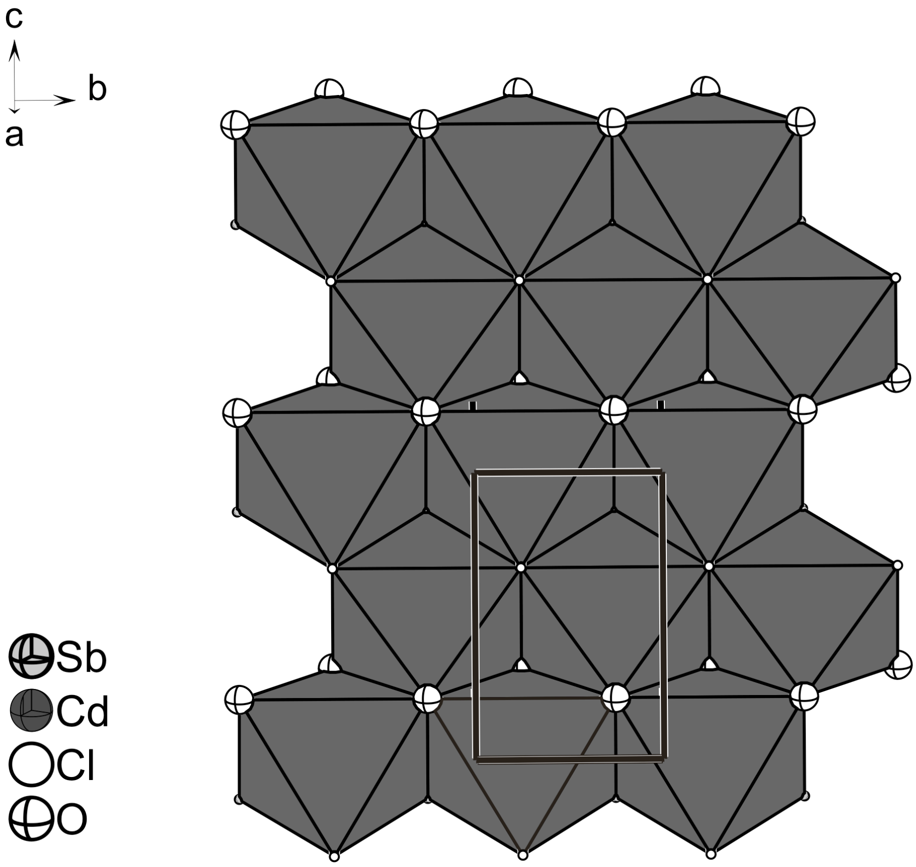

Figure 3.69.: Projection of a layer extending in the *bc* plane, distinguishing blocks of edge-sharing octahedra $[CdO_3Cl_3]$.

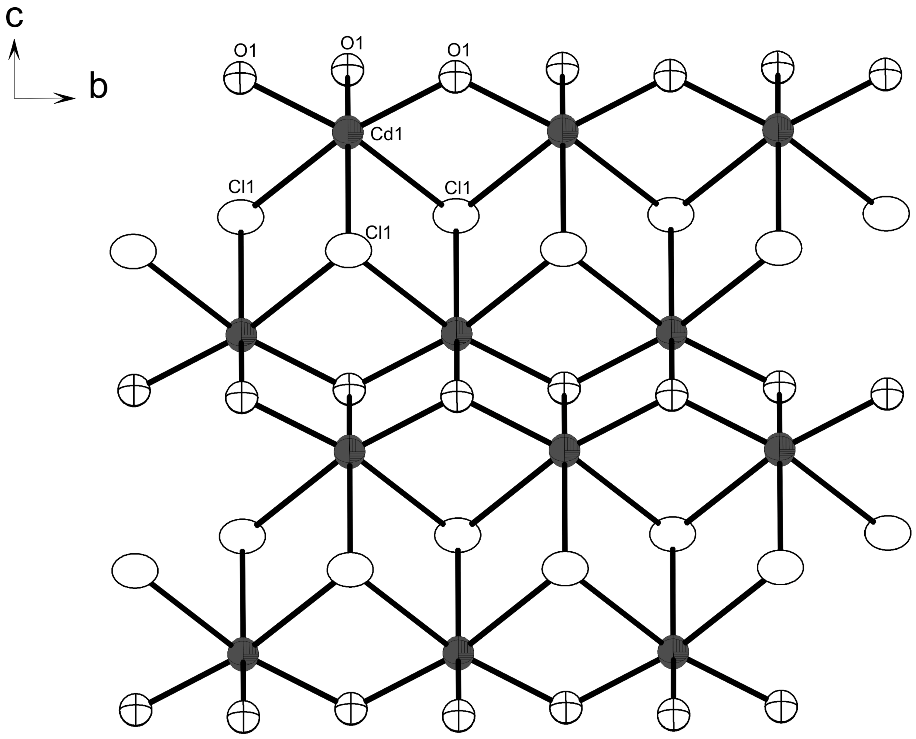

Figure 3.70.: Projection of the edge-sharing distorted [CdO_3Cl_3] octahedra. (90% probability level).

The antimony cations exhibit a regular one-sided four-fold coordination to oxygen atoms. Asymmetric coordination occurs due to the presence of lone pairs of $5s^2$ electrons, designed as E. The coordination polyhedron is a $[SbO_4]$ square pyramid or a $[SbO_4E]$ tetrahedron when the stereochemically active $5s^2$ is also taken into account. All polyhedra are connected, sharing common edges and forming one-dimensional $^1_\infty[SbO_2^-]$ polymers along the [010] crystallographic direction, as shown in Figure 3.71. The analysis of Sb-O bonding distances in the range 1.978(3)-2.1515(2) Å and O -Sb-O angles varying between 71.61(8)-83.96(1)° and 107.26(2)-135.58(2)° suggests slightly distorted polyherda. The average d(Sb-O) distance of 2.0903 Å is in reasonable agreement with the bond length d(Sb-O) = 1.9779 Å in senarmontite [104, 68] and with the average bond length d(Sb-O) = 2.0059 Å in valentinite [69, 70]. This type of Sb^{3+} coordination has previously been observed in $BaSbO_2Cl$ [163], $PbSbO_2Cl$ [158, 164], and in the crystal structure of $CdSbO_2Br$, first reported in this thesis.

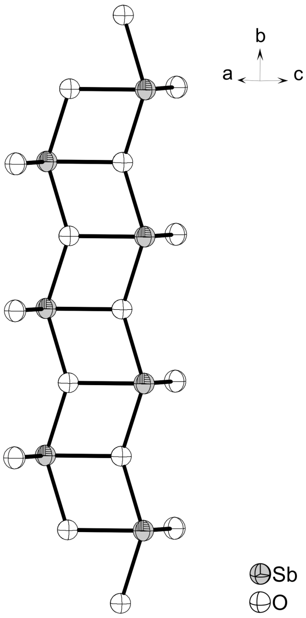

Figure 3.71.: Projection of Sb^{3+} cations four-coordinated by oxygen, forming one-dimensional polymers $^1_\infty[SbO_2^-]$.

The extended structure can be considered as parallel $^2_\infty[CdOCl]^-$ slabs interlinked by polymers of four-coordinated Sb^{3+} cations, as shown in Figure 3.72. The Sb^{3+} cations interconnect the close-shell, semiconducting $^2_\infty[CdOCl]^-$ slabs to maintain charge balance.

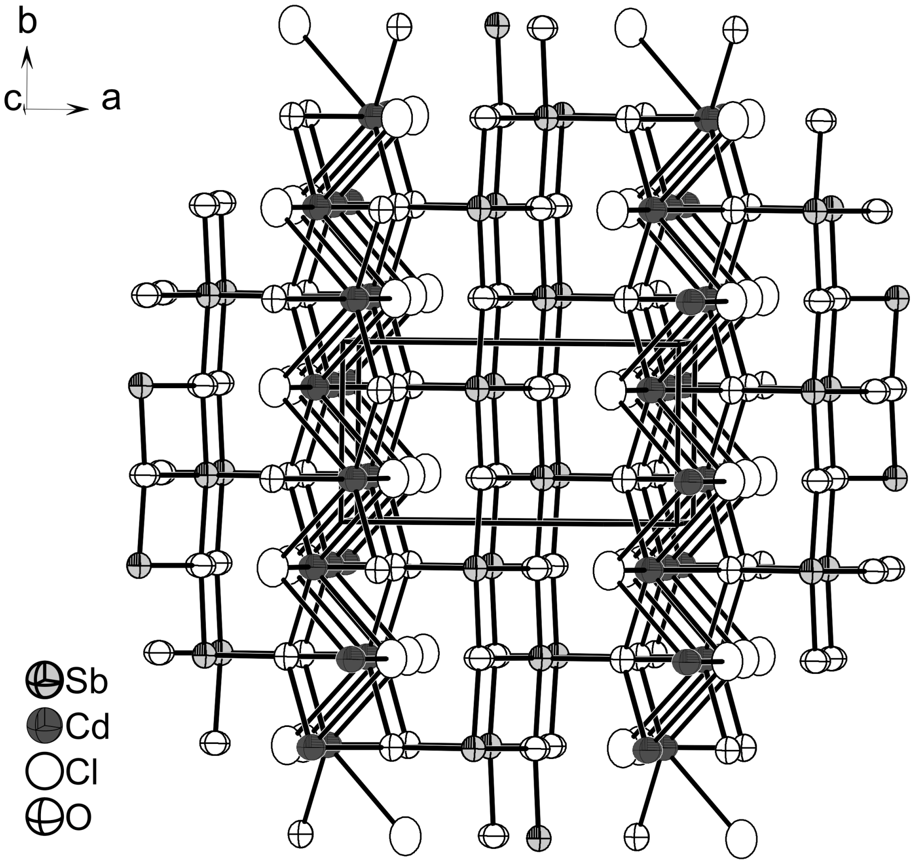

Figure 3.72.: Projection of $CdSbO_2Cl$ emphasizing the puckered layers of parallel $^{2}_{\infty}[CdOCl]^{-}$ slabs interlinked by polymers of four-coordinated pnicogen cations.

3.6.3. Raman spectroscopy

The Raman spectrum of $CdSbO_2Cl$ was recorded in the wavenumber range of 130-4000 cm^{-1} at a resolution of 2 cm^{-1}. It was possible to identify 12 modes in the frequency range of 100-705 cm^{-1}, as seen in Figure 3.73. The modes exhibit clear vibrations at 141, 156, 166, and 228 cm^{-1} for $\nu_{\mathrm{Cd-Cl}}$ [98, 99, 100, 101], and at 773 cm^{-1} for $\nu_{\mathrm{Cd-O}}$ [97]. The peaks which can be attributed to the Sb-O lattice vibrations [77, 78, 102, 103] occur at 182, 202, 295, 331, 373, 553, and 620 cm^{-1}. One weak band at 702 cm^{-1} could not be identified.

An exact identification of the peaks in the Raman spectra can only be carried out by way of a theoretical calculation of the Raman spectra based on the extracted crystal structures. These calculations will be one of the goals of future work in this area.

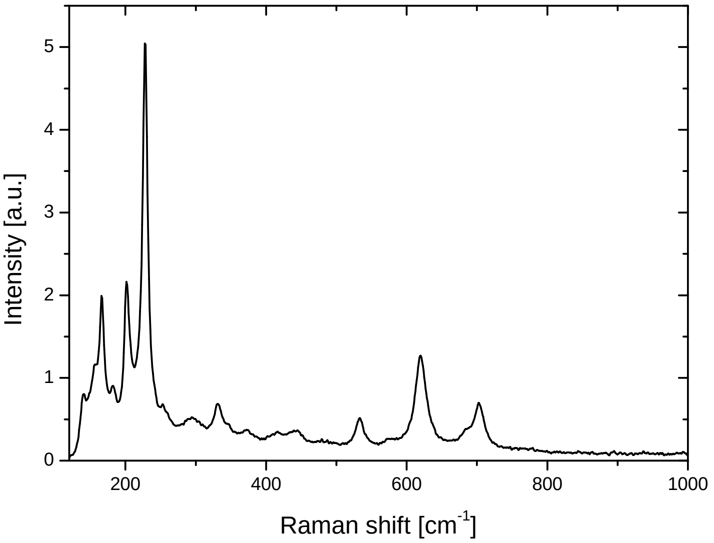

Figure 3.73.: Raman spectrum of $CdSbO_2Cl$ showing significant vibrations only for $\nu_{\mathrm{Sb-O}}$, $\nu_{\mathrm{Cd-Cl}}$ and $\nu_{\mathrm{Cd-O}}$

The infrared spectrum of $CdSbO_2Cl$ was recorded using the ATR technique, on a diamond crystal sampling area, located in the center of the plate. Analysis of FT-IR spectra were performed using *Resolution Pro* [T]. IR measurement was performed in range 130-400 cm^{-1} (F-IR) and 400-4000 cm^{-1} (M-IR) with resolution 2 cm^{-1} and in the range 120-400 cm^{-1} (F-IR) with 4 cm^{-1} resolution. Table 3.30 presents a comparison of Raman and IR spectral data for $CdSbO_2Cl$.

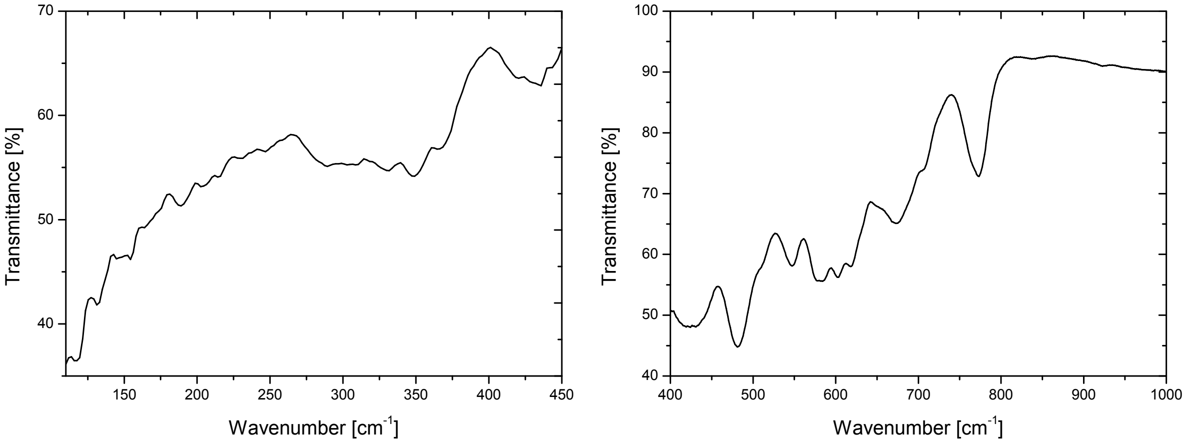

(a) (b)

Figure 3.74.: F-IR and M-IR spectra of $CdSbO_2Cl$ showing significant vibrations only for ν_{Sb-O}, ν_{Cd-Cl} and ν_{Cd-O}. There were no vibrations in range 1000-4000 cm^{-1}.

Table 3.30.: Summary of modes occurring in Raman and IR spectra of $CdSbO_2Cl$.

Raman (cm^{-1})	IR (cm^{-1})	Comments
141	145	ν(Cd-Cl)/(Sb-O) lattice vibrations
156	154	ν(Cd-Cl)/(Sb-O) lattice vibrations
166		ν(Cd-Cl)
182	188	δ(Sb-O) twisting
202	203	δ(Sb-O) wagging
228	229	ν(Cd-Cl)
	246	δ(Sb-O) scissoring
295	289	ν(Cd-Cl)
331	331	ν_{sym}(Sb-O)
	348	ν_{sym}(Sb-O)/?(Cd-Cl)
373	368	ν_{sym}(Sb-O)
533	547	ν_{sym}(Sb-O)
620	618	ν_{asym}(Sb-O)
	673	ν(Cd-Cl)
702		
	773	ν(Cd-O)

3.6.4. UV-VIS spectroscopy

The optical properties of $CdSbO_2Cl$ were investigated using diffuse reflectivity measurements. The electronic bandgap was calculated as the intercept of the straight line obtained by the construction of the Tauc plot [53], carried out by plotting $(\mathrm{F(R)} \cdot h\nu)^n$ versus $h\nu$, see Figure 3.75. A band gap of 2.06 eV was obtained by extrapolating the linear region of the plot for exponent $n = 0.5$, indicating an indirect band gap.

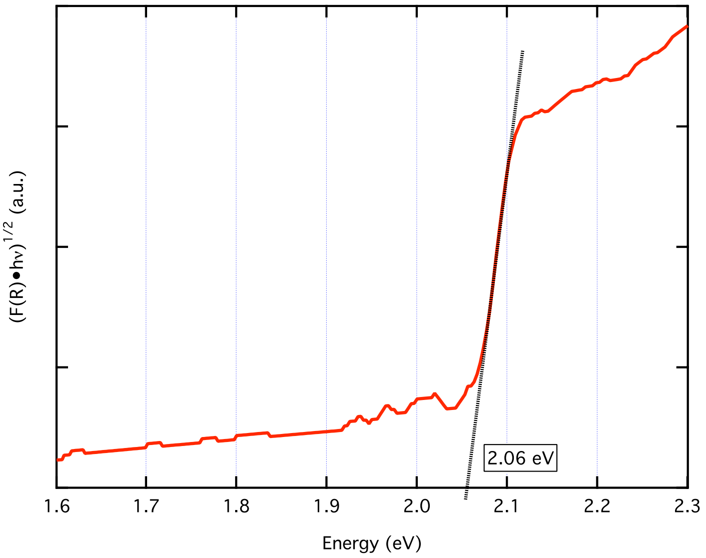

Figure 3.75.: Tauc plot of $CdSbO_2Cl$ with exponent ½, suggesting a semiconductor with indirect electronic band gap.

$CdSbO_2Br$

3.6.5. Synthesis

Single crystals of $CdSbO_2Br$ were obtained by pre-reacting a mixture of CdO, $SbBr_3$ and Sb_4O_6 in a 6:2:1 molar ratio in water for one week at 90°C. After this solvothermal reaction in an acidic medium (pH $\approx$ 3), the precipitate was filtrated, dried, and annealed in a sealed evacuated quartz ampoule at 500°C for one week. The products of this reaction were colourless, needle-shaped crystals and an additional white powder identified to be $Sb_8O_{11}Br_2$ (see Appendix Figures B.42 and B.43).

3.6.6. Single crystal analysis and powder X-ray diffraction

A single colourless needle-shaped crystal was fixed on the top of a glass capillary and mounted on a STOE IPDS single ϕ-axis diffractometer using Mo-Kα radiation (λ = 0.71073 Å). The intensities of the reflections were integrated with *X-Area* [D]. Absorption correction was carried out numerically after crystal shape optimization using *X-RED* [L] and *X-SHAPE* [M]. The crystal structure was solved using direct methods (*SHELXS-97* [I]), which provided the positions of four metal atoms, two Br, and four O atoms, and refined by full matrix least squares on F^2 (*SHELXL-97* [J]). All atoms were refined with anisotropic displacement parameters. Further information concerning the crystal structure solution and refinement data are presented in Table 3.31. Final atomic coordinates and equivalent isotropic displacement parameters for $CdSbO_2Br$ are listed in the appendix in Table B.25, while Table B.26 includes anisotropic displacement parameters.

The final composition of $CdSbO_2Br$ was additionally confirmed by EDX analysis and powder X-ray diffraction. On the basis of 41 reflections from the X-ray powder diffraction pattern of $CdSbO_2Br$ the cell ($Pnma$, $a = 15.877(1)$Å, $b = 4.085(3)$Å, $c = 12.234(1)$Å) was determined. Phase analysis for 4 reflections, which could not be indexed with the lattice constants shown above indicates the existence of an additional phase identified as $Sb_8O_{11}Br_2$. Subsequently lattice parameters obtained by powder X-ray diffraction were employed in single crystal refinement. To verify the structural model for $CdSbO_2Br$, the theoretical pattern was compared against the X-ray powder diffraction pattern. All figures are presented in the appendix (see Figures B.42 and B.43). EDX analysis of the crystal confirmed the presence and stoichiometry of the heavy elements as $Cd_{1.11}SbO_{2.53}Br_{1.32}$. Those obtained values are in resonable agreement with the solution of the structural refinement which gives $CdSbO_2Br$.

$CdSbO_2Br$ consists of corrugated layers perpendicular to the [100] direction, as seen in Figure 3.76. All ten atoms occupy ($4c$) symmetry sites. There are two crystallographically different positions of cadmium atoms. Cd1 is coordinated by four oxy-

Table 3.31.: Details of the data collection and results of the structure refinement for $CdSbO_2Br$.

Crystal data	
Chemical formula	$CdSbO_2Br$
Crystal colour/habit	colourless/needle
Crystal size	0.18 × 0.08× 0.03 mm
Molecular weight	692.12 g mol^{-1}
Calculated density	5.794 g cm^{-3}
Space group	$Pnma$ (No. 62)
Lattice parameters	$a = 15.8770(1)$ Å
	$b = 4.0850(3)$ Å
	$c = 12.2340(1)$ Å
Cell volume, Z	793.47(1) $Å^3$, 4
Data collection	
Device	STOE IPDS I
Radiation	Mo-Kα, 0.71073 Å
	graphite monochromator
Temperature	293(2)K
Scan range	$2.10° \leqslant 2\theta \leqslant 26.56°$
hkl range	$-19 \leqslant h \leqslant 19$
	$-5 \leqslant k \leqslant 5$
	$-15 \leqslant l \leqslant 15$
Structure solution and refinement	$CdSbO_2Br$
Measured reflections	11632
Independent reflections	937
Independent reflections with $F_O > 4\sigma(F_O)$	905
R_{int}	0.0321
R_σ	0.0108
Structure solution	SHELXS97 [I]
Structure refinement	SHELXL97 [J]
Number of parameters	62
Absorption correction	numerical: X-RED [L], X-SHAPE [M]
Absorption coefficient	22.045 mm^{-1}
$R_1, wR_2[I > 3\sigma(I)]$	0.0159, 0.0381
$R_1, wR_2[\text{all reflections}]$	0.0168, 0.0384
GooF	1.197
Residual electron density	0.736, -0.672 e $Å^{-3}$

gen, and two bromine atoms resulting in distorted octahedra [Cd(1)O_4Br_2] as shown in Figure 3.77. The bond distances d(Cd-O) in the range 2.221-2.361 Å are almost equal to the 2.348 Å in CdO [90]. The distances d(Cd-Br) = 2.998 Å are about 0.2 Å longer than 2.785 Å in pure $CdBr_2$ [85, 86]. All equatorial bonds in the basal plane are longer than the vertical ones. The Cd2 atom is located at the centre of the octahedron [Cd(2)O_2Br_4] built by four bromine and two oxygen atoms. The d(Cd-O) distances of 2.339 Å, and d(Cd-Br) of 2.690, 2.738, 2.965 Å are comparable to those found in pure CdO [90] and $CdBr_2$ [85,86]. Selected interatomic distances and angels for $CdSbO_2Br$ are shown in Table 3.32. The values for effective coordination numbers (ECoN(Cd(1)$^{2+}$/O^{2-}/Br^-) = 6.3 and ECoN(Cd(2)$^{2+}$/O^{2-}/Br^-) = 5.8) calculated using MAPLE [87,88] clearly demonstrate that both the Cd^{2+} have octahedral coordination. As depicted in Figure 3.78 and Figure 3.79 each octahedron is connected via common equatorial edges, resulting in strands of octahedra along the [100] crystallographic direction, as shown in Figure 3.80. These blocks of edge-sharing octahedra form entities in the structure reminiscent of the crystal structures of CdX_2 [84, 85, 86]. The [Cd(1)O_4Br_2] and [Cd(2)O_2Br_4] units share an axial and an equatorial edge with two square pyramids [SbO_4] (or [SbO_4E] trigonal bipyramid, taking the lone pair of electrons E into account).

Each of the layers extends in the bc-plane. The nearest cation-cation separation within the chains built by common equatorial edge sharing [Cd(1)O_4Br_2] and [Cd(2)O_2Br_4] octahedra is Cd(1)...Cd(1) = 4.085(1) Å and Cd(2)...Cd(2) = 4.085(1) Å, which corresponds to the *b* axis. The distance between cations from neighbouring chains of [Cd(1)O_4Br_2] units is 3.446(0) Å and the distance from chains of [Cd(2)O_2Br_4] is 4.102(0) Å. The Cd(1)...Cd(2) intralayer distance is 3.599(0) Å, whereas the closest interlayer Cd^{2+}-Cd^{2+} distance amounts to 8.021(1) Å. However, the shortest cation-cation interlayer separations have values ranging from 5.004(2) Å for [Cd(2)...Sb(2)] to 6.711(1) Å for [Cd(1)...Sb(2)]. The shortest cation-anion distances between neighboring layers are: Sb(1)...Br(2) = 3.91(0) Å, Sb(2)...Br(1) = 4.006(0) Å, Sb(1)...Br(1) = 4.865(3) Å, Sb(2)...Br(2) = 4.261(0) Å. These are almost the same lengths as the cation-cation separations within the layers, indicating that the layers are held together only by weak van der Waals forces.

Sb^{3+} cations are one-side four-coordinate due to the presence of oxygen $5s^2$ lone pairs, forming one-dimensional $^1_\infty[SbO_2^-]$ polymers, as seen in Figure 3.81. Polymers are built by edge-sharing [Sb(1)O_4] and [Sb(2)O_4] square pyramids. If taking into account the presence of lone pairs of electrons E, then [Sb(1)O_4E] and [Sb(2)O_4E] trigonal bipyramids participate in the creation of $^1_\infty[SbO_2^-]$ polymers. The lone pairs of electrons belonging to Sb^{3+} cations protrude from the layers into non-bonding interlayer space. A similar structural entity was previously reported in the crystal structure of L-SbOF [165].

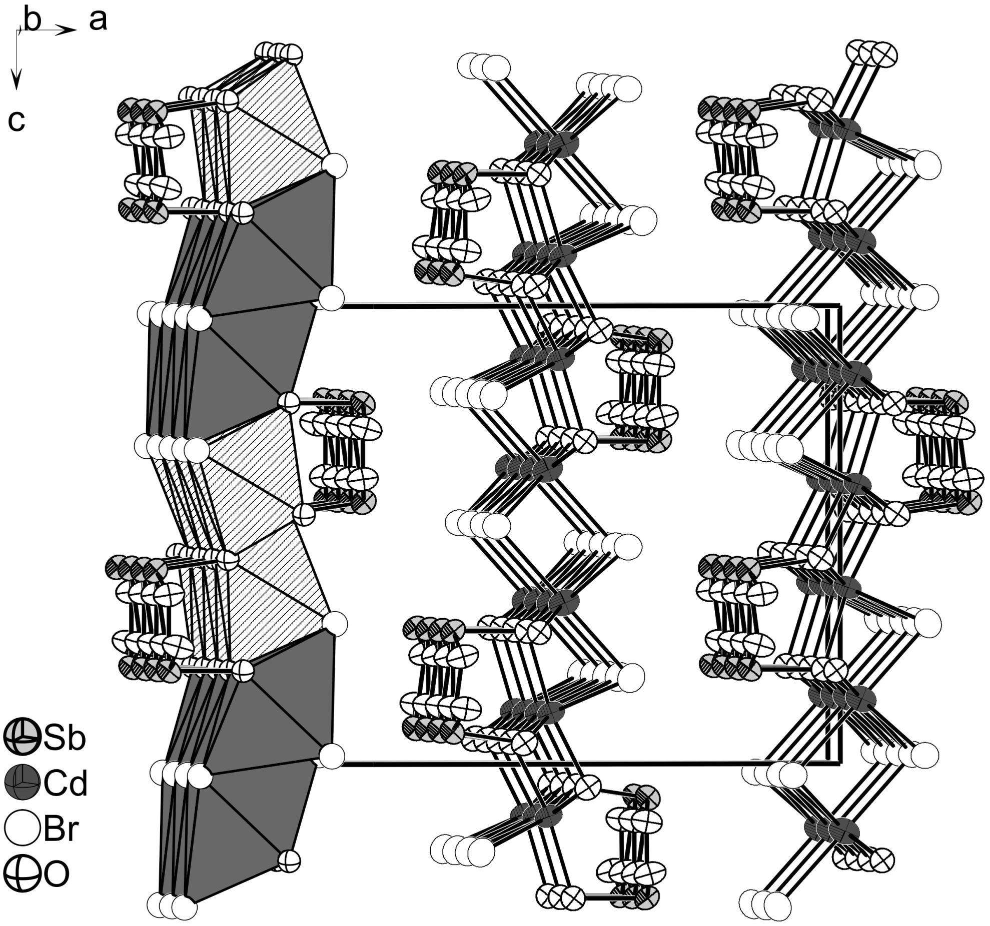

Figure 3.76.: Projection of of the crystal structure of CdSbO$_2$Br emphasizing the corrugated puckered layers of edge-sharing [Cd(1)O$_4$Br$_2$] and [Cd(2)O$_2$Br$_4$] octahedra, and Sb^{3+} cations four-coordinate by oxygen forming one-dimensional polymers $^1_\infty$[SbO$_2^-$]. (90% probability level).

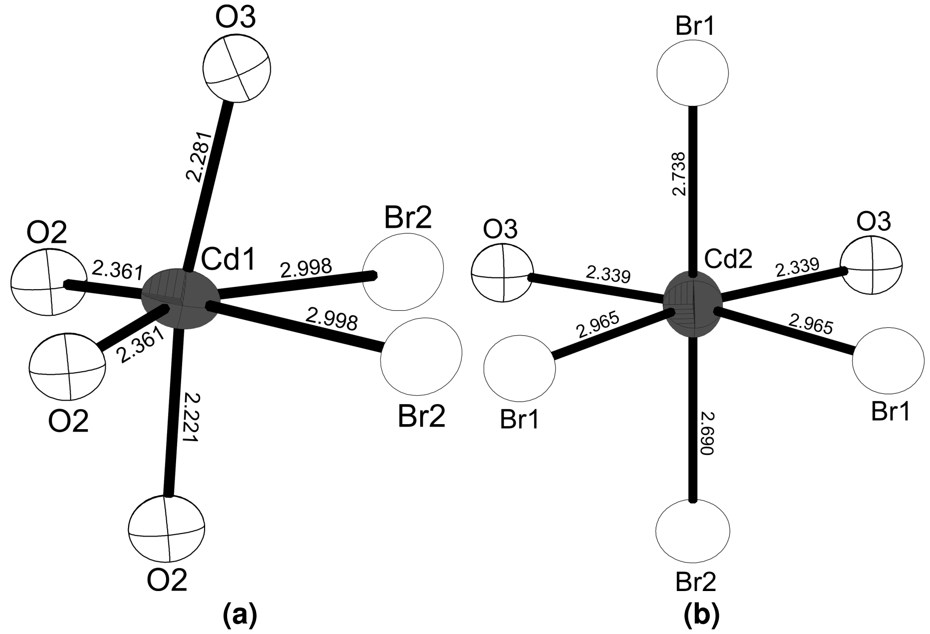

Figure 3.77.: Coordination geometry about the Cd1 and Cd2 atoms. Cd-O and Cd-Br distances are shown in units of Å, (90% probability level).

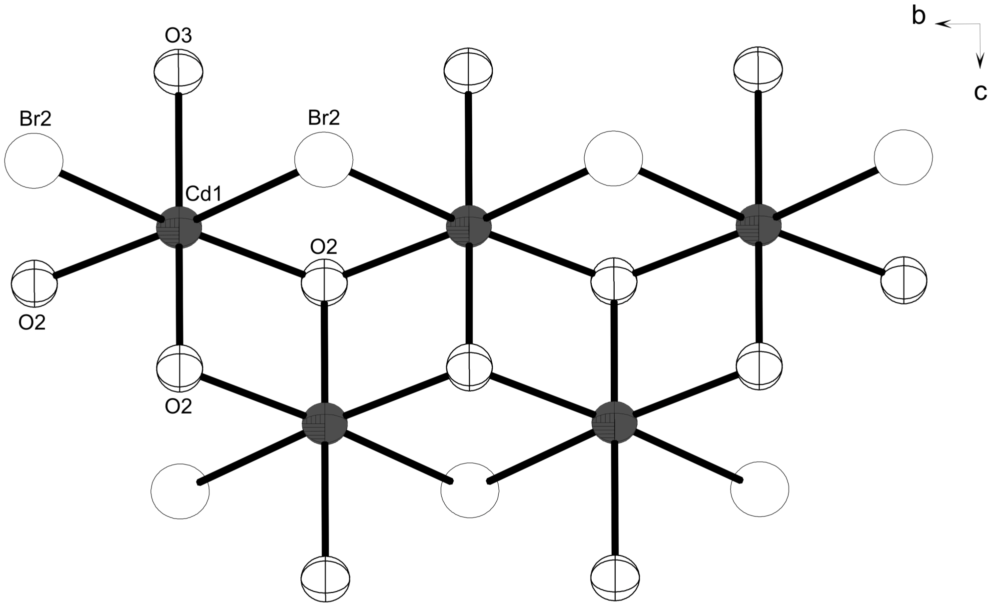

Figure 3.78.: Projection of the edge-sharing distorted [Cd(1)O_4Br_2] octahedra. (90% probability level).

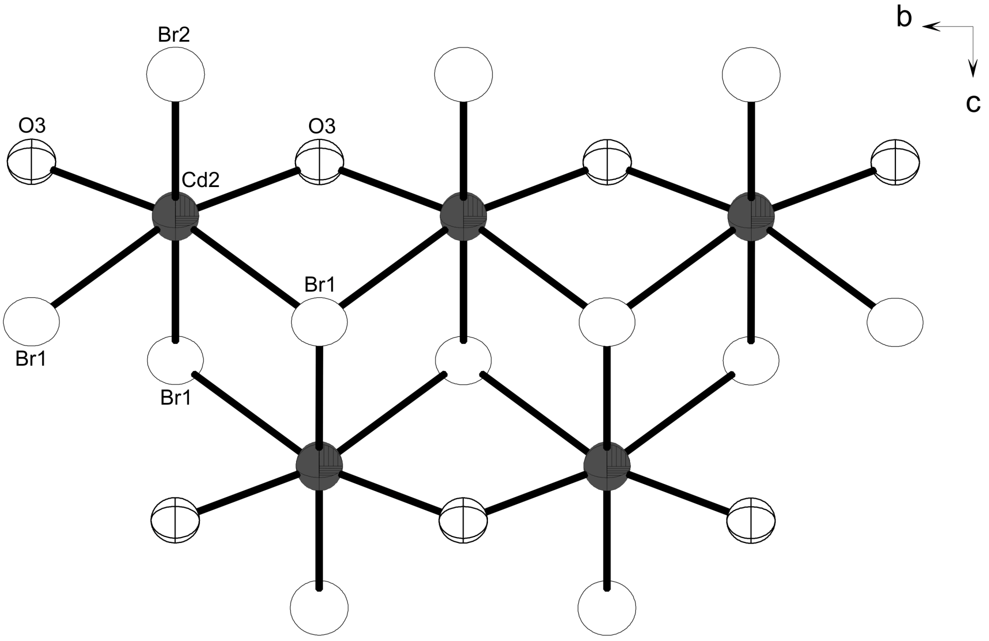

Figure 3.79.: Projection of the edge-sharing distorted [Cd(2)O_2Br_4] octahedra. (90% probability level).

Table 3.32.: Selected interatomic distances (in Å) and angles (in degrees) for $CdSbO_2Br$ at room temperature.

Cd(1)-O(2)	2x	2.3609(2)	O(2)-Cd(1)-O(2)	2x	82.50(8)
Cd(1)-O(2)		2.221(3)	O(2)-Cd(1)-O(2)		119.79(1)
Cd(1)-O(3)		2.281(3)	O(3)-Cd(1)-O(2)	2x	102.24(8)
Cd(1)-Br(2)	2x	2.988(4)	O(2)-Cd(1)-O(3)		170.08(1)
			O(2)-Cd(1)-Br(2)	2x	89.33(6)
			O(3)-Cd(1)-Br(2)		83.42(6)
			O(2)-Cd(1)-Br(2)	2x	160.44(6)
			O(2)-Cd(1)-Br(2)	2x	76.32(6)
			O(3)-Cd(1)-Br(2)		83.42(6)
			Br(2)-Cd(1)-Br(2)		85.889(2)
Cd(2)-O(3)	2x	2.3394(2)	O(3)-Cd(2)-Br(2)	2x	89.61(7)
Cd(2)-Br(2)		2.6905(6)	O(3)-Cd(2)-Br(1)	2x	90.40(7)
Cd(2)-Br(1)		2.7381(6)	O(3)-Cd(2)-O(3)		121.64(1)
Cd(2)-Br(1)	2x	2.9651(4)	Br(2)-Cd(2)-Br(1)		179.986(2)
			O(3)-Cd(2)-Br(1)		162.69(7)
			O(3)-Cd(2)-Br(1)		75.63(6)
			Br(2)-Cd(2)-Br(1)	2x	91.896(1)
			Br(1)-Cd(2)-Br(1)		88.094(2)
			O(3)-Cd(2)-Br(1)		75.63(6)
			O(3)-Cd(2)-Br(1)		162.69(7)
			Br(1)-Cd(2)-Br(1)		88.094(1)
			Br(1)-Cd(2)-Br(1)		87.077(2)

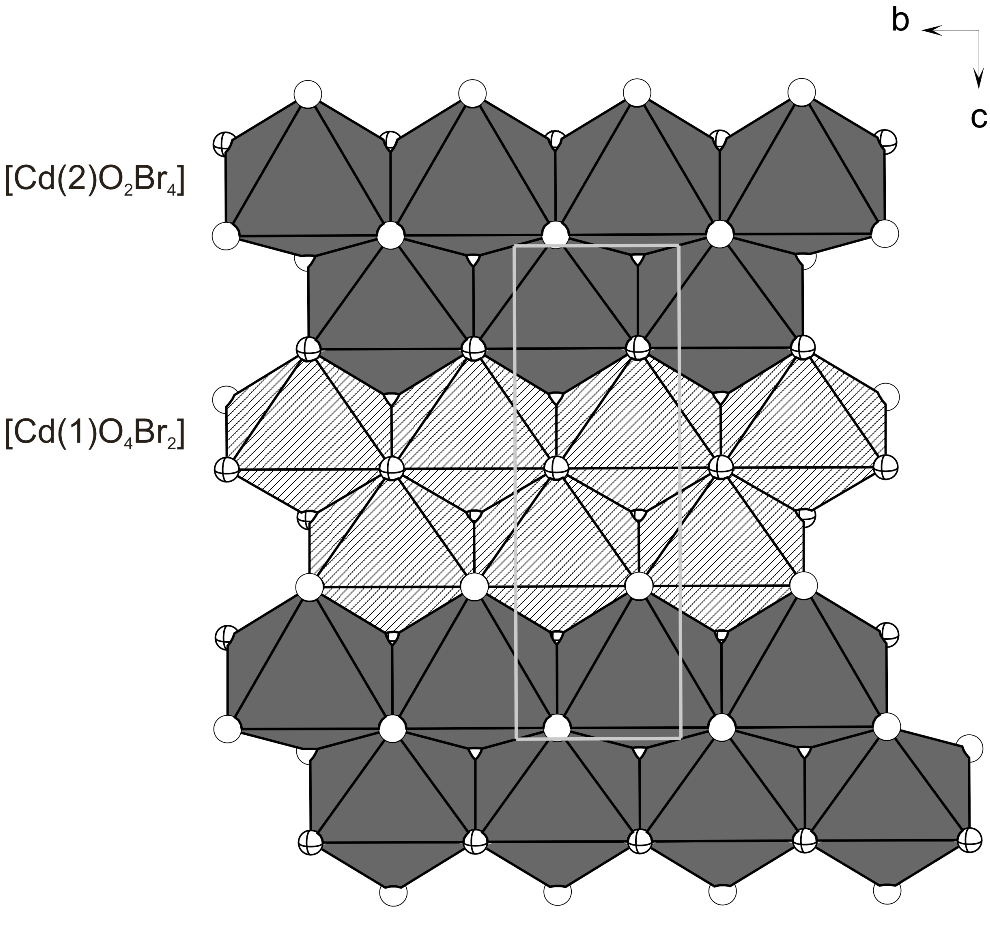

Figure 3.80.: Projection of the $CdSbO_2Br$ structure with distinguished blocks of edge-sharing $[Cd(1)O_4Br_2]$ and $[Cd(2)O_2Br_4]$ octahedra.

The average d(Sb-O) distance of 2.0493 Å in CdSbO$_2$Br is in reasonable agreement with the bond length d(Sb-O) = 1.9779 Å in senarmontite [104,68] and with the average bond length d(Sb-O) = 2.0059 Å in valentinite [69,70].

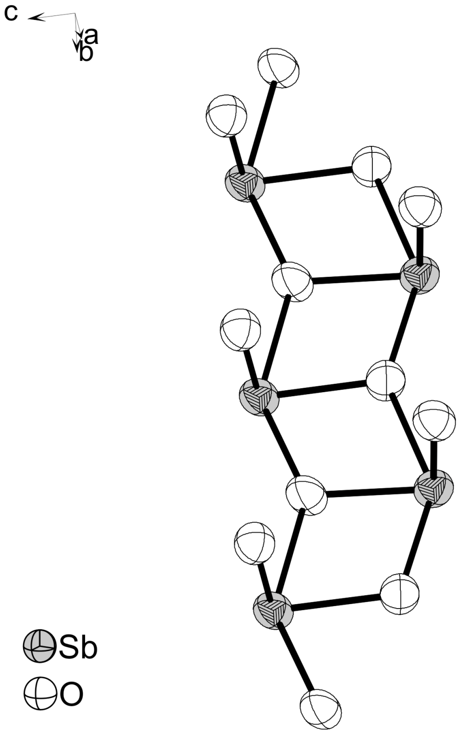

Figure 3.81.: Projection of four-coordinate by oxygen Sb^{3+} cations forming one-dimensional polymers $^{1}_{\infty}$[SbO$_2^-$].

3.6.7. Raman and infrared spectroscopy

The Raman spectrum of CdSbO$_2$Br was recorded in the manner described in Section 2.3.5, in the 130-4000 cm^{-1} wavenumber range at a resolution of 2 cm^{-1}. The Raman spectrum of CdSbO$_2$Br exhibits clear vibrations at 161 cm^{-1} for $\nu_{\mathrm{Cd-Br}}$ [98,99,100,101], and at 452 cm^{-1} for $\nu_{\mathrm{Cd-O}}$ [97]. The frequencies which can be attributed to Sb-O lattice vibrations [77,78,102,103] occur at 191, 200, 255, 374, 452, 561, 596, and 677 cm^{-1}.

An exact identification of the modes in the Raman spectrum can only be carried out by way of a theoretical calculation of the Raman spectra based on the extracted crystal structures. These calculations will be one of the goals of future work in this area.

The irfrared spectrum of CdSbO$_2$Br was recorded using the ATR technique, on a diamond crystal sampling area, located in the center of the plate. Analysis of FTIR spectra was performed using *Resolution Pro* [T]. IR measurement was performed in the ranges 120-400 cm^{-1} (F-IR) and 400-4000 cm^{-1} (M-IR). Table 3.33 presents a comparison of Raman and IR spectral data for CdSbO$_2$Br.

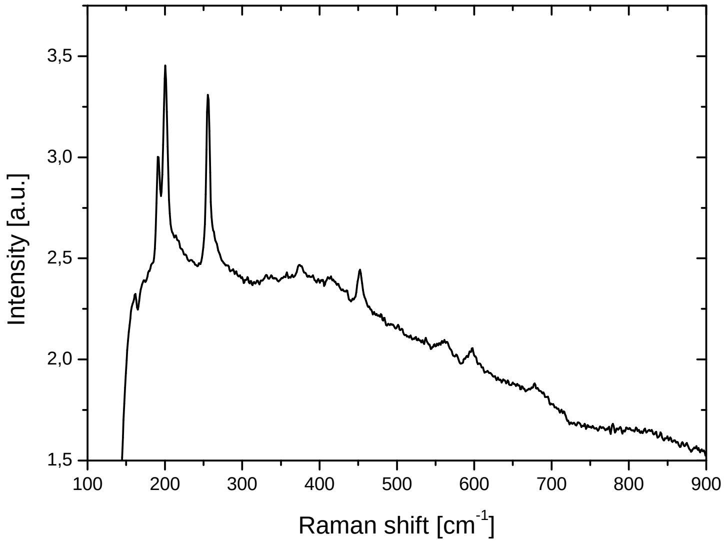

Figure 3.82.: Raman spectrum of $CdSbO_2Br$ showing significant vibrations only for $\nu_{\text{Sb-O}}$, $\nu_{\text{Cd-Br}}$ and $\nu_{\text{Cd-O}}$

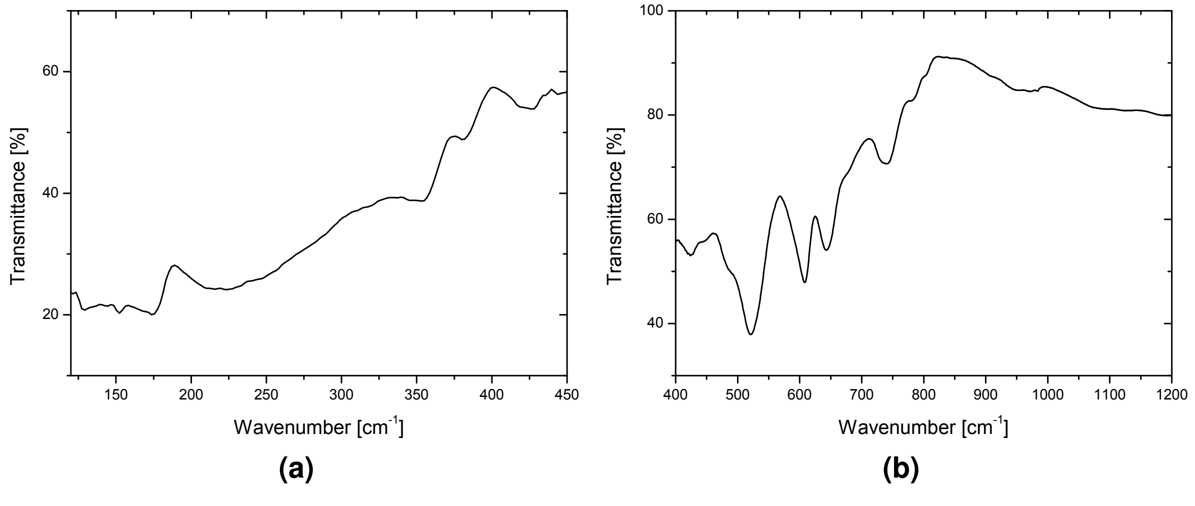

Figure 3.83.: F-IR and M-IR spectra of $CdSbO_2Br$ showing significant vibrations only for $\nu_{\text{Sb-O}}$, $\nu_{\text{Cd-Br}}$ and $\nu_{\text{Cd-O}}$. There were no vibrations in the range 1200-4000 cm^{-1}.

Table 3.33.: Summary of modes occurring in Raman and IR spectra of $CdSbO_2Br$.

Raman (cm^{-1})	IR (cm^{-1})	Comments
	152	ν(Cd-Br)/(Sb-O) lattice vibrations
161		ν(Cd-Br)
	174	δ(Sb-O) twisting
191		δ(Sb-O) twisting
200	222	δ(Sb-O) wagging
255		δ(Sb-O) scissoring
	353	ν_{sym}(Sb-O)
374	381	ν_{sym}(Sb-O)
452	444	ν_{sym}(Sb-O)/ ν(Cd-O)
	521	
561		ν_{asym}(Sb-O)
596	608	ν_{asym}(Sb-O)
	643	
677		ν_{sym}(Sb-O)
	739	ν(Cd-Br)
	783	ν(Cd-O)
	952	

3.6.8. UV-Vis spectroscopy and band gap calculations

Diffuse reflectivity measurements were used to investigate the optical properties of $CdSbO_2Br$. The absorption data were derived from the measured values using the Kubelka-Munk function [51, 52, 166]. The energy gaps were determined from Tauc plots [53]. The analysis suggests an indirect band gap around 3.65 eV, as shown in Figure 3.84.

The electronic band structure of $CdSbO_2Br$ was calculated by LDA and GGA methods. The calculations correspond well to experimental UV-Vis results and suggest an indirect band gap of about 3.4 eV (LDA) or 3.3 eV (GGA).

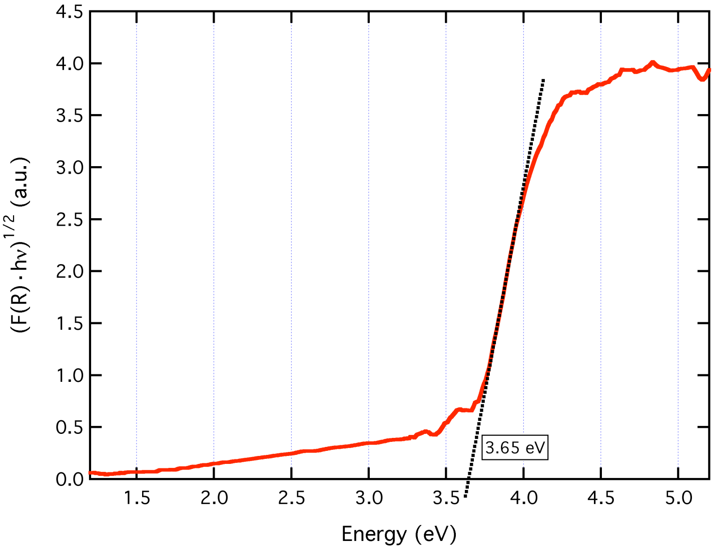

Figure 3.84.: Tauc plot of $CdSbO_2Br$ with exponent ½, suggesting a semiconductor with indirect electronic band gap.

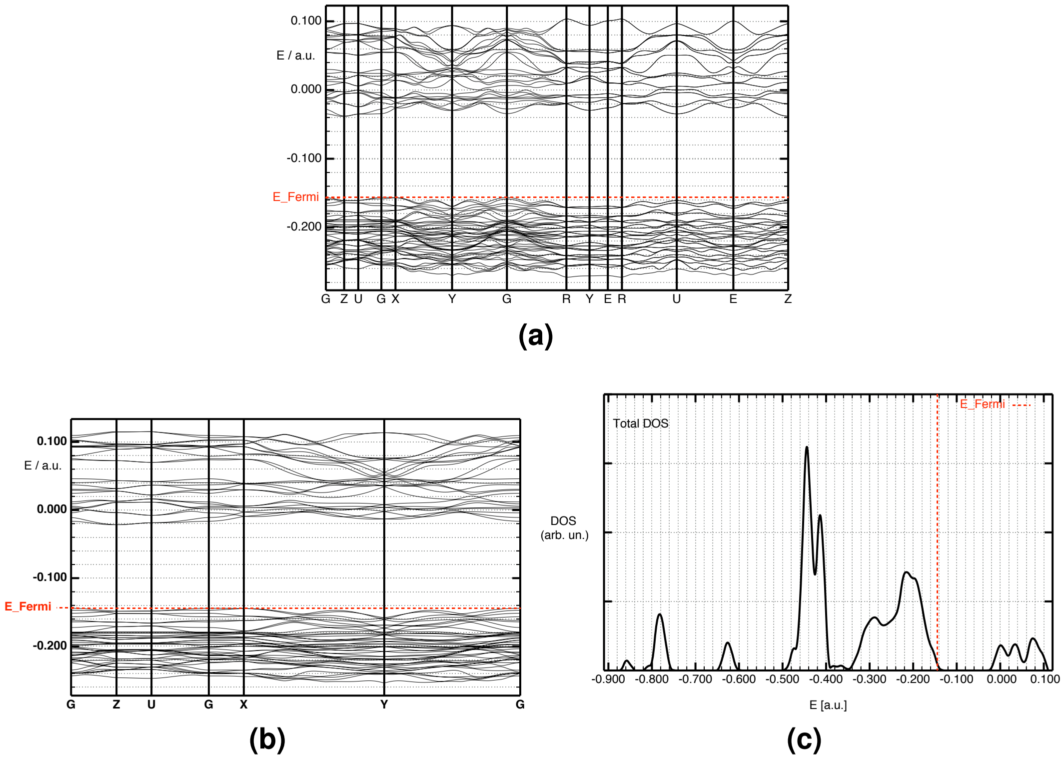

(a)

(b)

(c)

Figure 3.85.: Electronic band structure obtained from LDA (a) and form GGA (b), as well as the density of states from GGA (c). The energy is calculated in absolute units of Rydberg constants (13.6 eV).

3.7. $CoSb_2O_3Cl_2$

3.7.1. Synthesis

The new quaternary compound $CoSb_2O_3Cl_2$ was obtained by solid state reaction in sealed evacuated silica tubes of anhydrous $CoCl_2$ and Sb_4O_6 in 2:1 molar ratio. The amount of starting materials was 0.5g. All preparatory work was carried out in a glovebox. The reactants were annealed at 450°C for 14 days. The synthesis product contained blue, plate-like single crystals of $CoSb_2O_3Cl_2$ isostructural to $CoSb_2O_3Br_2$ investigated by Z. Hugonin *et al.* [33], colourless single crystals of SbOCl and a dark blue crystalline powder, which could not be identified by the powder X-ray diffraction method. The fraction of single crystals in the reaction products was about 10%. Attempts were made to synthesise the analogous $CoSb_2O_3I_2$ by a similar synthesis method, which were however unsuccessful. The chemical composition of $CoSb_2O_3Cl_2$ was additionally confirmed by EDX analysis. The investigated crystal confirmed the presence of elements to be $Co_1Sb_{2.2}O_{2.67}Cl_{2.1}$. Those values are in reasonable agreement with the X-ray single crystal data.

3.7.2. Single crystal and powder X-ray diffraction analysis

X-ray diffraction data collection of a single crystal of $CoSb_2O_3Cl_2$ was performed with a STOE IPDS I, using Mo-Kα radiation (λ = 0.71073 Å) with a graphite monochromator. The description of the crystal shape was optimized by using *X-SHAPE* [M]. Furthermore numerical absorption correction were applied by using *X-RED* [L]. The crystal structure solution was performed using *SIR-92* [G], and provided the positions of the three metal atoms, two Cl and three O atoms. The refinement was performed by full matrix least squares on F^2 using *SHELXL-97* [J]. Anisotropic displacement parameters were used for the description of all atoms. All eight atoms occupy lowest symmetry sites ($2i$). The list of final atomic coordinates for atoms in standard positions found by a *Structur Tidy* routine (*PLATON* [K]), equivalent isotropic displacement parameters and anisotropic displacement parameters for $CoSb_2O_3Cl_2$ is presented in the appendix (Tables B.27 and B.28).

The new layered compound crystallizes in the space group $P\bar{1}$, with lattice parameters of $a = 5.2956(2)$ Å, $b = 7.342(3)$ Å, $c = 8.028(3)$ Å, $\alpha = 90.98(2)°$, $\beta = 81.38(2)°$, $\gamma = 79.16(3)°$ and $Z = 2$. The structure refinement converged to $R_1(F_0 > 4\sigma(F_0)) = 0.0203$, $wR_2(\text{all data}) = 0.0455$, GooF = 1.061. Crystal data and details of the structure determination are given in Table 3.34.

The new crystal structure of $CoSb_2O_3Cl_2$ consists of puckered layers of edge-sharing [CoO_4Cl_2] octahedra, [Sb(1)O_3ClE] trigonal bipyramids and [Sb(2)O_3E] tetrahedra, as seen in Figure 3.86. The layers extend in the ac-plane. The lone pairs of electrons

Table 3.34.: Details of the data collection and results of the structure refinement for $CoSb_2O_3Cl_2$ and $CoSb_2O_3Br_2$ (crystallographic data for the latter taken from [33]).

Crystal data		
Chemical formula	$CoSb_2O_3Cl_2$	$CoSb_2O_3Br_2$ (data from [33])
Crystal colour/habit	dark blue/plate	dark blue/plate
Crystal size	0.1 × 0.07× 0.05 mm	0.04 × 0.04 × 0.02 mm
Molecular weight	421.33 g mol^{-1}	510.25 g mol^{-1}
Calculated density	4.622 g cm^{-3}	5.193 g cm^{-3}
Space group	$P\bar{1}$ (No. 2)	$P\bar{1}$ (No. 2)
Lattice parameters	$a = 5.2956(2)$ Å $\alpha = 90.98(2)°$ $b = 7.342(3)$ Å $\beta = 81.38(2)°$ $c = 8.028(3)$ Å $\gamma = 79.16(3)°$	$a = 5.306(3)$ Å $\alpha = 88.54(3)°$ $b = 7.812(4)$ Å $\beta = 82.17(3)°$ $c = 8.0626(10)$ Å $\gamma = 80.32(4)°$
Cell volume, Z	302.8(2) Å^3, 2	326.3(3) Å^3, 2
Data collection		
Device, Radiation, Temperature	STOE IPDS I, Mo-Kα, 0.71073 Å graphite monochromator, 293 (2)K	
Scan range	$2.57° \leqslant 2\theta \leqslant 25.47°$	
hkl range	$-6 \leqslant h \leqslant 6$ $-8 \leqslant k \leqslant 8$ $-9 \leqslant l \leqslant 9$	
Structure solution and refinement	$CoSb_2O_3Cl_2$	$CoSb_2O_3Br_2$ [33]
Measured reflections	4134	
Independent reflections	1055	
Independent reflections with $F_O > 4\sigma(F_O)$	926	
R_{int}	0.0275	0.0702
R_σ	0.0219	
Structure solution, refinement	SIR92[G], SHELXL97 [J]	
Number of parameters	74	73
Absorption correction	numerical: X-RED [L], X-SHAPE [M]	CrysAlis
Absorption coefficient	12.36 mm^{-1}	22.89 mm^{-1}
$R_1, wR_2[I > 3\sigma(I)]$	0.0203, 0.0445	0.0308, 0.0652
R_1, wR_2[all reflections]	0.0254, 0.0455	0.0437, 0.0659
GooF	1.061	0.964
F(000)	374	
Residual electron density	0.956, -0.814 e Å^{-3}	1.204, -1.256 e Å^{-3}

belonging to the Sb^{3+} cation are noted as E.

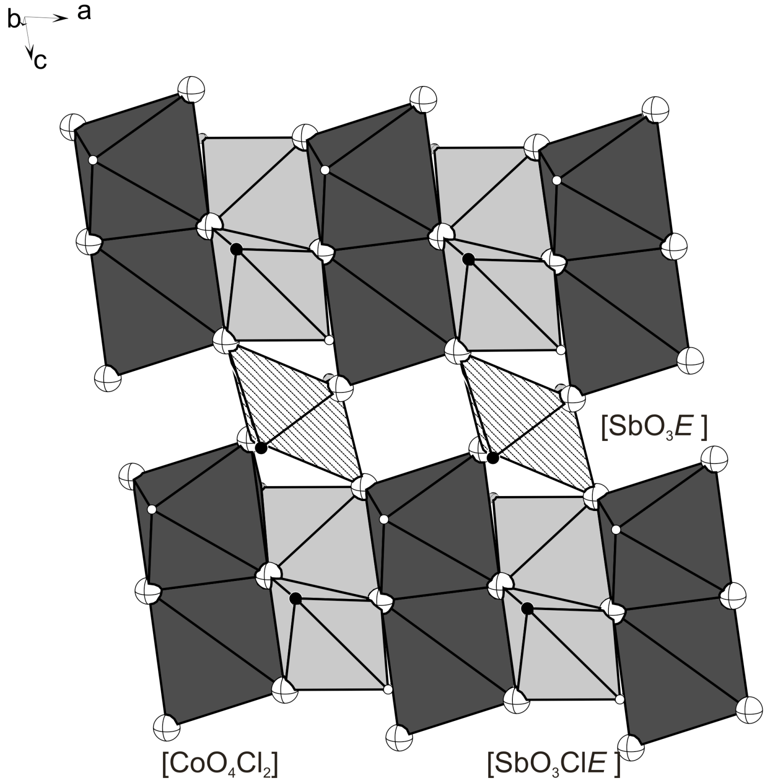

Figure 3.86.: Projection of layers made up of three building blocks: edge-sharing distorted [CoO_4Cl_2] octahedra, edge-sharing trigonal bipyramids [SbO_3ClE], and [SbO_3E] tetrahedra.

The cation-anion distances between adjacent layers are: Sb1...Cl1 = 3.723(4) Å, Sb1...Cl2 = 3.849(5) Å, Sb2...Cl2 = 4.095(5) Å, and Sb2...Cl1 = 3.816(4) Å, while cation-cation separation within the layers are significantly smaller: Co1...Co1 = 3.354(7) Å, Sb1...Sb1 = 3.259(3) Å, and Sb2...Sb2 = 3.160(4) Å. This suggests that the layers are held together only by week van der Waals forces. Each layer may thus be considered as an infinite two-dimensional neutral molecule, see Figure 3.87.

There are two differently coordinated Sb^{3+} cations. Coordination of Sb1 by three oxygen and one chlorine atoms results in a tetragonal pyramidal environment. On the other hand, Sb2 is asymmetrically threefold coordinated by oxygen forming trigonal pyramids. If we consider a lone pair of electrons ($5s^2$) participating in the creation of the coordination polyhedra, the trigonal bipyramids [$Sb(1)O_3ClE$] and tetrahedra [$Sb(2)O_3E$] are formed. As can be seen in Figure 3.89 the edge- and corner-sharing [$Sb(1)O_3Cl$] and [$Sb(2)O_3$] polyhedra form one-dimensional $^1_\infty[Sb_4O_5Cl_2]$ polymers. The average distance d(Sb1-O) = 2.0633 Å and d(Sb2-O) = 2.01 Å are in reasonable agreement with the bond length d(Sb-O) = 1.9779 Å in senarmontite [104, 68] and with the average bond length d(Sb-O) = 2.0059 Å in valentinite [69, 70]. Analysis of the bond lengths shows that d(Sb2-Cl1)=3.016 Å, d(Sb2-Cl2)=3.228 Å, and d(Sb1-

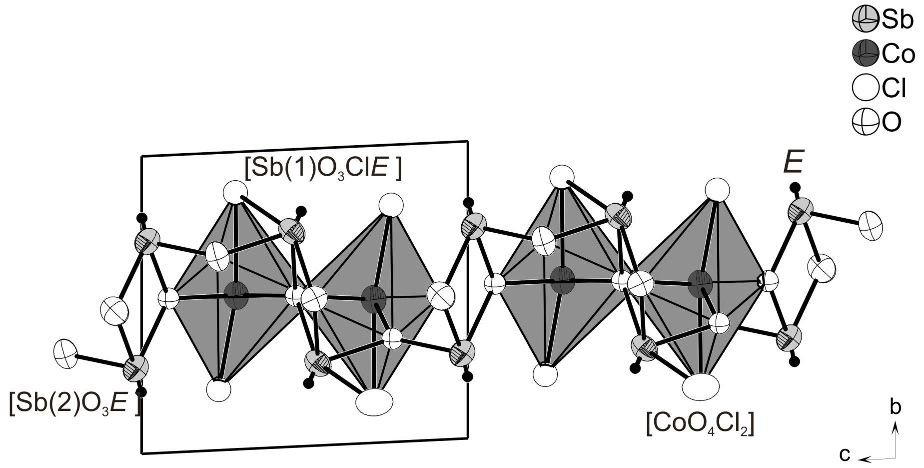

Figure 3.87.: Projection of $CoSb_2O_3Cl_2$ viewed along [100] showing $^2_\infty$ $[CoSb_2O_3Cl_2]$ layers separated by chlorine ions and stereochemically active electron lone pairs E.

Cl2)=3.149 Å have a predominantly ionic character, as seen in Figure 3.88. The distance d(Sb1-Cl1) = 2.655(3) Å is about 0.3 Å longer than the average 2.359 Å bond length in pure $SbCl_3$ [167].

Bond valence sum (BVS) calculations are a useful tool to consider which atom belongs to the primary coordination sphere of Sb^{3+}. The bond valence contribution for each atom and BVS for each ligand are presented in Table 3.35 and Table 3.36. All calculations were performed according to the Brown theory [95] using BVS calculator [W]. The bond valences were determined using empirical parameters: $b = 0.37$ Å, $r_0(Sb^{3+}$-O) = 1.973 Å,$r_0(Sb^{3+}$-Cl) = 2.368 Å, $r_0(Co^{2+}$-O) = 1.692 Å, $r_0(Co^{2+}$-Cl) = 2.033 Å. As is clear from calculation results, the short d(Sb-Cl) = 2.655(2) Å corresponds to a bond valence of 0.46, indicating a large contribution, and thereby allowing one to consider chlorine as belonging to the primary coordination sphere of Sb1. The BVS values for chlorine atoms amounts to 0.85 for Cl1 and 0.62 for Cl2, and are far from the expected value 1. Calculations of Madelung Part of Lattice Energy (MAPLE) [87, 88] confirmed the BVS calculations. The value of MAPLE for chlorine atoms equals 117.23 and 85.37 for Cl1 and Cl2, respectively. This suggests that the absence of Sb-Cl2 results in rather significant underbonding of the Cl2 atom compared to Cl1.

This is a rather unexpected finding, since compounds of composition M-Sb-O-X (M = transition metal, X = Cl. Br, I) previously described in the literature, more precisely copper(I) antimony(III) oxidehalides [168, 169, 170], show a different bonding preference. The lone pair elements prefer to bond with oxygen anions, while the transition metals accept both O^{2-} and X^- in an oxyhalide environment. Those preferences based on the Lewis acidity/alkalinity are confirmed in all other structures presented in this work. Only a limited number of investigations of crystal structures with bonding preferences similar to those of $CoSb_2O_3Cl_2$ have been reported in the literature [33, 171, 172].

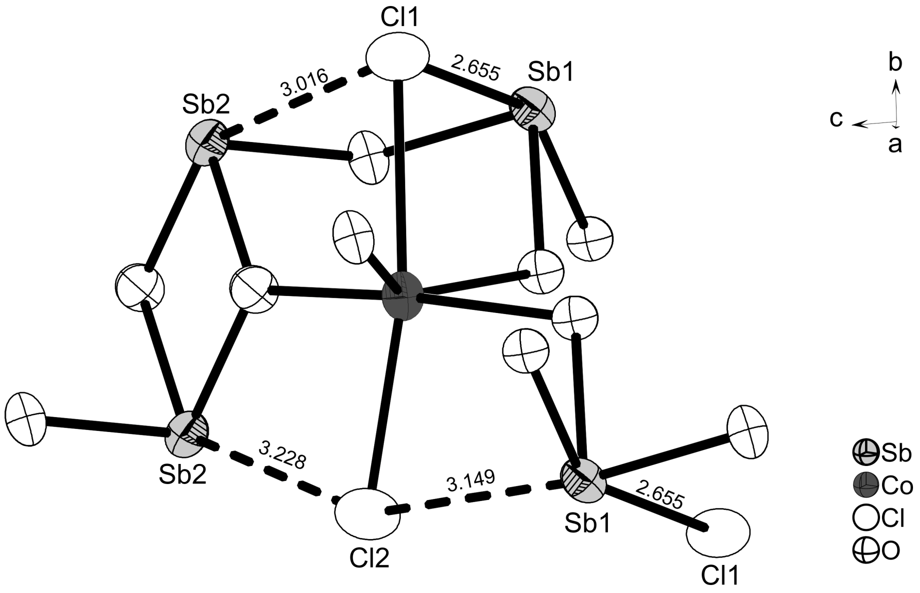

Figure 3.88.: Overview of $[CoO_4Cl_2]$ octahedra with $[Sb(1)O_3Cl(1)]$ square pyramids and $[Sb(2)O_3]$ trigonal pyramids. All distances are given in Å. Ionic interactions are indicated with dashed lines.

Table 3.35.: Geometric parameters and bond valence for $CoSb_2O_3Cl_2$. Symmetry codes: (i) -x, 1-y, 1-z; (ii) -1+x, y, z; (iii) 1-x, 1-y, z; (iv) 1-x, 1-y, 1-z

	Bond distance (Å)	Bond valence
Sb(1)-O(1)^{i}	2.035(4)	0.85
Sb(1)-O(1)	2.140(4)	0.64
Sb(1)-O(2)	2.015(3)	0.89
Sb(1)-Cl(1)^{ii}	2.655(2)	0.46
Sb(1)-Cl(2)	3.149(4)	0.12
Sb(2)-O(2)	1.988(4)	0.96
Sb(2)-O(3)^{iii}	2.019(4)	0.88
Sb(2)-O(3)^{ii}	2.023(4)	0.87
Sb(2)-Cl(1)	3.016(4)	0.17
Sb(2)-Cl(2)	3.228(4)	0.10
Co(1)-O(1)^{iv}	2.101(4)	0.32
Co(1)-O(1)	2.241(4)	0.22
Co(1)-O(2)	2.092(4)	0.33
Co(1)-O(3)	2.004(4)	0.41
Co(1)-Cl(1)	2.6073(2)	0.22
Co(1)-Cl(2)	2.3916(2)	0.39

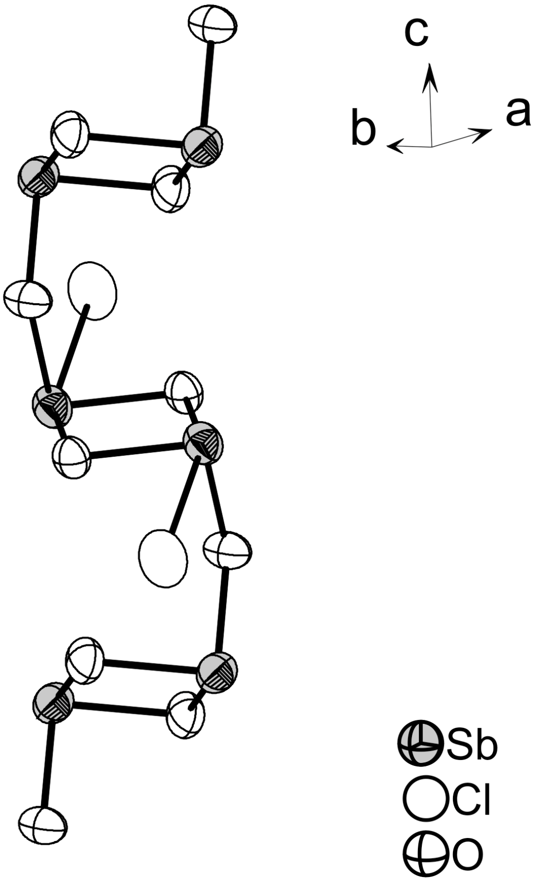

Figure 3.89.: Projection of edge- and corner-sharing [Sb(1)O_3Cl] and [Sb(2)O_3] polyhedra forming one-dimensional polymers $^1_\infty[Sb_4O_5Cl_2]$. (90% probability level).

Table 3.36.: Atomic coordinate equivalent isotropic displacement parameter [Å^2] and bond valence sum for $CoSb_2O_3Cl_2$.

Atom	x	y	z	U^{eq}	BVS
Sb(1)	0.42965(7)	0.27631(4)	0.46001(4)	0.01572(1)	2.96
Sb(2)	0.38976(7)	0.28697(5)	0.01781(4)	0.01606(1)	2.98
Co(1)	0.02130(2)	0.51758(9)	0.71040(8)	0.01545(2)	1.89
Cl(1)	0.7451(3)	0.13638(2)	0.28762(2)	0.0238(3)	0.85
Cl(2)	0.1561(3)	0.7964(2)	0.23643(2)	0.0290(3)	0.62
O(1)	0.7154(8)	0.4830(5)	0.0825(4)	0.0179(8)	2.03
O(2)	0.2722(8)	0.3476(5)	0.2321(4)	0.0164(8)	2.18
O(3)	0.2655(7)	0.5065(5)	0.5284(4)	0.0149(7)	2.16

The cobalt atom is four coordinated by oxygens and two coordinated by chlorine atoms, resulting in a slightly distorted octahedral environment as seen in Figure 3.90.

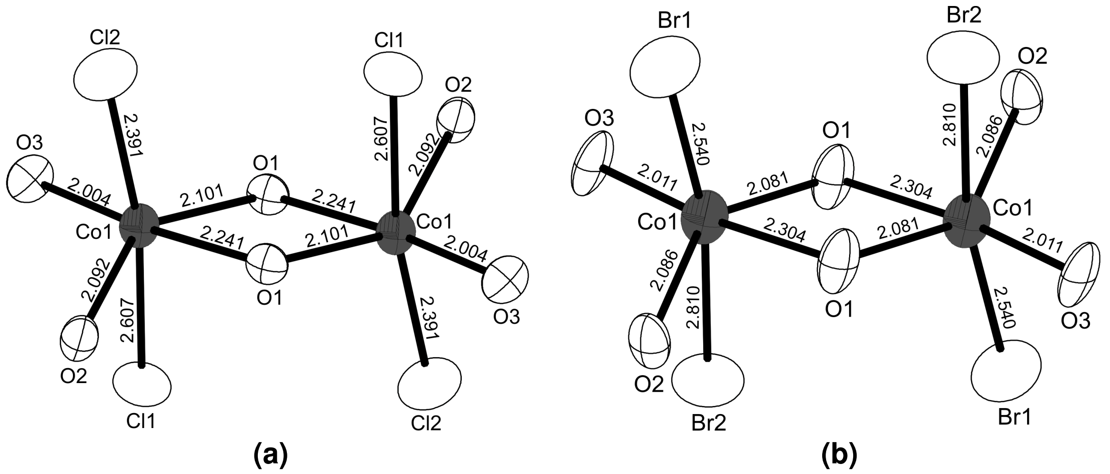

Figure 3.90.: Projection of the Co-Co dimer consisting of two edge-sharing distorted (a) $[CoO_4Cl_2]$ and (b) $[CoO_4Br_2]$ [33] octahedra. All distances are given in Å. (90% probability levels).

The edge-sharing $[CoO_4Cl_2]$ octahedra form Co^{2+}-Co^{2+} dimers in the structure, isolated by surrounding Sb^{3+}-centred polyhedra, as seen in Figure 3.86. The average distance d(Co-O) = 2.1095 Å within the equatorial plane are in reasonable agreement with bond lengths in previously reported cobalt tellurite chlorides: d(Co-O) = 2.1218 Å [173], d(Co-O) = 2.1258 Å [174], d(Co-O) = 2.068 Å [175]. The longer axial bonds d(Co-Cl) with lengths in the range 2.391-2.607 Å are relatively close to d(Co-Cl) = 2.453(7) Å distances in pure $CoCl_2$ [176], and with the average length d(Co-Cl) = 2.4518 Å in $Co_5Te_4O_{11}Cl_4$ [173], d(Co-Cl) = 2.474 Å in $Co_5(TeO_3)_4X_2$ (X = Cl, Br) [174], and d(Co-Cl) = 2.497 Å in $Co_2TeO_3Cl_2$ [175]. The shortest Co^{2+}-Co^{2+} distance intra-dimer is 3.354(7) Å, while between dimers the distance is 4.698(7) Å, and between adjacent layers the distance is 7.342(3) Å. A similar structural entity to such M^{2+}-M^{2+} (M = transition metal) dimers was previously reported for $CuTe_2O_5$ [28].

The final composition of $CoSb_2O_3Cl_2$ was additionally confirmed by powder X-ray diffraction analysis. Using (Mo-Kα) radiation, on the basis of 147 reflections the cell $P\bar{1}$ with $a = 5.284(1)$ Å, $b = 7.329(1)$ Å, $c = 7.980(1)$ Å, $\alpha = 90.95(8)°$, $\beta = 81.68(8)°$, $\gamma = 78.79(1)°$) was determined. Additionally from powder X-ray diffraction measurement performed using Cu-Kα radiation, on the basis of 99 reflections the cell $P\bar{1}$, $a = 5.2956(2)$ Å, $b = 7.342(3)$ Å, $c = 8.028(3)$ Å, $\alpha = 90.980(2)°$, $\beta = 81.375(2)°$, $\gamma = 79.16(3)°$ was determined. An additional colourless crystalline phase was identified as SbOCl. A dark blue powder could not be identified. All details concerning powder X-ray analysis are present in the appendix, refer to Figures B.44-B.47.

3.7.3. Thermal analysis of $CoSb_2O_3Cl_2$

Thermal analysis for $CoSb_2O_3Cl_2$ performed using DTA/TG equipment provides temperature control for a small quantity of sample. The sample of $CoSb_2O_3Cl_2$ was heated in an evacuated ampoule under flowing argon, followed by cooling to determine reversibility. As presented in Figure 3.91, the compound is stable above the synthesis temperature (450 °C). In the following observations, the values given in parentheses refer to the second heating/cooling run. The melting point was determined to be 505 (507)°C. The small endothermic effects at 239 (242)°C correspond to the thermal decomposition of SbOCl [177]. Two transitions were observed on the cooling curve at 220 (211)°C and at 470 (472)°C, corresponding to the crystallisation temperature of SbOCl and $CoSb_2O_3Cl_2$, respectively.

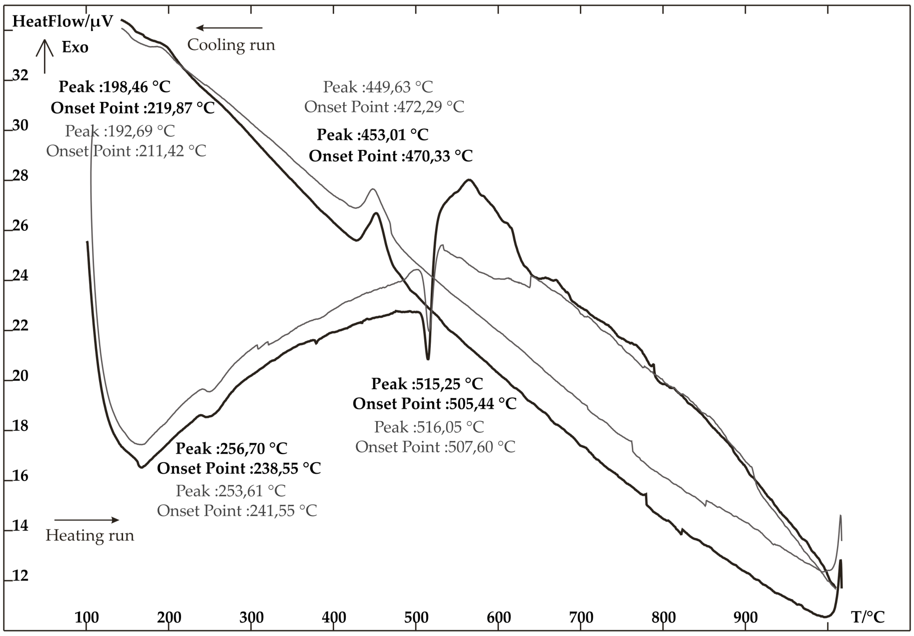

Figure 3.91.: DTA measurement of $CoSb_2O_3Cl_2$. The measurement was performed in the temperature range 100-1000 °C with a heating speed 10°C/min. The figure presents two series of sample heating/cooling. The direction of the heating and cooling runs are indicated by the corresponding arrows.

3.7.4. Magnetic properties

Magnetic-moment measurement of $CoSb_2O_3Cl_2$ was carried out using a SQUID (Superconducting Quantum Interference Device) magnetometer at 2 K, shown in Figure 3.92. The measured magnetic moment as a function of applied field was fitted using the Brillouin function for an ideal paramagnet. The magnetisation is given by

$$M = Ng\mu_B J \cdot B_J(x) \tag{3.1}$$

dependent on the Brillouin function

$$B_J(x) = \frac{2J+1}{2J} \coth\left(\frac{2J+1}{2J}x\right) - \frac{1}{2J} \coth\left(\frac{1}{2J}x\right) \tag{3.2}$$

where x is the ratio of the Zeeman energy of the magnetic moment in the external field to the thermal energy.

$$x = \frac{g\mu_B JB}{k_B T} \tag{3.3}$$

In these equations N is the number of atoms per unit volume, g is the g-factor, J is the total angular momentum quantum number, and μ_B is the Bohr magneton, and k_B is the Boltzmann constant. An additional term was added to the fit representing diamagnetic behaviour, which explains the falling absolute value of the magnetisation at higher applied fields. The function was fit to $J = 3/2$ and $g = 2.09$. Spin-only magnetism with $J = 3/2$ corresponds to the Co^{2+} with $3d^7$ high-spin-configuration and groud state $^4A_2$. This result would be expected for tetrahedral crystal field symmetry [178] and is surprising due to the slightly distorted octahedral environment for Co atoms in $CoSb_2O_3Cl_2$. It is however the same as the value measured for $CoSb_2O_3Br_2$ [33]. It should be noted that the value of g in the curve fit is very sensitive to small measurement errors. A temperature dependent measurement was attempted but was unsuccessful due to limitations in the apparatus.

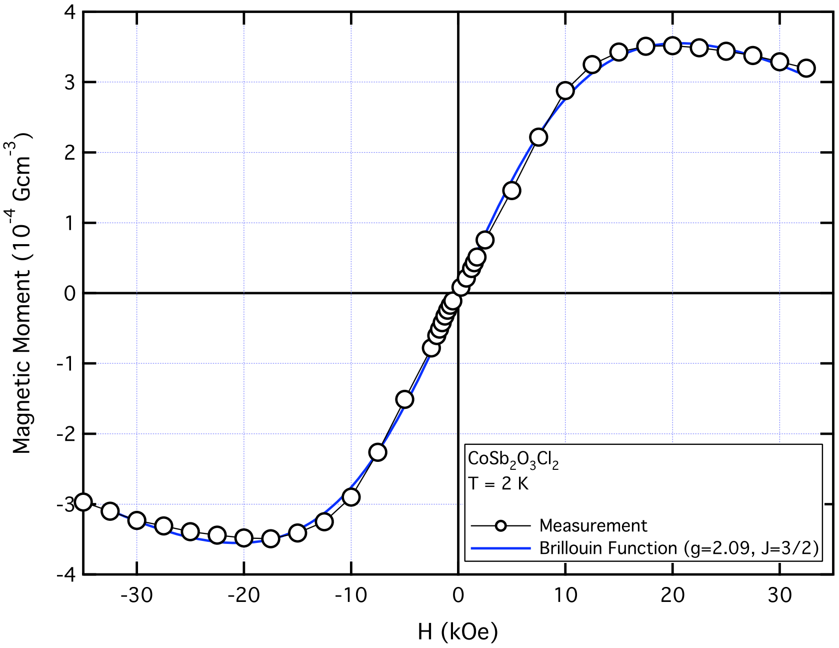

Figure 3.92.: Magnetic moment vs applied field at 2K for $CoSb_2O_3Cl_2$. The solid line represents the best fit to the Brillouin function with a diamagnetic correction term.

3.8. $Sb_4O_5Cl_2$

Several antimony (III) oxychlorides have been widely used in various industries, mostly because of excellent flame retardancy when utilized alone or in combination with halogenated organic compounds [179]. The architecture of the crystal structure of $Sb_4O_5Cl_2$ has been the subject of several investigations. Research on the structure was performed as a part of general study of the O coordination of Sb(III). Antimony (III) oxychloride was first prepared by Sabanejew in 1871 [180]. A detailed study of the system $Sb_2O_3/HCl/H_2O$ resulting in the discovery of stable solid compounds $Sb_4O_5Cl_2$, SbOCl and Sb_2O_3 was carried out by Lea and Wood [181], whereas the structure was first solved by Edstrand in 1947 [182]. It was later redetermined by Särnstrand in 1978 [183]. Due to rather old investigations and scant information about the details of the data collection and results of the structure refinement, the crystal structure of $Sb_4O_5Cl_2$ has been reinvestigated and is discussed in this work. Recently published scientific works also provide informations about the synthesis on a large scale of $Sb_4O_5Cl_2$ and $Sb_8O_{11}Cl_2$ as nanomaterials [184].

3.8.1. Synthesis

Initially $Sb_4O_5Cl_2$ was prepared according to Edstrand [35]. Solid α-Sb_2O_3 was disolved in HCl and then various amounts of water were added. The precipitates were filtered off with suction and dried in an desiccator with P_2O_5.

Subsequently the best crystals of $Sb_4O_5Cl_2$ were obtained by solvothermal reaction of α-Sb_2O_3 and HCl in a sealed evacuated silica tube placed into a teflon tube with water, and annealed at 180°C for 8 days. The synthesis products were a mixture of white powder and colourless plate-like crystals.

3.8.2. Single crystal and powder X-ray diffraction analysis

Single-crystal X-ray diffraction data were collected at room temperature on a STOE IPDS image-plate diffractometer equipped with graphite-monochromator and Mo-Kα radiation (λ = 0.71073 Å). The structural model was solved by direct methods using the program *SHELXS-97* [I] and refined by full-matrix least squares fit on F^2 using *SHELXL-97* [J]. Intensity data were corrected for absorption effects using the numerical absorption correction for a 3-dimentional integration over all X-ray beam paths in the crystal with *X-RED* [L]. The crystal shape and size for numerical absorption correction using symmetry-equivalent reflections or reflections measured more than once was performed by *X-SHAPE* [M]. All data pertaining to the single-crystal X-ray experiment are given in Table 3.37.

Tables containing information about final atomic coordinates and equivalent isotropic displacement parameters for $Sb_4O_5Cl_2$ are listed in the appendix (Table B.29). Table B.30 includes anisotropic displacement parameters. An extinction parameter was included in the last refinement cycles.

Table 3.37.: Details of the data collection and results of the structure refinement for $Sb_4O_5Cl_2$.

Crystal data	
Chemical formula	$Sb_4O_5Cl_2$
Crystal colour/habit	colourless/plate
Crystal size	0.09 × 0.06× 0.03 mm
Molecular weight	637.90 g mol^{-1}
Calculated density	4.900 g cm^{-3}
Space group	$P2_1/c$ (No. 14)
Lattice parameters	$a = 6.2900(5)$ Å
	$b = 5.115(3)$ Å $\beta = 97.280(5)°$
	$c = 13.5470(8)$ Å
Cell volume, Z	432.3(3) Å^3, 2
Data collection	
Device	STOE IPDS I
Radiation	Mo-Kα, 0.71073 Å
	graphite monochromator
Temperature	293(2)K
Scan range	$3.03° \leqslant 2\theta \leqslant 26.56°$
hkl range	$-7 \leqslant h \leqslant 7$
	$-6 \leqslant k \leqslant 6$
	$-16 \leqslant l \leqslant 16$
Structure solution and refinement	$Sb_4O_5Cl_2$
Measured reflections	6175
Independent reflections	884
Independent reflections with $F_O > 4\sigma(F_O)$	795
R_{int}	0.0285
R_σ	0.0161
Structure solution	SHELXS97 [I]
Structure refinement	SHELXL97 [J]
Number of parameters	53
Absorption correction	numerical: X-RED [L], X-SHAPE [M]
Absorption coefficient	12.969 mm^{-1}
$R_1, wR_2[I > 3\sigma(I)]$	0.0178, 0.0382
$R_1, wR_2[\text{all reflections}]$	0.0219, 0.0390
GooF	1.105
F(000)	556
Residual electron density	0.760, -0.972 e Å^{-3}

The final composition of $Sb_4O_5Cl_2$ was additionally confirmed by powder X-ray diffraction, followed by successful stoichiometric synthesis. All peaks of the X-ray powder diffraction diagram were indexed in an monoclinic unit cell. On the basis of 86 reflections the cell ($P2_1/c$, a = 6.290(5)Å, b = 5.115(3)Å, c = 13.547(8)Å, β = 97.28(5)°) was determined. The parameters obtained from powder X-ray diffraction measurement were subsequently employed in single crystal refinement. Verification of the structural model for $Sb_4O_5Cl_2$ was performed by comparision of theoretical and measured powder X-ray diffraction patterns. In parallel, the compound $Sb_4O_5Br_2$ was synthesized. The final product was inspected by powder X-ray diffraction analysis. On the basis of 48 reflections lines the cell ($P2_1/c$, a = 6.620(1)Å, b = 5.1480(8)Å, c = 13.475(3)Å, β = 97.889(1)°) was determined. All figures are presented in the appendix (refer to Figures B.48, B.49, and B.50).

The structure consists of layers perpendicular to [100] made up of antimony oxide building blocks and chlorine atoms positioned in the non-bonding volume between adjacent $^1_\infty[Sb_4O_5^{2+}]$ polymers, as shown in Figure 3.93.

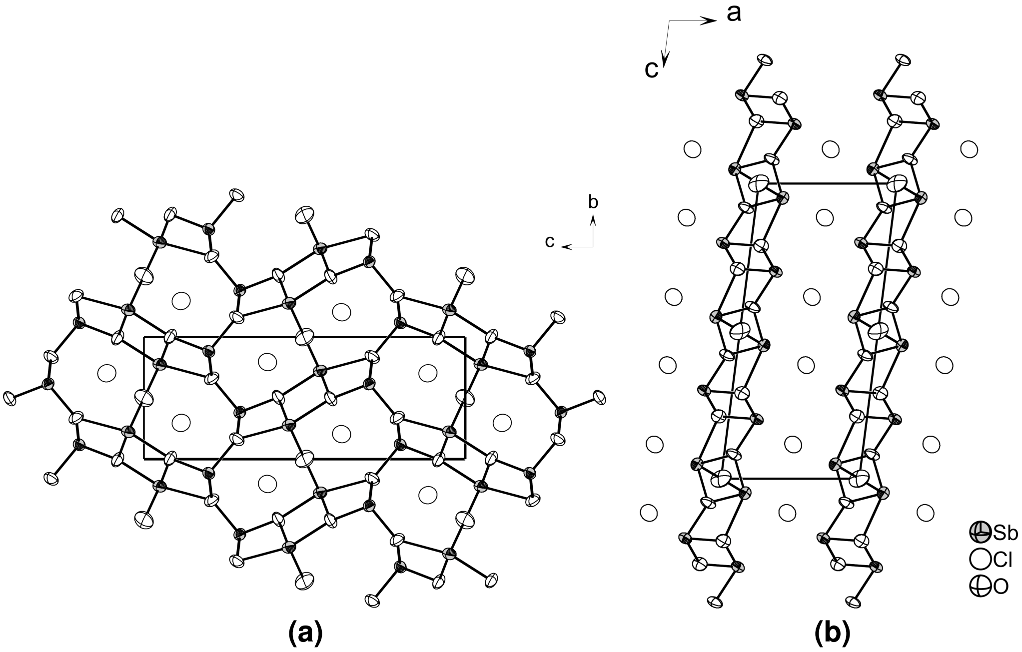

(a) **(b)**

Figure 3.93.: Projection of the crystal structure of $Sb_4O_5Cl_2$ a) along the a axis, b) onto the [010] direction, presenting the isolated rods of $^1_\infty[Sb_4O_5^{2+}]$ and chlorine atoms.

The tendency for segregation of the oxidic and halidic parts was also observed for other antimony (III) oxyhalides: Sb_3O_4X (X = Cl, I) [185, 186], $Sb_8O_{11}X_2$ (X = Cl, Br, I) [187,91,188], SbOCl [189], and Sb_5O_7I [190,191,192]. All antimony (III) oxychlorides are presented in Figure 3.94. The creation of such a structural motif can be explained by the chemical nature of the Sb^{3+} cation. Antimony as a rather strong and hard Lewis acid prefers to bond to an oxygen anion, which is a stronger Lewis base and harder ion in comparision with a halide ion.

The environment around Sb(III) results in two types of polyhedra. The coordination polyhedra of Sb1 is trigonal bipyramid, where one of the equatorial corners is occupied by a lone electron pair, which was considered by J. Galy *et al.* [14] to occupy a volume of the same size as an O^{2-} ion. Sb2 is coordinated by three oxygen atoms and one chlorine atom in its second coordination sphere, which results in a trigonal bipyramid coordination polyhedron. However analysis of the bond lengths shows that d(Sb2-Cl1) = 2.920(4) Å have a predominantly ionic character, since normal covalent bond lengths d(Sb-Cl) $\approx$ 2.35 Å in pure $SbCl_3$ [193]. Additionally a bond valence of 0.22 was obtained for d(Sb2-Cl1) = 2.920(4) Å from BVS calculations, indicating a small contribution, which indicates that the chlorine atom is ionically bonded (refer to Table 3.38 and 3.39). The bond valences were determined using empirical parameters: $b = 0.37$ Å, $r_0(Sb^{3+}$-O) = 1.997 Å, $r_0(Sb^{3+}$-Cl) = 2.368 Å. This suggest that the coordination polyhedron of Sb(2) is a tetrahedron, where one of the vertices is occupy a lone pair. Bonding distances d(Sb-O) in the range 1.9037-2.463 Å are appropriate compared to the value 1.977 Å for senarmontite [104, 68] and slightly longer than the average bond length of 2.006 Å for valentinite [69, 68]. The projection of coordination polyhedra for antimony atoms in $Sb_4O_5Cl_2$ is shown in Figure 3.95.

According to Galy *et al.* [14] it is suggested that only a slight displacement of the Sb atom out of the equatorial plane of the trigonal bipyramid enforces the change of coordination from four to three, as shown in Figure 3.96. Table 3.38 presents the bond lengths and angles in $Sb_4O_5Cl_2$, which were additionally compared with those obtained by Särnstrand [183].

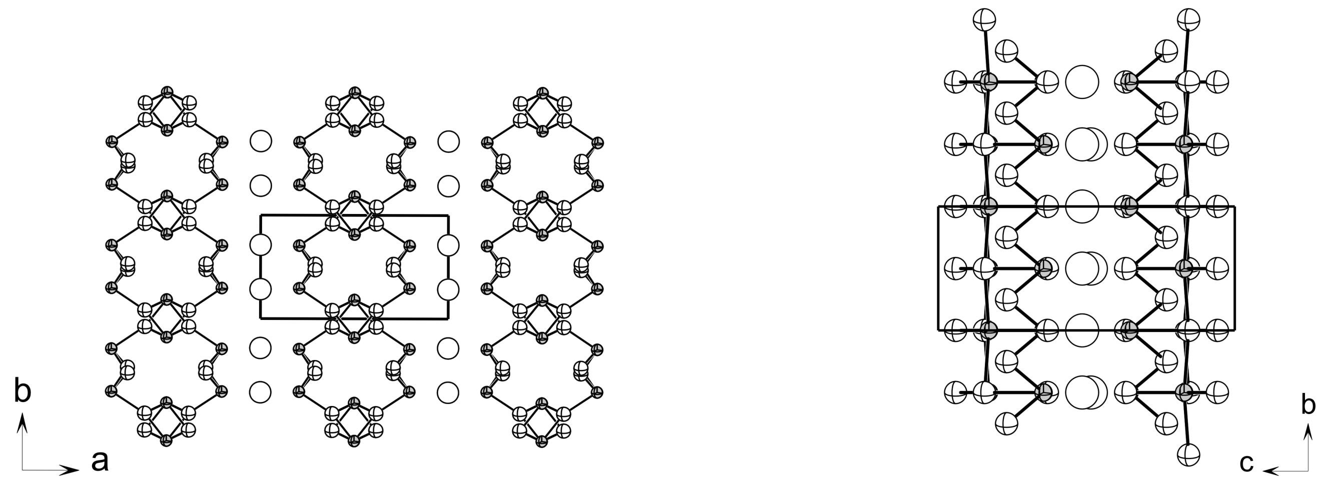

(a) Sb_3O_4Cl [185]

(b) $Sb_8O_{11}Cl_2$ [187]

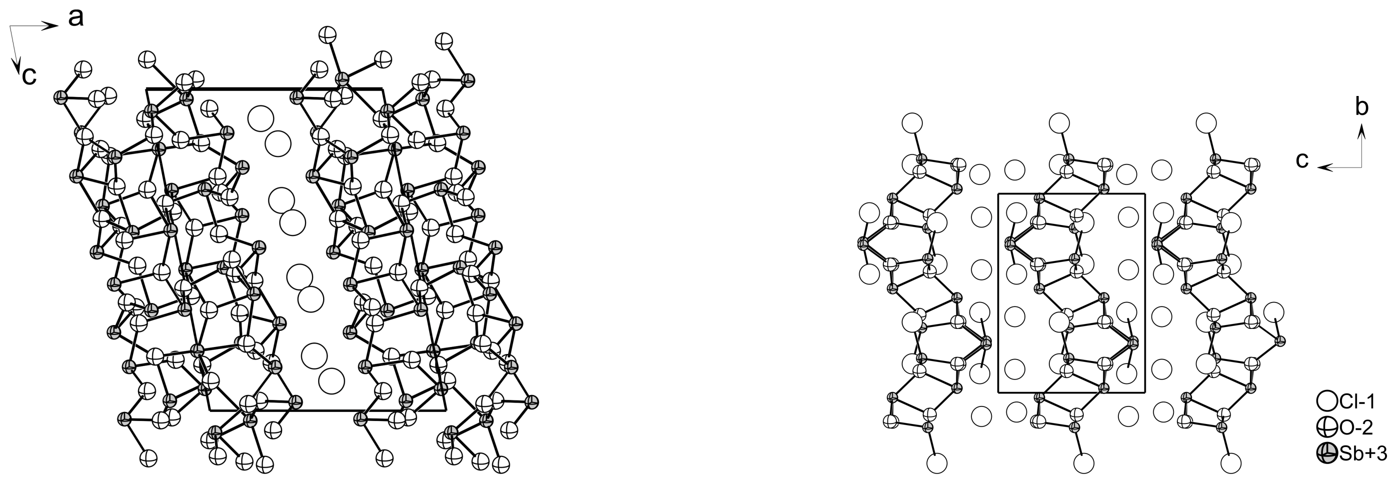

(c) $Sb_8O_{11}Cl_2$ [91]

(d) SbOCl [189]

Figure 3.94.: View of a general tendency for segregation of the oxidic and halidic parts in previously reported antimony (III) oxychlorides: Sb_3O_4Cl, $Sb_8O_{11}Cl_2$ (monoclinic), $Sb_8O_{11}Cl_2$ (triclinic) and SbOCl.

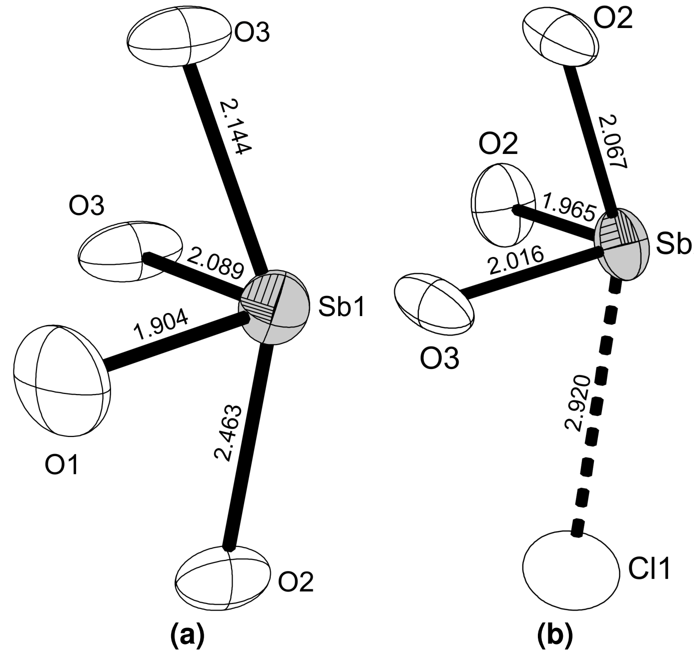

Figure 3.95.: Coordination of Sb1 and Sb2 in $Sb_4O_5Cl_2$. Bond lengths are shown in Å. The thermal vibration ellipsoids were scaled to include 80% probability.

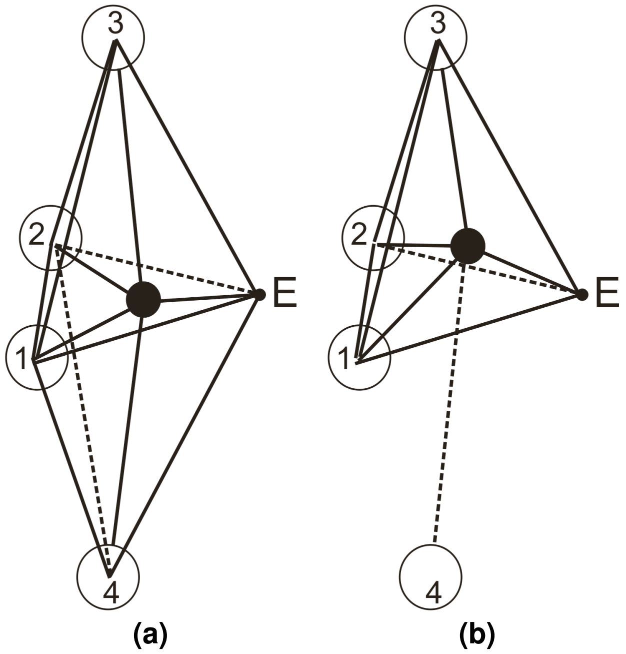

Figure 3.96.: Coordination polyhedra of Sb (III). Oxygen atoms are denoted as 1, 2, 3, and 4, and lone pairs of Sb (III) as E. Subfigures: a) trigonal bipyramid $[SbO_4E]$, b) tetrahedron $[SbO_3E]$ with one next-nearest neighbour (dotted line) [183].

Table 3.38.: Bond lengths (Å) and angles(°) for $Sb_4O_5Cl_2$. Values in square brackets are from Särnstrand [183]. Symmetry codes: (i) x, y, -1+z; (ii) 1-x, -0.5+y, 0.5-z

	Bond distance (Å)		Bond valence		
Sb(1)-O(1)	1.9037(7)	[1.898(0)]	1.21		
Sb(1)-O(3)	2.089(3)	[2.081(4)]	0.73		
Sb(1)-O(3)^{i}	2.144(3)	[2.141(4)]	0.63		
Sb(1)-O(2)	2.463(3)	[2.459(4)]	0.27		
Sb(2)-O(2)^{ii}	1.965(3)	[1.960(4)]	1.02		
Sb(2)-O(3)	2.016(3)	[2.009(4)]	0.89		
Sb(2)-O(2)	2.067(3)	[2.059(4)]	0.78		
Sb(2)-Cl(1)	2.920(4)	[2.909(2)]	0.22		
Angles (°)					
O(1)-Sb(1)-O(3)	91.65(9)	[92.0(1)]	Sb(1)-O(1)-Sb(1)	180.000(2)	[180]
O(1)-Sb(1)-O(3)	88.21(9)	[88.3(1)]	Sb(2)-O(2)-Sb(2)	135.73(2)	[135.7(2)]
O(1)-Sb(1)-O(2)	84.19(8)	[84.4(1)]	Sb(2)-O(2)-Sb(1)	124.43(1)	[124.8(2)]
O(3)-Sb(1)-O(3)	72.06(1)	[72.2(2)]	Sb(2)-O(2)-Sb(1)	98.73(1)	[98.4(2)]
O(3)-Sb(1)-O(2)	67.86(1)	[68.0(1)]	Sb(2)-O(3)-Sb(1)	114.26(1)	[114.0(2)]
O(3)-Sb(1)-O(2)	138.88(1)	[139.2(1)]	Sb(2)-O(3)-Sb(1)	133.84(2)	[134.2(2)]
O(2)-Sb(2)-O(3)	94.44(1)	[94.6(2)]	Sb(1)-O(3)-Sb(1)	107.94(1)	[107.8(2)]
O(2)-Sb(2)-O(2)	94.46(7)	[94.7(1)]			
O(3)-Sb(2)-O(2)	77.63(1)	[78.0(2)]			

Table 3.39.: Atomic coordinates, equivalent isotropic displacement parameter [Å^2] and bond valence sum for $Sb_4O_5Cl_2$.

Atom	x	y	z	U^{eq}	BVS
Sb(1)	0.18690(4)	0.22347(5)	0.04889(2)	0.01539(1)	2.84
Sb(2)	0.79666(4)	0.11702(5)	0.20158(2)	0.01494(1)	2.92
O(1)	0	½	0	0.0355(1)	1.21
O(2)	0.0739(5)	0.3377(6)	0.2110(2)	0.0195(6)	2.07
O(3)	0.0703(5)	0.0048(6)	0.9181(2)	0.0195(6)	2.25

3.8.3. Raman spectroscopy

Vibrational spectra were recorded on a Varian FT-Raman module with dielectric YAG rejection filters, with 2 cm^{-1} resolution. Raman spectroscopic investigations of samples show only vibrations which can be attributed to α-Sb_2O_3 and β-Sb_2O_3 [77, 78], (Figure 3.97). The bands at 466, 388, 367 correspond to vibrations caused by the deformation of Sb-O-Sb bonds, considered as symmetric or asymmetric combinations of stretching vibrations. Combinations of scissoring, wagging, and twisting deformation vibrations appear at lower Raman shifts.

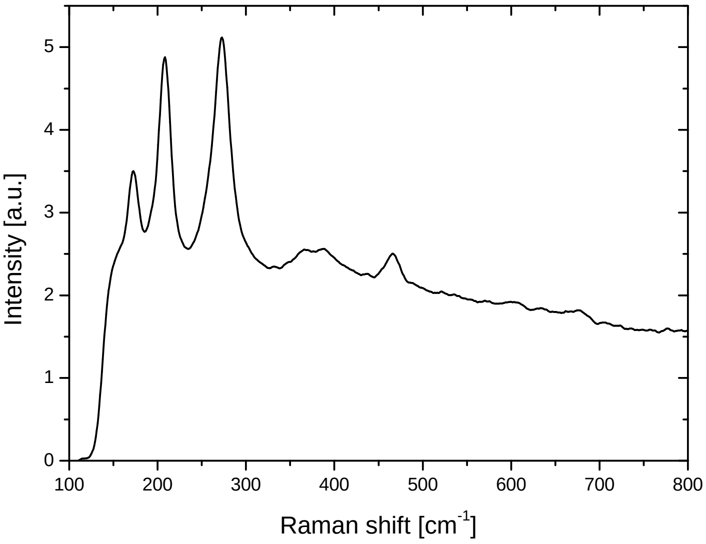

Figure 3.97.: Raman spectrum of $Sb_4O_5Cl_2$ showing significant vibrations only for $\nu_{\mathrm{Sb-O}}$.

An exact correlation of the Raman modes with the peaks in the Raman spectra can only be carried out by way of a theoretical calculation of the Raman spectra based on the extracted crystal structures. These calculations will be one of the goals of future work in this area.

3.8.4. ATR-IR

The irfrared spectrum of $Sb_4O_5Cl_2$ was recorded on Varian 670-IR FT-IR spectrometer. A sample was measured using the ATR technique, on a Gladi ATR Base Optic Assembly with a 2.2 mm $\times$ 3.0 mm ATR diamond crystal sampling area, located in the center of the plate. Analysis of FT-IR spectra was performed using *Resolution Pro* [T]. IR measurements were performed in range 150-400 cm^{-1} (F-IR) and 400-4000 cm^{-1} (M-IR). Table 3.40 presents Raman and IR spectral data for $Sb_4O_5Cl_2$.

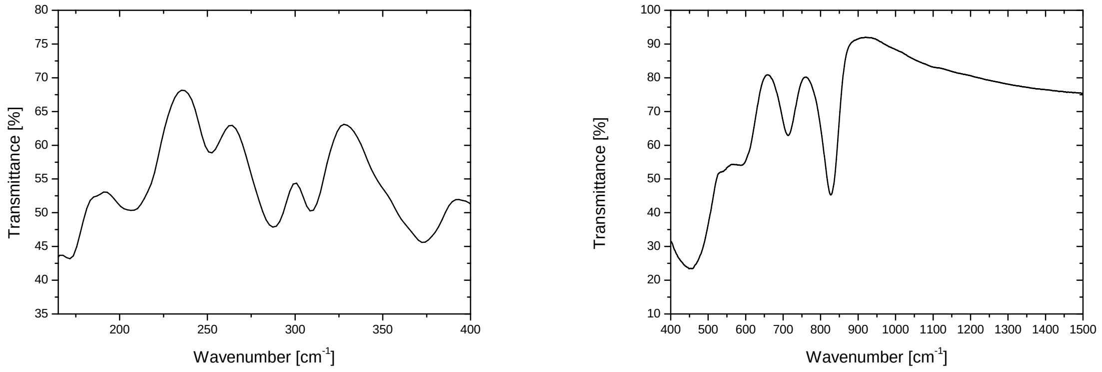

(a) **(b)**

Figure 3.98.: F-IR and M-IR spectra of $Sb_4O_5Cl_2$ showing significant vibrations only for $\nu_{\mathrm{Sb-O}}$. There were no vibrations in the range 1500-4000 cm^{-1}.

Table 3.40.: Summary of modes occuring in Raman and IR spectra of $Sb_4O_5Cl_2$.

Raman (cm^{-1})	IR (cm^{-1})	Comments
172	172	twisting, sym. and asym. comb. $\delta(SbO_2)$
208	208	wagging, sym. and asym. comb. $\delta(SbO_2)$
	252	scissoring, sym. and asym. comb. $\delta(SbO_2)$
273	288	scissoring, sym. and asym. comb. $\delta(SbO_2)$
	309	scissoring, sym. and asym. comb. $\delta(SbO_2)$
367	373	ν_{asym} (SbO_3), sym. comb. ν_{sym} (Sb→O←Sb)
388		ν_{sym} (SbO_3), asym. comb. ν_{sym} (Sb→O←Sb)
466	456	ν_{sym} (SbO_3), sym. comb. ν_{sym} (Sb→O←Sb)
	587	sym. and asym. comb. ν_{asym} (Sb→O→Sb)
	713	sym. and asym. comb. ν_{asym} (Sb→O→Sb)
	827	sym. and asym. comb. ν_{asym} (Sb→O→Sb)

3.9. SbOCl

3.9.1. Synthesis

Crystals of SbOCl were obtained by solvothermal reaction of Sb_4O_6 and HCl in a sealed evacuated silica tube placed into a teflon tube with water, and annealed at 90°C for 5 days. The synthesis products were a mixture of white powder and colourless needle-shaped crystals.

3.9.2. Single crystal and powder X-ray diffraction analysis

The crystal structrure of SbOCl was previously described by Edstrand in 1953 [189]. Due to rather old investigations and scant information about the details of the data collection and results of the structure refinement, the crystal structure of SbOCl has been reinvestigated and discussed in this work. The crystal structures of SbOCl was determined from a colourless needle-shaped crystal by single crystal X-ray diffraction at room temperature. The structural solution was performed by direct methods using the program *SIR-92* [G]. Refinement of the model structure was done by the least squares method using *SHELXL-97* [J]. The compound crystallises in the monoclinic system, space group $P2_1/a$ (No. 14) with Z = 12, $a = 9.5917(2)$ Å, $b = 10.837(2)$ Å, $c = 7.9789(2)$ Å, $\beta = 76.33(3)°$. The refinement converged at $R_1, wR_2[I > 3\sigma(I)] = 0.0234, 0.0545$ and $R_1, wR_2[\mathrm{alldata}] = 0.0253, 0.0553$. Further information concerning the crystal structure solution and refinement data are presented in Table 3.41. Final atomic coordinates and equivalent isotropic displacement parameters for SbOCl are listed in the appendix in Table B.31, while Table B.32 includes anisotropic displacement parameters.

The crystal structure of SbOCl consists of corrugated 2-dimensional layers perpendicular to the [001] crystallographic direction. The layers are built with edge-sharing [Sb(1)O_4], [Sb(3)O_3Cl] square pyramids and [Sb(2)O_2Cl] trigonal pyramids, or [Sb(1)O_4E], [Sb(3)O_3ClE] trigonal bipyramids and [Sb(2)O_2ClE] tetrahedra, if taking into account lone pairs of electrons designated as E. The Cl^- anions and lone pairs of electrons of Sb^{3+} are located in the empty interlayer space. The general network is shown in Figure 3.99 by the projection of the stucture onto the [100] plane.

The average d(Sb-O) bond distance amounts to 2.1319 Å and is about 0.1 Å longer than 1.977 Å for senarmontite [104, 68] and than the average bond length 2.006 Å for valentinite [69, 68]. Analysis of the bond lengths shows that d(Sb2-Cl3) = 2.3885(2) Å and d(Sb3-Cl1) = 2.3997(1) Å have a predominantly covalent character, since the normal covalent bond lengths in pure $SbCl_3$ [193] is d(Sb-Cl) $\approx$ 2.35 Å. It was also confirmed by bond valence sum calculations, that the distances d(Sb2-Cl3) = 2.3885(2) Å and d(Sb3-Cl1) = 2.3997(1) Å correspond to a bond valence of 0.95 and 0.92, respec-

Table 3.41.: Details of the data collection and results of the structure refinement for SbOCl.

Crystal data		
Chemical formula	SbOCl	
Crystal colour/habit	colourless/needle	
Crystal size	0.2 × 0.1× 0.1 mm	
Molecular weight	173.20 g mol^{-1}	
Calculated density	4.283 g cm^{-3}	
Space group	$P2_1/a$ (No. 14)	
Lattice parameters	$a = 9.5917(2)$ Å	
	$b = 10.837(2)$ Å	$\beta = 76.33(3)°$
	$c = 7.9789(2)$ Å	
Cell volume, Z	805.9(3) Å^3, 12	
Data collection		
Device	STOE IPDS I	
Radiation	Mo-Kα, 0.71073 Å	
	graphite monochromator	
Temperature	293(2)K	
Scan range	$2.63° \leqslant 2\theta \leqslant 26.44°$	
hkl range	$-11 \leqslant h \leqslant 11$	
	$-13 \leqslant k \leqslant 13$	
	$-9 \leqslant l \leqslant 9$	
Structure solution and refinement	SbOCl	
Measured reflections	11824	
Independent reflections	1639	
Independent reflections with $F_O > 4\sigma(F_O)$	1565	
R_{int}	0.0330	
R_σ	0.0152	
Structure solution	SIR92 [G]	
Structure refinement	SHELXL97 [J]	
Number of parameters	83	
Absorption correction	numerical: X-RED [L], X-SHAPE [M]	
Absorption coefficient	10.916 mm^{-1}	
$R_1, wR_2[I > 3\sigma(I)]$	0.0234, 0.0545	
R_1, wR_2[all reflections]	0.0253, 0.0553	
GooF	1.271	
F(000)	912	
Residual electron density	0.865, -0.910 e Å^{-3}	

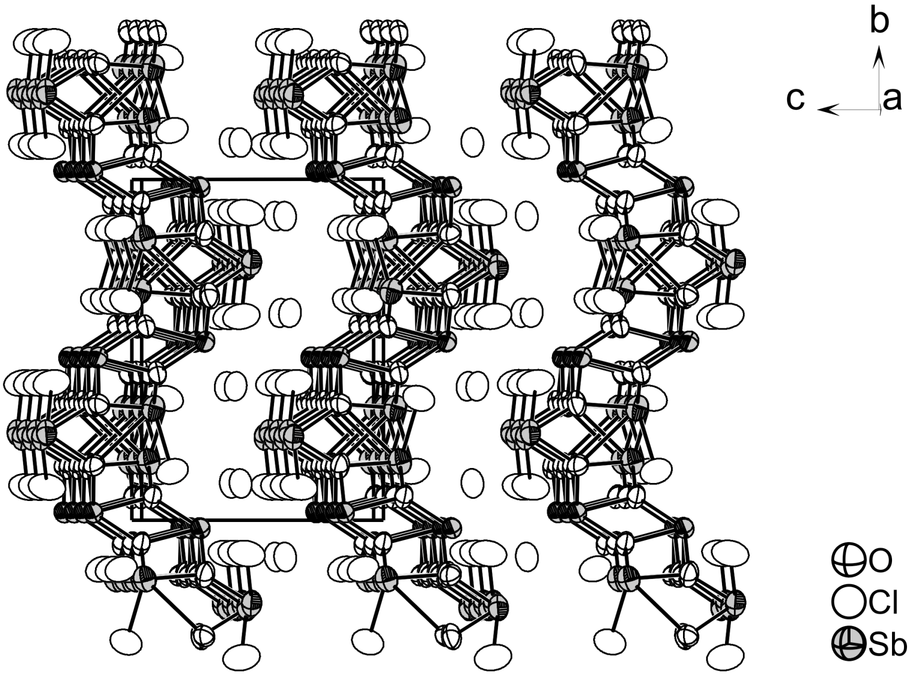

Figure 3.99.: Perspective view of the structure of SbOCl along [100], comprised of corrugated 2D layers separated by Cl$^-$ ions and lone pairs of electrons (5s^2) located in the free space between layers (90% probability level).

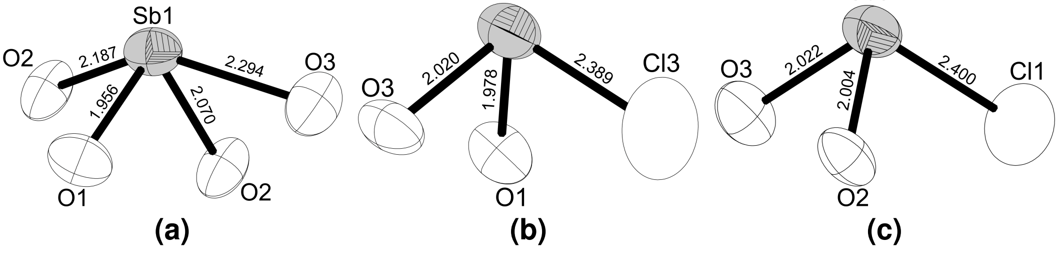

Figure 3.100.: Coordination of Sb1, Sb2 and Sb3 atoms in SbOCl. Bond lengths are shown in Å. (90% probability levels).

tively, indicating a large contribution and therefore must be considered as covalently bonded. On the other hand, the longer distance d(Sb1-Cl2) = 2.956(4) Å corresponds to a bond valence of 0.20 suggesting that Cl2 can not be considered to belong to the primary coordination sphere of Sb1, and one should tend to consider the chlorine atom Cl2 as ionically bonded (refer to Table 3.42 and Table 3.43). The bond valences were determined according to Brown [95, 194], using empirical parameters: $b = 0.37$ Å, r_0(Sb^{3+}-O) = 1.997 Å, r_0(Sb^{3+}-Cl) = 2.368 Å.

Table 3.42.: Bond distances and bond valence for SbOCl. Symmetry code: (i) 0.5+x, 0.5-y, z

	Bond distance (Å)	Bond valence
Sb(1)-O(1)	1.956(3)	1.05
Sb(1)-O(2)	2.070(3)	0.77
Sb(1)-O(2)^i	2.187(3)	0.56
Sb(1)-O(3)	2.294(3)	0.42
Sb(2)-O(1)	1.978(3)	0.99
Sb(2)-O(3)	2.020(3)	0.88
Sb(2)-Cl(3)	2.3885(2)	0.95
Sb(3)-O(3)	2.022(3)	0.88
Sb(3)-O(2)	2.004(3)	0.92
Sb(3)-Cl(1)	2.3997(1)	0.92

Table 3.43.: Atomic coordinates, equivalent isotropic displacement parameter [Å^2] and bond valence sum for SbOCl.

Atom	x	y	z	U^{eq}	BVS
Sb(1)	0.42519(3)	0.02302(3)	0.21845(4)	0.01747	2.80
Sb(2)	0.09038(3)	0.24350(3)	0.41703(4)	0.02104	2.81
Sb(3)	0.26922(3)	0.67180(3)	0.01865(4)	0.02089	2.71
Cl(1)	0.13089(2)	0.85700(1)	0.09071(2)	0.0343	0.92
Cl(2)	0.34491(1)	0.10777(1)	0.60599(1)	0.0267	0.67
Cl(3)	0.41092(2)	0.40240(1)	0.3880(2)	0.0400	0.95
O(1)	0.0565(4)	0.3390(3)	0.2191(4)	0.0197	2.03
O(2)	0.0943(3)	0.5686(3)	0.0269(4)	0.0184	2.25
O(3)	0.2395(4)	0.1588(3)	0.2315(4)	0.0214	2.18

3.9.3. Raman and infrared spectroscopy

The sample of SbOCl was additionally studied by Raman spectroscopy. Vibrational spectra were recorded on in the range 130-4500 cm^{-1}, with 2 cm^{-1} resolution. Eight modes were identified in the Raman spectra, in the frequency range 130-1000 cm^{-1} as presented in Figure 3.101.

All lattice vibrations can be attributed to the modes occuring in $SbCl_3$ [195] with a weak band at 139 cm^{-1}, and to α- and β-Sb_2O_3 with strong bands at 171, 205, 271, 363, 382, 464, and 675 cm^{-1}. As can be seen in Table 3.40 and Table 3.44, modes corresponding to ν_{Sb-O} in the Raman spectra of SbOCl and $Sb_4O_5Cl_2$ appear at comparable values of Raman shift. This suggest that both structures are based on the same Sb-O vibrations.

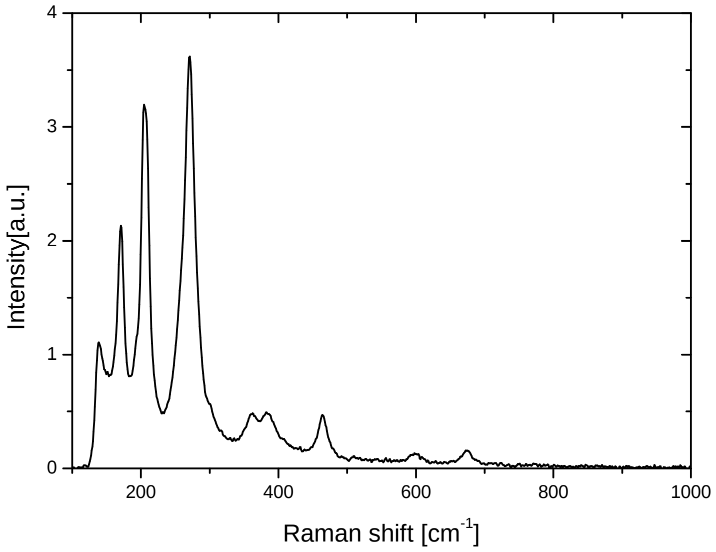

Figure 3.101.: Raman spectrum of SbOCl showing significant vibrations only for ν_{Sb-Cl} and ν_{Sb-O}.

In order to complete the picture of spectral information concerning SbOCl, the infrared absorption spectrum was recorded. A sample was measured using ATR technique in 150-400 cm^{-1} (F-IR) and 400-4000 cm^{-1} (M-IR) ranges. All spectroscopic data are summarized in Table 3.44.

An exact correlation of the Raman and IR modes with the peaks in the Raman and IR spectra can only be carried out by way of a theoretical calculation of the Raman and IR spectra based on the extracted crystal structures. These calculations will be one of the goals of future work in this area.

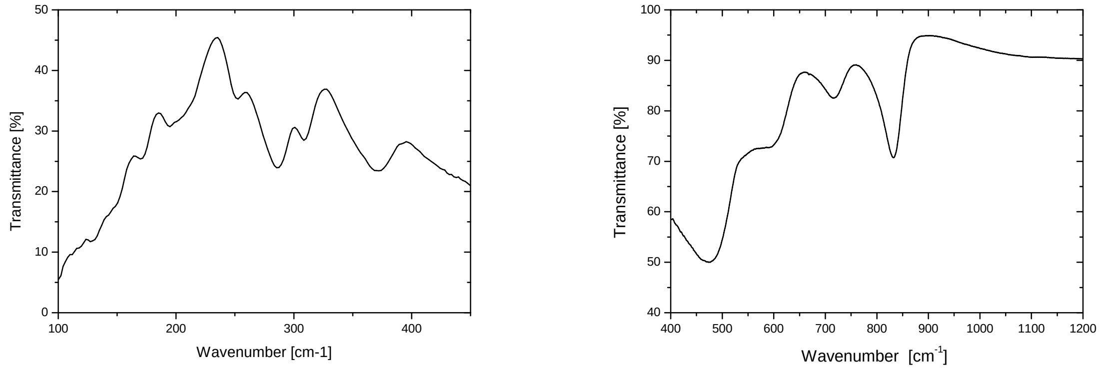

(a) **(b)**

Figure 3.102.: Infrared spectra of SbOCl showing significant vibrations only for ν_{Sb-Cl} and ν_{Sb-O}. There were no vibrations in the range 1200-4000 cm^{-1}.

Table 3.44.: Summary of modes occuring in Raman and IR spectra of SbOCl.

Raman (cm^{-1})	IR (cm^{-1})	
139	127	ν_{Sb-Cl}, intramolecular bending
171	170	twisting, sym. and asym. comb. $\delta(SbO_2)$
	194	twisting, sym. and asym. comb. $\delta(SbO_2)$
205		wagging, sym. and asym. comb. $\delta(SbO_2)$
	252	scissoring, sym. and asym. comb. $\delta(SbO_2)$
271	286	scissoring, sym. and asym. comb. $\delta(SbO_2)$
	308	scissoring, sym. and asym. comb. $\delta(SbO_2$
363	372	ν_{asym} (SbO$_3$), sym. comb. ν_{sym} (Sb→O←Sb)
382		ν_{sym} (SbO$_3$), asym. comb. ν_{sym} (Sb→O←Sb)
464	476	ν_{sym} (SbO$_3$), sym. comb. ν_{sym} (Sb→O←Sb)
	589	sym. and asym. comb. ν_{asym} (Sb→O→Sb)
675		sym. and asym. comb. ν_{asym} (Sb→O→Sb)
	717	sym. and asym. comb. ν_{asym} (Sb→O→Sb)
	832	sym. and asym. comb. ν_{asym} (Sb→O→Sb)

3.10. $Sb_8O_{11}I_2$

3.10.1. Synthesis

Needle shaped single crystals of $Sb_8O_{11}I_2$ were initially prepared by solid state reaction of a mixture of NH_4I and Sb_2O_3 in 2:1 molar ratio in an attempt to obtain a $NH_4Sb_2O_3I$ phase. All reactants were thoroughly ground and sealed in an evacuated silica tube. The quartz ampoule was heated at 450°C for 8 days. The results of the single crystal X-ray diffraction analysis indicated the presence of $Sb_8O_{11}I_2$ crystal structure. The final composition was also confirmed by EDX analysis giving $Sb_{7.77}O_{11.21}I_{2.02}$. Subesquently a compound was synthesised from SbI_3 and Sb_4O_6 mixed in a 4:11 molar ratio. The starting materials were ground, sealed in an evacuated quartz ampoule and heated at 450°C for 8 days. The synthesis product besides white powder contained several single crystals of $Sb_8O_{11}I_2$.

3.10.2. Single crystal and powder X-ray diffraction analysis

Antimony (III) oxide iodides have been a subject of several previous investigations [196, 197, 198, 199]. They typically show a preferences to segregation of the structure to oxidic and halidic parts. This phenomenon can be easily explained with Lewis acidity/alkalinity, which plays the main role in bond formation preferences. Similar structural entities were observed in onoratoite family with composition $Sb_8O_{11}X_2$ (X = Cl, Br, I) [187,188,197,198]. The chemical nature of Sb^{3+} and the presence of the lone pairs of electrons have a large influence on the structural architecture. They consist of 2D slabs built by 1D Sb_8O_{11} units with halide cations between adjacent building blocks, resulting in a crystal structure somewhere between slab and columnar. The crystal structure of $Sb_8O_{11}I_2$ was solved by Kraemer *et al.* [200] and described in the monoclinic space group $C2/m$. It was later redetemined by Lidin *et al.* [188] and reported as an incommensurately modulated structure. Two Cl and Br analogues of $Sb_8O_{11}X_2$ have been previously solved in a triclinic unit cell combined wtih complex twinning [91] without presenting a structural model.

In this section, the crystal structure of $Sb_8O_{11}I_2$ refined in a triclinic unit cell is reported. The crystal structures were determined from a colourless needle-shaped crystals by single crystal X-ray diffraction at room temperature. The structural solution was performed by direct methods using the program *SHELXS-97* [I]. The structural model was refined by full matrix least squares of F using the program *JANA2000* [R]. The structure exhibits a pseudomerohedral twinning, mimicking monoclinic symmetry with a twin law -¾ ¼ ¼, ½ -½ ½, $\frac{5}{4}$ $\frac{5}{4}$ ¼. Details of the data collection and results of the structure refinement for $Sb_8O_{11}I_2$ are presented in Table 3.45. The lattice $Sb_8O_{11}I_2$ is expected to be isostructural to Cl and Br analogues, however a closer look at the structural model reveals a different setting of the unit cells, as shown in Figure 3.103. Attempts were made to describe the structure in a cell corresponding to that found for $Sb_8O_{11}X_2$ (X = Cl, Br) [91]. The transformation matrix was 010, 011, -100. After transformation the unit cell $a = 11.604(2)$ Å, $b = 17.356(4)$ Å, $c = 9.914(2)$ Å, $\alpha = 68.281(2)°$, $\beta = 76.212(2)°$, $\gamma = 62.290(2)°$ was found. The angles are now all acute and not too different to the angles reported in [91] but the b and c axes are very different. This suggests that when going from the chloride to the iodide, rather large shear processes take place in the structure, so that in spite of the topological relationship the structures are not exactly isostructural. The differences between the I - and Cl- compounds were discussed by Lidin [188].

Anisotropic displacement parameters were used for all atoms except oxygen O24, because of high displacement parameter for this atom, amounting to 0.1369(2). Final atomic coordinates and equivalent isotropic displacement parameters for $Sb_8O_{11}I_2$ are listed in the appendix in Table B.33, while Table B.34 includes anisotropic displacement parameters.

The sample was additionally analyzed by powder X-ray diffraction, showing that the white powder beside colourless crystals is mainly the target phase. All data concerning phase analysis is presented in the appendix in Figure B.51 and Figure B.52.

The crystal structure consists of building blocks of $[Sb_8O_{11}]$ units and layers of halide ions located in between $[Sb_8O_{11}]_\infty$ slabs, as seen in Figure 3.104. The lone pairs of electrons and the halide ions are located in empty spaces between Sb-O tubes.

Two types of antimony (III) arrangement appear in the structure, resulting in trigonal pyramid $[SbO_3]$ and tetragonal pyramid $[SbO_4]$ or, taking into account the lone pair of electrons, tetrahedra $[SbO_3E]$ and trigonal bipyramid $[SbO_4E]$, respectively. These polyhedra, through edge and corner sharing, form two types of ladder chains in the structure, as shown in Figure 3.105. The Sb-O bond lengths fall in the range 1.92(2)-2.497(1) Å, which is in good agreement with Sb-O distances reported for $Sb_8O_{11}X_2$ (X = Cl, Br).

The shortest cation-anion separation Sb11...I4 = 3.397(4) Å is much longer than the bond lengths for covalent Sb-I in monoclinic SbI_3 [201], suggesting only ionic interaction between antimony and iodine anions within the structure.

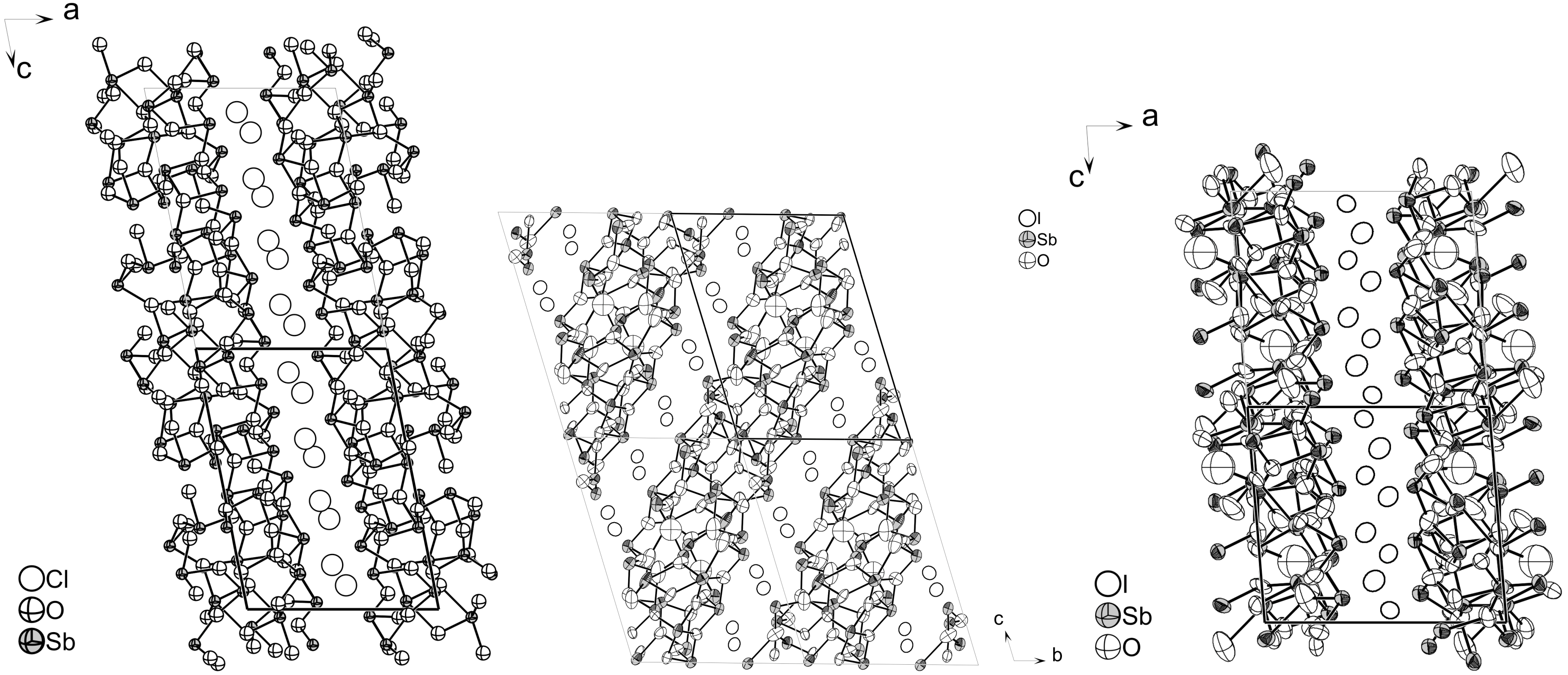

(a) $Sb_8O_{11}Cl_2$ [91] **(b)** $Sb_8O_{11}I_2$ before cell transformation **(c)** $Sb_8O_{11}I_2$ after cell transformation

Figure 3.103.: Projection of the crystal structures of $Sb_8O_{11}X_2$ (X = Cl, I) along [010] for $Sb_8O_{11}Cl_2$ and $Sb_8O_{11}I_2$ after cell transformation and [100] for $Sb_8O_{11}I_2$ before cell transformation, showing differences between the two structures. (90% probability level)

Table 3.45.: Details of the data collection and results of the structure refinement for $Sb_8O_{11}I_2$.

Crystal data	
Chemical formula	$Sb_8O_{11}I_2$
Crystal colour/habit	colourless/needle
Crystal size	0.05 × 0.04× 0.15 mm
Molecular weight	1403.80 g mol^{-1}
Calculated density	4.906 g cm^{-3}
Space group	$P-1$ (No. 2)
Lattice parameters	$a = 9.914(2)$ Å $\alpha = 102.951(2)°$ $b = 11.604(2)$ Å $\beta = 103.412(2)°$ $c = 15.767(3)$ Å $\gamma = 103.788(2)°$
Cell volume, Z	1636.9(6) $Å^3$, 4
Data collection	
Device	STOE IPDS I
Radiation	Mo-Kα, 0.71073 Å graphite monochromator
Temperature	293(2)K
Scan range	$1.89° \leqslant 2\theta \leqslant 25.37°$
hkl range	$-11 \leqslant h \leqslant 11$ $-13 \leqslant k \leqslant 13$ $-18 \leqslant l \leqslant 18$
Structure solution and refinement	$Sb_8O_{11}I_2$
Measured reflections	16101
Independent reflections	5525
Independent reflections with $F_O > 4\sigma(F_O)$	4345
R_{int}	0.0382
R_σ	0.0325
Structure solution	SHELXS97 [I]
Structure refinement	JANA2000 [R]
Number of parameters	375
Absorption correction	numerical: X-RED [L], X-SHAPE [M]
Absorption coefficient	14.917 mm^{-1}
$R_1, wR_2[I > 3\sigma(I)]$	0.0472, 0.1000
R_1, wR_2[all reflections]	0.0628, 0.1070
GooF	1.118
F(000)	2196
Residual electron density	3.241, -2.764 e $Å^{-3}$

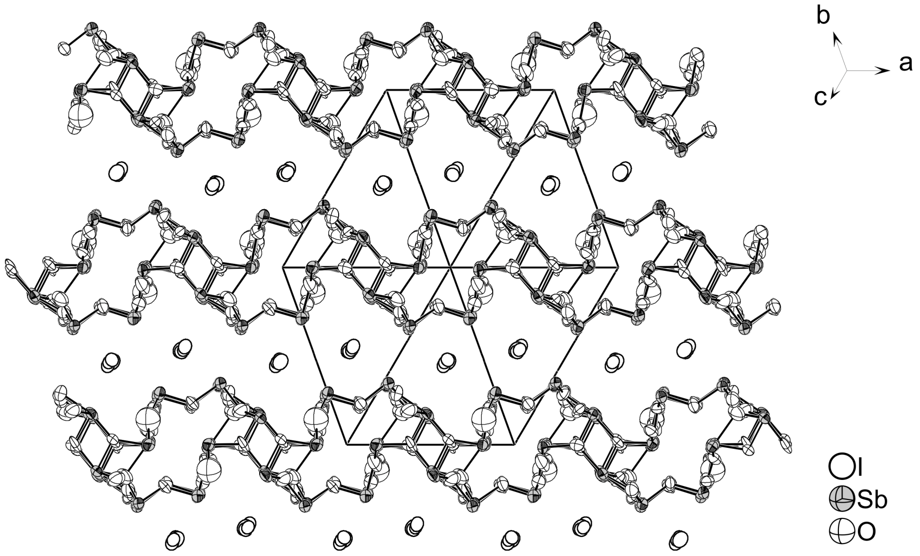

Figure 3.104.: Projection on the crystal structure of $Sb_8O_{11}I_2$ along [111], emphasizing the layers built by antimony (III) oxide infinite tubes and iodide ions located in between (70% probability level).

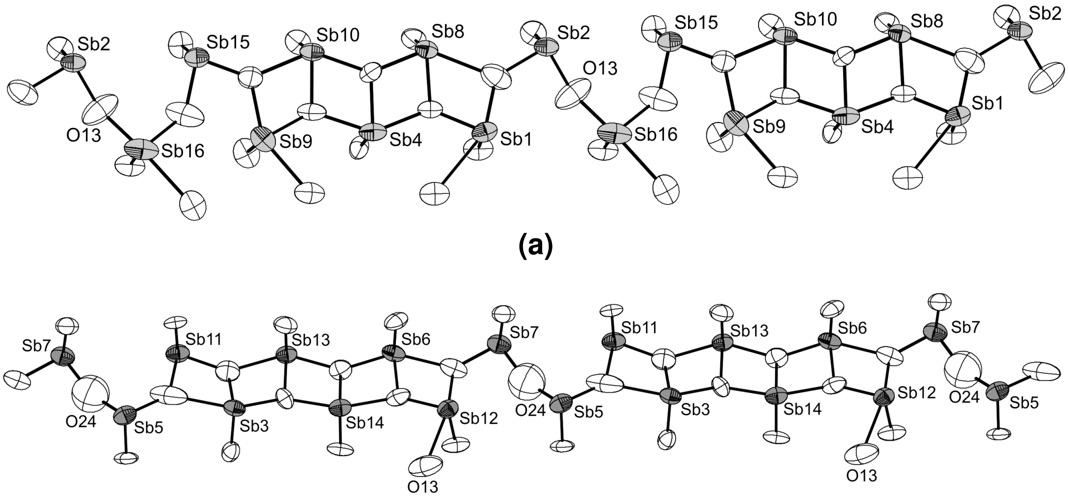

Figure 3.105.: Projection of two types of ladder chains built by Sb^{3+} three and four coordinated by oxygens, forming infinite tubes along [111].

4. Conclusions

This work was dedicated to research into a group of new compounds belonging to the transition metal antimony (III) oxidehalides, following the synthesis concept of forming oxidehalides containing transition metal and p-element cations. The principle area of concern was the use of Sb^{3+} as a lone pair element, since only a limited number of investigations have been reported in the literature. Transition metal cations Co^{2+}, Zn^{2+}, and Cd^{2+} were used. New synthetic compounds were obtained by solid state and hydrothermal synthesis techniques. Subsequently all materials were characterized by single crystal and powder X-ray diffraction measurements. Since it was difficult to distinguish antimony and cadmium atoms based on X-ray diffraction data, the crystal structure solutions were supported by MAPLE, ECoN, and BVS calculations. The composition of new compounds was additionally confirmed by EDX material analysis. For two samples ICP-OES measurements were performed. Thermal behaviour was characterised using thermoanalytical methods DTA, DSC and TG. In order to demonstrate the complementary information concerning the nature of bonding in investigated compounds, the vibrational spectra (Raman and IR) were recorded. Optical properties were investigated using UV-Vis spectroscopy, followed by electronic band gap calculations based on DFT theory.

All investigated crystal structures except $CoSb_2O_3Cl_2$ and SbOCl follow the general tendency in bonding preferences based on Lewis acidity or alkalinity that one expects to observe in this class of compounds. Antimony is a rather strong Lewis acid, and hence bonds to oxygen anions, which are a stronger Lewis base and harder ion than halides. Transition metals accept both oxygen and halide ions, resulting in an oxidehalide environment. This tendency resulted in a separation into oxidic and halidic parts in the reinvestigated ternary compounds SbOCl, $Sb_4O_5Cl_2$, and $Sb_8O_{11}I_2$. The halide anions are generally found in the volume between adjacent antimony oxide building blocks.

The presence of Sb^{3+} pnicogen cations has a large influence on the architecture of the compounds. They are asymmetrically coordinated due to the presence of stereochemically active lone pairs of electrons and have variable coordination (III or IV). The lone pairs of electrons, belonging to the Sb^{3+}, usually shared the non-bonded volumes with halide anions. Coexistence of lone pair elements and halide ions in the structure forced low-dimensional arrangements. These two factors are often called “structural scissors.” As a result of this, structures often takes the form of layers, chains, or tubes.

Several structural motifs obtained in the investigated crystal structures of transition metal antimony(III) oxidehalides are presented in Figure 4.1.

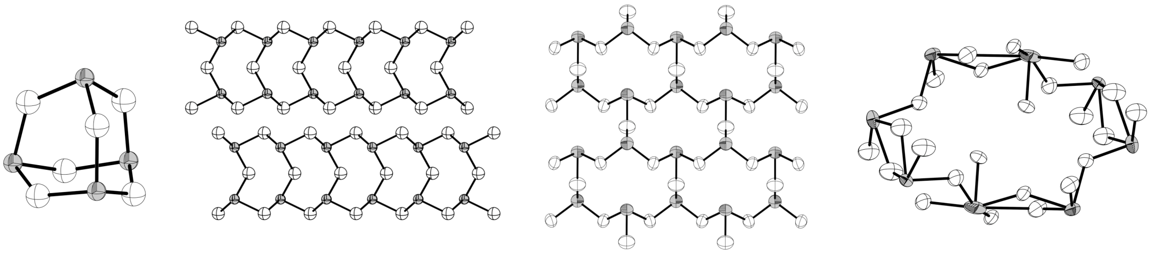

$[Sb_4O_6]$ in α-Sb_2O_3

$[Sb_{10}O_{15}]$ in β-Sb_2O_3

sechserrings $[Sb_6O_9]$ in $ZnSb_2O_3X_2$ (X=Cl,Br)

$[Sb_8O_{12}]$ in $Cd_4Sb_8O_{12.5}X_7$ (X=Cl,Br)

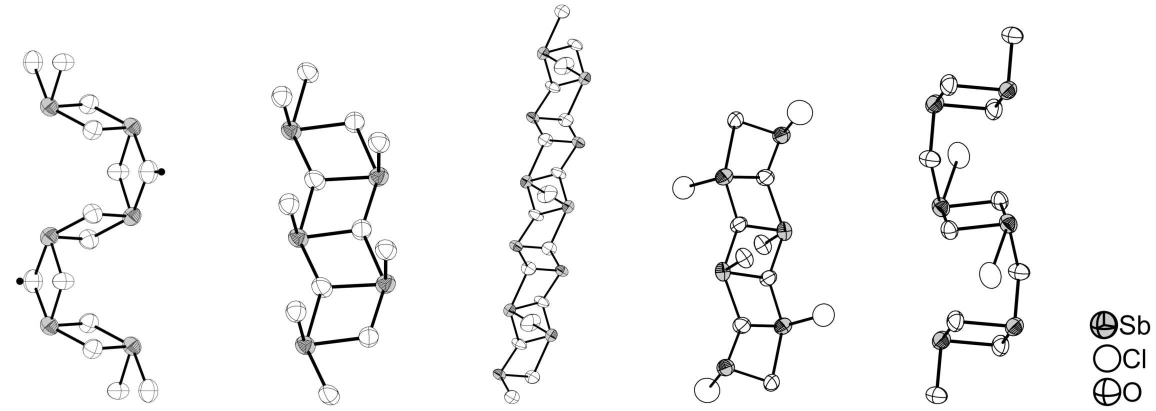

$[Sb_2O_4H]^-$ in $MSb_2O_3X(OH)$ (M=Zn,Cd; X=Cl,Br,I)

$[SbO_2]^-$ in $CdSbO_2X$ (X=Cl,Br)

$[Sb_4O_5]^{2+}$ in $Sb_4O_5X_2$ (X=Cl,Br)

$[Sb_2O_3Cl]^-$ in SbOCl

$[Sb_2O_3Cl]^-$ in $CoSb_2O_3X_2$ (X=Cl,Br)

Figure 4.1.: Topological comparison of several structural entities obtained in crystal structures of transition metal antimony (III) oxidehalides, investigated and described in this thesis.

In the investigated structures with composition $MSb_2O_3X(OH)$ (M=Zn, Cd; X=Cl, Br, I), the possibility of hydrogen bonding of the type O-H...X (X = Cl, Br, I) occurred. The presence of hydroxy groups in the crystal structures were confirmed by infrared and Raman spectroscopy. On the basis of comparative analysis of O-H stretching modes in other solid hydroxides, hydrogen bonds O-H...X were considered to be weak interactions. The next group of layered materials were oxidehalide semiconductors with the composition $CdSbO_2X$ (X=Cl, Br), which crystallize in an orhthorombic or monoclinic crystallographic system depending upon the halide anions. It is still open question, how strong an influence different halides have on structural architecture in this system. Both structures consist of puckered layers of edge-sharing cadmium-centred octahedra, and asymmetrically four-coordinated Sb^{3+} cations, forming bands of $[SbO_2]^-$.

A material exhibiting interesting magnetic properties was $CoSb_2O_3Cl_2$. The metal-centred octahedra form Co^{2+}-Co^{2+} dimers in the structure, isolated by surrounding Sb^{3+}-centred polyhedra. A surprising finding in this crystal structure, confirmed by

BVS and MAPLE calculations, was the oxidehalide environment around antimony(III) cations. Magnetic-moment measurements resulted in spin-only magnetism with J = $\frac{3}{2}$, corresponding to Co^{2+} with $3d^7$ high-spin configuration and groud state $4A^2$. This result would be expected for tetrahedral crystal field symmetry and is surprising due to the slightly distorted octahedral environment for Co atoms in $CoSb_2O_3Cl_2$.

These results extend knowledge of the chemistry of transition metal antimony(III) oxidehalides. They also demonstrate that even in this area are still many questions open, and further studies are needed to answer the remaining questions.

Appendix A.

Definitions and Symbols

$$R_{int} = \frac{\sum\limits_{hkl} |F_0^2 - F_0^2(mean)|}{\sum\limits_{hkl} F_0^2} \tag{A.1}$$

$$R_{\sigma} = \frac{\sum\limits_{hkl} \sigma(F_0^2)}{\sum\limits_{hkl} F_0^2} \tag{A.2}$$

$$R_1 = \frac{\sum\limits_{hkl} ||F_0| - |F_c||}{\sum\limits_{hkl} |F_0|} \tag{A.3}$$

$$wR_2 = \sqrt{\frac{\sum\limits_{hkl} w(F_0^2 - F_c^2)^2}{\sum\limits_{hkl} w(F_0^2)^2}} \quad ; \quad w = \frac{1}{\sigma^2(F_0^2)} \tag{A.4}$$

$$GooF = \sqrt{\frac{\sum\limits_{hkl} w(F_0^2 - F_c^2)^2}{n - p}} \tag{A.5}$$

$a, b, c, \alpha, \beta, \gamma$	lattice constants and angles
F_c	calculated structure factor
F_0	observed structure factor
FOM	figure of merit
hkl	Miller indices
U	atomic displacement factor ($B/8\pi^2$)
R	conventional residual, calculated from F_0 data
w	weight of structure factor
wR_2	weighted residual, calculated from F_0^2
x, y, z	atomic coordinates
Z	number of formula unit per unit cell

Appendix B.

Tables

Table B.1.: Atomic coordinates and equivalent isotropic displacement parameters [Å^2] for $ZnSb_2O_3Cl_2$.

Atom	Wyck.	x	y	z	U_{eq}
Sb(1)	4c	0.38310(2)	¼	0.17556(6)	0.02026(2)
Sb(2)	4c	0.24211(2)	¼	0.75179(5)	0.02023(2)
Zn(1)	4c	0.09008(4)	¼	0.01731(1)	0.0270(2)
Cl(1)	4c	0.97162(1)	¼	0.8676(3)	0.0347(4)
Cl(2)	4c	0.12326(1)	¼	0.3520(2)	0.0353(4)
O(1)	4c	0.2834(3)	¼	0.0324(7)	0.0273(9)
O(2)	8d	0.34023(2)	0.9836(5)	0.3482(4)	0.0213(6)

Table B.2.: Atomic coordinates and equivalent isotropic displacement parameters [Å^2] for $ZnSb_2O_3Br_2$.

Atom	Wyck.	x	y	z	U_{eq}
Sb(1)	4c	0.37749(3)	¼	0.20676(7)	0.0154(2)
Sb(2)	4c	0.24503(3)	¼	0.78977(7)	0.0157(2)
Zn(1)	4c	0.09330(5)	¼	0.02883(1)	0.0225(3)
Br(1)	4c	0.97672(5)	¼	0.84456(1)	0.0275(2)
Br(2)	4c	0.12594(5)	¼	0.37542(1)	0.0274(3)
O(1)	4c	0.2810(3)	¼	0.0643(8)	0.0213(1)
O(2)	8d	0.33645(2)	0.9830(5)	0.3753(5)	0.0170(7)

Table B.3.: Anisotropic displacement parameters U_{ij} [Å^2] for $ZnSb_2O_3Cl_2$.

Atom	U_{11}	U_{22}	U_{33}	U_{12}	U_{13}	U_{23}
Sb(1)	0.0184(2)	0.0204(2)	0.0220(2)	0	0.00194(1)	0
Sb(2)	0.0216(2)	0.0214(2)	0.0176(2)	0	0.00252(1)	0
Zn(1)	0.0222(4)	0.0408(4)	0.0179(3)	0	-0.0002(3)	0
Cl(1)	0.0242(8)	0.0472(1)	0.0328(7)	0	-0.0042(7)	0
Cl(2)	0.0454(1)	0.0393(9)	0.0214(7)	0	-0.0090(6)	0
O(1)	0.023(2)	0.034(2)	0.0242(2)	0	-0.0063(2)	0
O(2)	0.0237(2)	0.0172(1)	0.0231(1)	0.0028(1)	-0.0021(1)	-0.0023(1)

Table B.4.: Anisotropic displacement parameters U_{ij} [Å^2] for $ZnSb_2O_3Br_2$.

Atom	U_{11}	U_{22}	U_{33}	U_{12}	U_{13}	U_{23}
Sb(1)	0.0144(3)	0.0141(3)	0.0177(3)	0	0.00157(2)	0
Sb(2)	0.0166(3)	0.0162(3)	0.0142(4)	0	0.00170(2)	0
Zn(1)	0.0187(5)	0.0337(5)	0.0150(4)	0	0.0003(4)	0
Br(1)	0.0214(5)	0.0332(4)	0.0280(4)	0	-0.0050(3)	0
Br(2)	0.0375(5)	0.0273(4)	0.0172(5)	0	-0.0070(3)	0
O(1)	0.017(3)	0.028(2)	0.019(3)	0	0.000(2)	0
O(2)	0.0193(18)	0.0155(1)	0.0161(2)	0.0015(1)	-0.0009(1)	-0.0015(1)

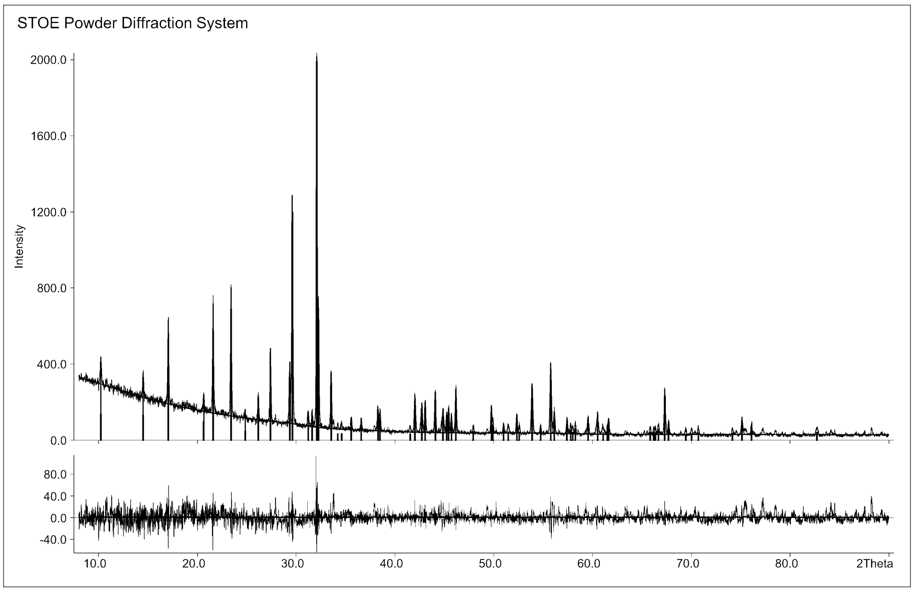

Figure B.1.: X-ray powder diffraction pattern of $ZnSb_2O_3Cl_2$. On the basis of 41 reflections, of which 33 single and 0 unindexed lines the cell ($Pnma$, a = 17.116(6)Å, b = 5.5563(1)Å, c = 6.4796(1)Å) was determined.
(Figure of Merit F(30) = 36.9).

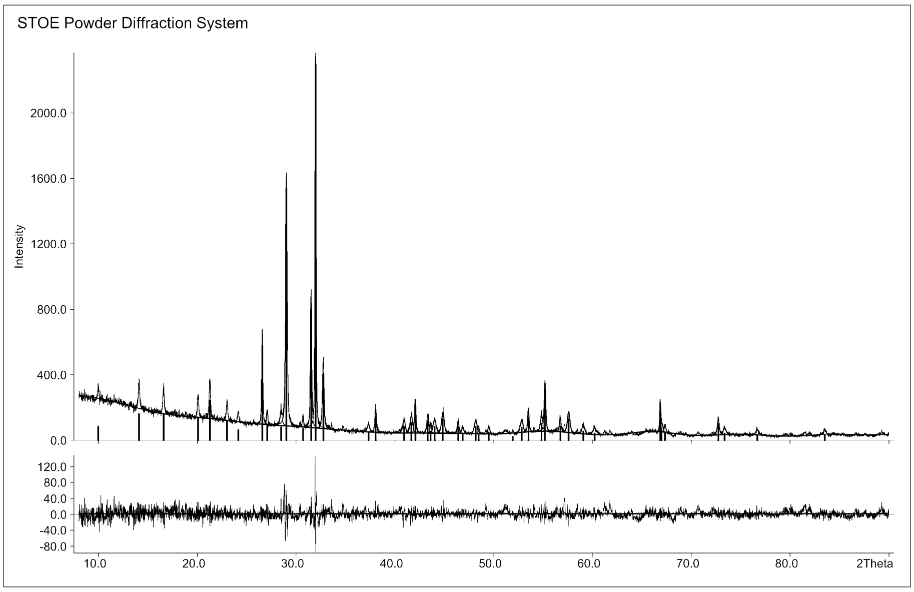

Figure B.2.: X-ray powder diffraction pattern of $ZnSb_2O_3Br_2$. On the basis of 45 reflections, of which 37 single and 0 unindexed lines the cell (*Pnma*, a = 17.597(4)Å, b = 5.5832(9)Å, c = 6.6912(1)Å) was determined.
(Figure of Merit F(30) = 33.3).

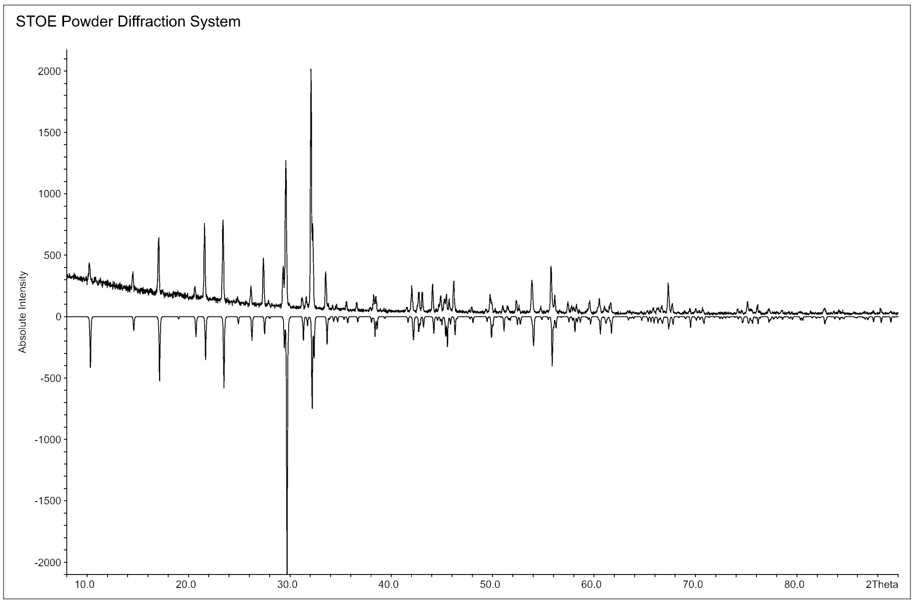

Figure B.3.: Comparison of measured and calculated X-ray powder diffraction pattern of $ZnSb_2O_3Cl_2$. The measured diffractogram is shown with positive intensities and calculated with negative intensities.

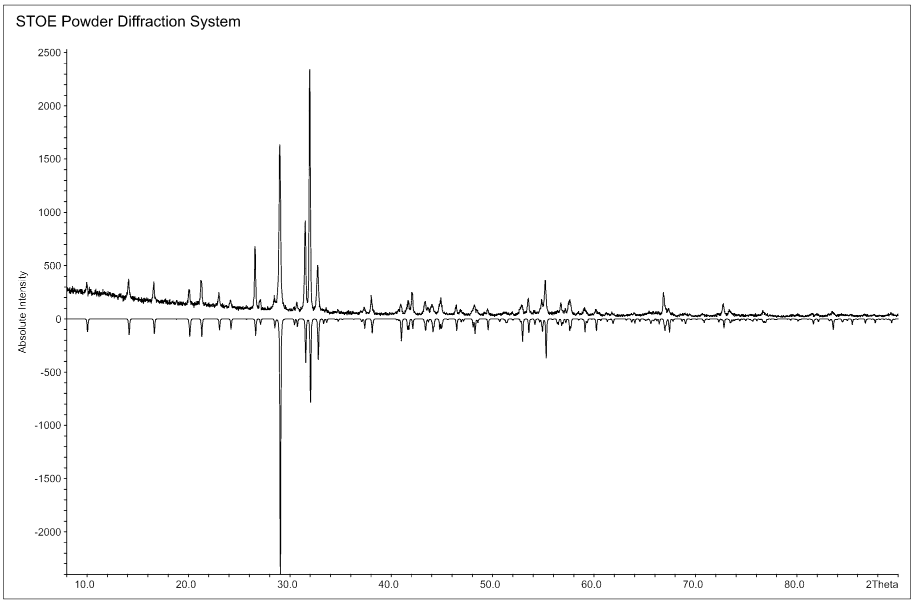

Figure B.4.: Comparison of measured and calculated X-ray powder diffraction pattern of $ZnSb_2O_3Br_2$. The measured diffractogram is shown with positive intensities and calculated with negative intensities.

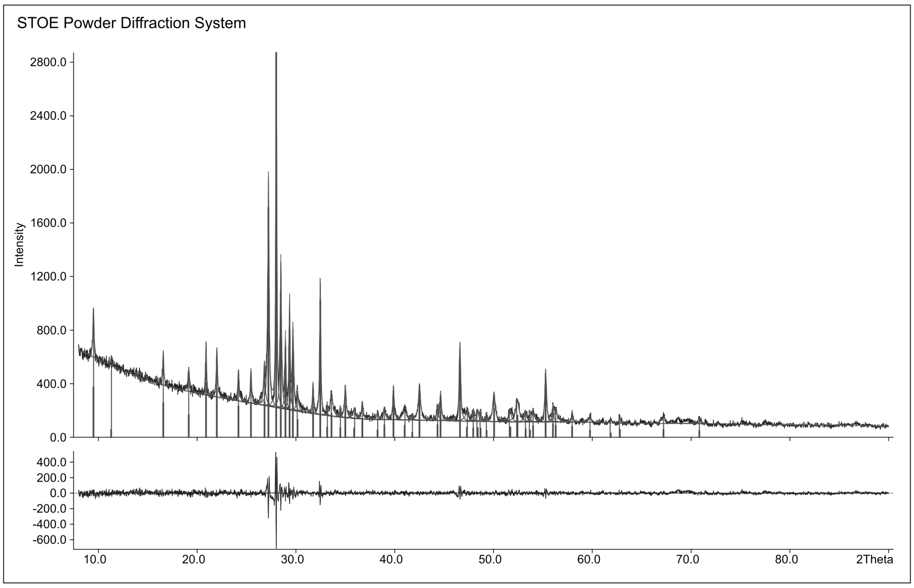

Figure B.5.: X-ray powder diffraction pattern of unsuccessful attempts to synthesise $ZnSb_2O_3I_2$.

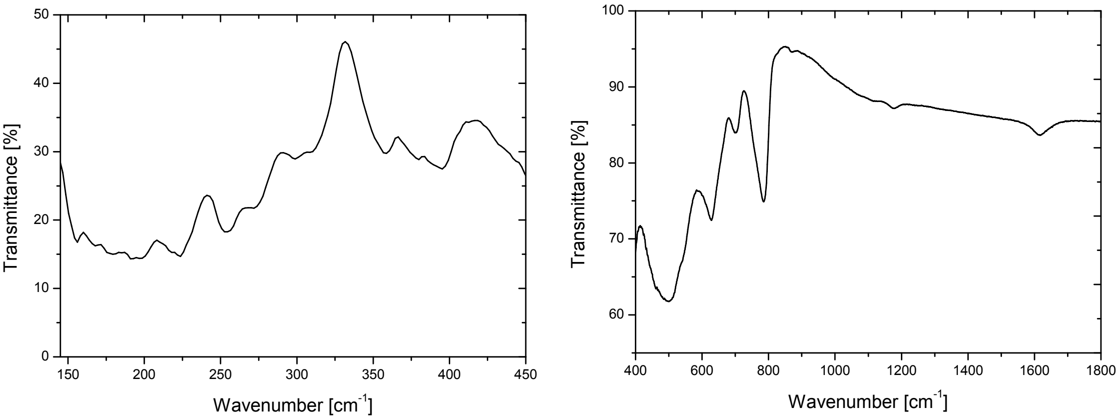

Figure B.6.: Infrared spectra of $ZnSb_2O_3Cl_2$ showing significant vibrations only for $\nu_{\mathrm{Sb-O}}$ and $\nu_{\mathrm{Zn-Cl}}$.

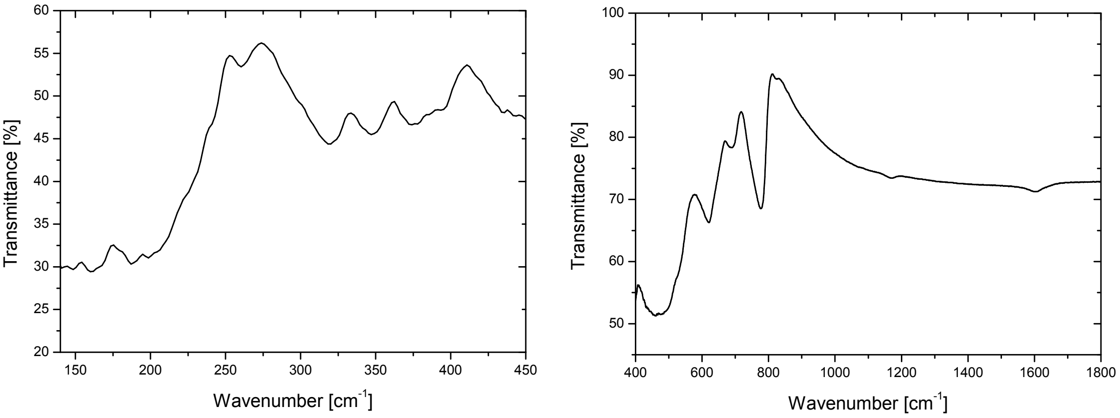

Figure B.7.: Infrared spectra of $ZnSb_2O_3Br_2$ showing significant vibrations only for $\nu_{\mathrm{Sb-O}}$ and $\nu_{\mathrm{Zn-Br}}$.

Table B.5.: Atomic coordinates and equivalent isotropic displacement parameters [Å^2] for $Cd_4Sb_8O_{12.5}Cl_7$.

Atom	Wyck.	x	y	z	U_{eq}
Sb(1)	4i	0.05724(4)	0	0.16707(7)	0.0245(3)
Sb(2)	4i	0.37018(5)	0	0.38843(8)	0.0397(4)
Sb(3)	4i	0.52167(4)	0	0.33082(8)	0.0330(3)
Sb(4)	4i	0.71755(7)	0	0.27925(9)	0.0603(5)
O(1)	4i	0.0450(7)	0	0.299(1)	0.063(4)
O(2)	4i	0.1497(5)	0	0.2624(9)	0.058(4)
O(3)	4i	0.166(1)	0	0.611(2)	0.056(5)
O(4)	4i	0.2781(7)	0	0.343(1)	0.052(5)
O(5)	4i	0.2787(5)	0	0.5805(8)	0.039(2)
O(6)	4i	0.3928(5)	0	0.5422(8)	0.046(3)
O(7)	4i	0.5583(8)	0	0.225(1)	0.068(4)
Cd(1)	4i	0.17676(5)	0	0.44488(8)	0.0351(4)
Cd(2)	4i	0.33326(4)	0	0.04905(7)	0.0251(3)
Cl(1)	4i	0.1174(2)	0	0.8151(3)	0.0358(8)
Cl(2)	4i	0.2358(1)	0	0.0893(2)	0.0252(7)
Cl(3)	4i	0.5852(2)	0	0.0129(3)	0.0399(9)
Cl(4)	2c	0	0	½	0.0424(1)

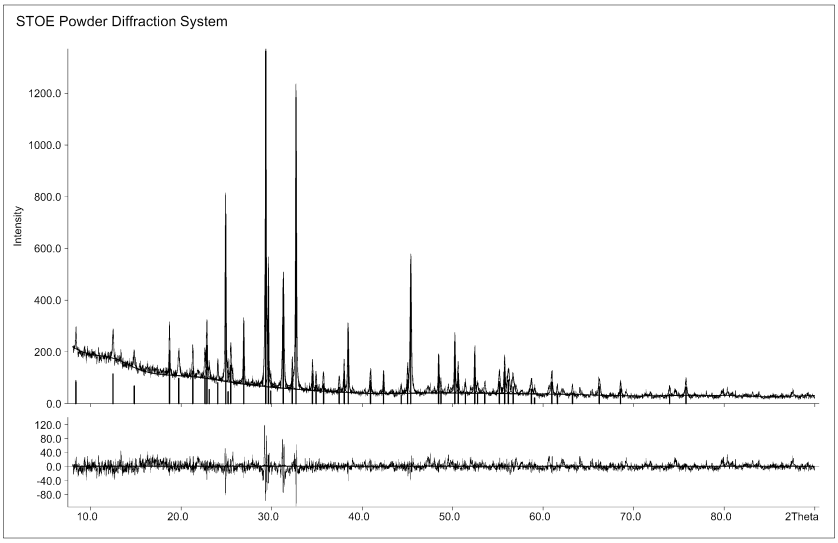

Figure B.8.: X-ray powder diffraction pattern of $Cd_4Sb_8O_{12.5}Cl_7$. On the basis of 52 reflections, of which 32 single and 0 unindexed lines the cell ($C2/m$, $a = 23.923(5)$Å, $b = 3.9927(7)$Å, $c = 14.252(4)$Å, $\beta = 118.811(1)°$) was determined.
(Figure of Merit F(30) = 33.7).

Table B.6.: Atomic coordinates and equivalent isotropic displacement parameters [Å^2] for $Cd_4Sb_8O_{12.5}Br_7$.

Atom	Wyck.	x	y	z	U_{eq}
Sb(1)	4i	0.05927(6)	0	0.18097(9)	0.0287(4)
Sb(2)	4i	0.36442(7)	0	0.3869(1)	0.0415(5)
Sb(3)	4i	0.52695(6)	0	0.3404(1)	0.0312(4)
Sb(4)	4i	0.7158(1)	0	0.2854(1)	0.0838(9)
O(1)	4i	0.0512(9)	0	0.313(1)	0.060(4)
O(2)	4i	0.1516(7)	0	0.271(1)	0.050(4)
O(3)	4i	0.170(1)	0	0.612(2)	0.055(7)
O(4)	4i	0.2750(9)	0	0.347(2)	0.048(6)
O(5)	4i	0.2778(7)	0	0.578(1)	0.050(4)
O(6)	4i	0.3888(6)	0	0.536(1)	0.047(4)
O(7)	4i	0.559(1)	0	0.234(1)	0.078(6)
Cd(1)	4i	0.17797(8)	0	0.4477(1)	0.0443(5)
Cd(2)	4i	0.33531(6)	0	0.0453(1)	0.0265(5)
Br(1)	4i	0.11017(9)	0	0.8120(1)	0.0324(5)
Br(2)	4i	0.23843(8)	0	0.0973(1)	0.0254(5)
Br(3)	4i	0.58220(9)	0	0.01960(2)	0.0337(5)
Br(4)	2c	0	0	½	0.0349(7)

Table B.7.: Anisotropic displacement parameters U_{ij} [Å^2] for $Cd_4Sb_8O_{12.5}Cl_7$.

Atom	U_{11}	U_{22}	U_{33}	U_{12}	U_{13}	U_{23}
Sb(1)	0.0286(5)	0.0218(5)	0.0211(5)	0	0.0102(4)	0
Sb(2)	0.0354(6)	0.0605(8)	0.0299(5)	0	0.0210(4)	0
Sb(3)	0.0257(5)	0.0235(6)	0.0384(6)	0	0.0066(4)	0
Sb(4)	0.0746(9)	0.0873(1)	0.0225(6)	0	0.0262(6)	0
O(1)	0.065(8)	0.08(1)	0.051(7)	0	0.033(6)	0
O(2)	0.030(5)	0.11(1)	0.033(6)	0	0.013(5)	0
O(3)	0.05(1)	0.08(2)	0.052(1)	0	0.031(9)	0
O(4)	0.024(8)	0.10(2)	0.030(8)	0	0.014(7)	0
O(5)	0.041(6)	0.055(7)	0.019(4)	0	0.012(4)	0
O(6)	0.033(5)	0.075(9)	0.028(5)	0	0.015(4)	0
O(7)	0.09(1)	0.07(1)	0.054(8)	0	0.042(8)	0
Cd(1)	0.0442(7)	0.0305(7)	0.0302(6)	0	0.0176(5)	0
Cd(2)	0.0240(5)	0.0228(6)	0.0290(5)	0	0.0131(4)	0
Cl(1)	0.039(2)	0.025(2)	0.026(2)	0	0.003(1)	0
Cl(2)	0.0282(2)	0.025(2)	0.0250(2)	0	0.015(1)	0
Cl(3)	0.032(2)	0.041(2)	0.055(2)	0	0.027(2)	0
Cl(4)	0.043(3)	0.032(3)	0.048(3)	0	0.018(2)	0

Table B.8.: Anisotropic displacement parameters U_{ij} [Å^2] for $Cd_4Sb_8O_{12.5}Br_7$.

Atom	U_{11}	U_{22}	U_{33}	U_{12}	U_{13}	U_{23}
Sb(1)	0.0323(7)	0.0285(8)	0.0191(7)	0	0.0077(5)	0
Sb(2)	0.0340(8)	0.068(1)	0.0222(7)	0	0.0132(6)	0
Sb(3)	0.0280(7)	0.0293(8)	0.0266(7)	0	0.0058(5)	0
Sb(4)	0.065(1)	0.168(3)	0.0174(8)	0	0.0196(8)	0
O(1)	0.06(1)	0.07(1)	0.046(9)	0	0.028(8)	0
O(2)	0.031(7)	0.07(1)	0.037(8)	0	0.010(6)	0
O(3)	0.06(2)	0.6(2)	0.04(1)	0	0.02(1)	0
O(4)	0.017(9)	0.08(2)	0.04(1)	0	0.005(9)	0
O(5)	0.045(8)	0.07(1)	0.029(7)	0	0.017(7)	0
O(6)	0.033(7)	0.08(1)	0.024(7)	0	0.009(6)	0
O(7)	0.1(2)	0.09(2)	0.038(9)	0	0.02(1)	0
Cd(1)	0.061(1)	0.040(1)	0.0321(9)	0	0.0231(8)	0
Cd(2)	0.0271(7)	0.0237(8)	0.0269(7)	0	0.0118(6)	0
Br(1)	0.037(1)	0.023(1)	0.0224(9)	0	0.0025(8)	0
Br(2)	0.0274(9)	0.024(1)	0.0227(9)	0	0.0106(7)	0
Br(3)	0.031(1)	0.035(1)	0.038(1)	0	0.0192(8)	0
Br(4)	0.044(2)	0.027(2)	0.032(1)	0	0.017(1)	0

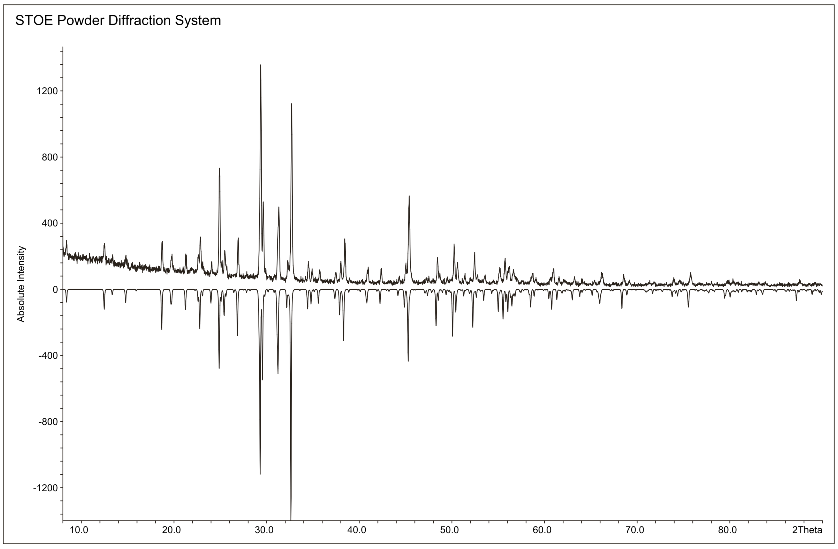

Figure B.9.: Comparison of measured and calculated X-ray powder diffraction pattern of $Cd_4Sb_8O_{12.5}Cl_7$. The measured diffractogram is shown with positive intensities and calculated with negative intensities.

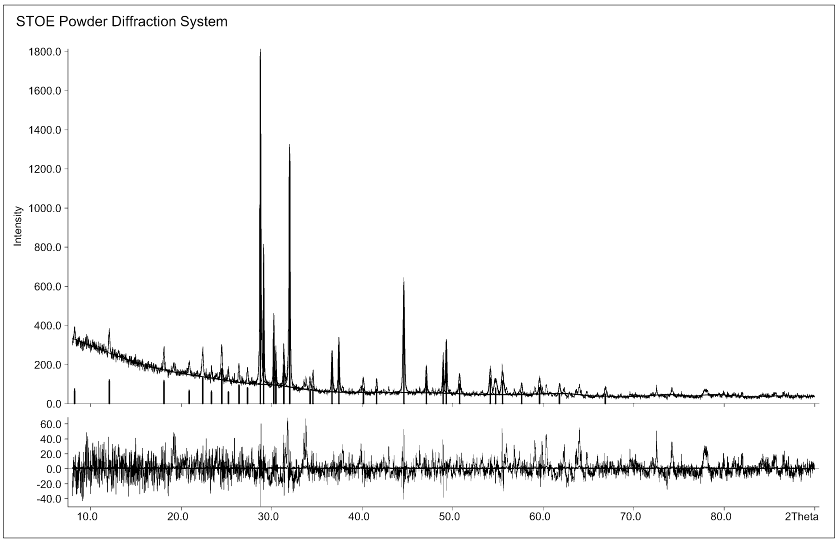

Figure B.10.: X-ray powder diffraction pattern of $Cd_4Sb_8O_{12.5}Br_7$. On the basis of 34 reflections, of which 26 single and 0 unindexed lines the cell ($C2/m$, $a = 24.4650(5)$Å, $b = 4.0569(7)$Å, $c = 14.7510(3)$Å, $\beta = 119.348(1)°$) was determined.
(Figure of Merit F(30) = 22.6).

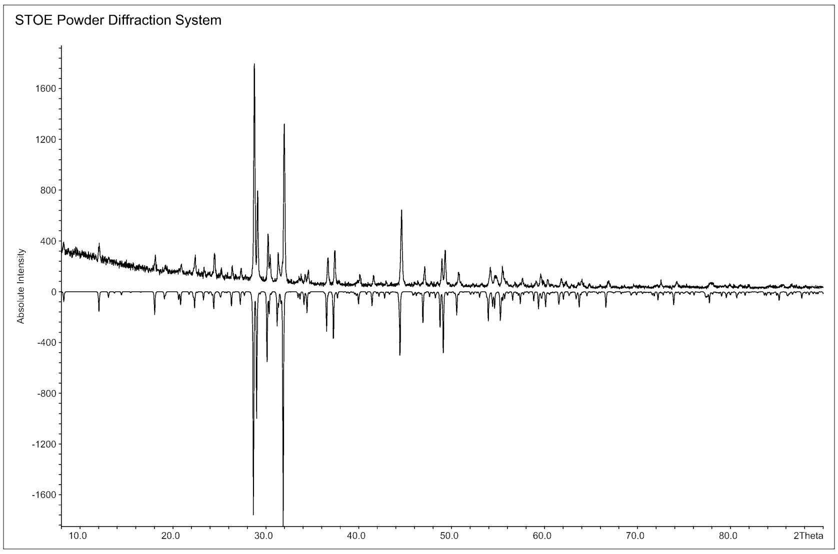

Figure B.11.: Comparison of measured and calculated X-ray powder diffraction pattern of $Cd_4Sb_8O_{12.5}Br_7$. The measured diffractogram is shown with positive intensities and calculated with negative intensities.

Table B.9.: Atomic coordinates and equivalent isotropic displacement parameters [Å^2] for $ZnSb_2O_3Cl(OH)$.

Atom	Wyck.	x	y	z	U_{eq}
Sb(1)	4f	0.45094(5)	0.54503(3)	0.27306(3)	0.01869(1)
Zn(1)	2e	0.04001(1)	¼	0.49772(9)	0.02109(2)
Cl(1)	2e	0.9014(3)	¼	0.1666(2)	0.0311(3)
O(1)	2e	0.2679(7)	¼	0.3474(6)	0.0188(8)
O(2)	4f	0.2742(6)	0.0584(3)	0.5106(4)	0.0206(6)
O(3)	2e	0.3091(9)	¼	0.8215(7)	0.0237(8)
H(1)	2e	0.25(3)	¼	0.90(2)	0.08(4)

Table B.10.: Atomic coordinates and equivalent isotropic displacement parameters [Å^2] for $ZnSb_2O_3Br(OH)$.

Atom	Wyck.	x	y	z	U_{eq}
Sb(1)	4f	0.44652(5)	0.54614(4)	0.27814(4)	0.01911(1)
Zn(1)	2e	0.04661(1)	¼	0.50556(1)	0.0218(2)
Br(1)	2e	0.89715(1)	¼	0.15868(9)	0.02964(2)
O(1)	2e	0.2654(9)	¼	0.3522(6)	0.0197(9)
O(2)	4f	0.2776(6)	0.0589(4)	0.5107(5)	0.0207(7)
O(3)	2e	0.3121(1)	¼	0.8102(8)	0.0251(1)
H(1)	2e	0.27(3)	¼	0.881(2)	0.06(5)

Table B.11.: Atomic coordinates and equivalent isotropic displacement parameters [Å^2] for $ZnSb_2O_3I(OH)$.

Atom	Wyck.	x	y	z	U_{eq}
Sb(1)	4f	0.44133(5)	0.54873(3)	0.29000(4)	0.01722(1)
Zn(1)	2e	0.05565(1)	¼	0.51055(1)	0.02010(2)
I(1)	2e	0.89442(8)	¼	0.14922(6)	0.02617(1)
O(1)	2e	0.2641(7)	¼	0.3655(6)	0.0177(8)
O(2)	4f	0.2808(5)	0.0593(4)	0.5104(4)	0.0184(6)
O(3)	2e	0.3129(9)	¼	0.7915(8)	0.0216(1)
H(1)	2e	0.285(1)	¼	0.869(1)	0.02(2)

Table B.12.: Anisotropic displacement parameters U_{ij} [Å^2] for $ZnSb_2O_3Cl(OH)$.

Atom	U_{11}	U_{22}	U_{33}	U_{12}	U_{13}	U_{23}
Sb(1)	0.01855(2)	0.01785(2)	0.01964(2)	0.00101(8)	0.00113(1)	0.00258(8)
Zn(1)	0.0164(3)	0.0221(4)	0.0252(3)	0	0.0043(2)	0
Cl(1)	0.0299(7)	0.0392(9)	0.0240(7)	0	0.0003(5)	0
O(1)	0.0158(2)	0.0140(2)	0.0271(2)	0	0.0056(2)	0
O(2)	0.0185(1)	0.0201(2)	0.0228(1)	0.0026(1)	-0.0009(1)	-0.0008(1)
O(3)	0.024(2)	0.023(2)	0.026(2)	0	0.0103(2)	0

Table B.13.: Anisotropic displacement parameters U_{ij} [Å^2] for $ZnSb_2O_3Br(OH)$.

Atom	U_{11}	U_{22}	U_{33}	U_{12}	U_{13}	U_{23}
Sb(1)	0.01806(2)	0.0197(2)	0.01953(2)	0.00099(1)	0.00137(1)	-0.00248(1)
Zn(1)	0.0160(3)	0.0230(4)	0.0267(4)	0	0.0047(3)	0
Br(1)	0.0273(4)	0.0394(5)	0.0220(3)	0	0.0013(3)	0
O(1)	0.016(2)	0.017(2)	0.027(2)	0	0.0082(2)	0
O(2)	0.0181(2)	0.0218(2)	0.0225(2)	0.0037(1)	0.0030(1)	-0.0017(1)
O(3)	0.025(2)	0.031(3)	0.021(2)	0	0.009(2)	0

Table B.14.: Anisotropic displacement parameters U_{ij} [Å^2] for $ZnSb_2O_3I(OH)$.

Atom	U_{11}	U_{22}	U_{33}	U_{12}	U_{13}	U_{23}
Sb(1)	0.01618(2)	0.01704(2)	0.01837(2)	-0.00216(1)	0.00079(1)	0.00085(1)
Zn(1)	0.0139(3)	0.0209(4)	0.0258(4)	0	0.0043(3)	0
I(1)	0.0241(2)	0.0345(3)	0.0198(2)	0	0.00097(2)	0
O(1)	0.0121(1)	0.015(2)	0.026(2)	0	0.0039(2)	0
O(2)	0.0166(1)	0.0169(2)	0.0213(2)	-0.0017(1)	-0.0014(1)	0.0029(1)
O(3)	0.020(2)	0.027(3)	0.019(2)	0	0.0089(2)	0

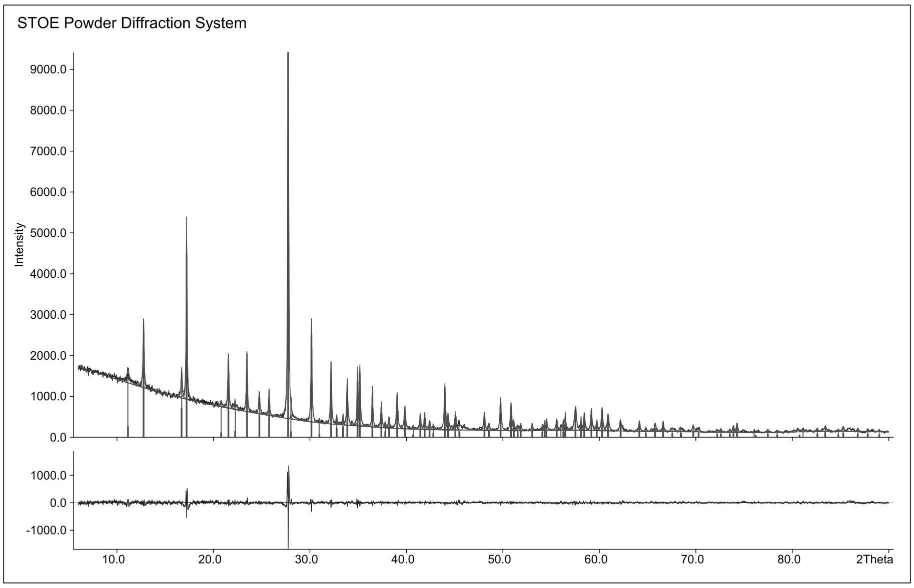

Figure B.12.: X-ray powder diffraction pattern of $ZnSb_2O_3Cl(OH)$ synthesized from ZnO, $SbCl_3$ (2:1). On the basis of 82 reflections, of which 40 single and 5 unindexed lines the cell ($P2_1/m$, a = 5.1328(1)Å, b = 8.2104(2)Å, c = 6.899(3)Å, β = 93.95(3)°) was determined.
(Figure of Merit F(30) = 54.8).

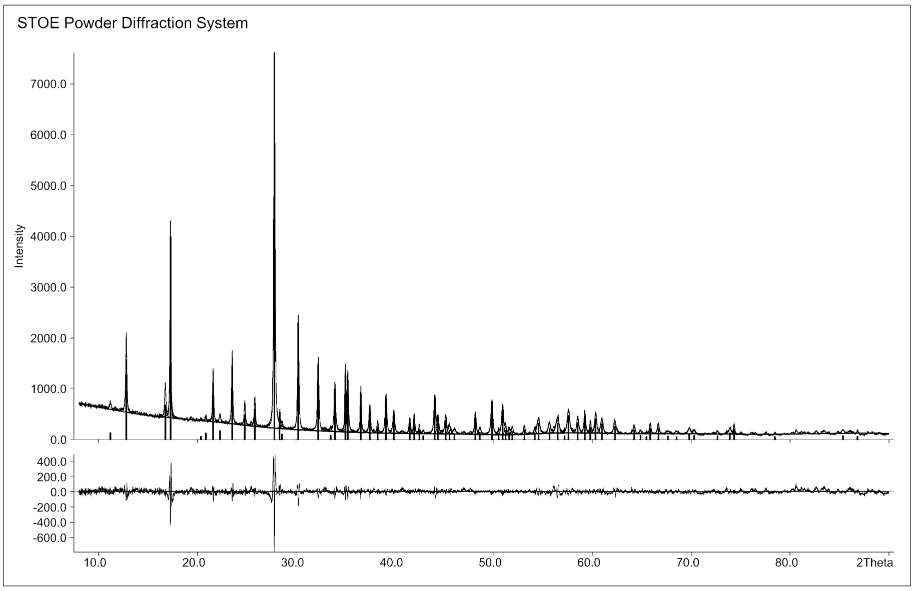

Figure B.13.: X-ray powder diffraction pattern of $ZnSb_2O_3Cl(OH)$ synthesized from ZnO, $SbCl_3$ and Sb_4O_6 (6:2:1). On the basis of 70 reflections, of which 43 single and 5 unindexed lines the cell ($P2_1/m$, a = 5.1339(1)Å, b = 8.2153(2)Å, c = 6.9075(2)Å, β = 93.936(2)°) was determined.
(Figure of Merit F(30) = 53.0).

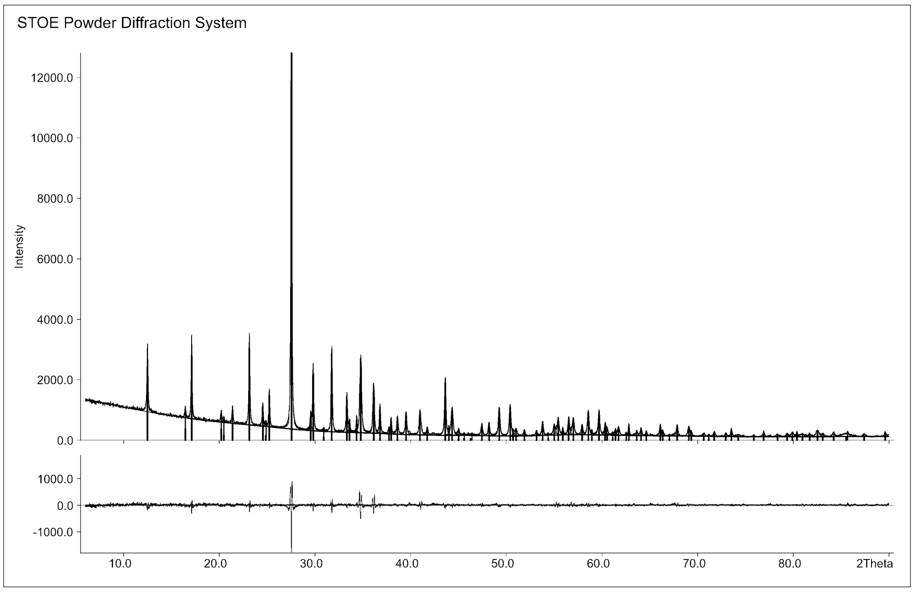

Figure B.14.: X-ray powder diffraction pattern of $ZnSb_2O_3Br(OH)$ synthesized from ZnO, $SbBr_3$ (2:1). On the basis of 88 reflections, of which 39 single and 10 unindexed lines the cell ($P2_1/m$, a = 5.187(3)Å, b = 8.283(6)Å, c = 7.106(6)Å, β = 94.01(6)°) was determined.
(Figure of Merit F(30) = 11.3).

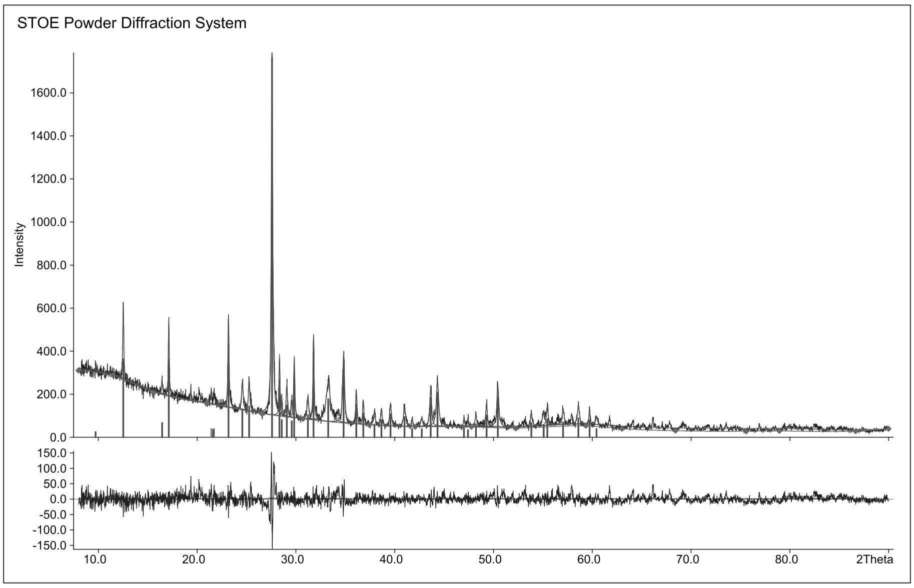

Figure B.15.: X-ray powder diffraction pattern of $ZnSb_2O_3Br(OH)$ synthesized from ZnO, $SbBr_3$ and Sb_4O_6 (6:2:1). On the basis of 71 reflections, of which 33 single and 5 unindexed lines the cell ($P2_1/m$, a = 5.1739(2)Å, b = 8.2763(2)Å, c = 7.055(4)Å, β = 94.308(2)°) was determined.
(Figure of Merit F(30) = 36.7).

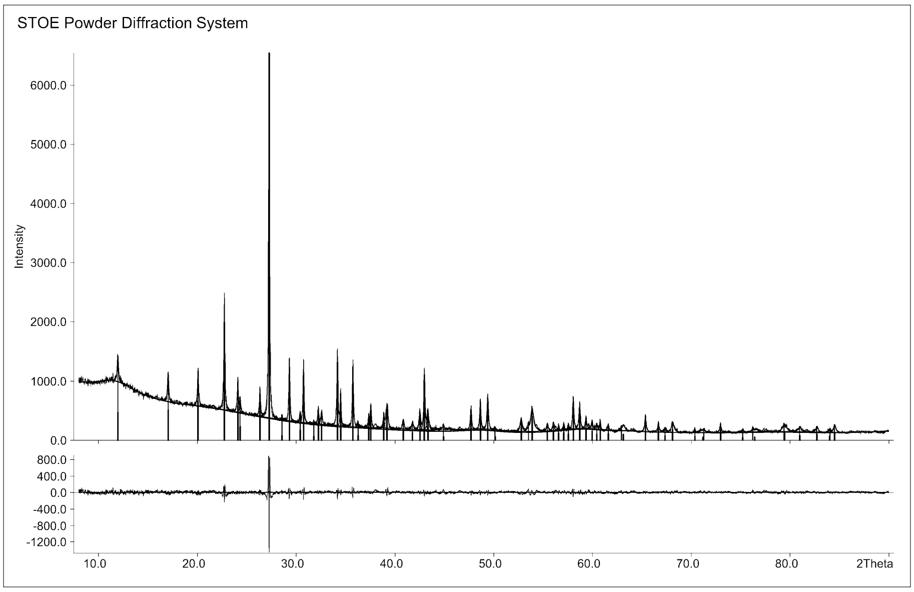

Figure B.16.: X-ray powder diffraction pattern of $ZnSb_2O_3I(OH)$ synthesized from ZnO, SbI_3 (2:1). On the basis of 61 reflections, of which 30 single and 3 unindexed lines the cell ($P2_1/m$, a = 5.230(5)Å, b = 8.418(5)Å, c = 7.443(5)Å, β = 94.37(5)°) was determined.
(Figure of Merit F(30) = 11.7).

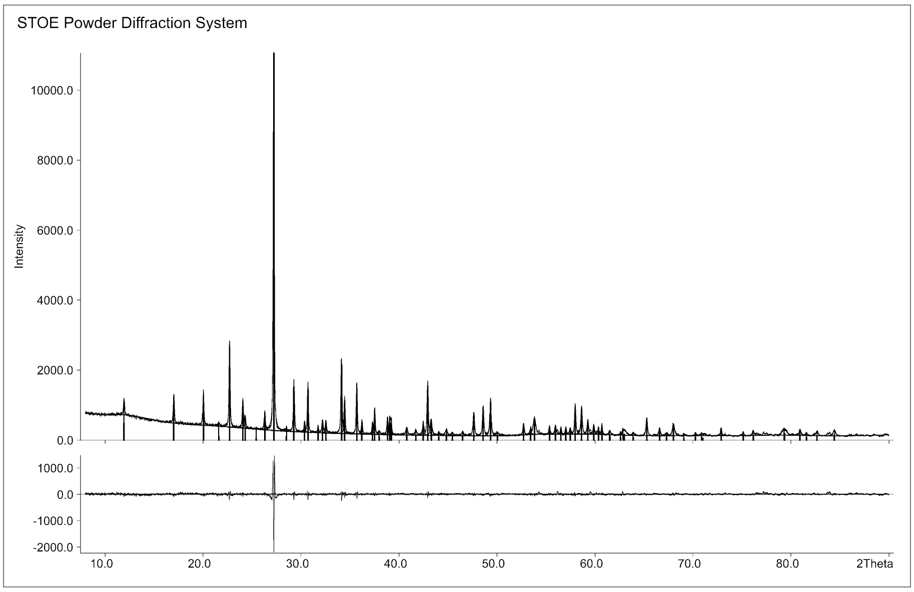

Figure B.17.: X-ray powder diffraction pattern of $ZnSb_2O_3I(OH)$ synthesized from ZnO, SbI_3 and Sb_4O_6 (6:2:1). On the basis of 67 reflections, of which 37 single and 1 unindexed lines the cell ($P2_1/m$, a = 5.2107(1)Å, b = 8.4163(2)Å, c = 7.4091(2)Å, β = 94.409(2)°) was determined.
(Figure of Merit F(30) = 66.8).

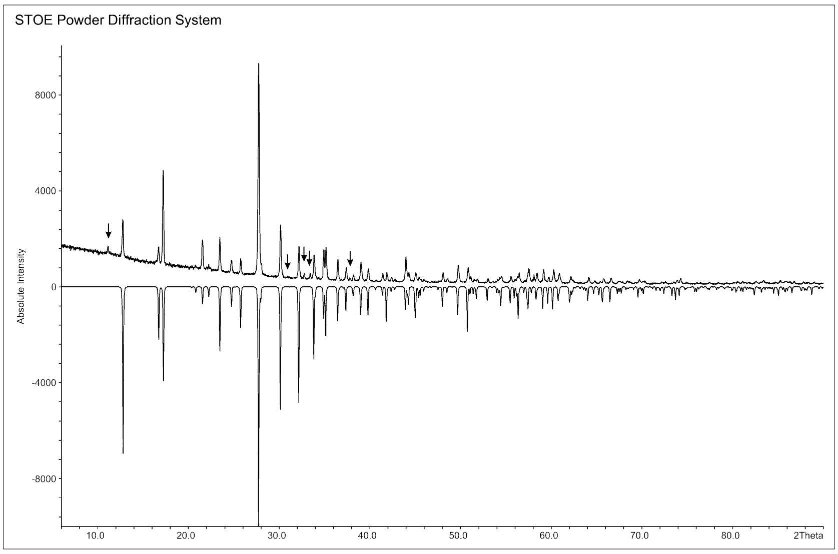

Figure B.18.: Comparison of measured and calculated X-ray powder diffraction pattern of $ZnSb_2O_3Cl(OH)$ [synthesized from ZnO, $SbCl_3$ (2:1)]. The measured diffractogram is shown with positive intensities and calculated with negative intensities. Unindexed lines are marked with arrows. Comparision of the measured powder X-ray characteristic to reference patterns from the PDF database resulted in the identification of the additional crystalline product SbOCl.

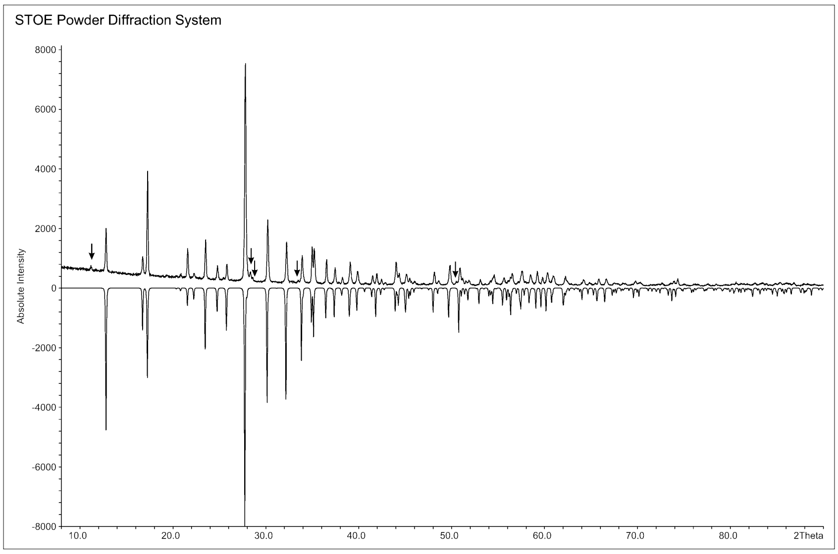

Figure B.19.: Comparison of measured and calculated X-ray powder diffraction pattern of $ZnSb_2O_3Cl(OH)$ [synthesized from ZnO, $SbCl_3$, Sb_4O_6, (6:2:1)]. The measured diffractogram is shown with positive intensities and calculated with negative intensities. Unindexed lines are marked with arrows. Comparision of the measured powder X-ray characteristic to reference patterns from the PDF database resulted in the identification of the additional crystalline product $Sb_8O_{11}Cl_2$.

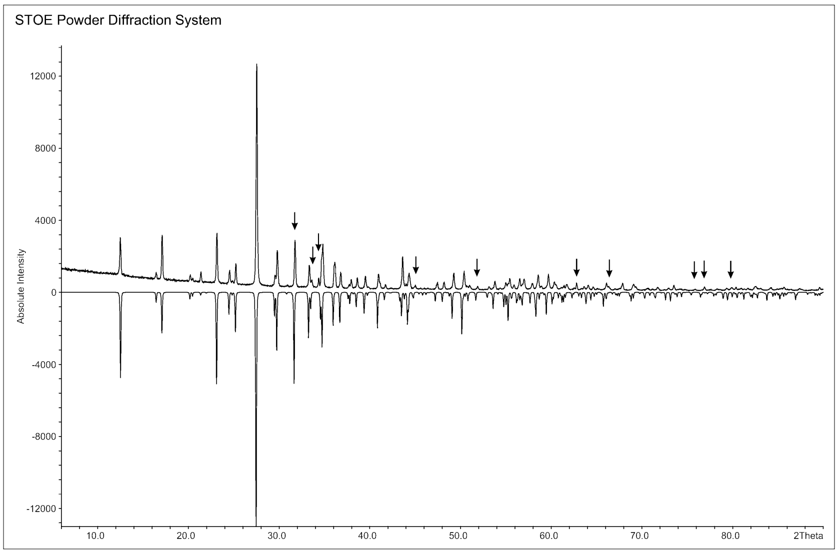

Figure B.20.: Comparison of measured and calculated X-ray powder diffraction pattern of $ZnSb_2O_3Br(OH)$ [synthesized from ZnO, $SbBr_3$ (2:1)]. The measured diffractogram is shown with positive intensities and calculated with negative intensities. Unindexed lines are marked with arrows. Comparision of the measured powder X-ray characteristic to reference patterns from the PDF database resulted in the identification of the additional crystalline product ZnO.

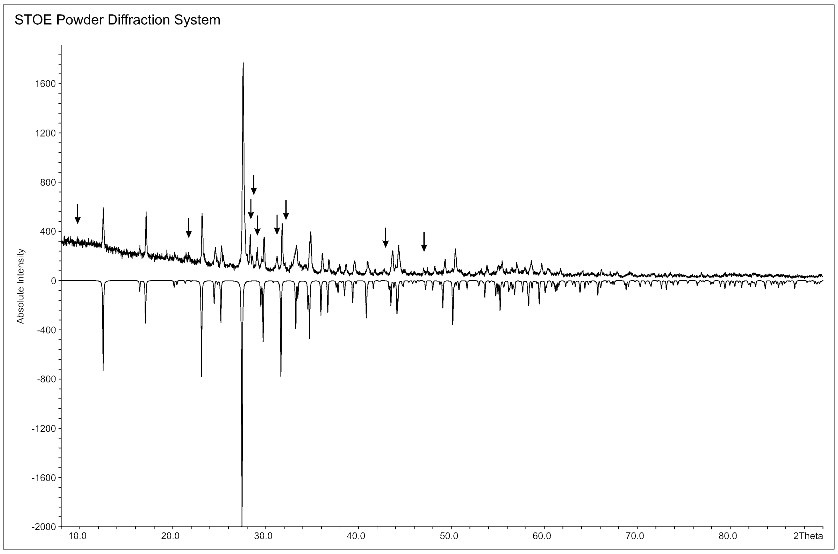

Figure B.21.: Comparison of measured and calculated X-ray powder diffraction pattern of $ZnSb_2O_3Br(OH)$ [synthesized from ZnO, $SbBr_3$, Sb_4O_6, (6:2:1)]. The measured diffractogram is shown with positive intensities and calculated with negative intensities. Unindexed lines are marked with arrows. Comparision of the measured powder X-ray characteristic to reference patterns from the PDF database resulted in the identification of the additional crystalline product $Sb_8O_{11}Br_2$.

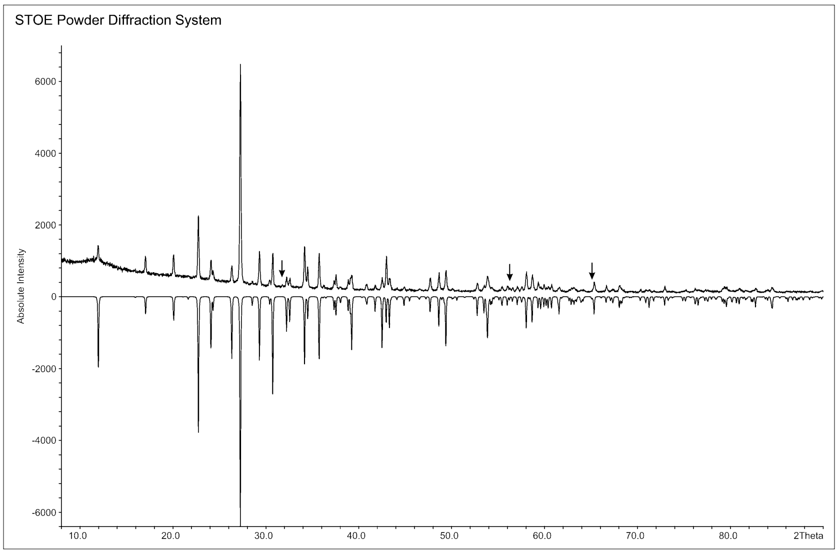

Figure B.22.: Comparison of measured and calculated X-ray powder diffraction pattern of $ZnSb_2O_3I(OH)$ [synthesized from ZnO, SbI_3, (2:1)]. The measured diffractogram is shown with positive intensities and calculated with negative intensities. Unindexed lines are marked with arrows. Comparision of the measured powder X-ray characteristic to reference patterns from the PDF database resulted in the identification of the additional crystalline product ZnO.

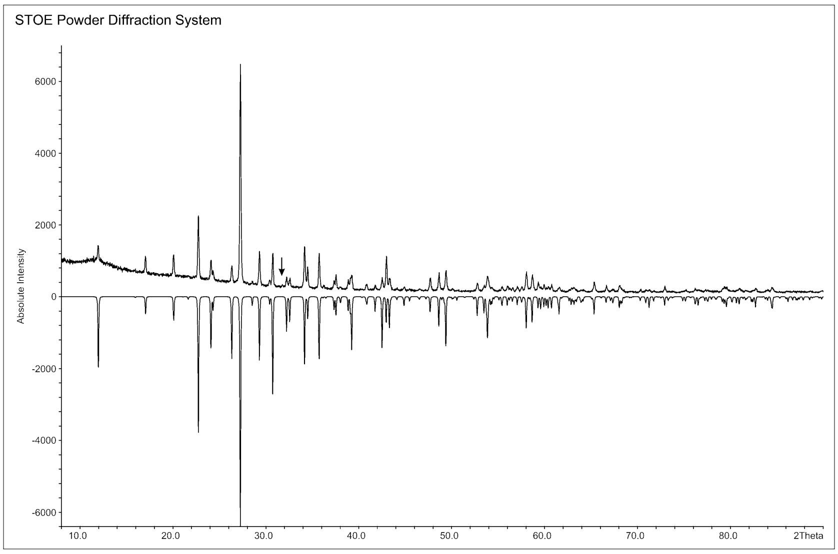

Figure B.23.: Comparison of measured and calculated X-ray powder diffraction pattern of $ZnSb_2O_3I(OH)$ [synthesized from ZnO, SbI_3, Sb_4O_6 (6:2:1)]. The measured diffractogram is shown with positive intensities and calculated with negative intensities. Unindexed lines are marked with arrows. Comparision of the measured powder X-ray characteristic to reference patterns from the PDF database resulted in the identification of the additional crystalline product $Sb_8O_{11}I_2$.

Table B.15.: Atomic coordinates and equivalent isotropic displacement parameters [Å^2] for $CdSb_2O_3Cl(OH)$.

Atom	Wyck.	x	y	z	U_{eq}
Sb(1)	4e	0.22175(4)	0.02288(4)	0.26980(3)	0.02374(1)
Sb(2)	4e	0.22759(4)	0.43200(4)	0.25979(3)	0.02424(1)
Cd(1)	4e	0.00949(4)	0.72680(4)	0.49671(3)	0.02510(1)
Cl(1)	4e	0.63455(2)	0.2441(2)	0.44869(1)	0.0446(3)
O(1)	4e	0.0002(4)	0.0204(4)	0.1377(3)	0.0262(7)
O(2)	4e	0.0023(4)	0.9332(4)	0.3634(3)	0.0271(7)
O(3)	4e	0.1582(4)	0.2314(4)	0.3455(3)	0.0248(6)
O(4)	4e	0.3006(5)	0.2338(4)	0.1391(3)	0.0290(7)
H(1)	4e	0.394(1)	0.225(8)	0.121(6)	0.036(2)

Table B.16.: Anisotropic displacement parameters U_{ij} [Å^2] for $CdSb_2O_3Cl(OH)$.

Atom	U_{11}	U_{22}	U_{33}	U_{12}	U_{13}	U_{23}
Sb(1)	0.02066(2)	0.02935(2)	0.02138(2)	-0.00174(1)	0.00291(1)	0.00296(1)
Sb(2)	0.02103(2)	0.03056(2)	0.02139(2)	0.00140(1)	0.00342(1)	-0.00375(1)
Cd(1)	0.02451(2)	0.0330(2)	0.01838(2)	-0.00003(1)	0.00503(1)	-0.00059(1)
Cl(1)	0.0232(5)	0.0711(2)	0.0398(7)	0.0050(6)	0.0042(5)	-0.0015(5)
O(1)	0.0262(2)	0.0317(2)	0.0207(1)	0.0043(1)	0.0029(1)	-0.0017(1)
O(2)	0.0233(2)	0.0366(2)	0.0212(1)	0.0040(1)	0.0014(1)	-0.0025(1)
O(3)	0.0272(2)	0.0255(2)	0.0229(2)	-0.0012(1)	0.0084(1)	-0.0005(1)
O(4)	0.0206(2)	0.038(2)	0.0300(2)	0.0005(1)	0.0096(1)	0.0025(1)

Table B.17.: Atomic coordinates and equivalent isotropic displacement parameters [Å^2] for $CdSb_2O_3Br(OH)$.

Atom	Wyck.	x	y	z	U_{eq}
Sb(1)	4e	0.21627(5)	0.02667(5)	0.27013(3)	0.02229(1)
Sb(2)	4e	0.22104(5)	0.43636(5)	0.26290(3)	0.02274(1)
Cd(1)	4e	0.00532(5)	0.73109(6)	0.49525(3)	0.02379(1)
Br(1)	4e	0.62990(8)	0.24363(1)	0.44963(6)	0.03767(2)
O(1)	4e	0.0006(6)	0.0245(5)	0.1385(3)	0.0245(9)
O(2)	4e	0.0011(6)	0.9376(6)	0.3618(3)	0.0259(9)
O(3)	4e	0.1544(5)	0.2343(5)	0.3469(3)	0.0227(8)
O(4)	4e	0.2910(6)	0.2367(6)	0.1421(4)	0.0278(9)
H(1)	4e	0.377(1)	0.238(8)	0.125(6)	0.017(2)

Table B.18.: Anisotropic displacement parameters U_{ij} [Å^2] for $CdSb_2O_3Br(OH)$.

Atom	U_{11}	U_{22}	U_{33}	U_{12}	U_{13}	U_{23}
Sb(1)	0.0192(2)	0.0295(2)	0.01820(2)	-0.00291(1)	0.00186(1)	0.00351(2)
Sb(2)	0.0194(2)	0.0307(2)	0.01809(2)	0.00293(1)	0.00206(1)	-0.00420(2)
Cd(1)	0.02234(2)	0.0344(3)	0.01501(2)	-0.00023(2)	0.00397(1)	-0.00075(2)
Br(1)	0.0206(3)	0.0598(5)	0.0326(3)	0.0033(3)	0.0031(2)	-0.0011(3)
O(1)	0.022(2)	0.033(3)	0.0184(2)	0.0035(2)	0.0020(2)	-0.0041(2)
O(2)	0.021(2)	0.039(3)	0.0179(2)	0.0011(2)	0.0012(2)	-0.0036(2)
O(3)	0.0270(2)	0.025(2)	0.0173(2)	-0.0005(2)	0.0085(1)	-0.0009(2)
O(4)	0.0187(2)	0.043(3)	0.023(2)	-0.0024(2)	0.0102(2)	0.0021(2)

Table B.19.: Atomic coordinates and equivalent isotropic displacement parameters [Å^2] for $CdSb_2O_3I(OH)$.

Atom	Wyck.	x	y	z	U_{eq}
Sb(1)	4f	0.46311(1)	0.54666(1)	0.29345(8)	0.0351(3)
Cd(1)	2e	0.0135(2)	0.2500	0.49438(1)	0.0383(3)
I(1)	2e	0.9010(2)	0.2500	0.12377(1)	0.0418(4)
O(1)	2e	0.3030(2)	0.7500	0.3562(1)	0.031(2)
O(2)	4f	0.2799(1)	0.0431(1)	0.5009(9)	0.0377(2)
O(3)	2e	0.290(2)	0.2500	0.7749(2)	0.039(3)
H(1)	2e	0.27(3)	0.2500	0.861(2)	0.01(4)

Table B.20.: Anisotropic displacement parameters U_{ij} [Å^2] for $CdSb_2O_3I(OH)$.

Atom	U_{11}	U_{22}	U_{33}	U_{12}	U_{13}	U_{23}
Sb(1)	0.0212(4)	0.0601(6)	0.0239(4)	-0.0047(3)	0.0018(2)	0.0057(4)
Cd(1)	0.0171(5)	0.0721(1)	0.0263(5)	0	0.0045(4)	0
I(1)	0.0325(6)	0.0693(9)	0.0235(4)	0	0.0030(4)	0
O(1)	0.023(5)	0.037(6)	0.033(4)	0	0.004(4)	0
O(2)	0.017(3)	0.071(6)	0.025(3)	-0.002(3)	-0.001(2)	0.005(4)
O(3)	0.032(6)	0.064(9)	0.024(5)	0	0.009(4)	0

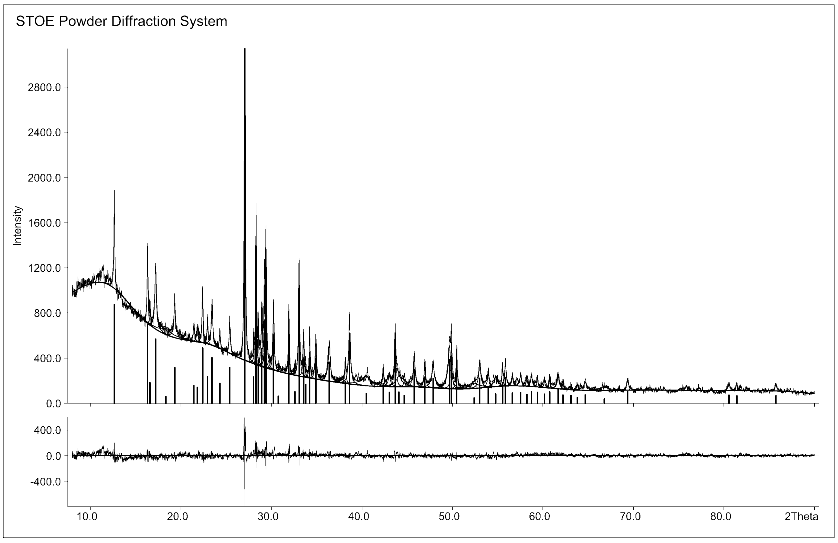

Figure B.24.: X-ray powder diffraction pattern of $CdSb_2O_3Cl(OH)$ synthesized from CdO, $SbCl_3$ (2:1). On the basis of 67 reflections, of which 27 single and 9 unindexed lines, the cell ($P2_1/c$, $a = 7.023(6)$ Å, $b = 8.274(5)$ Å, $c = 10.874(9)$ Å, $\beta = 95.93(5)°$) was determined.
(Figure of Merit F(30) = 10.2).

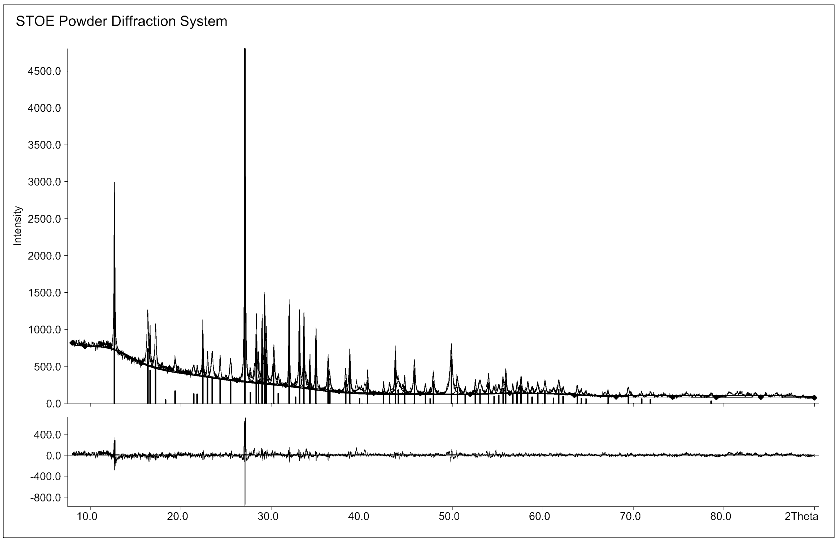

Figure B.25.: X-ray powder diffraction pattern of $CdSb_2O_3Cl(OH)$ synthesized from CdO, $SbCl_3$, Sb_4O_6 (6:2:1). On the basis of 71 reflections, of which 29 single and 8 unindexed lines, the cell ($P2_1/c$, $a = 7.021(6)$ Å, $b = 8.284(5)$ Å, $c = 10.896(1)$ Å, $\beta = 95.87(5)°$) was determined.
(Figure of Merit F(30) = 11.9).

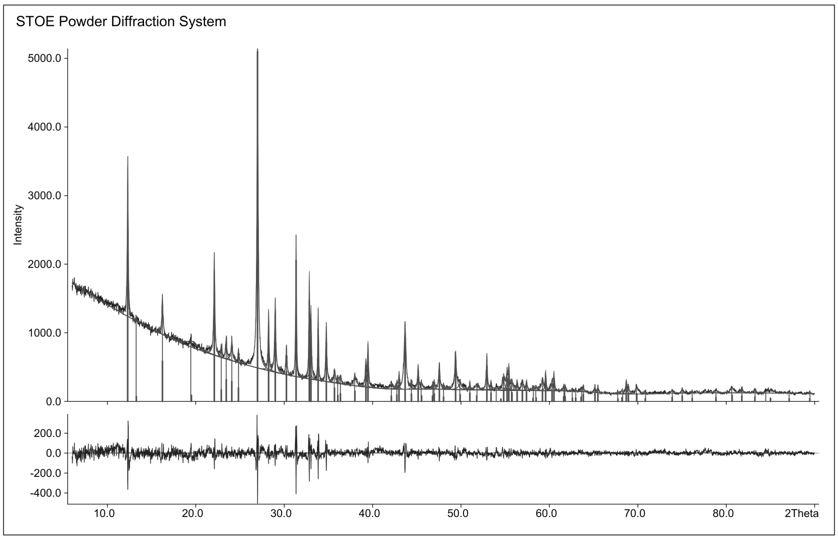

Figure B.26.: X-ray powder diffraction pattern of $CdSb_2O_3Br(OH)$ synthesized from CdO, $SbBr_3$ (2:1). On the basis of 79 reflections, of which 32 single and 5 unindexed lines, the cell ($P2_1/c$, $a = 7.232(5)$ Å, $b = 8.307(3)$ Å, $c = 10.993(7)$ Å, $\beta = 95.98(4)°$) was determined.
(Figure of Merit F(30) = 11.1).

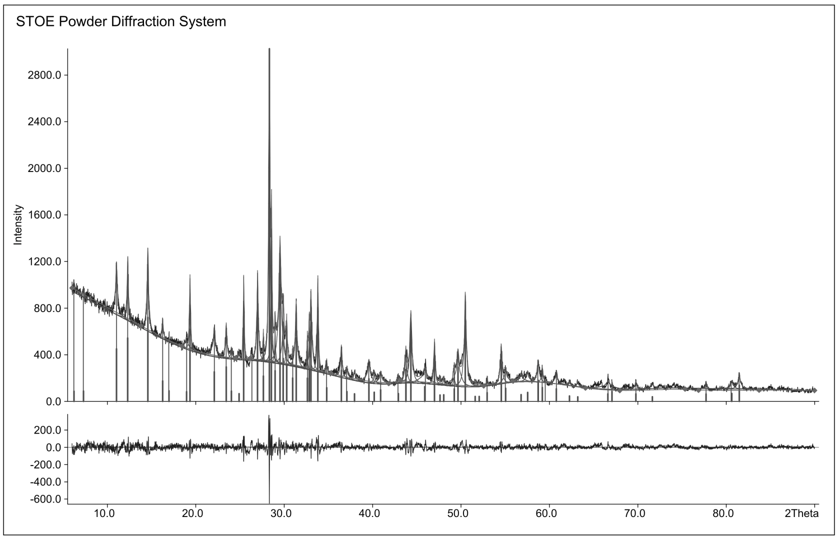

Figure B.27.: X-ray powder diffraction pattern of $CdSb_2O_3Br(OH)$ synthesized from CdO, $SbBr_3$, Sb_4O_6 (6:2:1). On the basis of 64 reflections, of which 15 single and 14 unindexed lines, the cell ($P2_1/c$, $a = 7.197(1)$ Å, $b = 8.295(1)$ Å, $c = 10.990(2)$ Å, $\beta = 96.31(1)°$) was determined.
(Figure of Merit F(30) = 6.6).

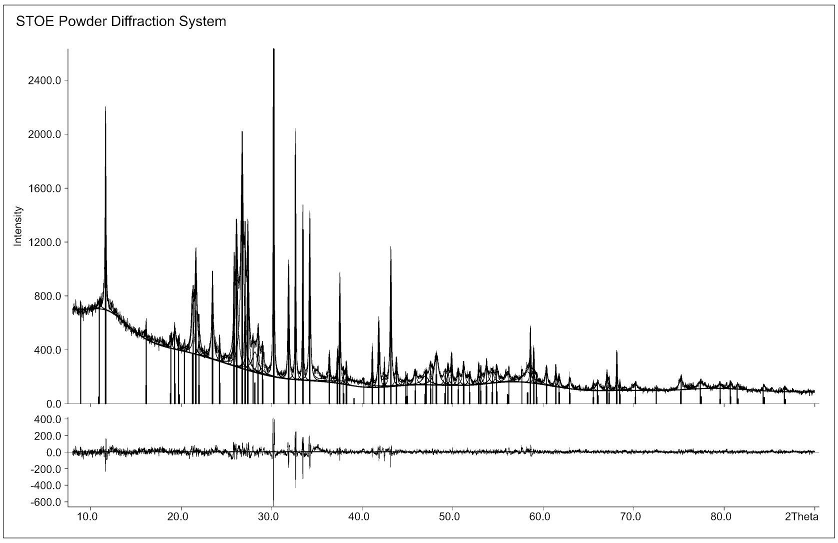

Figure B.28.: X-ray powder diffraction pattern of $CdSb_2O_3I(OH)$ synthesized from CdO, SbI_3 (2:1). On the basis of 77 reflections, of which 35 single and 16 unindexed lines, the cell ($P2_1/m$, $a = 5.498(4)$ Å, $b = 8.345(5)$ Å, $c = 7.538(5)$ Å, $\beta = 96.70(5)°$) was determined.
(Figure of Merit F(30) = 8.3).

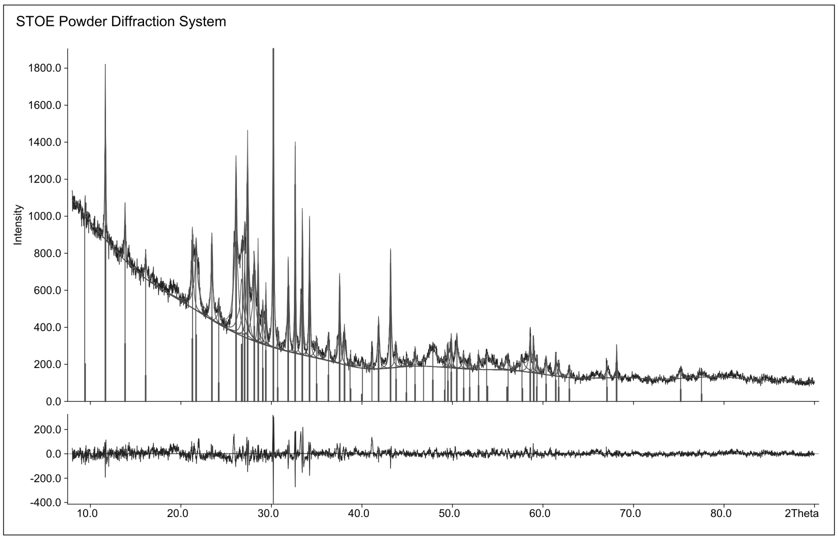

Figure B.29.: X-ray powder diffraction pattern of $CdSb_2O_3I(OH)$ synthesize from CdO, SbI_3, Sb_4O_6 (6:2:1). On the basis of 56 reflections, of which 28 single and 15 unindexed lines, the cell ($P2_1/m$, $a = 5.505(5)$ Å, $b = 8.319(9)$ Å, $c = 7.540(6)$ Å, $\beta = 96.50(7)°$) was determined.
(Figure of Merit F(30) = 5.5).

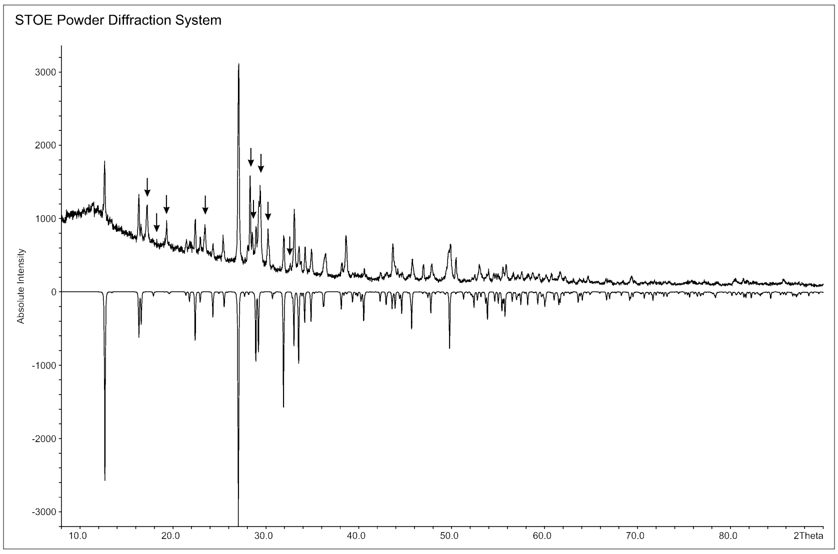

Figure B.30.: Comparison of measured and calculated X-ray powder diffraction pattern of $CdSb_2O_3Cl(OH)$ [synthesized from CdO, $SbCl_3$, (2:1)]. The measured diffractogram is shown with positive intensities and calculated with negative intensities. Unindexed lines are marks with arrows. Comparison of the measured powder X-ray characteristic to reference patterns from the PDF database resulted in the identification of the additional crystalline products Cd(OH)Cl and Sb_2O_3.

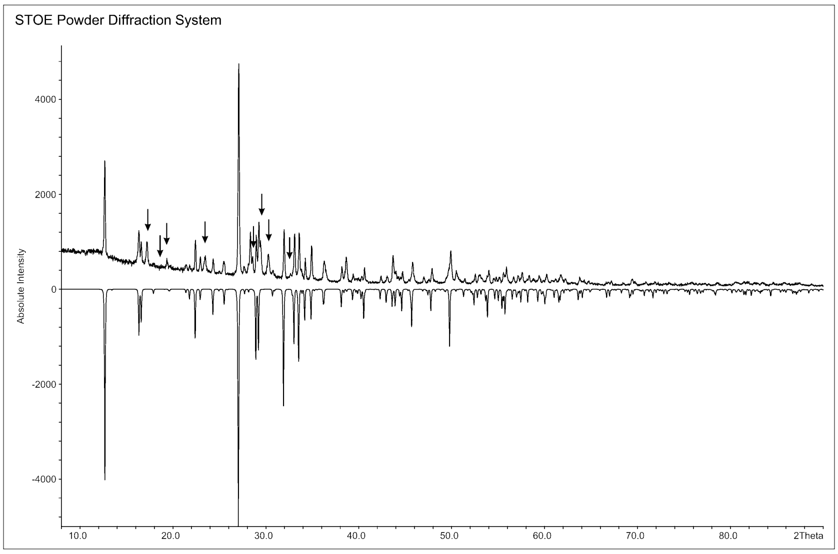

Figure B.31.: Comparison of measured and calculated X-ray powder diffraction pattern of $CdSb_2O_3Cl(OH)$ [synthesized from CdO, $SbCl_3$, Sb_4O_6 (6:2:1)]. The measured diffractogram is shown with positive intensities and calculated with negative intensities. Unindexed lines are marks with arrows. Comparison of the measured powder X-ray characteristic to reference patterns from the PDF database resulted in the identification of the additional crystalline products Cd(OH)Cl and Sb_2O_3.

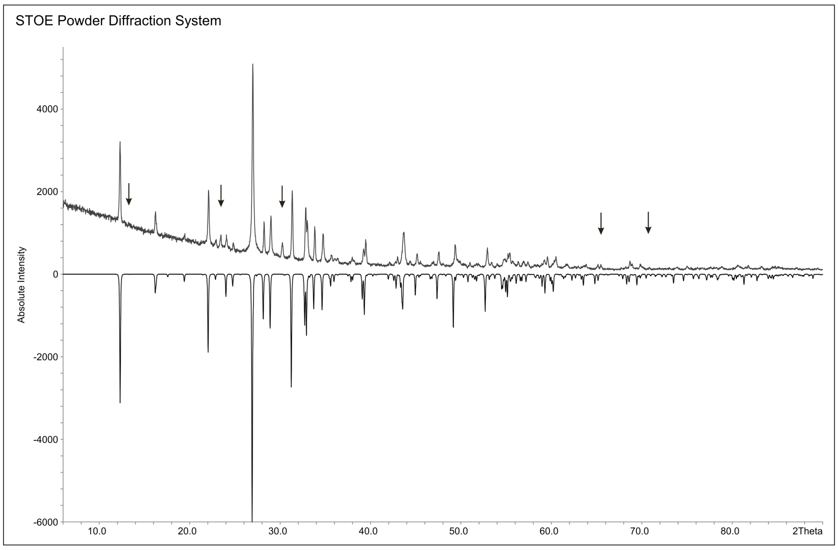

Figure B.32.: Comparison of measured and calculated X-ray powder diffraction pattern of $CdSb_2O_3Br(OH)$ [synthesized from CdO, $SbBr_3$ (2:1)]. The measured diffractogram is shown with positive intensities and calculated with negative intensities. Unindexed lines are marks with arrows. Comparison of the measured powder X-ray characteristic to reference patterns from the PDF database resulted in the identification of the additional crystalline products HSb_3O_8.

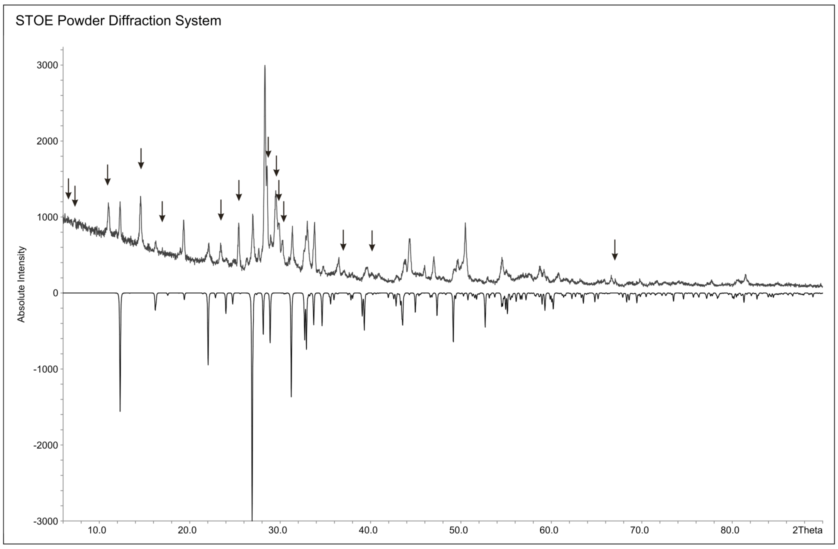

Figure B.33.: Comparison of measured and calculated X-ray powder diffraction pattern of $CdSb_2O_3Br(OH)$ [synthesized from CdO, $SbBr_3$, Sb_4O_6 (6:2:1)]. The measured diffractogram is shown with positive intensities and calculated with negative intensities. Unindexed lines are marks with arrows. Comparision of the measured powder X-ray characteristic to reference patterns from the PDF database resulted in the identification of the additional crystalline products $HSbBr_6(H_2O)_3$ and CdBr(OH).

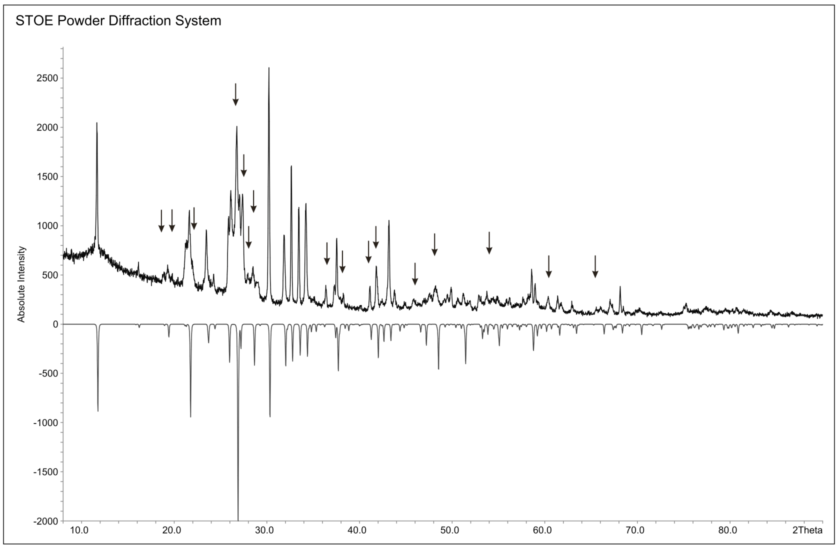

Figure B.34.: Comparison of measured and calculated X-ray powder diffraction pattern of $CdSb_2O_3I(OH)$ [synthesized from CdO, SbI_3 (2:1)]. The measured diffractogram is shown with positive intensities and calculated with negative intensities. Unindexed lines are marks with arrows. Comparision of the measured powder X-ray characteristic to reference patterns from the PDF database resulted in the identification of the additional crystalline products HSb_3O_8, SbI_3.

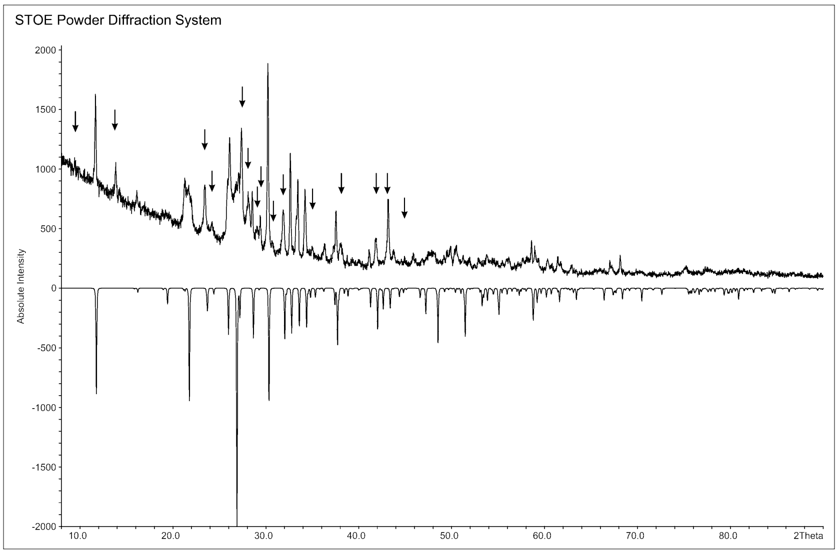

Figure B.35.: Comparison of measured and calculated X-ray powder diffraction pattern of $CdSb_2O_3I(OH)$ [synthesized from CdO, SbI_3, Sb_4O_6 (6:2:1)]. The measured diffractogram is shown with positive intensities and calculated with negative intensities. Unindexed lines are marks with arrows. Comparision of the measured powder X-ray characteristic to reference patterns from the PDF database resulted in the identification of the additional crystalline products $CdSbO_5I$, Sb_5O_7I.

Table B.21.: Atomic coordinates and equivalent isotropic displacement parameters [Å^2] for $Cd_2(OH)_3I$.

Atom	Wyck.	x	y	z	U_{eq}
Cd(1)	4c	0.21215(5)	¼	0.74054(3)	0.0248(1)
Cd(2)	4b	½	0	0	0.0249(2)
I(1)	4c	0.16682(4)	¼	0.04594(3)	0.0253(1)
O(1)	8d	0.0443(3)	0.5647(3)	0.2873(2)	0.0236(5)
O(2)	4c	0.1695(5)	¼	0.5181(3)	0.0228(7)
H(1)	4c	0.38(3)	0.41(3)	-0.061(2)	0.27(9)
H(2)	4c	0.10(3)	¼	0.565(2)	0.14(6)

Table B.22.: Anisotropic displacement parameters U_{ij} [Å^2] for $Cd_2(OH)_3I$.

Atom	U_{11}	U_{22}	U_{33}	U_{12}	U_{13}	U_{23}
Cd(1)	0.0206(2)	0.0277(2)	0.02617(2)	0	-0.0059(1)	0
Cd(2)	0.0292(2)	0.0217(2)	0.0239(2)	0.0048(1)	-0.0014(1)	-0.0018(1)
I(1)	0.0225(2)	0.0270(2)	0.0265(2)	0	0.00343(1)	0
O(1)	0.026(1)	0.022(1)	0.023(1)	-0.0013(9)	0.0025(9)	-0.0010(9)
O(2)	0.020(2)	0.024(2)	0.024(2)	0	0.0018(1)	0

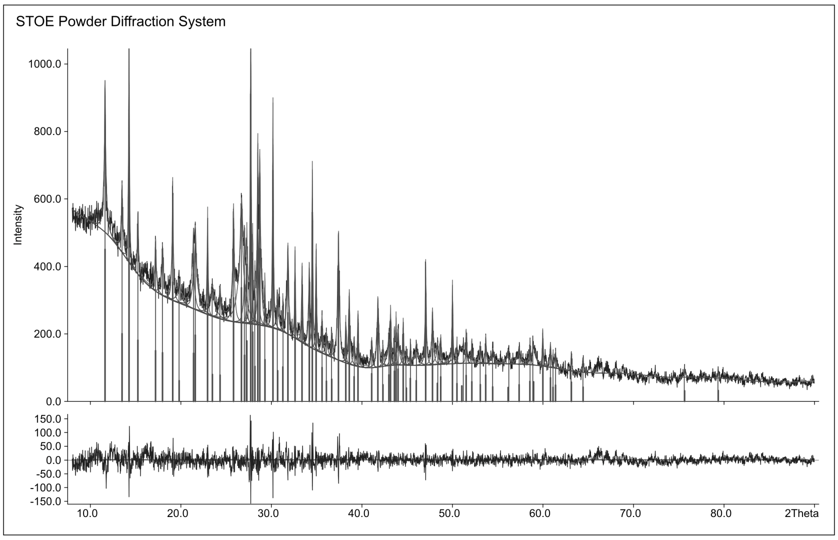

Figure B.36.: X-ray powder diffraction pattern of $Cd_2(OH)_3I$. On the basis of 76 reflections, of which 35 single and 24 unindexed lines the cell ($Pnma$, $a = 6.982(7)$ Å, $b = 7.706(6)$ Å, $c = 10.221(8)$ Å) was determined.
(Figure of Merit F(30) = 21.5).

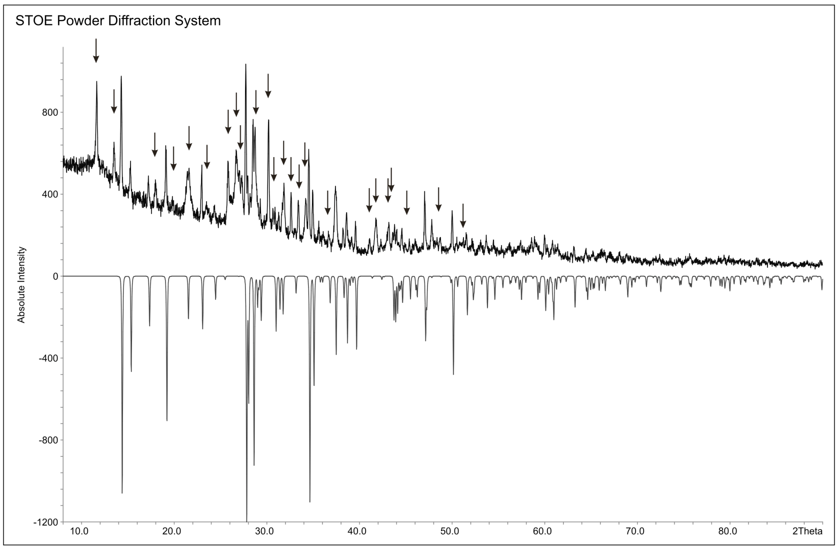

Figure B.37.: Comparison of measured and calculated X-ray powder diffraction pattern of $Cd_2(OH)_3I$. The measured diffractogram is shown with positive intensities and calculated with negative intensities. Unindexed lines are marks with arrows. Comparison of the measured powder X-ray characteristic to reference patterns from the PDF database resulted in the identification of the additional crystalline products $Cd_2(OH)_3I$ and Sb_5O_7I.

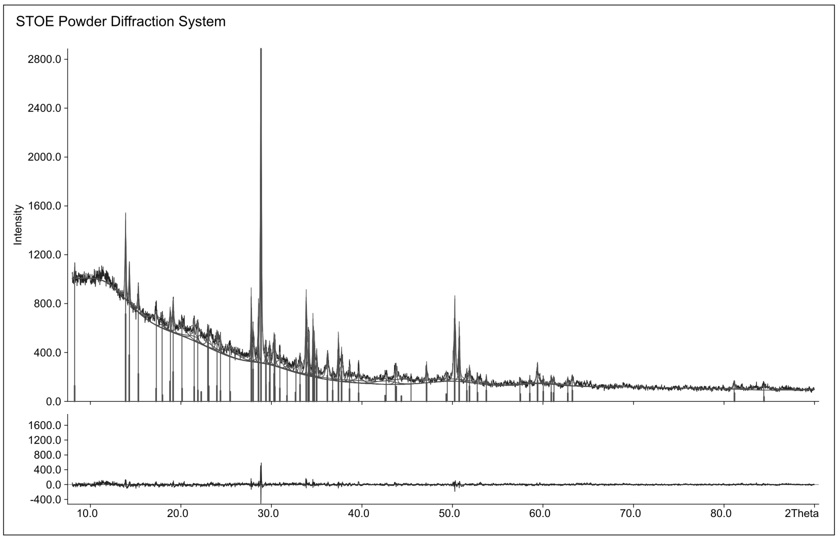

Figure B.38.: X-ray powder diffraction pattern of $Cd_2(OH)_3I$ (synthesized by hydrothermal reaction of $Cd(OH)_2$, I_2). On the basis of 61 reflections, of which 28 single and 29 unindexed lines the cell ($Pnma$, $a = 6.982(2)$ Å, $b = 7.699(1)$ Å, $c = 10.228(2)$ Å) was determined.
(Figure of Merit F(30) = 24.4).

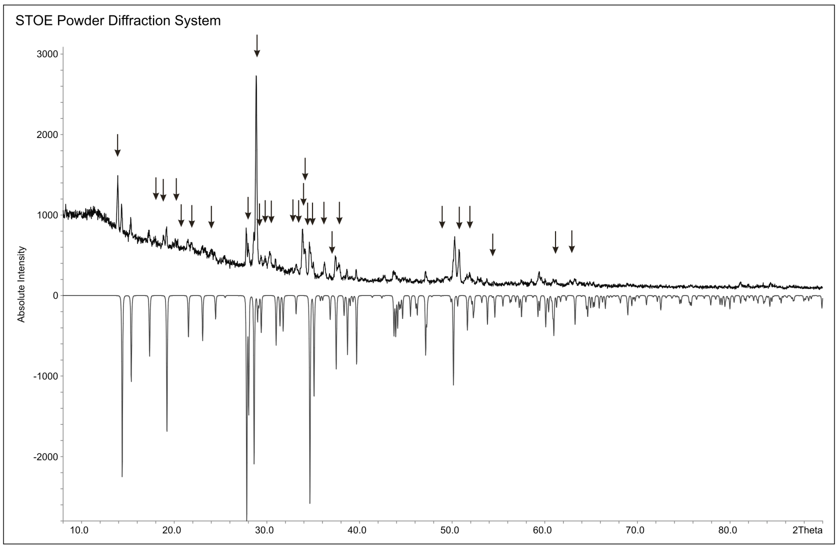

Figure B.39.: Comparison of measured and calculated X-ray powder diffraction pattern of $Cd_2(OH)_3I$. The measured diffractogram is shown with positive intensities and calculated with negative intensities. Unindexed lines are marks with arrows. Comparison of the measured powder X-ray characteristic to reference patterns from the PDF database resulted in the identification of the additional crystalline product $Cd_7(OH)_10I_4$.

Table B.23.: Atomic coordinates and equivalent isotropic displacement parameters [Å^2] for $CdSbO_2Cl$.

Atom	Wyck.	x	y	z	U_{eq}
Sb(1)	2e	0.40940(4)	¾	0.17532(5)	0.01272(2)
Cd(1)	2e	0.07259(5)	¼	0.81614(6)	0.01500(2)
Cl(1)	2e	0.17477(2)	¼	0.4470(2)	0.0211(3)
O(1)	2e	0.8426(4)	¼	0.0118(6)	0.0135(7)
O(2)	2e	0.4176(5)	¼	0.0445(6)	0.0173(8)

Table B.24.: Anisotropic displacement parameters U_{ij} [Å^2] for $CdSbO_2Cl$.

Atom	U_{11}	U_{22}	U_{33}	U_{12}	U_{13}	U_{23}
Sb(1)	0.0112(2)	0.0125(3)	0.0145(2)	0	0.00312(1)	0
Cd(1)	0.0170(2)	0.0133(3)	0.0160(3)	0	0.00637(2)	0
Cl(1)	0.0187(6)	0.0289(8)	0.0162(6)	0	0.0056(4)	0
O(1)	0.0117(2)	0.0141(2)	0.0144(2)	0	0.0024(1)	0
O(2)	0.0185(2)	0.0114(2)	0.0255(2)	0	0.0123(2)	0

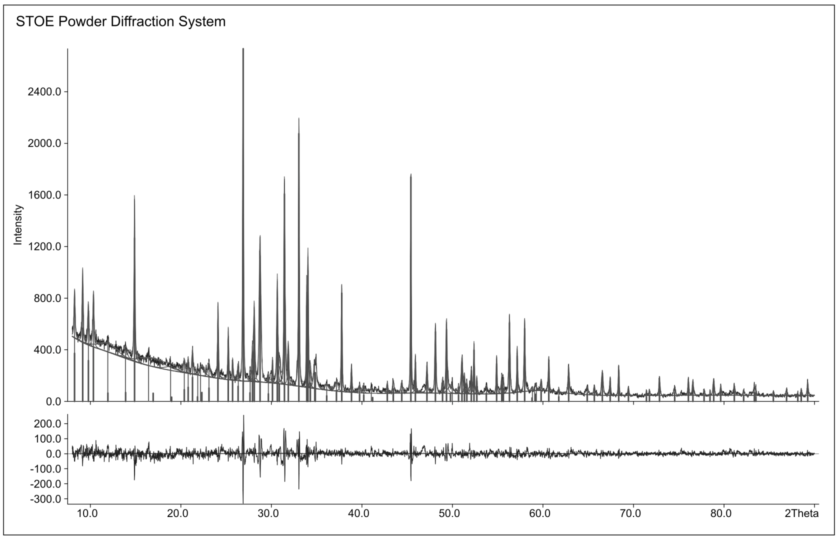

Figure B.40.: X-ray powder diffraction pattern of $CdSbO_2Cl$. On the basis of 97 reflections, of which 41 single and 28 unindexed lines the cell ($P2_1/m$, a = 7.5662(2)Å, b = 3.9838(1)Å, c = 6.0864(2)Å, β = 103.604(2)) was determined.
(Figure of Merit F(30) = 22.3).

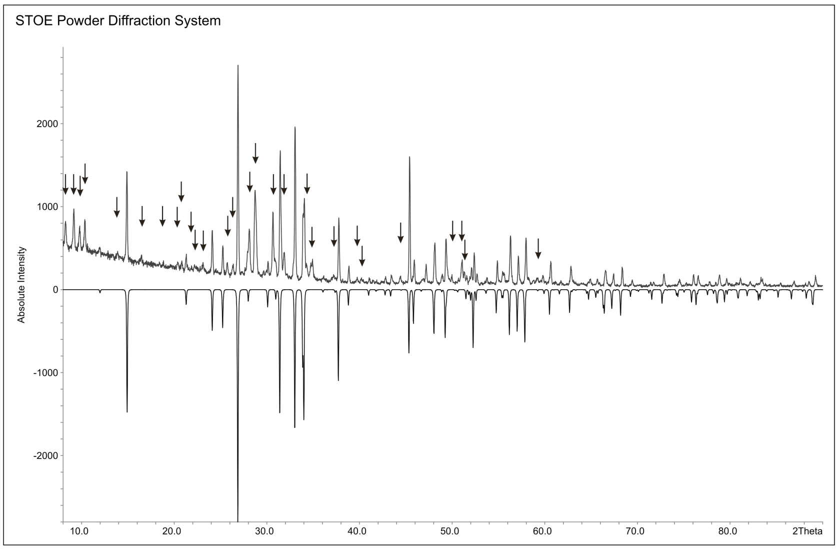

Figure B.41.: Comparison of measured and calculated X-ray powder diffraction pattern of $CdSbO_2Cl$. The measured diffractogram is shown with positive intensities and calculated with negative intensities. Unindexed lines are marks with arrows. Comparision of the measured powder X-ray characteristic to reference patterns from the PDF database resulted in the identification of the additional crystalline products $Sb_8O_{11}Cl_2$, CdO and $Sb_4O_5Cl_2$. Nine of unindexed lines could not be identified.

Table B.25.: Atomic coordinates and equivalent isotropic displacement parameters [Å^2] for CdSbO$_2$Br.

Atom	Wyck.	x	y	z	U$_{eq}$
Sb(1)	4c	0.16898(2)	¼	0.20813(2)	0.01515(1)
Sb(2)	4c	0.18081(2)	¾	0.42623(2)	0.01538(1)
Cd(1)	4c	0.00327(2)	¼	0.38664(2)	0.01746(1)
Cd(2)	4c	-0.00882(2)	¾	0.14495(3)	0.02121(1)
Br(1)	4c	0.39423(3)	¼	0.47768(4)	0.02221(1)
Br(2)	4c	0.12144(3)	¼	0.69072(4)	0.02396(1)
O(1)	4c	0.16847(2)	¼	0.3748(3)	0.0183(6)
O(2)	4c	0.05908(2)	¾	0.4509(3)	0.0179(6)
O(3)	4c	0.04419(2)	¼	0.2079(2)	0.0172(6)
O(4)	4c	0.1634(2)	¾	0.2623(3)	0.0186(6)

Table B.26.: Anisotropic displacement parameters U_{ij} [Å^2] for CdSbO$_2$Br.

Atom	U_{11}	U_{22}	U_{33}	U_{12}	U_{13}	U_{23}
Sb(1)	0.01672(2)	0.01367(2)	0.01504(2)	0	0.00315(9)	0
Sb(2)	0.01683(2)	0.01291(2)	0.01640(2)	0	-0.00209(9)	0
Cd(1)	0.02176(2)	0.0165(2)	0.01416(2)	0	0.00324(1)	0
Cd(2)	0.02658(2)	0.0176(2)	0.01948(2)	0	0.00363(1)	0
Br(1)	0.0222(2)	0.0252(3)	0.0192(2)	0	0.00002(2)	0
Br(2)	0.0209(2)	0.0270(3)	0.0239(2)	0	0.00226(2)	0
O(1)	0.0271(2)	0.0120(2)	0.0157(1)	0	-0.0020(1)	0
O(2)	0.0192(1)	0.0167(2)	0.0176(1)	0	0.0022(1)	0
O(3)	0.0165(1)	0.0188(2)	0.0164(1)	0	-0.0001(1)	0
O(4)	0.0287(2)	0.0114(2)	0.0157(14)	0	0.0041(12)	0

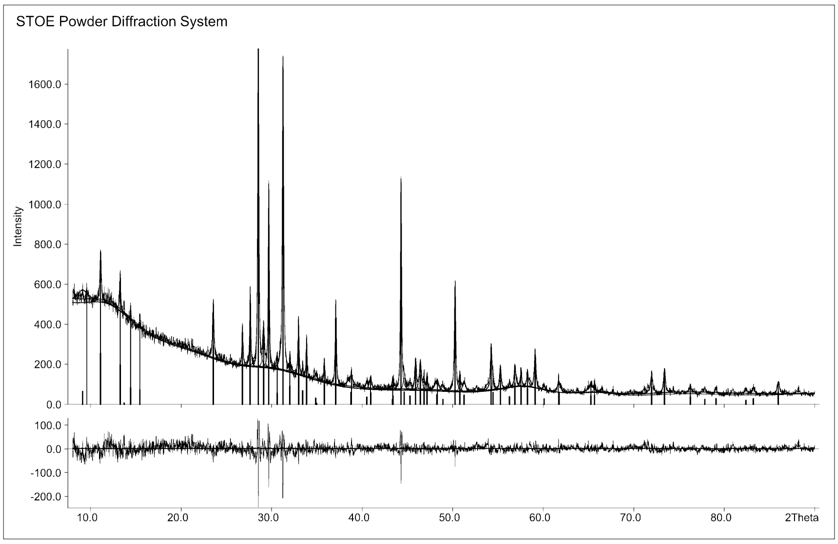

Figure B.42.: X-ray powder diffraction pattern of $CdSbO_2Br$. On the basis of 41 reflections, of which 16 single and 4 unindexed lines the cell ($Pnma$, a = 15.877(1)Å, b = 4.085(3)Å, c = 12.234(1)Å) was determined.
(Figure of Merit F(30) = 10.1).

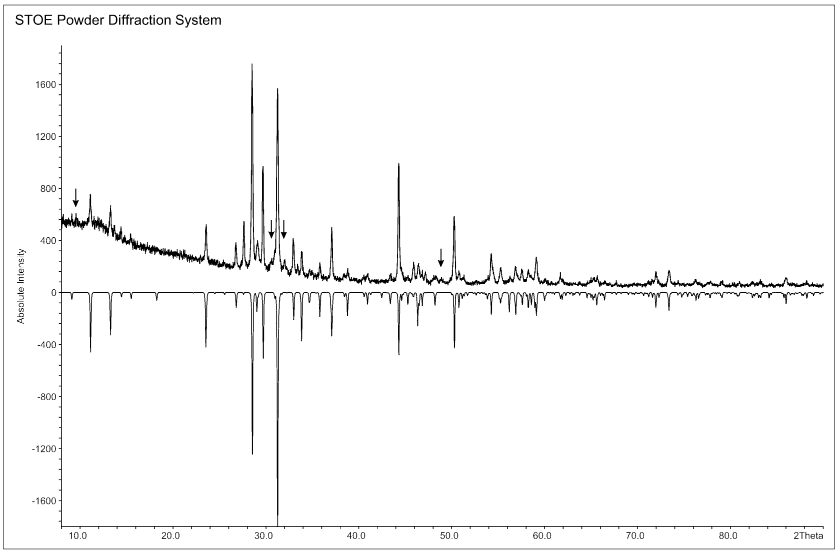

Figure B.43.: Comparison of measured and calculated X-ray powder diffraction pattern of $CdSbO_2Br$. The measured diffractogram is shown with positive intensities and calculated with negative intensities. Unindexed lines are marks with arrows. Comparision of the measured powder X-ray characteristic to reference patterns from the PDF database resulted in the identification of the additional crystalline product $Sb_8O_{11}Br_2$.

Table B.27.: Atomic coordinates and equivalent isotropic displacement parameters [Å^2] for $CoSb_2O_3Cl_2$.

Atom	Wyck.	x	y	z	U_{eq}
Sb(1)	2i	0.42965(7)	0.27631(4)	0.46001(4)	0.01572(1)
Sb(2)	2i	0.38976(7)	0.28697(5)	0.01781(4)	0.01606(1)
Co(1)	2i	0.02130(2)	0.51758(9)	0.71040(8)	0.01545(2)
Cl(1)	2i	0.7451(3)	0.13638(2)	0.28762(2)	0.0238(3)
Cl(2)	2i	0.1561(3)	0.7964(2)	0.23643(2)	0.0290(3)
O(1)	2i	0.7154(8)	0.4830(5)	0.0825(4)	0.0179(8)
O(2)	2i	0.2722(8)	0.3476(5)	0.2321(4)	0.0164(8)
O(3)	2i	0.2655(7)	0.5065(5)	0.5284(4)	0.0149(7)

Table B.28.: Anisotropic displacement parameters U_{ij} [Å^2] for $CoSb_2O_3Cl_2$.

Atom	U_{11}	U_{22}	U_{33}	U_{12}	U_{13}	U_{23}
Sb(1)	0.0132(2)	0.0168(2)	0.01690(2)	0.00441(1)	0.00204(1)	0.00217(1)
Sb(2)	0.0154(2)	0.0166(2)	0.01544(2)	-0.00159(1)	0.00156(1)	0.00213(1)
Co(1)	0.0119(4)	0.0197(4)	0.0150(3)	0.0013(3)	0.0014(2)	0.0041(3)
Cl(1)	0.0221(8)	0.0177(6)	0.0329(7)	0.0006(5)	0.0078(5)	0.00047(5)
Cl(2)	0.0271(9)	0.0219(7)	0.0340(7)	0.0053(6)	-0.0027(6)	0.0001(6)
O(1)	0.013(2)	0.0197(2)	0.0189(2)	0.0028(1)	-0.0005(1)	0.0006(2)
O(2)	0.016(2)	0.0212(2)	0.0138(1)	0.0033(1)	0.0035(1)	0.0066(2)
O(3)	0.012(2)	0.0160(2)	0.0171(2)	0.0004(1)	0.0038(1)	0.00026(1)

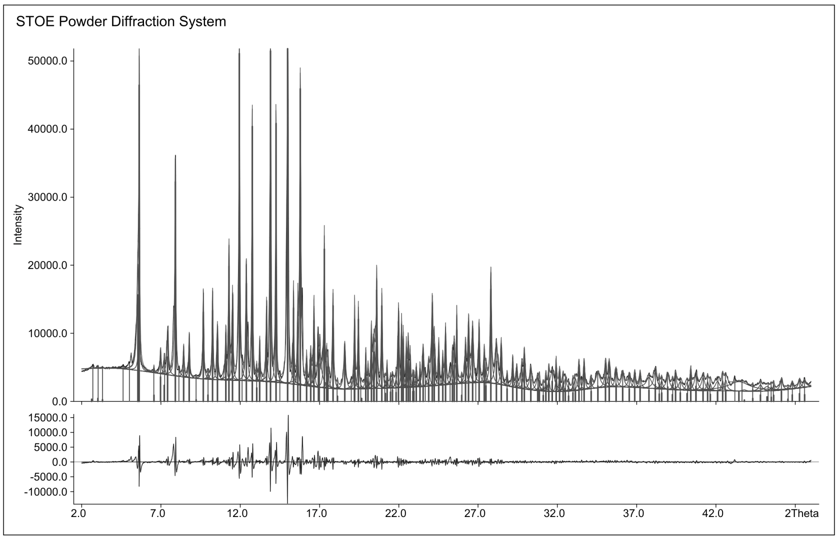

Figure B.44.: X-ray powder diffraction pattern of $CoSb_2O_3Cl_2$ (Mo-Kα). On the basis of 147 reflections, of which 23 single and 10 unindexed lines the cell ($P\bar{1}$, $a = 5.284(1)$Å, $b = 7.329(1)$Å, $c = 7.980(1)$Å, $\alpha = 90.95(8)°$, $\beta = 81.68(8)°$, $\gamma = 78.79(1)°$) was determined.
(Figure of Merit F(30) = 22.3).

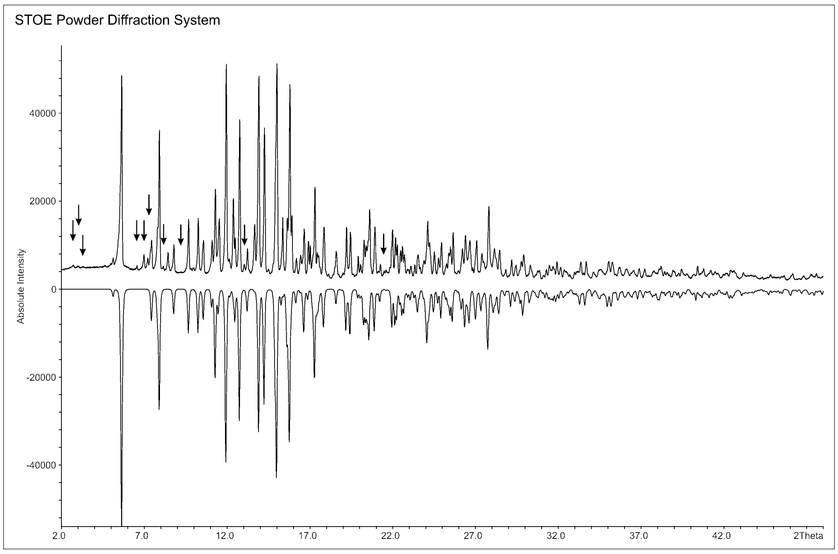

Figure B.45.: Comparison of measured (Mo-Kα) and calculated X-ray powder diffraction pattern of $CoSb_2O_3Cl_2$. The measured diffractogram is shown with positive intensities and calculated with negative intensities. Unindexed lines are marks with arrows. Comparison of the measured powder X-ray characteristic to reference patterns from the PDF database resulted in the identification of the additional crystalline product SbOCl.

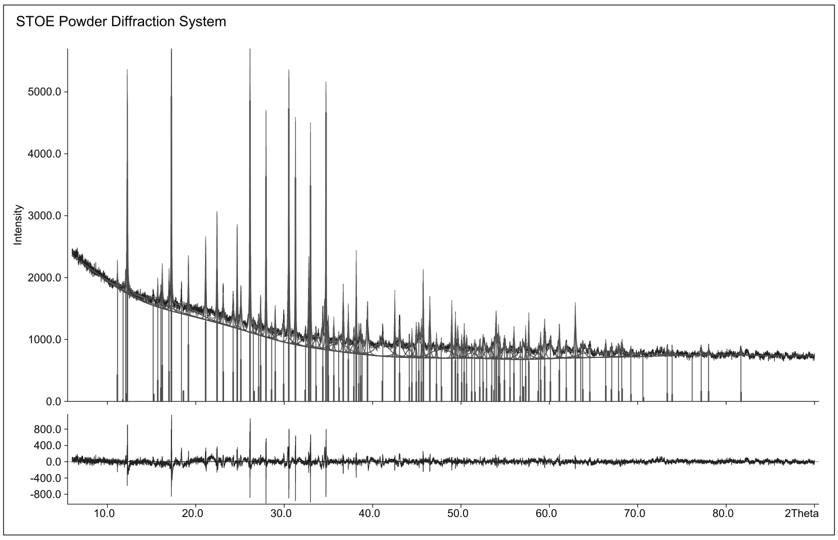

Figure B.46.: X-ray powder diffraction pattern of $CoSb_2O_3Cl_2$ (Cu-Kα). On the basis of 99 reflections, of which 36 single and 7 unindexed lines the cell ($P\bar{1}$, $a = 5.2956(2)$Å, $b = 7.342(3)$Å, $c = 8.028(3)$Å, $\alpha = 90.980(2)°$, $\beta = 81.375(2)°$, $\gamma = 79.16(3)°$) was determined.
(Figure of Merit F(30) = 42.1).

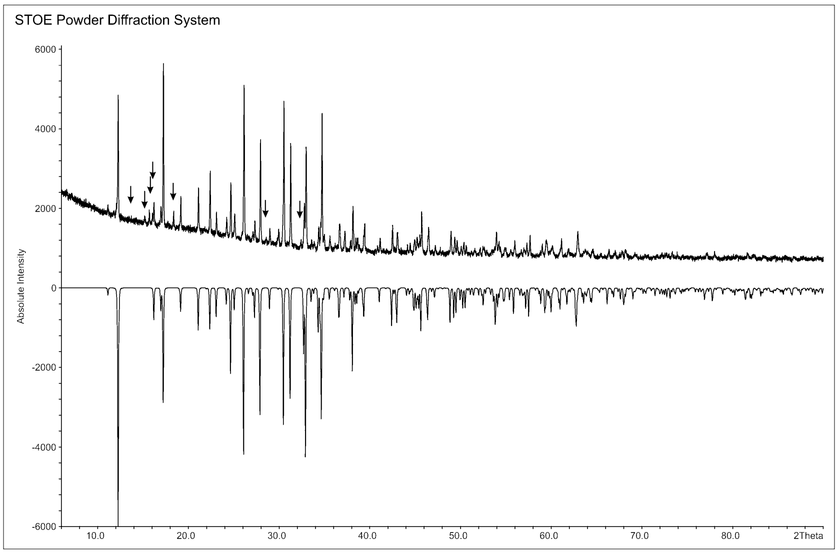

Figure B.47.: Comparison of measured (Cu-Kα) and calculated X-ray powder diffraction pattern of $CoSb_2O_3Cl_2$. The measured diffractogram is shown with positive intensities and calculated with negative intensities. Unindexed lines are marks with arrows. Comparison of the measured powder X-ray characteristic to reference patterns from the PDF database resulted in the identification of the additional crystalline product SbOCl.

Table B.29.: Atomic coordinates and equivalent isotropic displacement parameters [Å^2] for $Sb_4O_5Cl_2$.

Atom	Wyck.	x	y	z	U_{eq}
Sb(1)	4e	0.18690(4)	0.22347(5)	0.04889(2)	0.01539(1)
Sb(2)	4e	0.79666(4)	0.11702(5)	0.20158(2)	0.01494(1)
Cl(1)	4e	0.51038(2)	0.7041(2)	0.1157(1)	0.0304(3)
O(1)	2c	0	½	0	0.0355(1)
O(2)	4e	0.0739(5)	0.3377(6)	0.2110(2)	0.0195(6)
O(3)	4e	0.0703(5)	0.0048(6)	0.9181(2)	0.0195(6)

Table B.30.: Anisotropic displacement parameters U_{ij} [Å^2] for $Sb_4O_5Cl_2$.

Atom	U_{11}	U_{22}	U_{33}	U_{12}	U_{13}	U_{23}
Sb(1)	0.01545(2)	0.01275(2)	0.01759(2)	0.00135(1)	0.00053(1)	-0.00094(9)
Sb(2)	0.01918(2)	0.01321(2)	0.01335(2)	0.00149(9)	0.00527(1)	0.00320(9)
Cl(1)	0.0322(6)	0.0283(6)	0.0311(7)	-0.0013(5)	0.0068(5)	-0.00101(5)
O(1)	0.042(3)	0.029(3)	0.033(3)	0.007(2)	-0.004(2)	0.018(2)
O(2)	0.0241(1)	0.0152(1)	0.0193(2)	-0.0053(1)	0.0033(1)	-0.0064(1)
O(3)	0.0261(2)	0.0198(2)	0.0140(2)	-0.0060(1)	0.0085(1)	-0.0101(1)

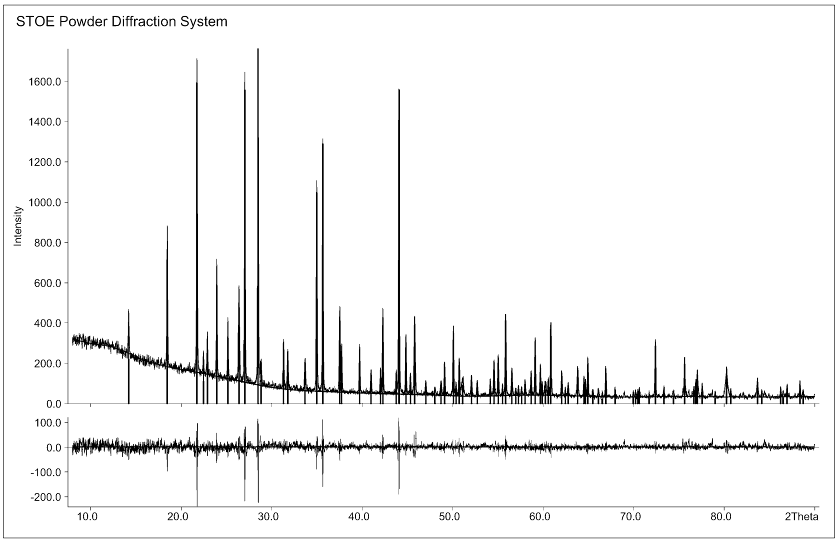

Figure B.48.: X-ray powder diffraction pattern of $Sb_4O_5Cl_2$. On the basis of 86 reflections, of which 40 single and 0 unindexed lines the cell ($P2_1/c$, $a = 6.290(5)$ Å, $b = 5.115(3)$ Å, $c = 13.547(8)$ Å, $\beta = 97.28(5)°$) was determined.
(Figure of Merit F(30) = 12.8).

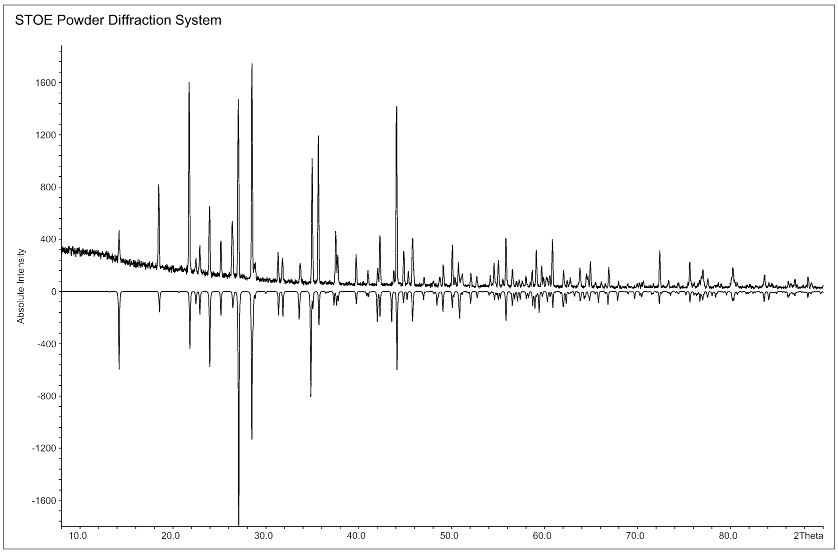

Figure B.49.: Comparison of measured and calculated X-ray powder diffraction pattern of $Sb_4O_5Cl_2$. The measured diffractogram is shown with positive intensities and calculated with negative intensities.

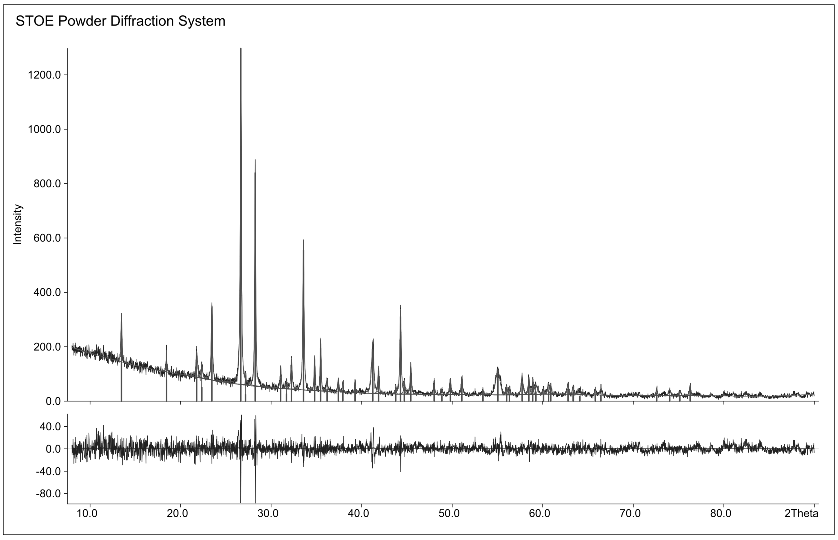

Figure B.50.: X-ray powder diffraction pattern of $Sb_4O_5Br_2$. On the basis of 48 reflections, of which 40 single and 0 unindexed lines the cell ($P2_1/c$, $a = 6.6200(1)$ Å, $b = 5.1480(8)$ Å, $c = 13.475(3)$ Å, $\beta = 97.889(1)°$) was determined.
(Figure of Merit F(30) = 33.6).

Table B.31.: Atomic coordinates and equivalent isotropic displacement parameters [Å^2] for SbOCl.

Atom	Wyck.	x	y	z	U_{eq}
Sb(1)	4e	0.42519(3)	0.02302(3)	0.21845(4)	0.01747
Sb(2)	4e	0.09038(3)	0.24350(3)	0.41703(4)	0.02104
Sb(3)	4e	0.26922(3)	0.67180(3)	0.01865(4)	0.02089
Cl(1)	4e	0.13089(2)	0.85700(1)	0.09071(2)	0.0343
Cl(2)	4e	0.34491(1)	0.10777(1)	0.60599(1)	0.0267
Cl(3)	4e	0.41092(2)	0.40240(1)	0.3880(2)	0.0400
O(1)	4e	0.0565(4)	0.3390(3)	0.2191(4)	0.0197
O(2)	4e	0.0943(3)	0.5686(3)	0.0269(4)	0.0184
O(3)	4e	0.2395(4)	0.1588(3)	0.2315(4)	0.0214

Table B.32.: Anisotropic displacement parameters U_{ij} [Å^2] for SbOCl.

Atom	U_{11}	U_{22}	U_{33}	U_{12}	U_{13}	U_{23}
Sb(1)	0.02115(2)	0.01673(2)	0.01456(2)	0.00102(1)	-0.00430(1)	-0.00246(1)
Sb(2)	0.02099(2)	0.02633(2)	0.01551(2)	-0.00042(1)	-0.00372(1)	0.00587(1)
Sb(3)	0.01740(2)	0.02599(2)	0.02035(2)	-0.00245(1)	-0.00661(1)	-0.00265(1)
Cl(1)	0.0340(7)	0.0260(6)	0.0406(7)	-0.00059(5)	-0.0040(5)	-0.0004(5)
Cl(2)	0.0264(6)	0.0339(6)	0.0199(5)	0.0015(4)	-0.0054(4)	-0.0049(5)
Cl(3)	0.0346(8)	0.0272(6)	0.0556(9)	0.0052(6)	-0.0056(6)	-0.0061(5)
O(1)	0.0225(2)	0.0176(2)	0.0177(2)	0.0021(1)	-0.0019(1)	0.0047(1)
O(2)	0.0212(2)	0.0217(2)	0.0128(1)	0.0021(1)	-0.0049(1)	-0.0083(1)
O(3)	0.0226(2)	0.0265(2)	0.0139(2)	-0.0024(1)	-0.0019(1)	0.0090(1)

Table B.33.: Atomic coordinates and equivalent isotropic displacement parameters [Å^2] for $Sb_8O_{11}I_2$.

Atom	Wyck.	x	y	z	U_{eq}
I(1)	2i	0.05659(1)	0.36405(1)	0.84217(8)	0.0250(3)
I(2)	2i	0.41654(1)	0.11302(1)	0.66562(8)	0.0284(3)
I(3)	2i	0.31853(1)	0.61815(1)	0.08336(8)	0.0249(3)
I(4)	2i	0.19251(1)	0.87505(1)	0.40874(9)	0.0308(3)
Sb(1)	2i	0.44409(1)	0.07095(1)	0.90806(8)	0.0211(3)
Sb(2)	2i	0.11220(1)	0.07774(1)	0.74910(8)	0.0201(2)
Sb(3)	2i	0.39250(1)	0.21442(1)	0.22980(8)	0.0197(3)
Sb(4)	2i	0.67271(1)	0.31451(1)	0.14229(8)	0.0215(3)
Sb(5)	2i	0.34717(1)	0.52388(1)	0.52454(8)	0.0230(3)
Sb(6)	2i	0.03986(1)	0.33188(1)	0.06220(8)	0.0219(3)
Sb(7)	2i	0.29554(1)	0.58671(1)	0.29675(9)	0.0241(3)
Sb(8)	2i	0.36626(1)	0.33628(1)	0.00181(8)	0.0188(2)
Sb(9)	2i	0.07807(1)	0.45280(1)	0.62635(8)	0.0238(3)
Sb(10)	2i	0.62020(1)	0.59122(1)	0.23985(8)	0.0188(2)
Sb(11)	2i	0.44165(1)	0.15044(1)	0.43928(8)	0.0233(3)
Sb(12)	2i	0.07648(1)	0.26578(1)	0.26602(8)	0.0209(3)
Sb(13)	2i	0.20504(1)	0.90594(1)	0.18620(8)	0.0197(2)
Sb(14)	2i	0.84099(1)	0.02572(1)	0.01474(8)	0.0204(3)
Sb(15)	2i	0.13389(1)	0.16973(1)	0.51595(8)	0.0208(3)
Sb(16)	2i	0.82014(1)	0.21574(1)	0.36488(9)	0.0298(3)
O(1)	2i	0.5802(1)	0.2076(1)	0.2091(8)	0.022(2)
O(2)	2i	0.6610(1)	0.0541(1)	0.0405(9)	0.024(3)
O(3)	2i	0.2135(1)	0.2739(1)	0.0563(8)	0.024(3)
O(4)	2i	0.4697(1)	0.5288(1)	0.2978(8)	0.025(3)
O(5)	2i	0.1087(1)	0.8345(1)	0.0396(8)	0.023(2)
O(6)	2i	0.0791(1)	0.6680(1)	0.6985(8)	0.026(3)
O(7)	2i	0.2828(1)	0.2192(1)	0.4553(8)	0.024(3)
O(8)	2i	0.2835(1)	0.0468(9)	0.1310(8)	0.020(2)
O(9)	2i	0.1686(1)	0.5507(1)	0.5547(8)	0.028(3)
O(10)	2i	0.0451(1)	0.9765(1)	0.1972(9)	0.026(3)
O(11)	2i	0.8885(2)	0.1000(1)	0.2792(1)	0.044(4)
O(12)	2i	0.7315(1)	0.4685(1)	0.2673(9)	0.025(3)
O(13)	2i	0.4681(1)	0.2039(1)	0.0213(8)	0.021(2)
O(14)	2i	0.5284(1)	0.4151(1)	0.1274(8)	0.024(2)
O(15)	2i	0.9738(1)	0.2085(1)	0.1316(8)	0.027(3)
O(16)	2i	0.2096(1)	0.3287(1)	0.6188(9)	0.027(3)
O(17)	2i	0.2667(1)	0.1237(1)	0.8694(9)	0.035(3)
O(18)	2i	0.3635(1)	0.0896(1)	0.3002(9)	0.028(3)
O(19)	2i	0.1483(1)	0.4195(1)	0.2216(9)	0.031(3)
O(20)	2i	0.5302(2)	0.3018(1)	0.4027(1)	0.050(4)
O(21)	2i	0.0173(1)	0.2702(1)	0.4627(1)	0.044(4)
O(22)	2i	0.282(2)	0.551(2)	0.4084(2)	0.079(6)

Table B.34.: Anisotropic displacement parameters U_{ij} [Å^2] for $Sb_8O_{11}I_2$.

Atom	U_{11}	U_{22}	U_{33}	U_{12}	U_{13}	U_{23}
I(1)	0.0203(5)	0.0266(6)	0.0295(7)	0.0114(5)	0.0083(5)	0.0062(4)
I(2)	0.0279(6)	0.0319(6)	0.0313(7)	0.0121(6)	0.0118(5)	0.0146(5)
I(3)	0.0238(5)	0.0262(5)	0.0295(7)	0.0116(5)	0.0095(5)	0.0117(4)
I(4)	0.0317(6)	0.0294(6)	0.0306(7)	0.0063(6)	0.0074(5)	0.0126(5)
Sb(1)	0.0228(5)	0.0212(5)	0.0278(7)	0.0118(5)	0.0157(5)	0.0098(4)
Sb(2)	0.0171(5)	0.0206(5)	0.0274(6)	0.0117(5)	0.0094(4)	0.0077(4)
Sb(3)	0.0148(5)	0.0209(5)	0.0270(6)	0.0096(5)	0.0089(4)	0.0068(4)
Sb(4)	0.0187(5)	0.0219(5)	0.0329(7)	0.0156(5)	0.0130(5)	0.0102(4)
Sb(5)	0.0265(6)	0.0246(6)	0.0254(6)	0.0109(5)	0.0129(5)	0.0134(5)
Sb(6)	0.0164(5)	0.0227(6)	0.0310(7)	0.0122(5)	0.0100(5)	0.0072(4)
Sb(7)	0.0207(5)	0.0232(6)	0.0332(7)	0.0102(5)	0.0117(5)	0.0098(4)
Sb(8)	0.0162(5)	0.0217(5)	0.0223(6)	0.0100(5)	0.0071(4)	0.0082(4)
Sb(9)	0.0152(5)	0.0304(6)	0.0262(7)	0.0131(6)	0.0080(5)	0.0020(4)
Sb(10)	0.0165(5)	0.0188(5)	0.0259(6)	0.0116(5)	0.0086(4)	0.0071(4)
Sb(11)	0.0211(5)	0.0279(6)	0.0279(7)	0.0133(5)	0.0116(5)	0.0114(5)
Sb(12)	0.0187(5)	0.0269(6)	0.0217(6)	0.0088(5)	0.0086(4)	0.0114(4)
Sb(13)	0.0187(5)	0.0226(5)	0.0229(6)	0.0101(5)	0.0090(4)	0.0096(4)
Sb(14)	0.0198(5)	0.0239(6)	0.0249(6)	0.0127(5)	0.0103(5)	0.0113(4)
Sb(15)	0.0181(5)	0.0210(5)	0.0273(6)	0.0103(5)	0.0098(5)	0.0075(4)
Sb(16)	0.0245(6)	0.0379(7)	0.0461(8)	0.0307(7)	0.0215(6)	0.0163(5)
O(1)	0.029(6)	0.017(5)	0.018(6)	0.004(5)	0.008(5)	0.005(5)
O(2)	0.020(6)	0.025(6)	0.038(7)	0.019(6)	0.017(5)	0.006(5)
O(3)	0.020(6)	0.039(7)	0.023(7)	0.013(6)	0.013(5)	0.016(5)
O(4)	0.020(6)	0.031(6)	0.027(7)	0.013(6)	0.010(5)	0.006(5)
O(5)	0.030(6)	0.018(5)	0.027(7)	0.011(5)	0.012(5)	0.009(5)
O(6)	0.026(6)	0.033(7)	0.034(7)	0.023(6)	0.020(5)	0.015(5)
O(7)	0.023(6)	0.029(6)	0.024(7)	0.012(6)	0.016(5)	0.004(5)
O(8)	0.019(5)	0.013(5)	0.024(7)	0.003(5)	0.003(5)	0.002(4)
O(9)	0.018(6)	0.043(7)	0.027(7)	0.014(6)	0.015(5)	0.003(5)
O(10)	0.018(6)	0.031(6)	0.031(7)	0.011(6)	0.011(5)	0.006(5)
O(11)	0.065(1)	0.029(7)	0.060(10)	0.018(7)	0.047(9)	0.020(7)
O(12)	0.020(6)	0.021(6)	0.039(8)	0.015(6)	0.008(5)	0.010(5)
O(13)	0.020(5)	0.020(5)	0.028(7)	0.012(5)	0.009(5)	0.010(4)
O(14)	0.030(6)	0.022(6)	0.024(7)	0.005(6)	0.010(5)	0.014(5)
O(15)	0.033(6)	0.030(6)	0.026(7)	0.015(6)	0.017(5)	0.010(5)
O(16)	0.021(6)	0.030(6)	0.029(7)	0.007(6)	0.006(5)	0.011(5)
O(17)	0.027(6)	0.054(8)	0.034(8)	0.024(7)	0.014(6)	0.019(6)
O(18)	0.026(6)	0.028(6)	0.033(7)	0.012(6)	0.011(5)	0.011(5)
O(19)	0.021(6)	0.031(7)	0.044(8)	0.017(6)	0.012(6)	0.005(5)
O(20)	0.041(8)	0.044(8)	0.083(1)	0.027(9)	0.042(9)	0.013(7)
O(21)	0.029(7)	0.043(8)	0.065(1)	0.032(8)	0.008(7)	0.013(6)

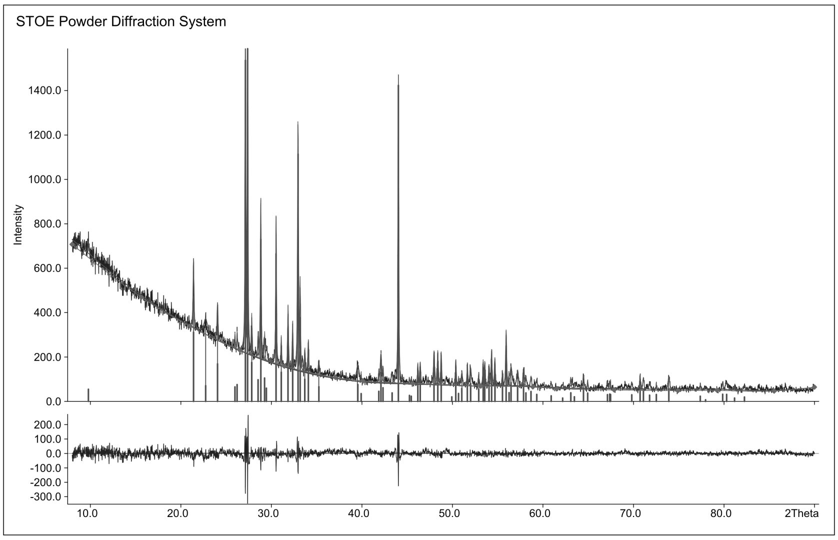

Figure B.51.: X-ray powder diffraction pattern of $Sb_8O_{11}I_2$. On the basis of 45 reflections, of which 16 single and 2 unindexed lines the cell ($P\bar{1}$, $a = 9.890(4)$ Å, $b = 11.602(5)$ Å, $c = 15.833(1)$ Å, $\alpha = 103.48(4)°$, $\beta = 103.54(4)°$, $\gamma = 103.97(3)°$) was determined.
(Figure of Merit F(30) = 4.1).

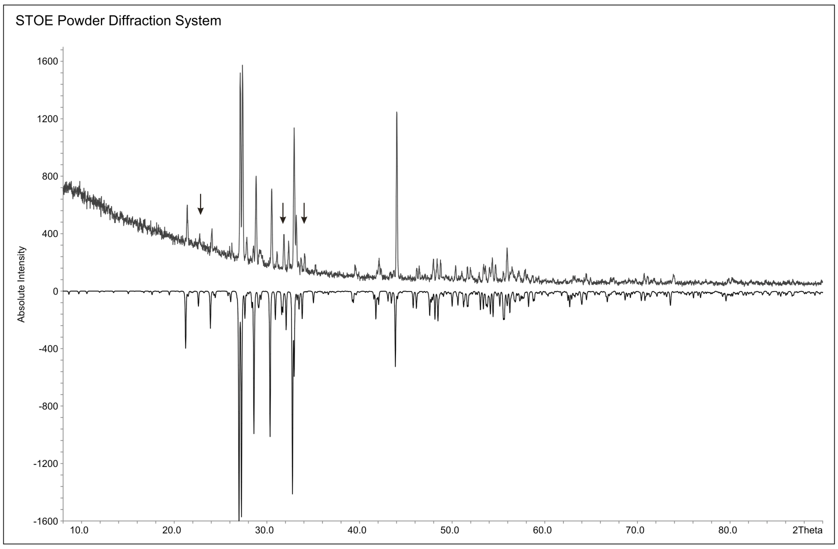

Figure B.52.: Comparison of measured and calculated X-ray powder diffraction pattern of $Sb_8O_{11}I_2$. The measured diffractogram is shown with positive intensities and calculated with negative intensities. Three unindexed lines could not be identified.

Bibliography

[1] A. Pfitzner, E. Freudenthaler
$(CuI)_3P_{12}$: Ein Feststoff mit einer neuen, theoretisch vorhergesagten Form des Phosphors.
Angew. Chem. **1995**, 107, 1784-1786 A. Pfitzner, E. Freudenthaler
$(CuI)_3P_{12}$: A Solid Containing a New Polymer of Phosphorus Predicted by Theory.
Angew. Chem. Int. Ed. Eng. **1995**, 34, 1647-1649

[2] A. Pfitzner
The use of Copper (I) Halides as a preparative tool.
Chem. Eur. J. **2000**, 6, 1891-1898

[3] M. H. Müller, W. Jeitschko
Preparation, properties, and crystal structure of the solid electrolytes $Cu_2P_3I_2$ and $Ag_2P_3I_2$.
Journal of Solid State Chemistry **1986**, 65, 178-189

[4] A. Pfitzner, E. Freudenthaler
$(CuI)_2P_{14}$: ein neues Phosphorpolymer in einer Kupferhalogenid-Matrix.
Zeitschrift fuer Naturforschung, Teil B. Anorganische Chemie, Organische Chemie **1997**, 52, 199-202

[5] M. F. Breau, A. Pfitzner
$HgI_2{\cdot}As_4S_4$: An Adduct from HgI_2 Molecules and Undistorted As_4S_4 Cages.
Angew. Chem. Int. Ed. **2006**,45, 4464-4467

[6] D. Hoppe, A. Pfitzner
Adduct compounds $(MCl_5)_2$ (beta-P_4Ch_4) with M = Nb, Ta and Ch = S, Se.
Zeitschrift fuer Naturforschung, Teil B. Anorganische Chemie, Organische Chemie **2009**, 64(1), 58-62

[7] D. Hoppe, D. Schemmel, M. Schuetz, A. Pfitzner
Nb and Ta adducts: Connecting d^0 metal chlorides and phosphorus sulfide cages.
Chemistry - A European Journal **2009**,15(29), 7129-7138

[8] D. Hoppe, D. Schemmel, M. Schuetz, A. Pfitzner
Nb and Ta adducts: Connecting d^0 metal chlorides and phosphorus sulfide cages.
Chemistry - A European Journal **2009**,15(29), 7129-7138

[9] P. Schwarz, J. Wachter, M. Zabel
Novel coordination modes for E_4S_3 cage molecules (E = P, As) in unprecedented quaternary As_4S_3 $(CuCl)_n$ (n = 1,2) solid-state phases.
European Journal of Inorganic Chemistry **2008**, 35, 5460-5463

[10] A. Pfitzner, S. Zimmerer
$(CuI)_3Cu_2TeS_3$: Layers of Cu_2TeS_3 in copper(I)-iodide.
Angewandte Chemie Int. Ed. **1997**, 36, 982-984

[11] A. Pfitzner
$CuClCu_2TeS_3$: synthesis, structure determination, and Raman spectroscopic characterization of a new zincblende derivative.
Inorganic Chemistry **1998**, 37, 5164-5167

[12] A. Pfitzner, F. Baumann, W. Kaim
TeS_2^- Radikalanionen in $CuBrCu_{1.2}TeS_2$.
Angew. Chem. **1998**, 110, 2057-2059 A. Pfitzner, F. Baumann, W. Kaim
TeS_2^- Radical Anions in $CuBrCu_{1.2}TeS_2$.
Angew. Chem. Intl. Ed. Engl. **1998**, 37, 1955-1957

[13] A. Pfitzner
$(CuI)_2Cu_3SbS_3$: Copper iodide as solid solvent for thiometalate ions.
Chemistry - A European Journal **1997**, 3, 2032-2038

[14] J. Galy, G. Meunier, S. Anderson, A. Astrom
Stéréochimie des elements comportant des paires non liées: Ge (II), As (III), Se (IV), Br (V), Sn (II), Sb (III), Te (IV), I (V), Xe (VI), Tl (I), Pb (II), et Bi (III) (oxydes, fluorures et oxyfluorures).
J. Solid State Chem., **1975**, 13, 142-159

[15] M. Johnsson, K. W. Tornroos
A synthetic zinc tellurium oxochloride, $Zn_2(TeO_3)Cl_2$.
Acta Cryst. C, **2003**, 59, i53-i54

[16] M. Johnsson, K.W. Toernroos
Zinc selenium oxochloride, beta-$Zn_2(SeO_3)Cl_2$, a synthetic polymorph of the mineral sophiite.
Acta Cryst. C, **2007**, 63(5), i34-i36

[17] Zhang Dong, M. Johnsson
$Zn_2(TeO_3)Br_2$.
Acta Cryst. E , Structure Reports Online, **2008**, 64(5), i26-i26.

[18] M. Johnsson, K. W. Tornroos
Synthesis and crystal structure of the layered compound $CuZn(TeO_3)Cl_2$.
Solid State Sciences, **2003**, 5, 263-266

[19] P. Lemmens, G. Guentherodt, C. Gros
Magnetic light scattering in low-dimensional quantum spin systems.
Physics Reports **2003**, 375, 1-103

[20] R. Becker, H. Berger, M. Johnsson
Monoclinic $Cu_3(SeO_3)_2Cl_2$: an oxohalide with an unusual CuO_4Cl trigonal-bipyramidal coordination.
Acta Crystallographica C **2007**, 63(1), i4-i6

[21] B. Bastide, P. Millet, M. Johnsson, J. Galy
Synthesis of copper(II) and selenium(IV) oxochlorides by chemical transport reaction: crystal structure of $Cu_9O_2(SeO_3)_4Cl_6$.
Materials Research Bulletin **2000**, 35, 847-855

[22] R. Becker, J. Mats
Crystal structure of $Cu_3Bi(TeO_3)_2O_2Cl$*: a Kagome lattice type compound.*
Solid State Sciences **2005**, 7, 375-380

[23] P. Millet, B. Bastide, V. Pashchenko, S. Gnatchenko, V. Gapon, Y. Ksari, A. Stepanov
Syntheses, crystal structures and magnetic properties of francisite compounds $Cu_3Bi(SeO_3)_2O_2X$ *(X= Cl, Br and I).*
Journal of Materials Chemistry **2001**, 11, 1152-1157

[24] M. Johnsson, K. W. Tornroos, P. Lemmens, P. Millet
Crystal structure and magnetic properties of a new two-dimensional S = 1 quantum system $Ni_5(TeO_3)_3X_2$ *(X = Cl, Br).*
Chemistry of Materials **2003**, 15, 68-73

[25] Y.-L. Shen, J.-G. Mao, H.-L. Jiang
Synthesis, crystal structure and magnetic property of a new nickel selenite chloride: $Ni_5(SeO_3)_4Cl_2$*.*
Journal of Solid State Chemistry **2005**, 178, 2942-2946

[26] M. Johnsson, K. W. Tornroos, F. Mila, P. Millet
Tetrahedral clusters of copper(II): crystal structures and magnetic properties of $Cu_2Te_2O_5X_2$ *(X = Cl, Br).*
Chemistry of Materials **2000**, 12, 2853-2857

[27] P. Lemmens, K.-Y. Choi, E. E. Kaul, C. Geibel, K. Becker, W. Brenig, R. Valenti, C. Gros, M. Johnsson, M. Millet, F. Mila
Evidence for unconventional magnetic instability in the spin-tetrahedra system $Cu_2Te_2O_5Br_2$*.*
Physical Review Letters **2001**, 87, 22, 227201-4

[28] K. Hanke, V. Kupcik, O. Lindqvist
The crystal structure of $CuTe_2O_5$*.*
Acta Crystallographica B, **1973**, 29, 963-970

[29] Z. Mayerova, M. Johnsson, S. Lidin
The crystal structure of $CuSb_2O_3Br$*: slabs from cubic* Sb_2O_3 *interspersed between puckered hexagonal CuBr-type layers.*
Journal of Solid State Chemistry **2005**, 178(11), 3471-3475

[30] Z. Mayerova, M. Johnsson, S. Lidin
Lone-Pair Interfaces That Divide Inorganic Materials into Ionic and Covalent Parts.
Angew. Chem. Int. ed. **2006**, 45(34), 5602-5606

[31] Z. Hugonin, M. Johnsson, S. Lidin
$Cu_{20}Sb_{35}O_{44}Br_{37}$ *- one structure, two temperature dependencies.*
Solid State Sciences **2008**, 10(2), 160-167

[32] R. Becker, M. Johnsson, R. Kremer, P. Lemmens
Crystal structure, magnetic properties and conductivity of $CuSbTeO_3Cl_2$*.*
Solid State Sciences **2003**, 5, 1411-1416

[33] Z. Hugonin, M. Johnsson, S. Lidin, D. Wulferding, P. Lemmens, R. K. Kremer
Anomalous low-temperature behavior of the Co dimers in the oxo-halide $CoSb_2O_3Br_2$.
J. of Solid State Chem., **2008**, 181, 2776-2782

[34] W.G. Brauer
Handbook of Preparative Inorganic Chemistry.
1960 Academic Press Inc.

[35] M. Edstrand
On the Crystal Structure of the Antimony Oxychloride $Sb_4O_5Cl_2$ *and Isomorphous Oxybromide.*
Acta Chemica Scandinavica **1947**, 1, 178-203

[36] P. Patnaik
Handbook of Inorganic Chemicals.
2004 Amsterdam: McGraw-Hill Professional,
ISBN 0070494398

[37] H. Schäfer
Chemische Transportreaktionen.
1962 Verlag Chemie GmbH.

[38] J. P. Hornak
Encyclopedia of Imaging Science and Technology.
2002 Wiley, New York

[39] W. F. Hemminger, H. K. Cammenga
Methoden der Thermischen Analyse.
1989 Springer Verlag Berlin

[40] M. E. Brown
Introduction to thermal analysis
1988 Chapman and Hall, London

[41] P.-E.Werner, L.Eriksson, M.Westdahl
TREOR, a semi-exhaustive trial-and-error powder indexing program for all symmetries.
J. Appl. Cryst. **1985**, 18, 367-370

[42] J.W.Visser
A fully automatic program for finding the unit cell from powder data.
J. Appl. Cryst. **1969**, 2, 89-95

[43] M. Ermrich, F. Hahn, E. R. Wölfel
Used of imaging plates in X-ray analysis.
Textures and Microstructures, **1997**, 29, 89-101

[44] Ch. Naether
Practical aspects of X-ray single crystal structure determination.
2002 Institute of Inorganic Chemistry, Christian-Albrechts-University, Kiel

[45] N. Steno
De solido intra solidum naturaliter contento dissertationis prodromus.
Firenze: Typographia sub signo Stellæ, **1669**.

[46] G. Friedel
Étude sur les groupements cristallins.
Extrait du Bullettin de la Société de l'Industrie minérale, Quatrième série, Tomes III e IV. Saint-Étienne, Société de l'imprimerie Thèolier J. Thomas et C., **1904**, 485

[47] T. Hahn, V. Janovec and H. Klapper
Bicrystals, twins and domain structures - A comparison.
Ferroelectrics, **1999**, 222, 11-21

[48] Th. Hahn, and H. Klapper
Twinning of crystals.
Section 3.3 in A. Authier, Ed., International Tables for Crystallography Volume D: Physical Properties of Crystals. International Union of Crystallography / Kluwer Academic Publishers, **2003**.

[49] W. Massa
Crystal structure determinations.
2002 Institute of Inorganic Chemistry, Christian-Albrechts-University, Kiel

[50] J. G. Sole, L. E. Bausa, D. Jaque
Optical spectroscopy of inorganic solids.
2005 John Wiley & Sons Ltd., England

[51] P. Kubelka, F. Munk
Zeits. Tech. Phys., **1931**, 12, 593

[52] P. Kubelka
New contributions to the optics of intensely light-scattering materials. Part I.
J. Opt. Soc. Am., **1948**, 38, 448-457

[53] J. Tauc, R. Grigorovici, A. Vancu
Optical properties and electronic structure of amorphous germanium.
Phys. Stat. Sol., **1966**, 15, 627-637

[54] J. P. Perdew, Y. Wang
Phys. Rev. B **1992**, 45, 13244

[55] N. Tigau, V. Ciupina, G. Prodan
Structural, optical and electrical properties of Sb_2O_3 *thin films with different thickness.*
J. Optoelectron. Adv. Mat., **2006**, 8,37-42

[56] K. Nakamoto
Infrared and Raman spectra of inorganic and coordination compounds.
2008 WILEY-VCH Verlag GmbH & Co.
ISBN 976-0-471-74493-1

[57] B. A. DeAngelis, R. N. Newnham, W. B. White
Factor group analysis of the vibrational spectra of crystals: a review and consolidation.
American Mineralogist, **1972**, 57, 255-268

[58] E.E. Coleyshaw, W.P. Griffith, R.J. Bowell
Fourier-transform Raman spectroscopy of minerals.
Spectrochim. Acta, Part A, **1994** 50A(11), 1909-18

[59] J. R. Ferrano, K. Nakamoto, Ch. W. Brown
Introductory Raman Spectroscopy.
2002 Academic Press

[60] *FT-IR spectroscopy. Attenualed Total Reflectance (ATR).*
2005 PekinElmer Life and Analytical Sciences

[61] *ATR Accessories.*
2004 PekinElmer Life and Analytical Sciences

[62] Pike Technologies Spectroscopic Creativity
Comparision of FTIR spectra collected by transmission and ATR sampling.

[63] P. E. Lippens
Mössbauer isomer shift of crystalline antimony compounds.
Solid State Communications **2000**,113, 399-403

[64] J. Olivier-Fourcade, A. Ibanez, J. C. Jumas, M. Maurin, I. Lefebvre, P. Lippens, M. Lannoo, G. Allan
Chemical bonding and electronic properties in antimony chalcogenides.
Journal of Solid State Chemistry, **1990**, 87, 366-377

[65] W. Kohn, A. D. Becke, R. G. Parr
Density functional theory of electronic structure
Journal of Physical Chemistry, **1996**, 100, 12974-12980

[66] N. Argaman, G. Makov
Density functional theory - an introduction
American Journal of Physics, **2000**, 68, 69-79

[67] J. A. Alonso
Antimony (III) tellurium (IV) chloride trioxide $SbTeO_3Cl$: synthesis and ab initio structure determination from X-ray and neutron powder diffraction data.
J. Chem. Soc., Dalton Trans.,**1998**, 1947-1949

[68] C. Wood, B. Van Pelt, A. Dwight
The optical properties of amorphous and crystalline Sb_2O_3.
Phys. State Sol., **1972** , 54, 701

[69] C. Svensson
The crystal structure of orthorhombic antimony trioxide, Sb_2O_3.
Acta Crystallographica B, **1974** , 30, 458-461

[70] P. Ballirano, A. Maras
Refinement of the crystal structure of arsenolite, As_2O_3.
Z. fuer Kristallographie - New Crystal Structures, **2002**, 217, 177-178

[71] V. Sundararajan, V. Kumar
Ab-Initio Molecular-Dynamics Study of Antimony Clusters.
Journal of Chemical Physics, **1995**, 102, 24, 9631-9637

[72] H. L. Yakel, J. Brynestad
Refinement of the crystal structure of orthorhombic zinc chloride.
Inorg. Chem., **1978**, 3294-3296

[73] C. Chieh, M. A. White
Crystal structure of anhydrous zinc bromide.
Zeitschrift fuer Kristallographie, **1984**, 166, 189-197.

[74] S. C. Abrahams, J. L. Bernstein
Remeasurement of the structure of hexagonal ZnO.
Acta Cryst., **1969**, B25, 1233-1236

[75] R. G. Orman, D. Holland
Thermal phase transition in antimony (III) oxides.
J. of Solid State Chem., **2007**, 180, 2587-2596

[76] L. F. Santos, R. M. Almeida
Zinc halide glasses with improved thermal characteristics.
Journal of Non-Crystalline Solids, **1995**, 184, 68-71

[77] S. J. Gilliam, J. O. Jensen, A. Benerjee, D. Zeroka, S. J. Kirkby, C. N. Merrow
A theoretical and experimental study of Sb_4O_6*: vibrational analysis, infrared, and Raman spectra.*
Spectrochimica Acta, **2004**, A 60, 425-434

[78] E. I. Voit, A. E. Panasenko, L. A. Zemnukhova
Vibrational spectroscopic and quantum chemical study of antimony (III) oxide.
Journal of Structural Chemistry, **2009**, 50, 1, 60-66

[79] H. Wakita, G. Johansson, M. Sandström, P. L. Goggin, H. Ohtaki
Structure determination of zinc iodide complexes formed in aqueous solution.
J of Sol. Chem., **1991**, 20, 7, 643-668

[80] S. N. Yannopoulos, A. G. Kalampounias, A. Chrissanthopoulos, G. N. Papatheodorou
Temperature induced changes on the structure and the dynamics of the tetrahedral glasses and melts of $ZnCl_2$ *and* $ZnBr_2$*.*
J. Chem. Phys., **2003**, 118, 7, 3197-3214

[81] K. Koepernik, and H. Eschrig
1999 Phys. Rev. B, 59, 1743

[82] H.-L. Jiang, J.-G. Mao
$[Cd_2(Te_6O_{13})][Cd_2Cl_6]$ *and* $Cd_7Cl_8(Te_7O_{17})$*: Novel tellurium(IV) oxide slabs and unusual cadmium chloride architectures.*
Inorganic Chemistry **2006**, 45(2), 717-721

[83] M. Kubiak, T. Glowiak and H. Kozlowski
Structure of 2-amino-4,5-dihydro-3H$^+$*-1,3-thiazolium trichlorocadmate(II),* $C_3H_7N_2S^+CdCl_3^-$*.*
Acta Crystallographica **1983**, C39, 1637

[84] D. E. Partin, M. O'Keeffe
The structures and crystal chemistry of magnesium chloride and cadmium chloride.
Journal of Solid State Chemistry, **1991**, 95, 176-183

[85] R. S. Mitchell
Single crystal x-ray study of structural polytypism in cadmium bromide.
Zeitschrift fuer Kristallographie, Kristallgeometrie, Kristallphysik, Kristallchemie, **1962**, 117, 309-318

[86] S. D. Sharma, G.L. Sharma, V.K. Agrawal
The crystal structure of a new polytype 12R of cadmium bromide.
Acta Crystallographica B, **1980**, 36, 26-28

[87] R. Hoppe
Madelung Constants.
Angew. Chem. Int. Ed., **1966**, 5, 95-106

[88] R. Hoppe
The Coordination Number-an "Inorganic Chameleon".
Angew. Chem.Int. Ed., **1970**, 9, 25-34

[89] S. G. Bratsch, J. J. Lagowski
Madelung Constants, Bond Lengths, and Coordination.
Journal of Physical Chemistry, **1985**, 89, 1692-1695

[90] M. E. Straumanis, P. M. Vora, P A. A. Khan
Gitterparameter und thermische Ausdehnungskoeffizienten des CdO zwischen 40 und 1300 K. Fehlbau des Oxids.
ZAAC, **1971**, 383, 211-219

[91] Z. Mayerova, M. Johnsson, S. Lidin
The structure of onoratoite, $Sb_8O_{11}X_2$ (X = Cl, Br) revisited.
Solid State Sciences, **2006**, 8(7), 849-854

[92] R. Becker, M. Johnsson, R. K. Kremer, H.-H. Klauss, P. Lemmens
Crystal Structure and Magnetic Properties of $FeTe_2O_5X$ (X = Cl, Br): A Frustrated Spin Cluster Compound with a New Te(IV) Coordination Polyhedron.
Journal of the American Chemical Society **2006**, 128, 15469-15475

[93] D. Zhang, M. Johnsson, H. Berger, R. K. Kremer, D. Wulferding, P. Lemmens
Separation of the oxide and halide part in the oxohalide $Fe_3Te_3O_{10}Cl$ due to high Lewis acidity of the cations.
Inorganic Chemistry **2009**,48, 6599-6603

[94] R. Becker, M. Johnsson
Three new tellurite halides with unusual Te(4+) coordinations and iron honeycomb lattice variants.
Journal of Solid State Chemistry **2007**, 180(5), 1750-1758

[95] I. D. Brown
Recent developments in the method and applications of the bond valence model.
Chemical Review, **2009**,109, 6858-6919

[96] R. Weihrich, S. Lange, T. Nilges
Chemical bonding and Mössbauer spectroscopic investigations on ternary polyphosphides $AgSbP_{14}$.
Solid State Sciences **2009**,11, 519-527

[97] G. Schaack, N. Uhle
Raman spectra in doped cadmium oxide.
Solid State Communications, **1976**,19, 315-318

[98] S. Nakashima, H. Yoshida, T. Fukumoto
Raman spectra of $CdCl_2$, $CdBr_2$ *and* CdI_2.
J. Phys.Soc. Japan, **1971**, 31, 1847

[99] Y. Morioka, I. Nakagava
Far-IR reflection spectra and lattice vibrations of cadmium chloride, bromide and iodide crystals.
Spectrochimica Acta, **1978**, 34A, 5-8

[100] D. J. Lockwood, R. W. G. Syme
Halogen impurity modes and secondary features in the Raman spectra of $CdBr_2$ *and* $CdCl_2$.
Chemical Physics Letters, **1986**, 131, 540 - 544

[101] D. J. Lockwood
Lattice vibrations of $CdCl_2$, $CdBr_2$, $MnCl_2$, *and* $CoCl_2$: *infrared and Raman spectra.*
Journal of the Optical Society of America, **1972**, 63, 374-382

[102] C. A. Cody, L. DiCarlo, R. K. Darlington
Vibrational and thermal study of antimony oxides.
Inorganic Chem., **1979**, 18, 6, 1572-1576

[103] B. S. Naidu, M. Pandey, V. Sudarsan, R. K. Vatsa, R. Tewari
Photoluminescence and Raman spectroscopic investigations of morphology assisted effects in Sb_2O_3.
Chem. Phys. Letters, **2009**, 474, 180-184

[104] C. Svensson
Refinement of the crystal structure of cubic antimony trioxide, Sb_2O_3.
Acta Crystallographica B, **1975** , 31, 2016-2018

[105] R. D. Shannon
Revised effective ionic radii and systematic studies of interatomic distances in halides and chalcogenides.
Acta Crystallographica, **1976**, A32, 751-767

[106] W. L. Jolly
Modern Inorganic Chemistry.
1984, McGraw-Hill, New York

[107] K. Dihlstroem
Ueber den Bau des wahren Antimontetroxyds und des damit isomorphen Stibiotantalits, $SbTaO_4$.
ZAAC, **1938**, 239, 57-64

[108] K. M. Ok, N. S. P. Bhuvanesh, P. S. Halasyamani
$SbSb_xM_{1-x}O_4$ (M = Nb(V) or Ta(V)): solid solution behavior and second-harmonic generating properties.
Journal of Solid State Chemistry, **2001**, 161, 57-62

[109] G. R. Teller, M. R. Antonio, J.F. Bradzil, R. K. Grasselli
New materials syntheses: Characterization of some metal-doped antimony oxides.
Journal of Solid State Chemistry, **1986**, 64, 249-260

[110] P. H. Fourcroy, D. Carre, J. Rivet
Structure cristalline de l'iodure de zinc ZnI_2.
Acta Crystallographica B, **1978**, 34, 3160-3162

[111] R. Stahl, C. Jung, H. D. Lutz, W. Kockelmann, H. Jacobs
Kristallstrukturen und Wassetoffbrueckenbindungen bei beta-$Be(OH)_2$ und epsilon-$Zn(OH)_2$.
ZAAC, **1998**, 624, 1130-1136

[112] A. Norlund Christensen
The crystal structure of gamma-$Zn(OH)_2$.
Acta Chemica Scandinavica, **1969**, 23, 2016-2020

[113] H. D. Lutz
Bonding and structure of water molecules in solid hydrates. Correlation of spectroscopic and structural data.
Structure and Bonding, **1988**, 69, 97-127

[114] H. D. Lutz, H. J. Christian
Raman and infrared spectra of barium and strontium halide monohydrates, $MX_2{\cdot}1H_2O$ (M = Ba, Sr; X = Cl, Br, I). A new interpretation of the frequency shiftings of OH stretching modes in solid hydrates.
Journal of Molecular Structure, **1982**, 96, 61

[115] O. Kristiansson, A. Eriksson, J. Lindgren
Hydration of Ions in Aqueous Solutions Studied by Infrared Spectroscopy. II. Application.
Journal of Acta Chemica Scandinavica, **1984**, A38, 613-618

[116] H. D. Lutz, W. Eckers, H. Haeuseler
OH stretching frequencies of solid hydroxides and of free OH^- ions .
Journal of Molecular Structure, **1982**, 80, 221-224

[117] J. C. Owrutsky, N. H. Rosenbaum, L. M. Tack, R. J. Saykallya
The vibration-rotation spectrum of the hydroxide anion (OH^-).
Journal of Chemical Physics, **1985**, 83, 5338-5339

[118] H. J. Werner, P. Rosmus, E. A. Reinsch
Molecular properties from MCSCF-SCEP wave functions. I. Accurate dipole moment functions of OH, OH^-, and OH^+.
Journal of Chemical Physics, **1983**, 79, 905-916

[119] M. Maltese, W. J. Orville-Thomas
The infrared spectra and structure of some complex hydroxosalts.
Journal of Inorganic and Nuclear Chemistry, **1967**, 29, 2533-2544

[120] H. D. Lutz, W. Eckers, H. Schneider, H. Haeuseler
Raman and infrared spectra of barium and strontium hydroxides and hydroxide hydrates.
Spectrochimica Acta, **1981**, 37A, 561-567

[121] G. R. Desiraju, T. Steiner
The weak hydrogen bond in structural chemistry and biology.
1999 , Oxford University Press Inc. New York

[122] V. A. Nikitenko, V. G. Plekhanov, S. V. Mukhin, M. V. Tkachev
Raman spectra of oxide zinc powders and single crystals.
J. Appl. Spectroscopy, **1996**, 63, 2, 290-292

[123] V. I. Ponomarev, O.S. Filipenko, L.O. Atovmyan, N. V. Rannev, S. A. Ivanov, Yu. N. Venevtsev
Structure and lattice dynamics of $SbNbO_4$ *crystals at 300-1000 K.*
ZAAC, **1962**, 318, 89-106

[124] V. I. Ponomarev, O.S. Filipenko, L.O. Atovmyan, N. V. Rannev, S. A. Ivanov, Yu. N. Venevtsev
Structure and lattice dynamics of $SbNbO_4$ *crystals at 300-1000 K.*
Phase Transition, **1992**, 38, 127-220

[125] R. F. W. Bader
Atoms in molecules. A Quantum Theory. **1990**, Oxford University Press: New York

[126] I. R. Beattie, P. J. Jones, B. R. Bowsher, T. R. Gilson
Gas phase Raman spectrum of cadmium iodide (CdI_2 *) and of a 1:8 mol ratio of cesium iodide to cadmium iodide.*
Vibrational Spectroscopy, **1993**, 4(3), 373-6

[127] J. D. Grice, J. T. Szymanski, J. L. Jambor
The crystal structure of clinoatacamite, a new polymorph of $Cu_2(OH)_3Cl$.
Canadian Mineralogist, **1996**, 34, 73-78

[128] T. Malcherek, J. Schlueter
Structures of the pseudo-trigonal polymorphs of $Cu_2(OH)_3$ *Cl.*
Acta Crystallographica B, **2009**, 65(3), 334-341

[129] H. R. Oswald, Y. Iitaka, S. Locchi, A. Ludi
Die Kristallstrukturen von $Cu_2(OH)_3Br$ *und* $Cu_2(OH)_3$ *I.*
Helvetica Chimica Acta, **1961**, 44, 2103-2109

[130] E. V. Sokolova, Yu. K. Egorov-Tismenko
Realization of the spinel structural type in the structure of beta-$Cd_2(OH)_3Cl$.
Kristallografiya, **1990**, 35, 995-997 E. V. Sokolova, Yu. K. Egorov-Tismenko
Realization of the spinel structural type in the structure of beta-$Cd_2(OH)_3Cl$.
Soviet Physics, Crystallography, **1990**, 35, 585-586

[131] Y. Cudennec, Y. Gerault, A. Lecerf
Synthese et structure cristalline de beta-$Cd_2(OH)_3Cl$.
Comptes Rendus Hebdomadaires des Seances de l'Academie des Sciences, Ser. II, **1997**, 324, 457-466

[132] A. Castro, I. Rasines, M. C. Sanchez-Martos, P. Garcia-Casado
Refinement of structural parameters for polycrystalline $CdSb_2O_6$*: a comparison of two methods.*
Powder Diffraction, **1988**, 3(4), 219-221

[133] A. Bystroem
Calcium pyroantimonates and similar compounds.
Arkiv foer Kemi, Mineralogi och Geologi, A, **1945**, 18(21), 8-8

[134] B. Bentria, D. Benbertal, Z. Hebboul, M. Bagieu-Beucher, A. Mosset
Polymorphism of anhydrous cadmium iodate. Structure of epsilon - $(Cd(IO_3)_2)$.
ZAAC **2005**, 631, 894-901

[135] L. Gulzari, G. K. Chadha, G. C. Trigunayat
Crystal structures of six new polytypes of cadmium iodide.
Acta Crystallographica, **1971**, B27, 2293-2298

[136] C. Stalhandske
Cadmium oxide chloride, $Cd_3O_2Cl_2$.
Crystal Structure Communications **1982**, 11, 1543-1547

[137] J. R. Rea, E. Kostiner
Cadmium fluorophosphate, Cd_2PO_4F.
Acta Crystallographica B **1974**, 30, 2901-2903

[138] A. Ivanov, M. A. Simonov, N. Belov
Kristallicheskaya struktura Cd-khlorapatita $Cd_5(PO_4)_3Cl$.
Zhurnal Strukturnoi Khimii **1976**, 17, 375-378

[139] O. Tougait, J. A. Ibers, A. Mar
Manganese antimony diselenide iodide $MnSbSe_2I$.
Acta Crystallographica C, **2003**, 59, 77-78

[140] C. Doussier, Y. Moelo, P. Leone
Synthesis and crystal structures of four new bromo-chalcogenides: $MnSbS_2Br$, $MnBiSe_2Br$ *and two allotropic forms of* $MnSbSe_2Br$*. Crystal chemistry of the* $MnPnQ_2X$ *family (Pn: Sb, Bi; Q: S, Se; X: Cl, Br, I).*
Solid State Sciences, **2006**, 8(6), 652-659

[141] H. Noel, J. Padiou
Structure cristalline de $FeUS_3$.
Acta Crystallographica B, **1976**, 32, 1593-1595

[142] A. Pfitzner, M. Zabel, F. Rau
Preparation and crystal structure of $MnBiSe_2I$.
ZAAC, **2005**, 631, 1439-1441

[143] A. Pfitzner, M. Zabel, F. Rau
Preparation and crystal structure of $MnBiS_2Br$.
Monatshefte für Chemie - Chemical Monthly, **2005**, 136, 1977-1983

[144] C. Doussier, P. Léone, Y. Moëlo
Single crystal structure and magnetic properties of $MnSbS_2Cl$.
Solid State Sciences, **2004**, 6, 1387-1391

[145] C. Doussier, G. André, P. Léone, E. Janod, Y. Moëlo
Magnetic study of two isotypic manganese chloro-sulfides: $MnSbS_2Cl$ *and the new compound* $MnBiS_2Cl$.
Journal of Solid State Chemistry, **2006**, 179(2), 486-491

[146] M.J. Buerger, T. Hahn
The crystal structure of berthierite, $FeSb_2S_4$.
American Mineralogist, **1955**, 40, 226-238

[147] L. Wang, Y-Ch. Hung, S-J. Hwu, H-J. Koo, M.- H. Whangbo
Synthesis, structure, and properties of a new family of mixed framework chalcohalide semiconductors: $CdSbS_2X$ *(X = Cl, Br),* $CdBiS_2X$ *(X = Cl, Br), and* $CdBiSe_2X$ *(X = Br, I).*
Chemistry of Materials, **2006**, 18(5), 1219-1225

[148] L. G. Sillén, A. S. Gjoerling-Husberg
Roentgenuntersuchung von Calcium/Wismutoxychloriden und -oxybromiden.
ZAAC, **1941**, 248, 121-134

[149] D. O. Charkin, P. S. Berdonosov, V.A. Dolgikh, P. Lightfoot
A reinvestigation of quaternary layered bismuth oxyhalides of the Sillen X1 type.
Journal of Solid State Chemistry, **2003**, 175, 316-321

[150] L. G. Sillén, A. S. Gjoerling-Husberg
Die Verbindungen $BaBiO_2Cl$ *und* $BaBiO_2Br$.
ZAAC, **1941**, 248, 135-136

[151] M. A. Kennard, J. Darriet, J. Grannec, A. Tressaud
Cation ordering in the Sillen X1-type oxychloride, $BaBiO_2Cl$.
Journal of Solid State Chemistry, **1995**, 117, 201-205

[152] L. G. Sillén
Roentgenuntersuchung von $LiBi_3O_4Cl_2$ *und verwandten Stoffen.*
ZAAC, **1939**, 242, 41-46

[153] L. G. Sillén, E. Joernstad
Einige gemischte Wismutoxyjodide.
ZAAC, **1942**, 250, 173-198

[154] D. O. Charkin, P. S. Berdonosov, A. M. Moisejev, R. R. Shagiakhmetov, V. A. Dolgikh, P. Lightfoot
A Novel Family of Layered Bismuth Compounds I. The Crystal Structures of $Pb_{0.6}Bi_{1.4}Cs_{0.6}O_2Cl_2$ *and* $Pb_{0.6}Bi_{3.4}Cs_{0.6}O_4Cl_4$.
Journal of Solid State Chemistry, **1999**,147, 527

[155] S. Fray, C. J. Milne, P. Lightfoot
Synthesis and structure of $CaBiO_2Cl$ *and* $SrBiO_2Cl$*.*
Journal of Solid State Chemistry, **1997**, 128, 115-120

[156] S. D. Kirik, E. G. Yakovleva, A. F. Shimanskii, Yu. G. Kovalev
$CdBiO_2Cl$*: synthesis and powder structure solution.*
Acta Crystallographica C, **2001**, 57, 1367-1368

[157] M. Gillberg
Perite, a new oxyhalide mineral from Langban, Sweden.
American Mineralogist, **1961**, 46, 765-765

[158] L. G. Sillen, L. Melander
X-ray studies on the oxihalide minerals nadorite (ochrolite) $PbSbO_2Cl$ *and ekdemite.*
Zeitschrift fuer Kristallographie, Kristallgeometrie, Kristallphysik, Kristallchemie, **1941**, 103, 420-430

[159] J. Ketterer, V. Kraemer
Structural characterization of the synthetic perites $PbBiO_2X$*, X=I, Br, Cl.*
Materials Research Bulletin, **1985**, 20, 1031-1036

[160] A. Pfitzner, P. Pohla
Syntheses and crystal structures of $PbSbO_2Br$*,* $PbSbO_2I$*, and* $PbBiO_2Br$*.*
ZAAC, **2009**, 635(8), 1157-1159

[161] P. Pohla
Quaternaere Oxidhalogenide der Gruppe 15
Universitaet Regensburg, Institut fuer Anorganische Chemie, Dissertation **2010**

[162] M. Braeu
Gruppe 11 und 12 Halogenide als präparatives Hilfsmittel.
Thesis, **2007**, University of Regensburg, Department of Inorganic Chemistry

[163] F. Thuillier-Chevin, P. Maraine, G. Perez
Structure cristalline du chlorodioxoantimoniate de baryum $BaSbO_2Cl$*.*
Revue de Chimie Minerale, **1980**, 17, 102-109

[164] G. Giuseppetti, C. Tadini
Riesame della struttura cristallina della nadorite: $PbSbO_2Cl$*.*
Periodico di Mineralogia **1973**, 42(3), 335-345

[165] A. Astroem, S. Andersson
The crystal structure of L-SbOF.
Journal of Solid State Chemistry, **1973**, 6, 191-194

[166] J. D. Lindberg, D. G. Snyder
Determination of the optical absorption coefficient of powdered materials whose particle size distribution and refractive indices are unknown.
Applied Optics, **1973**, 12, 573-578

[167] A. Lipka
An X-ray structure redetermination of antimony trichloride.
Acta Crystallographica B, **1979**,35, 3020-3022

[168] Z. Mayerova, M. Johnsson, S. Lidin
The crystal structure of $CuSb_2O_3Br$*: slabs from cubic* Sb_2O_3 *interspersed between puckered hexagonal CuBr-type layers.*
Journal of Solid State Chemistry, **2005**,178(11), 3471-3475

[169] Z. Mayerova, M. Johnsson, S. Lidin
Lone-Pair Interfaces That Divide Inorganic Materials into Ionic and Covalent Parts.
Angew. Chem. Int. ed., **2006**,45(34), 5602-5606

[170] Z. Hugonin, M. Johnsson, S. Lidin
$Cu_{20}Sb_{35}O_{44}Br_{37}$ *- one structure, two temperature dependencies.*
Solid State Sciences, **2008**,10(2), 160-167

[171] R. Becker, M. Johnsson, R. K. Kremer, H. H. Klauss, P. Lemmens
Crystal Structure and Magnetic Properties of $FeTe_2O_5X$ *(X = Cl, Br): A Frustrated Spin Cluster Compound with a New Te(IV) Coordination Polyhedron.*
Journal of the American Chemical Society, **2006**,128, 15469-15475

[172] M. Johnsson, S. Lidin, K. W. Toernroos, H.B. Buergi, P. Millet
Host-guest compounds in the family of tellurium-nickel oxohalogenides.
Angew. Chem. Int. ed., **2004**, 43(33), 4292-4295

[173] R. Becker, M. Johnsson, H. Berger
Crystal Structure of the New Cobalt Tellurite Chloride $Co_5Te_4O_{11}Cl_4$.
ZAAC, **2007**, 633(3), 422-424

[174] R. Becker, M. Prester, H. Berger, M. Johnsson, D. Drobac, I. Zivkovic
Crystal structure and magnetic properties of the new cobalt tellurite halide $Co_5(TeO_3)_4X_2$ *(X = Cl, Br).*
Solid State Sciences, **2007**, 9(3-4), 223-230

[175] R. Becker, H. Berger, M. Johnsson, M. Prester, Z. Morohnic, M. Miljak, R. Herak
Crystal structure and magnetic properties of $Co_2TeO_3Cl_2$ *and* $Co_2TeO_3Br_2$.
Journal of Solid State Chemistry, **2006**, 179(3), 836-842

[176] M. Wilkinson, J. Cable, W. C. Koehler
Neutron diffraction investigations of the magnetic ordering in $FeBr_2$, $CoRr_2$, $FeCl_2$, *and* $CoCl_2$.
Physical Review, **1959**, 113, 497-507

[177] Yang Wei-jun, Tang Mo-tang, Jin Sheng-ming
Thermal decomposition kinetics of antimony oxychloride in air.
Trans. Nonferrous Met. Soc. China, **2002**, 12, 156-159

[178] H. Lueken
Magnetochemie.
1999, B. G. Teubner Stuttgart

[179] L. Costa, P. Goberti, G. Paganetto, G. Camino, P. Sgarzi
Thermal behaviour of chlorine-antimony fire-retardant systems.
Polymer Degradation and Stability, **1990**, 30, 17

[180] A. Sabanejew
The action of water on antimonius chloride.
Zeitschrift fuer Chemie, **1871**, 204-207

[181] C. Lea, J. K. Wood
System antimonious oxide-hydrochloric acid-water.
Journal of the Chemical Society, Transactions, **1924**, 125, 137-48

[182] M. Edstrand
On the crystal structure of the antimony oxychloride $Sb_4O_5Cl_2$ and isomorphous oxybromide.
Acta Chemica Scandinavica, **1947**, 178-203

[183] C. Saernstrand
The crystal of antimony (III) chloride oxide $Sb_4O_5Cl_2$.
Acta Crastallographica B, **1978**, 34, 2402-2407

[184] X. Y. Chen, H. S. Huh, S. W. Lee
Hydrothermal synthesis of antimony oxychloride and oxide nanocrystals: $Sb_4O_5Cl_2$, $Sb_8O_11Cl_2$, and Sb_2O_3.
Journal of Solid State Chemistry, **2008**, 2127-2132

[185] H. Katzke, Y. Oka, Y. Kanke, K. Kato, T. Yao
Structure of triantimony tetraoxide chloride, Sb_3O_4Cl: twinning and one-dimensional disorder.
Zeitschrift fuer Kristallographie, **1999**, 214, 284-289

[186] Z. Hugonin, M. Johnsson, S. Lidin
Two for the price of one - Resolvable polymorphism in a 'single crystal' of alpha- and beta- Sb_3O_4I.
Solid State Sciences, **2009**, 11(1), 24-28

[187] F. Sgarlata
Struttura cristallina dell' onoratoite.
Periodico di Mineralogia, **1970**, 39, 315-328

[188] S. Lidin, M. Johnsson, Z. Hugonin
Modulations in the onoratoite system.
Solid State Sciences, **2009**, 11(11), 1198-1205

[189] M. Edstrand
On the structure of antimony(III) oxidehalides. II. The crystal structure of SbOCl.
Arkiv foer Kemi, **1953**, 6, 89-112

[190] V. Kraemer
The crystal structure of ferroelastic antimony(III) oxide iodide alpha Sb_5O_7I.
Acta Crystallographica B, **1975**, 31, 234-237

[191] V. Kraemer
The crystal structure of the ferroelastic/ferroelectric 2MA polytype of antimony(III) oxide iodide, Sb_5O_7I.
Acta Crystallographica B, **1978**, 34, 2695-269

[192] W. Altenburger, W. Hiller, I. R. Jahn
Crystal structure of the high-temperature phase of antimony(III) oxide iodide, polytype 2HA-Sb_5O_7I.
Zeitschrift fuer Kristallographie, **1987**, 181, 227-234

[193] A. Lipka
An X-ray structure redetermination of antimony trichloride.
Acta Crystallographica B, **1979**, 35, 3020-3022

[194] I. D. Brown
The chemical bond in inorganic chemistry. The bond valence model.
2002, Oxford University Press

[195] M. Fontana, G. Maisano, P. Migliardo, C. Vasi and, F. Wanderlingh
Raman scattering and melting point in $SbCl_3$.
Optica Acta **1980**, 27, 8, 1087-1093

[196] S. Menchetti, C. Sabelli, R. Trosti-Ferroni
The structures of onoratoite, $Sb_8O_{11}Cl_2$ and $Sb_8O_{11}Cl_2(H_2O)_6$.
Acta Crystallographica **1984**, C 40, 1506-1510

[197] Z. Hugonin, M. Johnsson, S. Lidin
Two for the price of one - Resolvable polymorphism in a 'single crystal' of alpha- and beta- Sb_3O_4I.
Solid State Sciences **2009**, 11(1), 24-28

[198] V. Kraemer
The crystal structure of ferroelastic antimony(III) oxide iodide alpha Sb_5O_7I.
Acta Crystallographica **1975**, B 31, 234-237

[199] V. Kraemer
The crystal structure of the ferroelastic/ferroelectric 2MA polytype of antimony(III) oxide iodide, Sb_5O_7I.
Acta Crystallographica **1978**, B 34, 2695-2698

[200] V. Kraemer, M. Schuhmacher, R. Nitsche
Synthesis and crystal growth of new antimony(III)-oxide-iodides.
Material Research Bulletin **1973**,8, 65-74

[201] S. Pohl, W. Saak
Zur Polymorphie von Antimontriiodid. Die Kristallstruktur von monoklinem SbI_3.
Zeitschrift fuer Kristallographie **1984**, 169, 177-184

Software

[A] EDAX, *Genesis*, Version 4.52, **2005**.

[B] Stoe WinXPOW, Version 1.08, STOE & Cie. GmbH, Darmstadt **2000**.

[C] FaceIt Video, Version 1.35d p3i, STOE & Cie. GmbH, Darmstadt **2000**.

[D] X-Area Softwarepaket, Version 1.35, STOE & Cie GmbH.

[E] XPREP-*Data Preparation & Reciprocal Space Exploration*, Version 5.1/NT, Bruker Analytical X-ray Systems, Madison, Wisconsin, USA **1997**.

[F] L. J. Farrugia, WinGX, *An Integrated System of Windows Programs for Solution, Refinement and Analysis of Single Crystal X-Ray Diffraction Data*, Version 1.70.01, University of Glasgow, Glasgow, Scotland **2005**.

[G] SIR92, *A program for crystal structure solution*
Altamare, A., Cascarano, G. Giacvazzo, C., Guagliardi, A.
J. Appl. Cryst. **1993** 26, 343-350

[H] G.-M. Sheldrick, SHELXS-86, *Program for the Solution of Crystal Structures*, Göttingen **1986**.

[I] G.-M. Sheldrick, SHELXS-97, *Program for the Solution of Crystal Structures*, Göttingen **1997**.

[J] G. M. Sheldrick, SHELXL-97, *Program for the Solution and Refinement of Crystal Structures*, University of Göttingen, Germany **1997**.

[K] A. L. Spek, PLATON - *A Multipurpose Crystallographic Tool*, Universität Utrecht, Netherlands **2007**.

[L] X-RED 32, Version 1.31, STOE & Cie. GmbH, Darmstadt **2005**.

[M] X-SHAPE, Version 2.07, STOE & Cie. GmbH, Darmstadt **2005**.

[N] K. Brandenburg, H. Putz, Endeavour, Version 1.5, Crystal Impact GbR, Bonn **2007**.

[O] Diamond, Version 3.0a, Crystal Impact GbR, Bonn **2007**.

[P] CRYSTALS; D. J. Watkin, General Crystallographic Software, Including Graphics.
Chemical Crystallography Laboratory: http://www.xtl.ox.ac.uk/

[R] JANA, *The Crystallographic Computing System*
V.Petříček, M. Dušek, Inst. Of Physics, Academy of Siences of the Czech Republic.
http://www-xray.fzu.cz/jana/jana.html

[S] Bruins Instruments OMEGA software with database function, Version 3.3, **1991**

[T] Resolutions Pro, (Molecular Spectroscopy Solutions) Version 4.1.0.101, Varian Inc.,
http://www.varianic.com

[U] CRYSTAL03, Version 1.0.44
V.R. Saunders, R. Dovesi, C. Roetti, R. Orlando, C.M. Zicovich-Wilson, N.M. Harrison, K. Doll, B. Civalleri, I.J. Bush, Ph. DÕArco, M. Llunell, Theoretical Chemistry Group at the University of Torino, and the Computational Materials Science Group at the Daresbury Laboratory in Cheshire, England.

[W] BOND VALENCE CALCULATOR, Version 2.0, February 1993.
Version 1.0 by Chris Hormillosa & Sean Healy. Revisions and additions by Tamon Stephen